Experimental and Numerical Modelling of Gravity Currents Preceding Backdrafts

---

A thesis submitted in partial fulfilment
of the requirements for the Degree
of Master of Engineering in Fire Engineering
in the University of Canterbury
by J. D. McBryde

University of Canterbury
Christchurch, New Zealand
2008

ABSTRACT

This study investigates the turbulent mixing within gravity currents preceding backdrafts and validates the ability of the computational fluid dynamics (CFD) software Fire Dynamics Simulator version 4 (FDS) to simulate these flows. Backdrafts are rapid deflagrations, which occur after the introduction of oxygen into compartments containing unburned gaseous fuel. They may form large fireballs out of the compartment opening and present a significant hazard to the safety of fire-fighters. Gravity currents which precede backdrafts are responsible for the formation of flammable gas mixtures required for ignition.

Scale saltwater modelling is used to generate Boussinesq, fully turbulent gravity currents for five different opening geometries, typical of fire compartments. Width-integrated concentration fields and two-dimensional velocity fields are generated using the non-intrusive light attenuation (LA) and particle tracking velocimetry (PTV) flow visualisation techniques respectively. Numerical simulations are carried out with FDS to replicate these flows. The experimental and numerical results are compared directly.

Front velocities are shown to be governed directly by local buoyancy conditions, in the later stages of the flows, and therefore the initial conditions associated with the opening geometries only influence the front velocities indirectly. The internal concentration structure, internal velocity structure and location of potential flammable regions are found to be highly opening geometry dependent. In general, the results of the numerical simulations are quantitatively similar to those from experiment, which suggests that the numerical model realistically predicted the experimental flows. However, the numerical concentration fields appear slightly lumpier than those from the experiments, possibly due to unresolved turbulence on scales smaller than the numerical grid ($0.01H$, where H = compartment height).

ACKNOWLEDGEMENTS

Firstly, I would like to thank my supervisors, Dr Roger Nokes, Dr Mark Davidson and Dr Charlie Fleischmann, for helping me throughout the research process and giving me the inspiration to begin this research in the first place.

I would also like to extend my gratitude to the University of Canterbury Fluids Laboratory technicians, Ian Sheppard and Kevin Wines, who helped sort out any technical difficulties associated with the experimental side of my project.

I am thankful for the financial support I have received to support during this research and would like to thank the Institute of Professional Engineers New Zealand (IPENZ), the New Zealand Fire Service (NZFS), the Todd Foundation and the University of Canterbury for their contributions.

Thank you to the other postgraduate students in the Masters of Fire Engineering degree and to Langford and Gustaaf in the Fluid Mechanics laboratory for your support, assistance and advice throughout the project.

TABLE OF CONTENTS

LIST OF FIGURES

LIST OF TABLES

LIST OF SYMBOLS

Lower Case Latin

Symbol	Definition	Units
a	Empirical constant relating dye concentration to light attenuation	$kg^{-1}.m^2$
b	Rate of light attenuation with no dye	m^{-1}
c	Mean across-channel dye concentration	$kg.m^{-3}$
c_0	Reference dye concentration	$kg.m^{-3}$
c_{max}	Maximum dye concentration	$kg.m^{-3}$
c_p	Specific heat at constant pressure	$J.kg^{-1}.K^{-1}$
d	Optical thickness of fluid	-
f	Calibration constant	-
$\overline{f}$	External force vector	$m.s^{-2}$
g	Gravitational acceleration	$m.s^{-2}$
g'	Reduced gravity	$m.s^{-2}$
$\overline{g}$	Gravitational acceleration vector	$m.s^{-2}$
h	Gravity current height	m
h_{ent}	Sensible enthalpy	$m^{2}.s^{-2}$
h_f	Width of dyed fluid	m
k	Thermal conductivity	$W.m^{-1}.K^{-1}$
k_{LES}	Smagorinsky conductivity	$W.m^{-1}.K^{-1}$
m	Mass of fluid	kg
$\hat{n}$	Unit vector	-
p	Distance along a light ray	m
$\overline{q}$	Radiative and convective heat	J
$\dot{q}'''$	Net heat gain from sources and sinks	$W.m^3$
t	Time	s
t^*	Dimensionless time	-
$\Delta t_{initial}$	Initial time step for numerical simulation	s
u	Velocity component in x-direction	$m.s^{-1}$

$\bar{u}$	Velocity vector	$m.s^{-1}$
v	Velocity component in y-direction	$m.s^{-1}$
w	Velocity component in z-direction	$m.s^{-1}$
x	Horizontal co-ordinate lengthways down compartment	m
x^*	Dimensionless distance lengthways down compartment	-
y	Horizontal co-ordinate across width of compartment	m
z	Vertical co-ordinate	m
z^*	Dimensionless distance vertically	-

Upper Case Latin

Symbol	Definition	Units
A	Area of compartment opening	m^2
A_L	Cross-sectional area of lock	m^2
C_i	Component fraction of total fuel	-
C_Q	Discharge co-efficient	-
C_s	Empirical Smagorinsky constant	-
D	Mass diffusivity	$m^2.s^{-1}$
H	Compartment height	m
H_o	Compartment opening height	m
I	Light intensity	-
I_0	Reference light intensity	-
$I_{\max}$	Light intensity at the maximum fluid dye concentration	-
FL_{comp}	Composite flammable limit	%
FL_i	Component flammable limit	%
Fr	Froude number with based on compartment height	-
Fr_{local}	Froude number with based on head height	-
M	Molecular weight	$kg.mol^{-1}$
P	Pressure	$kg.m^{-1}.s^{-2}$
P^*	Dimensionless pressure	-
Pr	Prandtl number	-
$Pr_{turbulent}$	Turbulent Prandtl number	-

Q	Volumetric flow-rate	$m^3.s^{-1}$
Q_{mass}	Mass flow-rate	$kg.s^{-1}$
R	Relative concentration	-
Re	Reynolds number with based on compartment height	-
Re_{local}	Reynolds number with based on head height	-
Re_x	Reynolds number based on distance from leading edge	-
R_g	Universal gas constant	$J.K^{-1}.mol^{-1}$
S	Dilution	-
$\lvert S \rvert$	Magnitude of the stress Tensor	s^{-1}
Sc	Schmidt number	-
$Sc_{turbulent}$	Turbulent Schmidt number	-
T	Temperature	K
T^*	Dimensionless temperature	-
U	Velocity scale	$m.s^{-1}$
W	Compartment width	m
W_o	Compartment opening width	m
Y_s	Salt mass fraction	-

Greek Symbols

Symbol	Definition	Units
β	Dimensionless density difference	-
β_{comp}	Dimensionless density difference relative to compartment fluid	-
$\beta_{initial}$	Dimensionless initial density difference	-
δ	Turbulent boundary layer thickness	m
δ_v	Viscous sub-layer thickness	m
δ_x	Cell-size in the x-direction	m
δ_y	Cell-size in the y-direction	m
δ_z	Cell-size in the z-direction	m
Δ	Characteristic cell length	m
η	Rate of light attenuation	m^{-1}

κ	Thermal diffusivity	$m^2.s^{-1}$
λ	Empirical constant	-
μ	Dynamic viscosity	$kg.m^{-1}.s^{-1}$
μ_{LES}	Smagorinsky viscosity	$kg.m^{-1}.s^{-1}$
ν	Kinematic viscosity	$m^2.s^{-1}$
ρ	Density	$kg.m^{-3}$
ρ_{comp}	Initial density of compartment	$kg.m^{-3}$
ρ^*	Dimensionless density	-
$\Delta\rho$	Density difference	$kg.m^{-3}$
$\Delta\rho_{initial}$	Initial density difference	$kg.m^{-3}$
τ_0	boundary shear stress	$N.m^{-2}$
τ_{ij}	viscous stress tensor	$N.m^{-2}$
υ^*	friction velocity	$m.s^{-1}$
ϕ	Dimensionless head height	-
Ω	Empirical constant	-

Chemical Symbols

CH_4	Methane
CO	Carbon monoxide
CO_2	Carbon dioxide
H_2O	Water
N_2	Nitrogen
NaCl	Sodium Chloride
O_2	Oxygen

Abbreviations

2D	Two-dimensional
3D	Three-dimensional
CFD	Computational fluid dynamics
DNS	Direct numerical simulation
FDS	Fire dynamics simulator
LA	Light attenuation

LED	Light emitting diode
LES	Large eddy simulation
LFL	Lower flammable limit
LOC	Limiting oxygen concentration
MMC	Maximum matching cost
MOC	Minimum oxygen concentration
NIST	National Institute of Standards and Technology
PIV	Particle image velocimetry
PTV	Particle tracking velocimetry
RAM	Random access memory
RANS	Reynolds averaged Navier-Stokes equations
SHS	Sub grid scale
UFL	Upper flammable limit
VBC	Velocity boundary condition

CHAPTER 1 INTRODUCTION

1.1 Backdrafts

Backdrafts are rapid deflagrations, which occur after the introduction of oxygen into compartments containing unburned gaseous fuel. They may form large fireballs, which propagate rapidly through, and out of, the compartment, presenting a significant hazard to the safety of fire-fighters.

Backdrafts have been responsible for a large number of fire-fighter fatalities (Bukowski 1996; Dunne 2002; Grimwood and Desmet 2003; Hume 2005). Typically, the fire-fighters were involved in search and rescue or suppression operations and did not observe warning signs commonly found in fire service training manuals (Grimwood and Desmet 2003). Delayed backdrafts have been reported to occur as long as 45 minutes after the arrival of the fire service and the initial application of water to the fire (Dunne 2002). Fire-fighters often manually ventilate fire compartments, by opening doors or breaking windows. However, this action may generate backdrafts rather than preventing them (Fleischmann 1994). Ventilation may also occur as the fire burns through walls or ceiling assemblies, or as heat fractures glass windows. In fire-fighting operations, backdrafts seem to be happening more frequently, possibly because buildings are now better sealed against draughts to improve energy efficiency (Bukowski 1996; Foster and Roberts 2003).

The following scenario has been used to describe the conditions that lead to backdrafts (Fleischmann 1994; Foster and Roberts 2003; Gottuk et al. 1999; Hume 2005). Backdrafts occur in under-ventilated compartment fire situations, where a hot smoky layer builds up and descends on the fire as it continues to burn. This leads to incomplete combustion and the accumulation of unburned gaseous fuel inside the compartment. Eventually the fire will consume enough oxygen to drop levels below the flammable limit, causing the flame to fluctuate, extinguish, or start smouldering (see Figure 1-1 part 1). If a source of ventilation is introduced to the compartment, due to a door opening or window breaking, a density-driven flow, or gravity current, of cool ambient air will flow into the compartment at ground level, while an exchange flow of hot compartment gases will flow out (see Figure 1-1 part 2). As the dense gravity current travels into the compartment, it generates turbulence, which mixes oxygen with the unburned combustion gases along the interface between the two flows,

creating a flammable mixture (see Figure 1-1 part 3). If the flammable mixture comes into contact with an ignition source, a rapidly propagating flame, or deflagration, will form and result in a blast-wave and possibly a fireball out of the compartment opening (see Figure 1-1 parts 3 to 6). This deflagration moving through the compartment and out of the opening is commonly termed a backdraft.

Past research, investigating gravity currents preceding backdrafts, has focused on the bulk flow characteristics, but the internal flow structure of these flows has not been studied in detail. The internal flow structure is important because internal turbulent mixing processes are responsible for formation of flammable mixtures prior to backdrafts (Fleischmann 1994; Foster and Roberts 2003). Greater levels of mixing increase backdraft severity. Therefore, a better understanding of the internal flow structure of gravity currents preceding backdrafts is essential to improve the understanding of, and ability to predict, backdrafts.

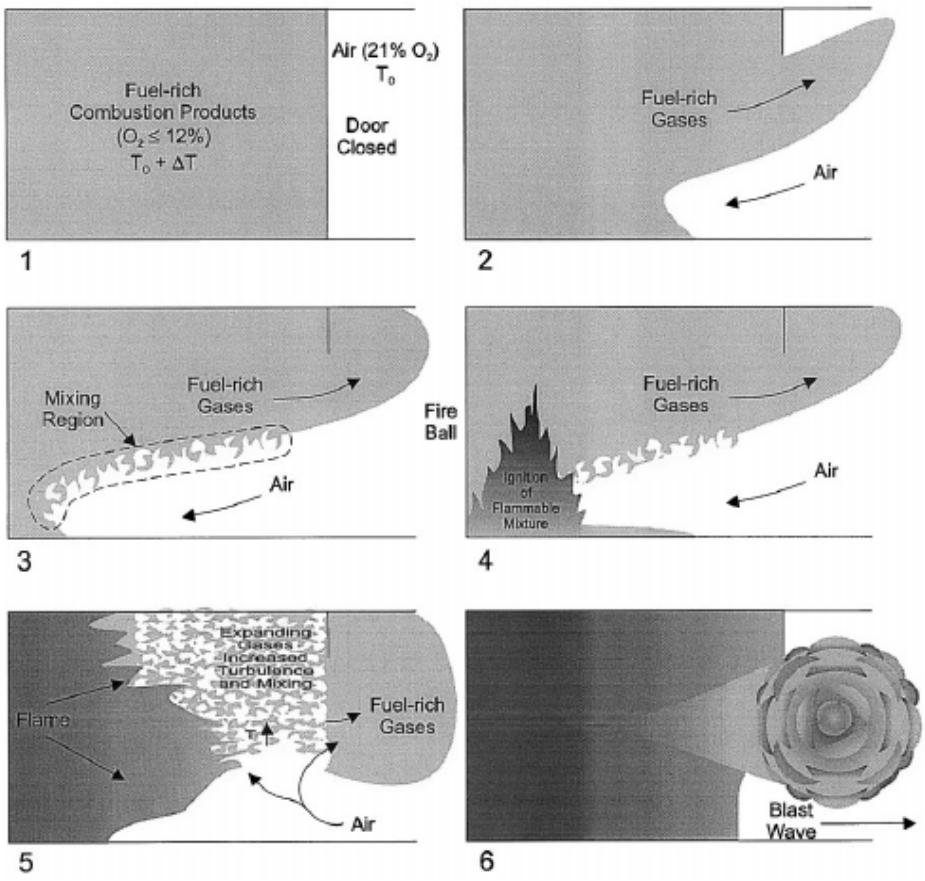

Figure 1-1: Steps in the development of backdrafts. This figure is an extract from Gottuk et al. (1999))

A recent literature study by Hume (2005) concluded that a better understanding of backdrafts, and the circumstances under which they occur, is needed to:

- allow better guidance and training to be given to the fire service.
- allow the development of more effective fire fighting tactics to detect and deal with potential backdraught conditions.
- allow consideration to be given to revision of the building codes for new buildings, to reduce the chance of backdrafts occurring and their severity should they occur.

1.2 Research Objectives and Scope

This study will focus on the experimental and numerical modelling of gravity currents preceding backdrafts and investigate the turbulent mixing that occurs within these flows. Experimentally, saltwater modelling and non-intrusive quantitative flow visualisation techniques will be applied. Numerically, these flows will be modelled using the computational fluid dynamics (CFD) software Fire Dynamics Simulator version 4 (FDS) (McGrattan 2005).

There are two major research objectives in the present study:

- To quantify the effect of different compartment opening geometries on the bulk flow characteristics and internal flow structure of gravity currents preceding backdrafts.
- To validate the ability of FDS to simulate these flows, by direct comparison of experimental and numerical results.

1.3 Outline

A literature review is presented in Chapter 2. Flammability of gas mixtures is discussed and the feasibility of using saltwater modelling to replicate backdraft gravity currents is presented. Past research into backdraft gravity currents is summarised and general flow dynamics, typical of all fully turbulent gravity currents, are outlined.

In Chapter 3 detail of the computational fluid dynamics software Fire Dynamics Simulator Version 4 (FDS) is provided. The mathematical basis of the model is outlined and a summary of past validation research for this model is presented.

Chapter 4 outlines the experimental approach adopted in this research. Experimental methodologies and equipment are detailed and an overview is provided of the Light Attenuation (LA) and Particle Tracking Velocimetry (PTV) flow visualisation techniques. The limitations and errors associated with these experimental techniques are described.

Chapter 5 describes how FDS was used in this research to simulate the experimental flows. The inputs and outputs of the model are presented and detail of an input parameter sensitivity analysis is presented.

In Chapter 6, the analysis methods which were used to process the experimental and numerical data are presented. Details of the co-ordinate system and dimensionless variables are summarised and bulk front characteristics are defined. The process used to determine the flow regions which correlate to flammable mixtures in backdraft gravity currents is outlined.

Chapter 7 presents and discusses the experimental and numerical results. The results generated from different compartment opening geometries are examined and comparisons are made between the experimental and numerical results. Comparisons to literature are also made where appropriate.

Finally, Chapter 8 draws conclusions from the research and outlines recommendations for the direction of possible future research.

CHAPTER 2 LITERATURE REVIEW

2.1 Introduction

Gravity currents are buoyancy driven flows generated by fluid density differences. They are encountered in a large variety of environmental and man-made situations, from avalanches to oil slicks. Gravity current flows are also responsible for the formation of flammable mixtures prior to backdrafts, and so play a crucial role in the occurrence and severity of backdrafts.

Flammable gas mixtures are discussed in Section 2.2. The feasibility of using scaled saltwater flows to investigate backdraft gravity currents is discussed in Section 2.3. In Section 2.4, the extent of past research into backdraft gravity currents is outlined. Finally, details of the general flow dynamics, typical of all fully turbulent gravity current flows, are presented in Section 2.5.

2.2 Flammable Mixtures

Three-conditions are necessary for fire: 1- fuel, 2- an oxidiser (typically oxygen), 3- heat energy (Perry et al. 1997). If any one of these conditions is not present, a fire will not occur, and if one is removed from a fire it will be extinguished.

Gravity currents preceding backdrafts are responsible for forming flammable mixtures, as they mix oxygen rich ambient air with unburned combustion gases (Fleischmann 1994). As ambient air and combustion gases are mixed together, the ratio of oxygen, dilutent (any gas which is not directly involved in the combustion, typically nitrogen and carbon dioxide) and fuel is altered, and a premixed gas mixture is created.

Premixed flames can only propagate within a limited range of fuel/oxidant/dilutent compositions (Beyler 2002). For a fuel/air mixture, the lower flammable limits (LFL) and upper flammable limits (UFL) define the limiting concentrations of fuel which will propagate a flame. However, for a more general representation of the flammable limits, a flammability diagram is required. The flammability diagram defines the limits of the flammability envelope, within which lie all possible flammable mixtures of fuel/oxidant/dilutent. A schematic of a flammability diagram, for fuel/nitrogen/oxygen mixtures, is shown in Figure 2-1. The concentration (percent by volume) of nitrogen and fuel are indicated by the x and y

axis respectively. The concentration of oxygen is inferred from the difference between the sum of the concentrations of the other two gases and 100 percent. The flammable region is shaded grey on the diagram, and the boundary of this region (or flammability envelope) is represented by a dashed line.

The flammability diagram may be used to understand the formation of flammable mixtures in gravity currents preceding backdrafts. Fresh air contains 21% oxygen and 79% nitrogen, by volume (Karlsson and Quintiere 2000), and is indicated by point D in Figure 2-1. Prior to backdrafts, non-flammable gas mixture of air, nitrogen and fuel would exist within the compartment. Oxygen levels would be low due to the fire consuming sufficient oxygen to self-extinguish. The limiting oxygen concentration (LOC) is the concentration of oxygen below which flames will not burn at any fuel concentration. In general, organic gases and vapours will not burn below 10.5% oxygen by volume (Perry et al. 1997), indicating the approximate oxygen concentration at which fires would self-extinguish. However, smouldering occurs at even lower oxygen concentrations.

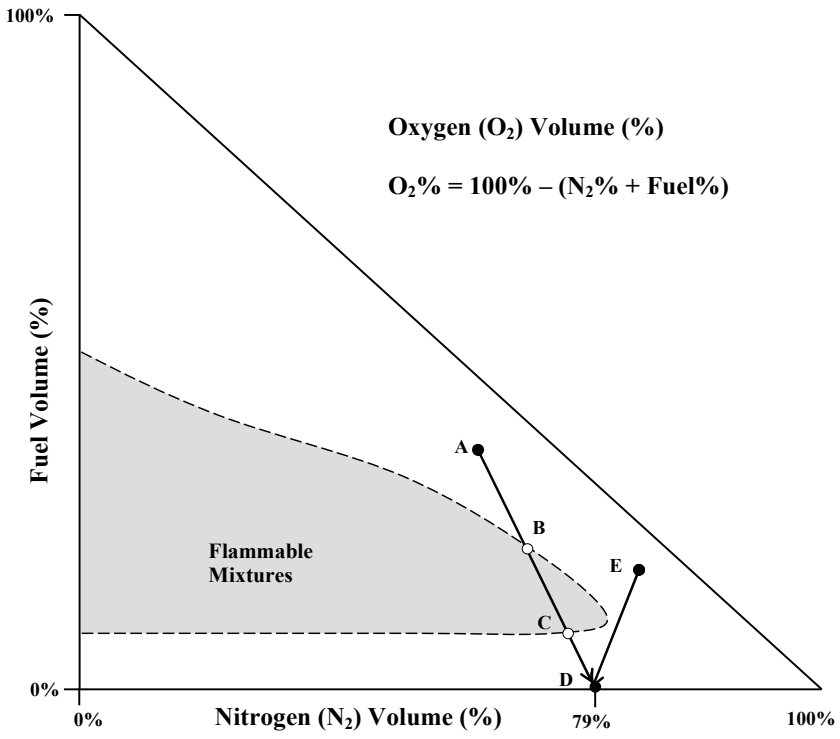

Figure 2-1: Two-axis flammability diagram. The area shaded grey represents flammable mixtures. The dotted line indicates the flammability envelope. Not to scale.

Two possible initial conditions are represented by points A and E in Figure 2-1. Ventilation of the compartment would generate a gravity current, which mixed ambient fresh air with the compartment gases. Variations in the gas mixture composition that occur during the ventilation process are represented by the ventilations lines A → D and E → D. Flammable mixtures exist only where these lines lie within the flammability envelope. Line A → D lies within the flammable envelope between points B and C, so has the potential to form a backdraft if an ignition source is present. However, as line E → D never passes within the flammability envelope, it would be unable to produce a backdraft.

For the ventilation lines to cross the flammability envelope, a minimum initial fuel concentration must exist in the compartment prior to ventilation, a concept which has been confirmed experimentally. The minimum mass fraction for backdrafts is 10% for methane fuel (Fleischmann 1994) and 16% for diesel fuel (Gottuk et al. 1999). Research also indicates that increasing the concentration of unburned hydrocarbons increases a backdrafts severity (Fleischmann 1994; Gottuk et al. 1999; Weng and Fan 2003). For example, for methane mass fractions between 10% and 15% small fireballs were produced, whereas mass fractions greater than 15% resulted in the formation of large fireballs out of the compartment opening (Fleischmann 1994).

2.3 Scale Saltwater Modelling

The concept of using scaled saltwater models to investigate gas and smoke flows was first formally documented by Steckler et al (1986). Since then, the use of saltwater modelling in the fire research community has increased. The use of scaled salt-water experiments, instead of full scale fire tests, is desirable as they are relatively inexpensive and can be easily dyed or seeded with particles, enabling excellent flow visualisation (Klote and Milke 2002; Linden 1999; Steckler et al. 1986). At reduced scales, turbulent flows can be achieved more easily using water as the fluid medium, because the kinematic viscosity of water is lower than that of air (Linden 1999). Also, fire experiments have much harsher environments than those with water, making accurate measurements more difficult (Steckler et al. 1986; Tieszen 2001).

The flow of hot air spreading across a ceiling into cooler ambient air has the same dynamics as saltwater spreading across the floor into fresh water (Baum et al. 1995). The driving force, a buoyancy force produced by density differences, is the same, so the two processes can be

related when the viscous and heat transfer effects are small (Baum et al. 1995; Steckler et al. 1986). Therefore, the results of scaled saltwater models can be used to investigate full-scale fire scenarios. The similarity of these flows can be investigated by performing a dimensional analysis and through analysis of the non-dimensional governing equations.

The Boussinesq assumption is made, which assumes that variations in fluid properties (viscosity, thermal diffusivity and mass diffusivity), except density, are completely ignored and that density variations are only included in terms involving gravity. This assumption is justified when the density difference between fluids is small (density differences less than approximately 10% (Shin et al. 2004)), which is relevant for some, but not all, backdraft gravity currents (as discussed in Section 2.3.4).

2.3.1 Initial Conditions

In past backdraft experiments, the compartment initial conditions (temperatures and mass fractions), which existed prior to compartment ventilation, were found to be relatively well mixed (Fleischmann 1994; Gottuk et al. 1999). Therefore, it is appropriate to use uniformly mixed salt and fresh water solutions to represent compartment gases and ambient air respectively.

2.3.2 Dimensional Analysis

A dimensional analysis identifies the significant dimensionless variables that govern both Boussinesq backdraft gravity currents and the equivalent flow in fresh and saltwater. A schematic showing the important parameters of the flow is presented in Figure 2-2. The parameters include both independent and dependent variables. The independent variables are those that are either selected or can be determined before the flow occurs. The dependent variables are unknown prior to the flow and so are influenced by the independent variables.

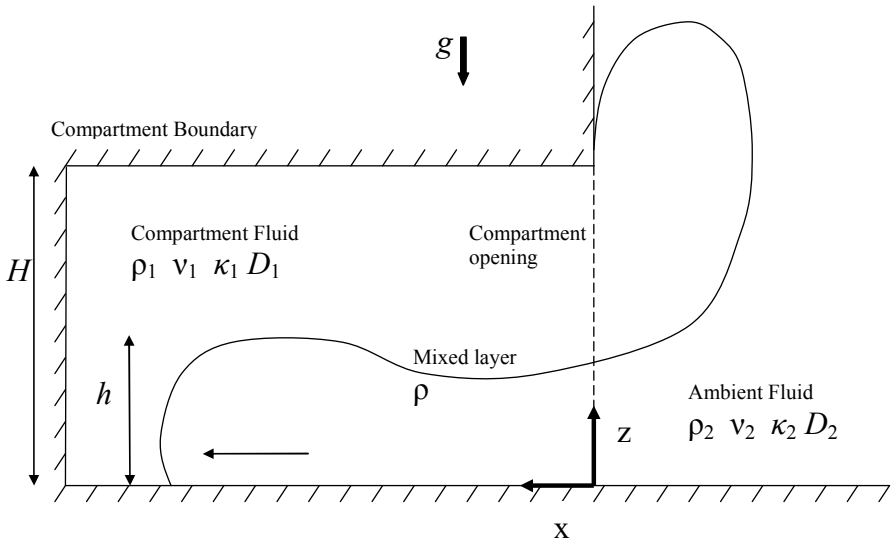

Figure 2-2: Schematic of a backdraft gravity current.

Independent variables:

$H =$ compartment height

$g =$ gravity

$\left.\begin{matrix}\rho_1 \\ \rho_2\end{matrix}\right] =$ initial fluid densities

$\nu =$ fluid viscosity

$\kappa =$ fluid thermal diffusivity

$D =$ fluid mass diffusivity

$t =$ time

$\left.\begin{matrix}x \\ y \\ z\end{matrix}\right] =$ distance co-ordinates

Important dependent variables:

$h(t) =$ gravity current head height

$\rho(x,y,z,t) =$ density of mixed fluid

$$\bar{u} = \begin{bmatrix} u(x,y,z,t) \\ v(x,y,z,t) \\ w(x,y,z,t) \end{bmatrix} = \text{velocity vector}$$

$$\left.\begin{matrix} u(x,y,z,t) \\ v(x,y,z,t) \\ w(x,y,z,t) \end{matrix}\right] = \text{fluid velocity in the x, y and z directions respectively}$$

Using dimensional analysis these variables may be reduced to a number of non-dimensional parameters that characterise the flow, as presented in Equation (2-1) to Equation (2-9).

$\beta = \frac{|\rho_2 - \rho|}{\rho_2} = \frac{\Delta\rho}{\rho_2}$ non-dimensional density difference (relative to the ambient fluid) (2-1)

$\beta_{initial} = \frac{|\rho_2 - \rho_1|}{\rho_2}$ initial non-dimensional density difference, $\rho = \rho_1$ (2-2)

$Fr = \frac{u}{\sqrt{\beta_{initial} g H}}$ Froude number (dimensionless velocity) (2-3)

$\mathrm{Re} = \frac{uH}{\nu}$ Reynolds number (2-4)

$\mathrm{Pr} = \frac{\nu}{\kappa}$ Prandtl number (2-5)

$Sc = \frac{\nu}{D}$ Schmidt number (2-6)

$t^* = \frac{t\sqrt{\beta_{initial} g H}}{H}$ non-dimensional time (2-7)

$x^* = \frac{x}{H}$ non-dimensional distance (2-8)

$\phi = \frac{h}{H}$ non-dimensional head height (2-9)

There is some subjectivity in the selection of the scales. By multiplying the non-dimensional variables with one another, other non-dimensional variables can be generated. For example, alternative definitions of Froude number and Reynolds number, based on the head height of the gravity current flow instead of the compartment height, are shown in Equation (2-10) and Equation (2-11) respectively.

$Fr_{local} = \frac{u}{\sqrt{\beta_{initial} g h}}$ local Froude number (gravity current head height used as length scale) (2-10)

$$\mathrm{Re}_{local} = \frac{uh}{\nu}$$ local Reynolds number (gravity current head height used as length scale) (2-11)

Temporal changes in density may be defined relative to the initial density difference, as shown in Equations (2-12) and (2-13).

$$S = \frac{\Delta\rho_{initial}}{\Delta\rho} = \frac{\beta_{initial}}{\beta}$$ dilution, relative to the initial density difference ($0 =$ compartment fluid, $\infty =$ ambient fluid) (2-12)

$$R = \frac{\Delta\rho}{\Delta\rho_{initial}} = \frac{\beta}{\beta_{initial}} = \frac{1}{S}$$ relative concentration / relative density ($0 =$ ambient fluid, $1 =$ compartment fluid) (2-13)

2.3.3 Dimensionless Governing Equations

Various forms of the dimensionless equations of motion that govern buoyant flows of both thermally driven gas and density driven saltwater flows have been formally documented by past researchers (Clement 2000; Rehm and Baum 1978; Rehm et al. 1997; Steckler et al. 1986). A dimensionless form of the governing equations, applicable to buoyancy driven gravity current flows, is developed below.

Gravity currents are driven by buoyancy forces, which typically generate differences in pressure significantly less than atmospheric pressure, 101kPa (Street et al. 1996), so the flow is assumed to be incompressible. Backdraft gravity currents occur prior to ignition so the flow is assumed to be inert.

The motion for an incompressible, inert buoyancy driven flow may be described by Equations (2-14) to (2-17) (Fleischmann 1994; Weng and Fan 2002). The equations represent conservation of mass, momentum and stratifying species respectively (where the stratifying species can be either temperature or salt mass). The stratifying species equation is different for temperature driven flows (Equation (2-16)) and salt concentration driven flows (Equation (2-17)).

Applicable to temperature and salt concentration driven flow

$$\frac{\partial\rho}{\partial t} + \nabla.(\rho\bar{u}) = 0$$ mass (2-14)

$$\rho\left[\frac{\partial \overline{u}}{\partial t}+\left(\nabla \cdot \overline{u}\right)\overline{u}\right]+\nabla P-\rho\overline{g}=\rho\nu\nabla^2\overline{u} \qquad \text{momentum} \qquad (2\text{-}15)$$

Applicable to temperature driven flow

$$\frac{\partial T}{\partial t}+(\overline{u}\cdot\nabla)T=\kappa\nabla^2 T \qquad \text{stratifying species - temperature} \qquad (2\text{-}16)$$

Applicable to salt concentration driven flow

$$\frac{\partial Y}{\partial t}+(\overline{u}\cdot\nabla)Y=D\nabla^2 Y \qquad \text{stratifying species – salt concentration} \qquad (2\text{-}17)$$

where: $\overline{u}=$ velocity vector

$t=$ time

$\rho=$ density

$P=$ pressure

$\nu=\frac{\mu}{\rho}=$ kinematic viscosity

$\mu=$ dynamic viscosity

$\overline{g}=$ gravitational acceleration vector

$T=$ temperature

$\kappa=\frac{k}{\rho c_p}=$ thermal diffusivity

$c_p=$ specific heat at constant pressure

$Y_s=$ salt mass fraction

$D=$ mass diffusivity

Making the Boussinesq assumption and manipulating the mass and momentum equations, reduces them to the form shown in Equations (2-14) and (2-15).

Applicable to temperature and salt concentration driven flow

$$\nabla.\overline{u}=0 \qquad \text{mass} \qquad (2\text{-}18)$$

$$\frac{\partial \overline{u}}{\partial t}+\left(\nabla\cdot\overline{u}\right)\overline{u}+\frac{1}{\rho}\nabla P-\beta\overline{g}=\nu\nabla^2\overline{u} \qquad \text{momentum} \qquad (2\text{-}19)$$

where: $\beta g=g'=$ reduced gravity

Non-dimensional variables can be defined by selecting scales relevant to the flow (Street et al. 1996). Relevant scales include a length scale, H, and a density scale, $\Delta\rho$. For flows such as this, in which no natural velocity scale exists, a velocity scale based on a typical length scale and the reduced gravity is commonly used, as shown in Equation (2-20). Past research (Marino et al. 2005; Shin et al. 2004; Simpson 1997) has shown that dimensionless velocities (using this scale) collapse for Boussinesq flows.

$$U = \sqrt{\beta_{initial} g H} \qquad (2\text{-}20)$$

Using these scales, the following dimensionless variables are created:

$$\nabla^* = H\nabla \quad \text{dimensionless del operator} \qquad (2\text{-}21)$$

$$t^* = \frac{tU}{H} \quad \text{dimensionless time} \qquad (2\text{-}22)$$

$$\bar{u}^* = \frac{\bar{u}}{U} = \hat{n}Fr \quad \text{dimensionless velocity} \qquad (2\text{-}23)$$

$$\rho^* = \frac{\rho}{\Delta\rho} \quad \text{dimensionless density} \qquad (2\text{-}24)$$

$$P^* = \frac{P_s}{\Delta\rho U^2} \quad \text{dimensionless pressure} \qquad (2\text{-}25)$$

$$T^* = \frac{T}{T_2} \quad \text{dimensionless temperature} \qquad (2\text{-}26)$$

where: H = compartment height

ρ_2 = ambient fluid density

T_2 = ambient fluid temperature

U = velocity scale

$\hat{n}$ = unit vector

The dimensionless form of the governing equations for mass and momentum are presented in Equation (2-27) and (2-28) respectively.

Applicable to temperature and salt concentration driven flow

$$\nabla^* \cdot \bar{u}^* = 0 \qquad \text{mass} \qquad (2\text{-}27)$$

$$\frac{\partial \bar{u}^*}{\partial t^*} + \left(\nabla^* \cdot \bar{u}^*\right)\bar{u}^* + \frac{1}{\rho^*}\nabla^* P^* - 1 = \frac{Fr}{\mathrm{Re}}\nabla^{*2}\bar{u}^* \qquad \text{momentum} \qquad (2\text{-}28)$$

The dimensionless conservation of species equations are presented in Equations (2-29) and (2-30). The difference between these equations is the scaling factor for the molecular transport terms. The Prandtl number (Pr) governs the diffusion of heat (for heated gas flows), while the Schmidt number (Sc) governs the diffusion of salt (for saltwater flows).

Applicable to gas flow (temperature driven)

$$\frac{\partial T^*}{\partial t^*} + (\bar{u}^* \cdot \nabla^*)T^* = \frac{Fr}{\mathrm{Pr}\,\mathrm{Re}}\nabla^{*2}T^* \qquad \text{stratifying species - temperature} \qquad (2\text{-}29)$$

Applicable to water flow (salt mass driven)

$$\frac{\partial Y}{\partial t^*} + (\bar{u}^* \cdot \nabla^*)Y = \frac{Fr}{Sc\,\mathrm{Re}}\nabla^{*2}Y \qquad \text{stratifying species - salt mass} \qquad (2\text{-}30)$$

The dimensionless variables from the development of these dimensionless governing equations are presented in Equations (2-21) to (2-26) and in Equations (2-31) to (2-35) below. These dimensionless variables are the same as those developed using the dimensional analysis in Section 2.3.2.

$$\beta = \rho^* = \frac{\Delta\rho}{\rho} \qquad \text{Dimensionless density difference} \qquad (2\text{-}31)$$

$$Fr = \frac{\bar{u}^*}{\hat{n}} = \frac{\bar{u}}{\hat{n}\sqrt{\beta g H}} \qquad \text{Froude Number} \qquad (2\text{-}32)$$

$$\mathrm{Re} = \frac{\bar{u}H}{\hat{n}\nu} \qquad \text{Reynolds Number} \qquad (2\text{-}33)$$

$$\mathrm{Pr} = \frac{\nu}{\kappa} \qquad \text{Prandtl Number} \qquad (2\text{-}34)$$

$$Sc = \frac{\nu}{D} \qquad \text{Schmidt Number} \qquad (2\text{-}35)$$

2.3.4 Limitations

A number of limitations must be considered when saltwater flows are used to investigate thermally driven flows:

Molecular Transport Terms

Exact matching of the Schmidt and Prandtl numbers would achieve exact dynamic similarity between hot gas flows and saltwater flows. However, a typical Sc for salt water is 700, while a typical Pr for air is 0.7 (Frederikse and Lide 1997), so matching the Pr and Sc is not feasible for gas and water flows. Fortunately, at large Reynolds numbers (Re), Pr and Sc independence is achieved and the inconsistency in the conservation of stratifying species equation becomes unimportant (Steckler et al. 1986). Gravity current flows essentially become independent of viscous and diffusive effects for $\mathrm{Re} > 1000$ (Linden 1999) and the gravity currents which occur prior to full scale backdrafts have Re of the order of $5\times10^3 < \mathrm{Re} < 5\times10^4$ (Fleischmann 1994). Therefore, saltwater may be used to simulate gas flows without matching Pr and Sc, when the flows are fully turbulent. At typical scales relevant to smoke transport in residential scale fire scenarios, numerical simulations have been found to be relatively insensitive to the Pr/Sc number magnitude (McGrattan et al. 1994).

Boundary Conditions

A limitation of using saltwater experiments to model gas flows, is that species transfer through the compartment boundaries is not accounted for (Steckler et al. 1986). For a heated gas flow, heat will be lost to enclosure boundaries by conduction and radiation. Conduction involves heat transfer from one material to another by direct contact and molecular processes and radiation is the exchange of thermal energy by electromagnetic waves. The net heat flux is proportional to the temperature difference between a heated surface and the surroundings (Incropera and DeWitt 2001). This energy loss is impractical to simulate, by means of salt transfer, in saltwater flows, so saltwater flows will retain buoyancy slightly longer than the corresponding gas flows. Saltwater flows are therefore not suitable for modelling high temperature gas flows where heat transfer effects are important, but may be used for Boussinesq flows, where the temperatures are low enough that heat transfer effects become negligible (Klote and Milke 2002).

Density Differences

For backdraft gravity currents, the magnitude of density differences is dependent on gas temperatures, which are in turn dependent on heat loss to compartment boundaries and the time until the compartment is ventilated. In a real-life backdraft incident, fire fighters reported a warm, but not hot, exhaust of gas from the compartment as they forced open the compartment door just prior to a backdraft (Bukowski 1996). Delayed backdraft have been reported to occur as long as 45 minutes after the arrival of the fire service and the initial application of water to the fire (Dunne 2002). In backdraft experiments by Fleischmann (1994) (using methane Fuel) and Gottuk (1999) (using diesel fuel), typical experimental compartment gas temperatures reached 550˚C - 700˚ deg C, as the fire self-extinguished, but cooled to 350˚C - 420˚C prior to backdraft.

It is expected that compartment gas temperatures prior to backdraft may range from near ambient levels, to approximately 700ºC. Using tabulated air densities from DiNenno (2002), the corresponding temperature induced dimensionless density difference ranges from $\beta_{initial} \sim 0.0$ to $\beta_{initial} \sim 0.7$.

In saltwater gravity current flows, density differences are caused by differences in the dissolved salt (sodium chloride - NaCl) concentration. The range of density differences achievable is approximately $0.0 \leq \beta_{initial} \leq 0.2$ (Frederikse and Lide 1997), approximately twice the Boussinesq limit, but still much lower than density differences achievable in air. At larger density differences the flow characteristics become dependent on $\beta_{initial}$, so any extrapolation of results to non-Boussinesq flows should be tentative.

2.4 Gravity Currents Preceding Backdrafts

Past research (Fleischmann 1994; Foster and Roberts 2003) of full and half residential scale backdraft has demonstrated that the extent of mixing in backdraft gravity currents is dependent on the opening geometry, the location of the ignition source and the time from compartment ventilation until ignition. These dependencies are all associated with the turbulent mixing that occurs. The greater this mixing, the greater the volume of flammable mixture produced and the more severe the backdraft (Foster and Roberts 2003).

2.4.1 Opening Geometries

A number of different compartment end-wall opening geometries are possible, including windows, doors, and skylights. The exchange flow formed at these openings would initially spread axi-symmetrically, but once the gravity current has spread laterally and reached the side walls of the compartment, the flow would be largely two-dimensional. Experiments carried out by Fleischmann (1994), over a variety of opening geometries in the end wall of a rectangular compartment (shown in Figure 2-3), showed that even flows passing through highly three-dimensional openings (windows and doors) spread rapidly, becoming predominantly two-dimensional in approximately 1.5 compartment depths.

The different possible ceiling opening geometries (shown in Figure 2-4) were investigated by Weng (2002a) and were located in the ceiling at one end of the compartment. For these openings, the transition to a predominantly two-dimensional flow occurred at approximately three compartment depths, twice that for the end-wall opening geometries of Fleischmann (1994).

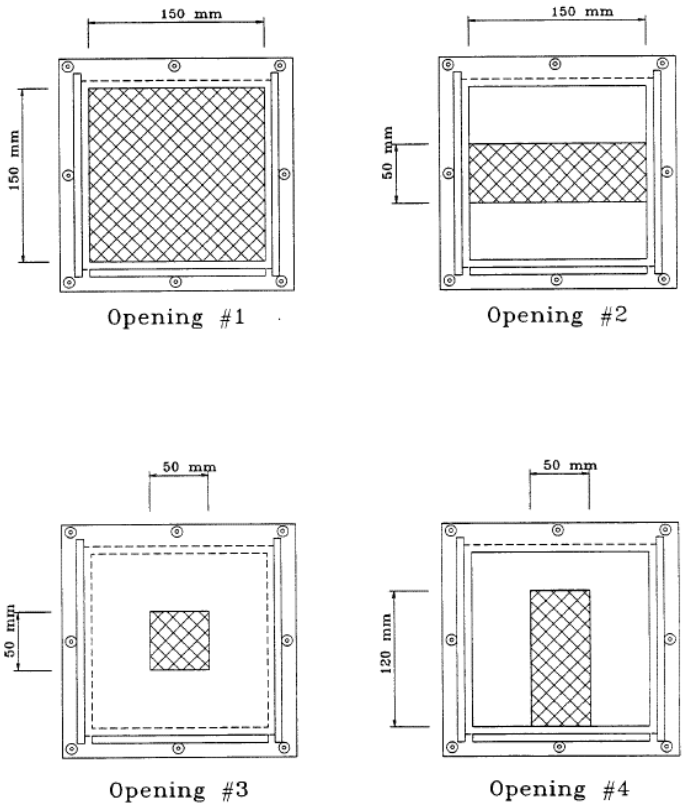

Figure 2-3: Different end-wall compartment opening geometries investigated by Fleischmann (1994). This figure is an extract from Fleischmann (1994).

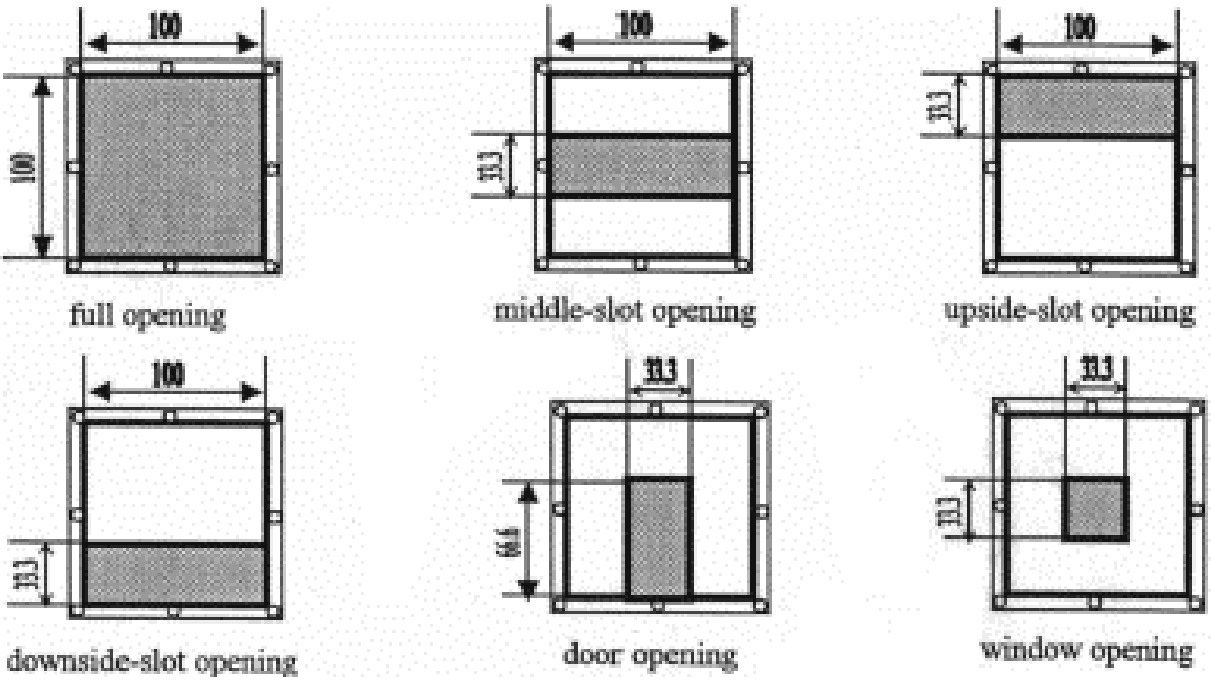

Figure 2-4: Different ceiling compartment opening geometries investigated by Weng (2002a). This figure is an extract from Weng (2002a).

2.4.2 Compartment Opening Mass-flow

An exchange flow develops as saltwater flows out of a compartment opening and is replaced by freshwater. The volume flux through one half of a rectangular opening can be calculated from Equation (2-36) (Brown and Solvason 1962; Linden 1999), which was derived from the hydrostatic pressure differences and integration of the velocity profile for an ideal fluid. The discharge coefficient accounts for streamline contraction, which reduces the effective area of the opening. A value of approximately $C_Q = 0.6$ is appropriate for sharp edged orifices (Linden 1999), such as doors and windows.

$$Q = C_Q \frac{1}{3} A \left(g' H_o \right)^{\frac{1}{2}} \qquad (2\text{-}36)$$

where: $Q =$ volumetric inflow rate

$C_Q =$ dimensionless inflow or discharge coefficient

$A =$ area of rectangular compartment opening

$H_o =$ compartment opening height

$g' = \beta g =$ reduced gravity

By assuming no mixing occurs, the mass flow through the compartment may be calculated as the product of the volumetric flow rate and the density difference, which leads to the definition of the discharge coefficient in Equation (2-37).

$$C_Q = \frac{Q_{mass}}{\Delta\rho \frac{1}{3} A \left(g' H_o\right)^{\frac{1}{2}}} \qquad (2\text{-}37)$$

where: Q_{mass} = mass inflow rate

$\Delta\rho$ = density difference

The velocity profile that forms at the opening prior to a backdraft was investigated by Fleischmann (1994). Results from two-dimensional numerical simulations were compared to those from a series of velocity probes in a half-scale experimental backdraft compartment. The results showed that a quasi-steady exchange flow would quickly develop and that the numerical results fell within the error bounds associated with the experimental data. Typical velocity profiles are shown in Figure 2-5.

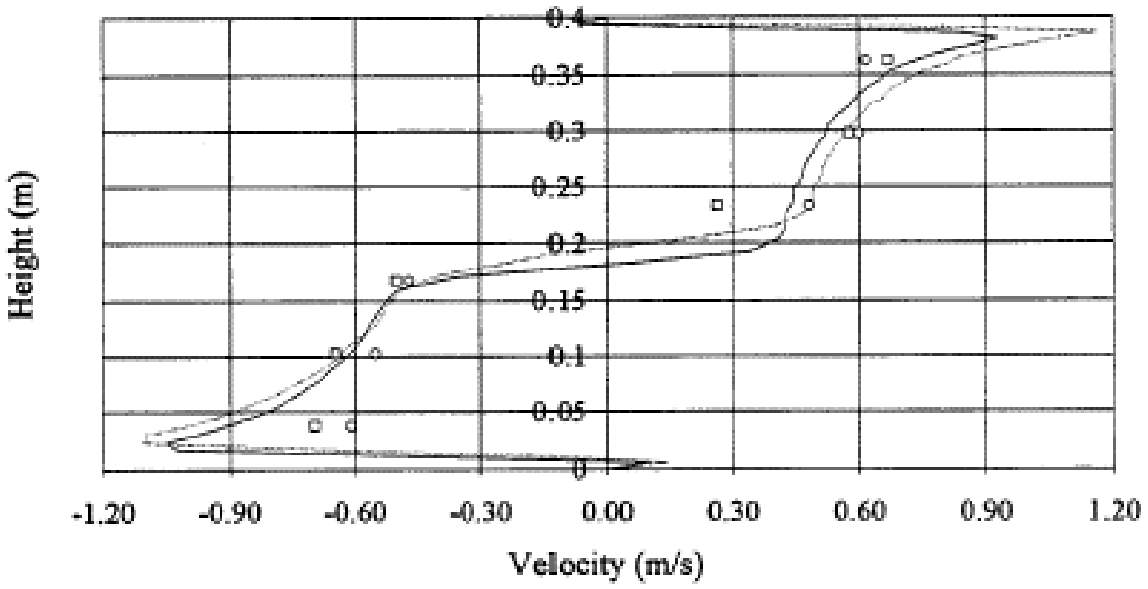

Figure 2-5: Velocity profiles at the compartment opening prior to backdraft for full compartment opening. The solid and dashed lines represent numerical simulations 4s and 8s after compartment was ventilated respectively. This figure is an extract from Fleischmann (1994).

The velocity structure of gravity currents prior to backdraft was studied by Weng (2002b) using scaled saltwater modelling and the particle image velocimetry (PIV) flow visualisation technique. Although the PIV technique generates detailed velocity field structures, the authors did not discuss the flow characteristics in detail and the results were not used to validate any numerical simulations.

2.4.3 Saltwater Modelling

Laboratory scale saltwater models have been used to investigate gravity currents prior to backdraft. Saltwater experiments have been conducted using a variety of different compartment opening geometries (see Figure 2-3 and Figure 2-4) to generate both two-dimensional and three-dimensional flows (Fleischmann 1994; Fleischmann and McGrattan 1999; Weng et al. 2002a; Weng and Fan 2002; Weng et al. 2002b). In all these experiments, phenolphthalein was used to identify the mixing region and the range of density differences investigated was limited to Boussinesq flows, $0.003 < \beta_{initial} < 0.10$. The time averaged average front velocity (Froude number) was found to be independent of $\beta_{initial}$, as shown in Figure 2-6, as was the time averaged gravity current visual head height .

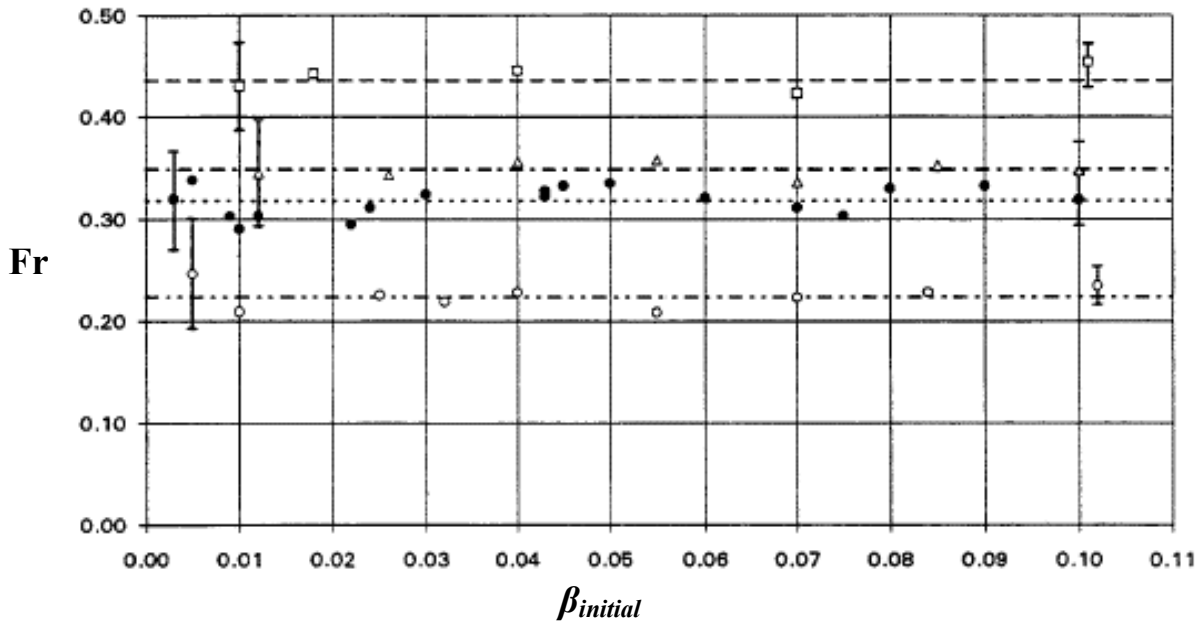

Figure 2-6: Plot of Froude number versus density difference for different compartment openings. Symbols: square = full, dark circle = horizontal slot, hollow circle = window, triangle = door. Horizontal lines represent the average value for each opening. This figure is an extract from Fleischmann (1994).

The dimensionless head height and Froude number for each end wall opening geometry are presented in Table 2-1 (Fleischmann 1994). These results show that the gravity current depth and velocity have a strong dependence on the opening geometry.

Similar measurements were made for the different ceiling opening geometries shown in Figure 2-4 (Weng et al. 2002a) and are presented in Table 2-2.

The internal flow structure of these flows was described qualitatively and indicated that the extent of the mixing within the gravity current was also highly dependent on the opening geometry, but relatively independent of density difference. These papers identified the need to apply improved flow visualisation techniques, to enable more flow detail to be resolved.

Table 2-1: Measurements of Froude number and dimensionless head height for different end wall opening geometries (Fleischmann 1994).

End wall Opening	Full	Middle-Slot	Door	Window
Fr	0.44	0.32	0.35	0.22
Visual head height	0.50	0.38	0.33	0.29

Table 2-2: Measurements of Froude number and dimensionless head height for different ceiling opening geometries (Weng et al. 2002a).

Ceiling Opening	Full	Middle-Slot	Door	Window	Downside-Slot	Upside-slot
Fr	0.39	0.33	0.30	0.24	0.31	0.34
Visual head height	0.50	0.41	0.44	0.35	0.40	0.40

2.4.4 Validation of Two-dimensional Numerical Simulations

The results of two-dimensional (2D) numerical simulations of backdraft gravity current have been compared to Boussinesq saltwater experiments (Fleischmann 1994; Fleischmann and McGrattan 1999). The numerical simulations were carried out using an early version of the source code to Fire Dynamics Simulator (FDS) (McGrattan 2005). A full compartment opening and horizontal slot opening were investigated and the front speed of the flow was found to be predicted accurately for the full opening, but under predicted for the horizontal opening. Due to limitations of the experimental flow visualisation technique, only qualitative comparison of the flow structure was possible, but the numerical and experimental results showed reasonable agreement, with similar scale turbulent structures. In addition, experiments on similar gravity current flows, by past researchers, showed similar flow structures to those predicted by the numerical simulations.

2.4.5 Validation of Three-dimensional Numerical Simulations

Three-dimensional numerical simulations, based on direct numerical simulation (DNS), have been compared to Boussinesq saltwater experiments (Weng and Fan 2002). The numerical simulations were carried out using Version 2.0 of FDS and direct numerical simulation (DNS), which assumes that the grid size is fine enough to capture all relevant turbulent length scales. Unfortunately, the grid resolution used in the simulations, compartment height divided by 60 (H/60), was likely to have been too course for the use of DNS to be justified. This may account for the poor match obtained between experimental and numerical results (see Figure 2-7 and Figure 2-8 and description below). The Large Eddy Simulation (LES) Smagorinsky sub-grid scale (SGS) turbulence model, which is available within the FDS software, may have been more appropriate, because it includes an eddy-viscosity model to account for turbulence on sub-grid scales.

Different ceiling opening geometries were investigated, as shown in Figure 2-4. The dimensionless transit times for the gravity current to reach the end wall of the compartment were compared for experiment and simulation, as shown in Figure 2-7 and Figure 2-8. The results from the numerical simulations were in agreement with experiment for the two-dimensional openings, but much less accurate for the three-dimensional openings, where the simulations overestimated transit times. The authors believed this was due to the coarse numerical grid. The internal flow structure was not investigated.

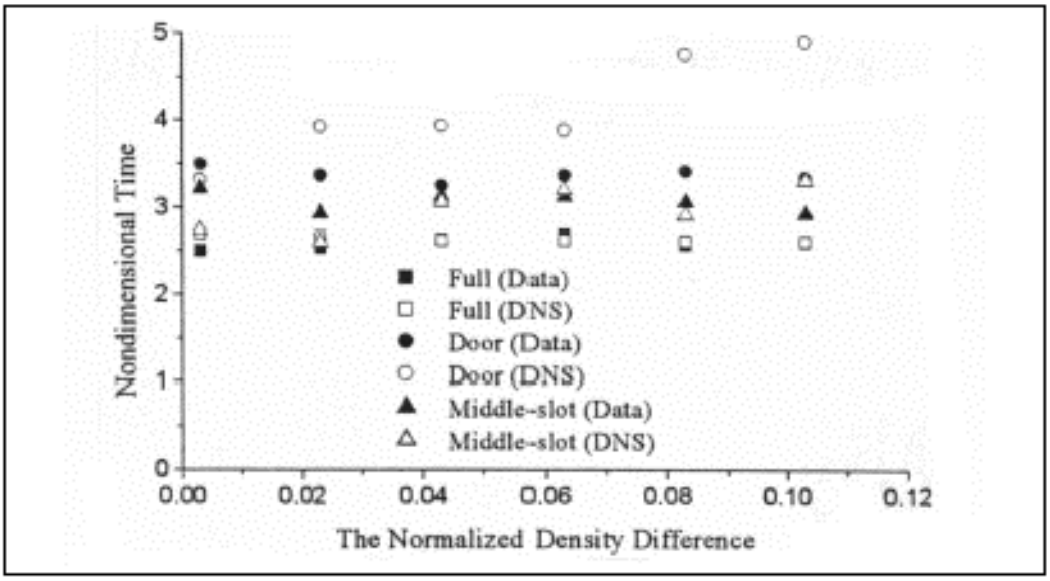

Figure 2-7: Dimensionless transit times to reach compartment end-wall versus density difference for different ceiling opening geometries; full, door and middle-slot. This figure is an extract from Weng and Fan (2002).

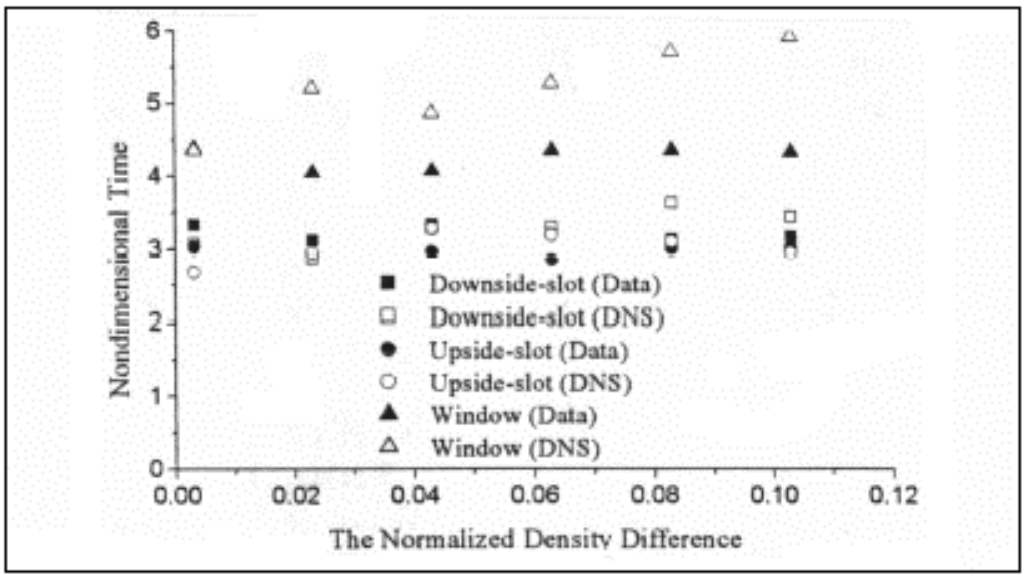

Figure 2-8: Dimensionless transit times to reach compartment end-wall versus density difference for different ceiling opening geometries; downside-slot, upside-slot and window. This figure is an extract from Weng and Fan (2002).

Three-dimensional numerical modelling, based on large eddy simulations (LES), has been used to simulate gravity currents preceding backdraft (Weng et al. 2005). The flows were simulated using Version 2 of FDS and LES, but no experimental comparison was made. A

variety of end-wall and ceiling opening geometries (similar to those in Figure 2-3 and Figure 2-4) were investigated. In this study, the dimensionless density difference was defined relative to the compartment fluid density as opposed to the ambient fluid density, as shown in Equation (2-38). The simulations were conducted for Boussinesq and non-Boussinesq flows, over the range of dimensionless density differences typical of real life backdraft, approximately $0.0 < \beta_{initial} < 0.7$ or $0.0 < \beta_{comp} < 2.3$ (in the Boussinesq limit $\beta_{initial} = \beta_{comp} \approx 0.0$).

$$\beta_{comp} = \frac{\Delta\rho}{\rho_{comp}} \qquad (2\text{-}38)$$

where: β_{comp} = dimensionless density difference (relative to the compartment fluid density)

ρ_{comp} = density of compartment fluid

$\Delta\rho$ = density difference

The results, presented in Figure 2-9, indicate that the dimensionless front velocity is dependent on the opening geometry, but independent of β_{gas} for both Boussinesq and non-Boussinesq flows.

Three dimensional numerical modelling has been used to investigate the effectiveness of different fire fighting tactics on reducing the extent of mixing in backdraft gravity currents (Gojkovic and Bengtsson 2001). The CFD model SOFIE (Rubini 2006), which is based on Reynolds averaged Navier-Stokes equations, was used in the simulations. The different fire fighting tactics investigated included natural and fan forced compartment ventilation. The research suggested that the choice of fire-fighting tactic was scenario dependent. For example, in a life-saving operation, offensive techniques such as internal extinguishment and positive pressure ventilation are appropriate, whereas in property protection operations, a defensive technique with external extinguishment and ventilation should be utilised.

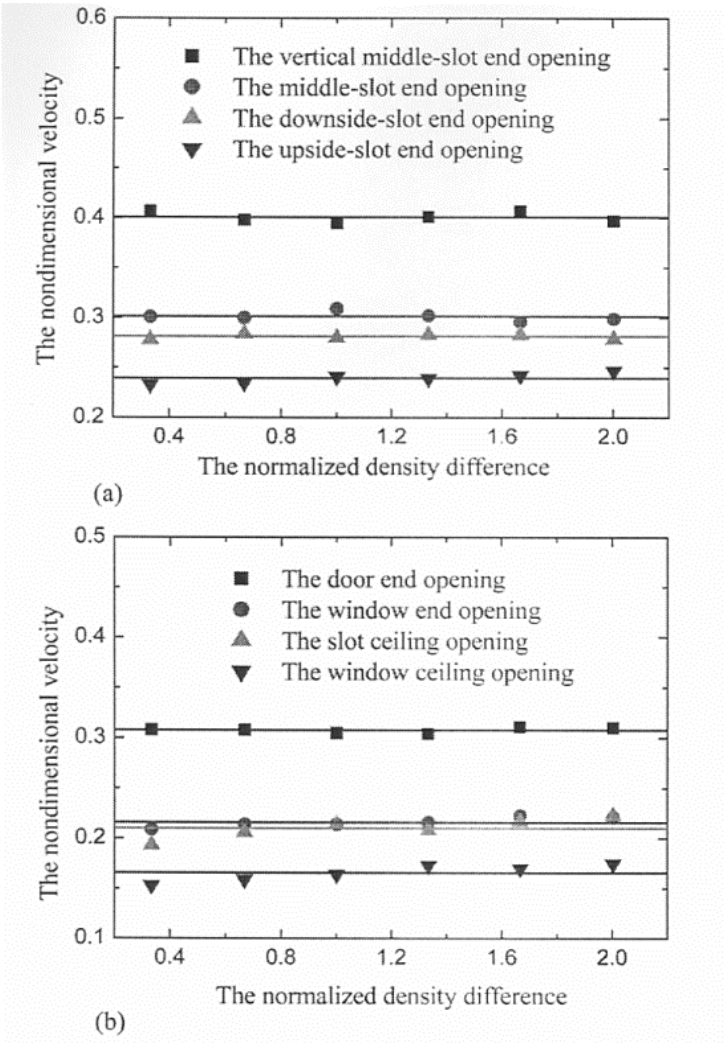

Figure 2-9: Plot of non-dimensional velocity (*Fr*) versus normalised density difference (β_{gas}) for a variety of different compartment opening geometries. The symbols represent the actual results and the lines represent average values. This figure is an extract from Weng et al. (2005).

2.5 General Characteristics of Gravity Currents

Gravity currents occur in a large variety of environmental situations, from avalanches to sea-breeze fronts and as a result, a large body of literature exists. The majority of past research has focussed on two-dimensional gravity currents, giving detail on the dynamics and anatomy of the current motion (Simpson 1997), but, to a lesser extent, past research has also investigated axi-symmetric and three-dimensional gravity currents (Ezer 2005; Patterson et al. 2005; Simpson 1997; Ungarish and Zemach 2005). Only those aspects relevant to the occurrence of backdraft are covered below. A detailed summary of pre-1997 research investigating all aspects of gravity current flows is provided by Simpson. (1997).

Gravity currents are generally divided into three main categories depending on the boundary on which the current propagates: rigid boundary, free surface, or intrusive. Backdraft gravity currents are a type of rigid boundary gravity current, so only rigid boundary gravity currents will be considered further in this review.

The discussion presented here will focus on Boussinesq gravity current flows, as they are achievable using saltwater modelling. Non-Boussinesq gravity current flows are only discussed briefly in Section 2.5.3.

2.5.1 Background

Gravity currents are generated in fluid systems where horizontal density gradients exist. The density differences may be caused by differences in temperature, fluid type, concentration, or turbidity. Gravity causes an imbalance of forces, which causes the fluids to flow in an attempt to reach equilibrium. These flows are driven by the conversion of the potential energy of the system into kinetic energy (Simpson 1997).

A simple way to understand the physics of a gravity current is to consider a dam break flow, which occurs when a dam breaks, releasing a body of water into the atmosphere (Simpson 1997). Gravity causes the water to collapse and spread horizontally, as shown in Figure 2-10. For the two-dimensional case, the kinetic energy gain and the potential energy loss terms can be equated (see the left and right hand sides of Equation (2-39) respectively) and rearranged to give an estimate of the spreading velocity (see Equation (2-40)).

$$\frac{mu^2}{2} \approx \frac{mgH}{2} \tag{2-39}$$

$$u \approx \sqrt{gH} \tag{2-40}$$

where: m = the mass of fluid

u = spreading velocity

g = gravitational acceleration

H = height of the dam fluid

In the case of a dam break, water is flowing into the atmosphere. As the density of the atmosphere is very small compared to the water, it's presence does not influence the flow significantly. However, for fluids of similar density the flow would behave like a slow motion version of the dam break, with a velocity given by Equation (2-41) (Simpson 1997).

$$u \approx \sqrt{\beta g H} \tag{2-41}$$

This derivation does not consider the effect of energy dissipation as the gravity current front propagates. In reality the effects of friction and turbulence would act to slow the gravity current, so these are upper bound estimates for velocity. The energy dissipating mechanisms are also responsible for the mixing within the gravity current and are discussed further in Section 2.5.7.

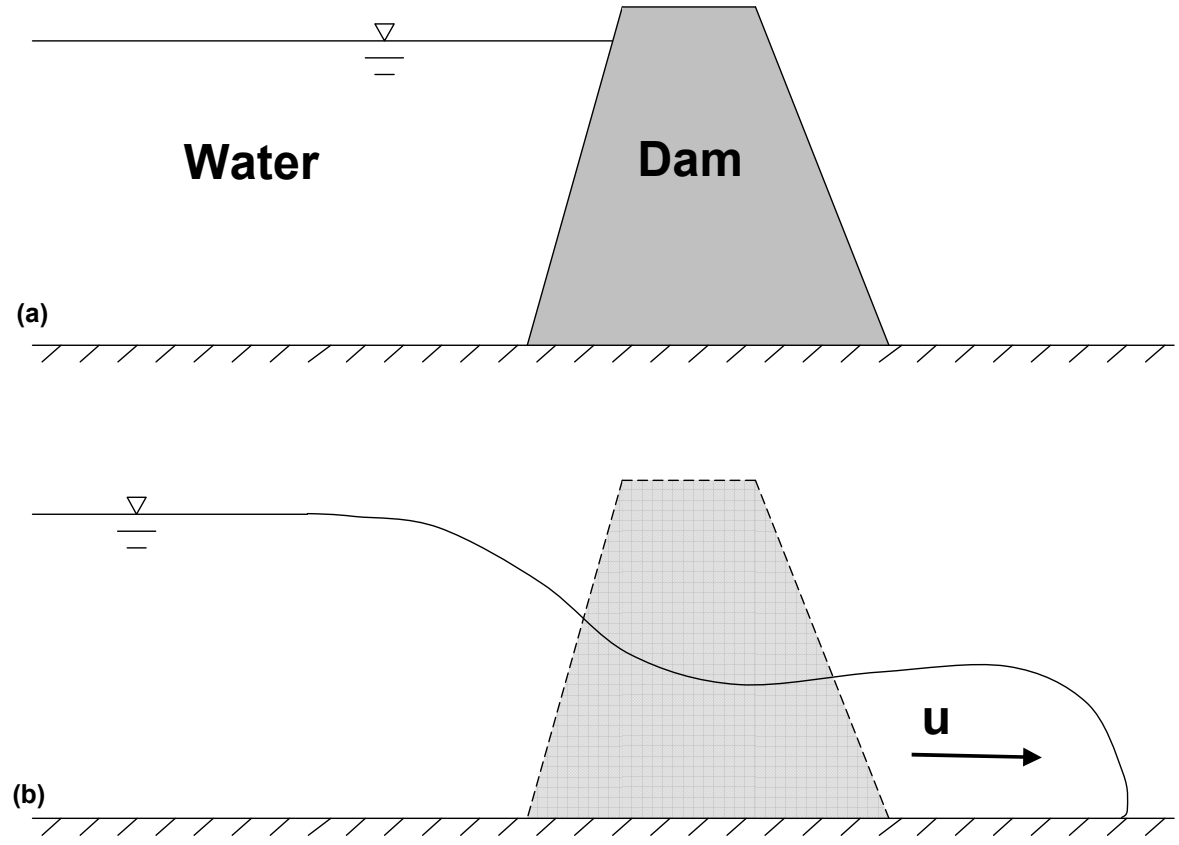

Figure 2-10: Schematic of a dam break flow: (a) the dam before it breaks, (b) dam break flow.

2.5.2 Lock Exchange Flows

Lock-exchanges are commonly used to generate gravity currents experimentally. Consider a rectangular channel containing two fluids of different density, separated by a vertical barrier. Once the vertical barrier is removed, the denser fluid will collapse and flow beneath the lighter fluid, resulting in the formation of two gravity currents, one along the bottom surface and a second along the top surface. Lock release type flows are experimentally simple to generate and exhibit dynamics which are also found in more complex gravity current flows (Hacker et al. 1996).

Lock-exchange gravity current flows transition through three different phases (Simpson 1997). After removal of the lock gate and the initial fluid collapse, the resulting gravity current front propagates at a constant velocity. In the constant-velocity phase, the nature of the flow is dependent on the initial conditions. The velocity may be estimated by the initial density difference and lock depth, as shown in Equation (2-42) (Simpson 1997). Experiments have shown the Froude number is approximately 0.44, when the flow is bounded above and below by rigid surfaces (Simpson 1997).

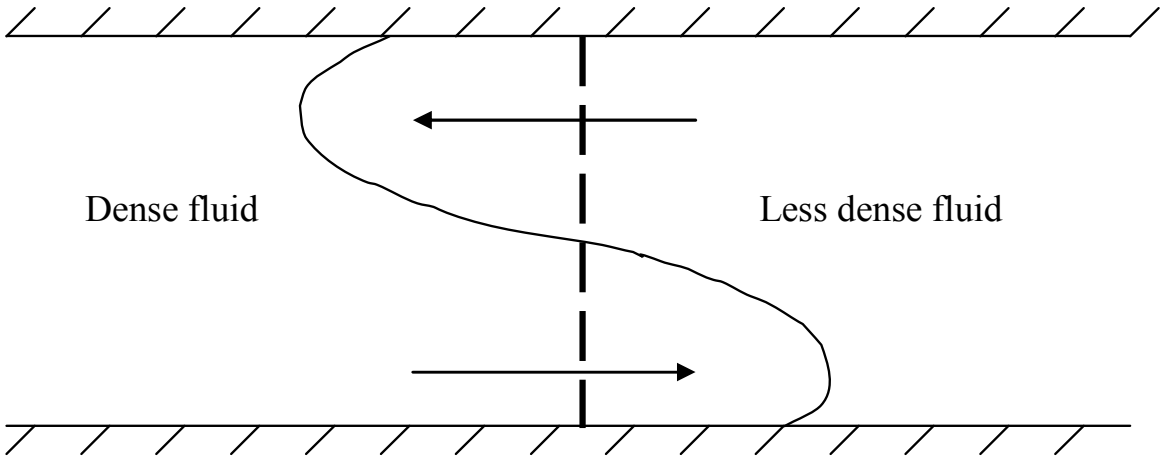

Figure 2-11: Side elevation of lock exchange flow. Gravity currents are forming at the upper and lower boundaries. The dashed line represents the initial location of the lock gate, which separated the different density fluids.

$$u = Fr\sqrt{\beta_{initial} gH} \tag{2-42}$$

where: $u =$ velocity

$Fr =$ Froude number (dimensionless constant)

$\beta_{initial} =$ initial dimensionless density difference

$g =$ gravity

$H =$ lock depth

A second phase, the self-similar phase, is reached if the fluid on one side of the lock has a finite length, *L*. This stage begins when an inverted bore disturbance, which is reflected from the end wall of the lock, overtakes the front of the current, as illustrated in Figure 2-12. The transition is rapid and occurs once the front has propagated approximately ten lock lengths for a full depth lock release, or approximately 3 lock lengths when the ambient fluid depth is much greater than the lock depth (Simpson 1997). The first and second phases of lock exchange flows represent a balance between inertial and buoyancy forces (Marino et al. 2005). Dimensional analysis implies that the velocity in the second phase decreases with time, as shown in Equation (2-43) (Marino et al. 2005). The constant in this equation has been found experimentally to be approximately 1.0.

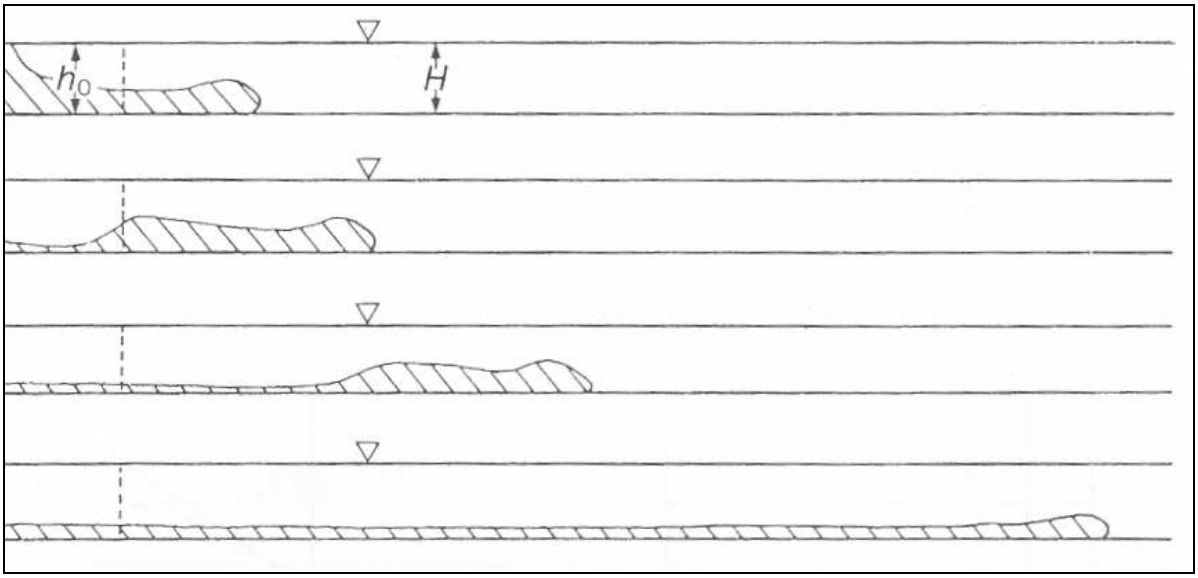

Figure 2-12: A lock exchange flow showing inverted bore overtaking the gravity current head (Simpson 1997). The dashed line represents the initial position of the lock gate. The dense fluid is hashed. This figure is an extract from Simpson (1997).

$$u = \Omega(\beta_{initial} g A_L)^{1/3} t^{-1/3} \tag{2-43}$$

where: $\Omega = \text{constant} \sim 1.0$

$A_L = HL = \text{cross-sectional area of lock}$

$L = \text{lock length}$

$t = \text{time}$

$\beta_{initial} g A_L = \text{initial buoyancy per unit width}$

A third phase, the viscous phase, is reached when the Reynolds number is low enough for viscous effects to become important. The viscous phase represents a balance between viscous and buoyancy forces, where the velocity of the front reduces even more rapidly with time. As volume is conserved in lock exchange flows, the velocity may be estimated from Equation (2-44) (Huppert 1982; Huppert 2006). The constant was found experimentally to be approximately 0.73. For viscous fluids, the viscous forces may dominate nearer to the start of the flow, meaning the second and/or first phases will be absent.

$$u = \Omega\left(\frac{\beta_{initial} g A_v^{\,3}}{\nu}\right)^{1/5} t^{-4/5} \tag{2-44}$$

$\Omega = \text{constant} \sim 0.73$

$A_v = \text{volume of dense gravity current fluid per unit width}$

The propagation of the gravity current front, x, can be calculated by integration of the velocity with time (t). Therefore, the front position in the first, second and third phases scales with t^1, $t^{2/3}$, $t^{1/5}$ respectively. These relationships were confirmed by the experimental results of Rottman and Simpson (1983), as shown in Figure 2-13.

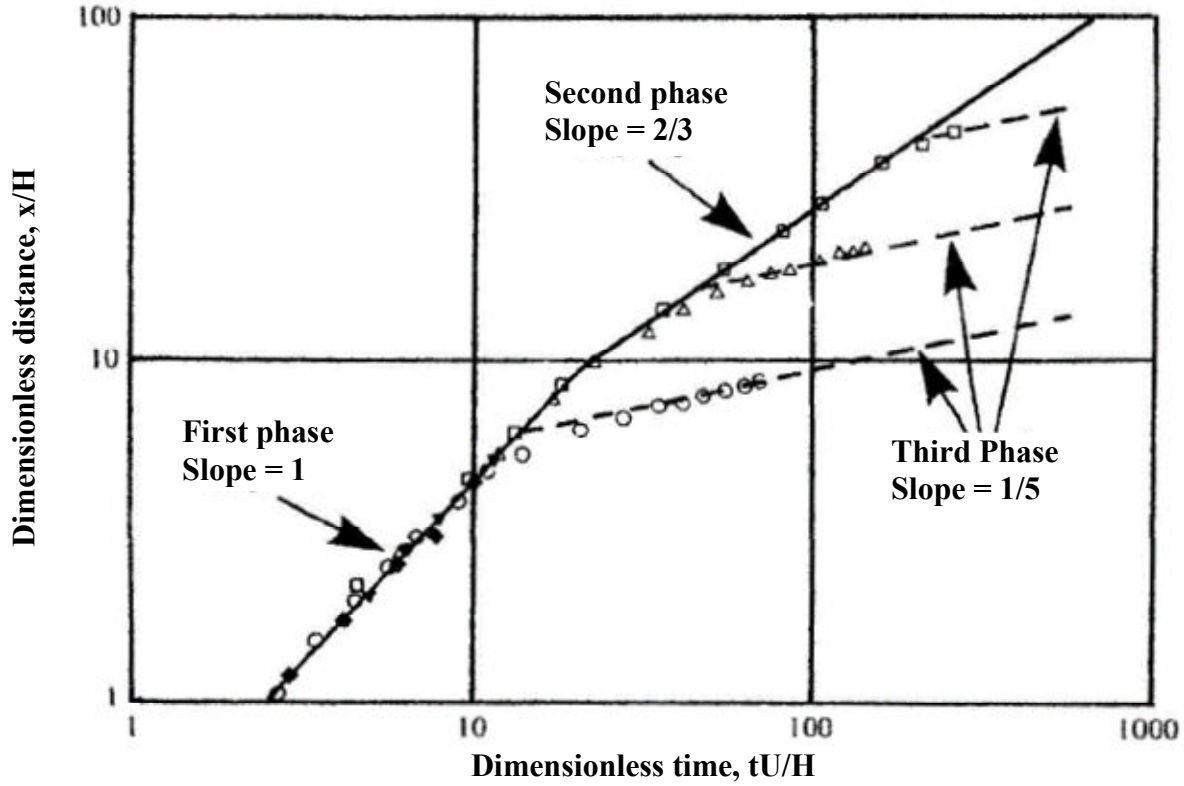

Figure 2-13: Log-log distance versus time plot for four different full depth lock release experiments. The three different phases are represented by the different gradients. This figure is an extract from Rottman and Simpson (1983).

Marino, Thomas and Linden (2005) have demonstrated that in the initial constant velocity phase the Froude number can be defined in terms of the lock depth. However, as the current propagates further, the Froude number is more appropriately defined in terms of the local head height.

For gravity currents preceding backdrafts, the first (constant velocity) phase of the flow will be the most important. The second and the third stages would not be relevant to a residential scale backdraft situation.

2.5.3 Density Difference Independence

Environmental gravity currents typically occur between fluids with density differences of a only a few percent (Simpson 1997). Therefore, the majority of past research has focussed on low density difference gravity current flows (Simpson 1997). For flows with $\beta < 0.1$, the Boussinesq approximation is valid (Shin et al. 2004), which means density variations may be neglected in the governing equations, except where they affect buoyancy. The velocity of

turbulent gravity currents have been found to be independent of β for Boussinesq flows (Simpson 1997). For lock exchange flows of Boussinesq fluids, the gravity currents of heavy and light fluids are practically symmetrical.

For non-Boussinesq flows (large β), the gravity currents of heavy and light fluids have slightly different characteristics and the resulting flow velocities must be treated separately (Simpson 1997). Lock exchange experiments, involving non-Boussinesq fluids, have shown that the gravity current of dense fluid travels significantly faster and with a smaller head height than that of the light fluid (Lowe et al. 2005). The larger the dimensionless density difference, the smaller the head height. In addition, the light fluid front is elongated and smooth with little mixing, while the gravity current of dense fluid has more evidence of turbulence and mixing (Grobelbauer et al. 1993; Lowe et al. 2005).

A plot showing the local Froude number of the gravity current head for dense and light fluids of varying density is shown in Figure 2-14 (Grobelbauer et al. 1993). The density ratio (ρ^*) is an alternative form of the dimensionless density difference. (where $\rho_2 > \rho_1$, $\rho^* = 0$ indicates fluids of the same density, and $\rho^* = 1.0$ indicates that one fluid has a negligible density relative to he other). Two theoretical solutions for Froude number are shown at the limit as the density ratio approaches 1.0. The dam-break solution represents a dense current propagating in a vacuum, while the solution of Benjamin (1968) represents a cavity flow (this solution is discussed further in Section 2.5.4).

Despite these differences, all fully turbulent gravity current flows exhibit similar mixing processes and structure. Therefore, investigation of Boussinesq gravity current flows gives an insight into the behaviour of non-Boussinesq gravity currents.

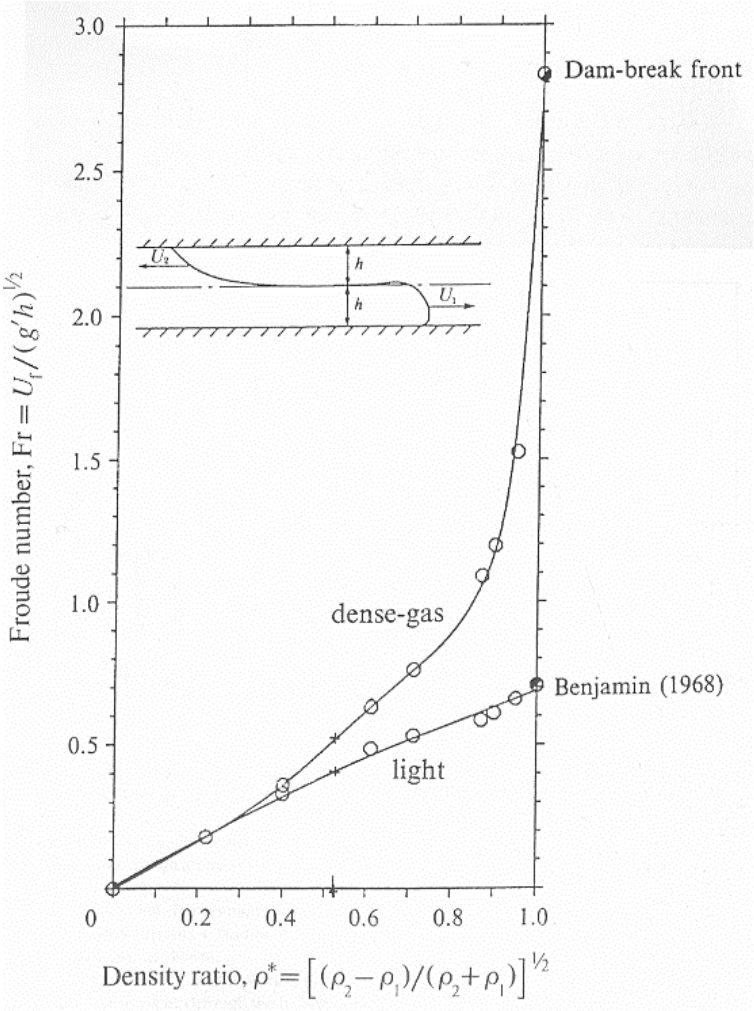

Figure 2-14: Plot of local Froude number versus density ratio. This figure is an extract from Simpson (1997).

2.5.4 Theory

A theory for the steady propagation of a two-dimensional gravity current in a rectangular channel was developed nearly 40 years ago by Benjamin (1968) and is still used today to describe gravity current phenomenon (Marino et al. 2005; Shin et al. 2004; Ungarish and Zemach 2005). The theory was originally developed to describe cavity flows, such as air moving between two rigid plates filled with water.

Consider a gravity current cavity flow moving into an ambient fluid of much higher density, as shown in Figure 2-15. It is assumed that the fluid flows with no mixing or energy dissipation. The fluid is assumed to be inviscid (viscous forces are absent) and incompressible. The gravity current is assumed to move as a slug of fluid, which avoids the need to specify relative flow velocities within the flow.

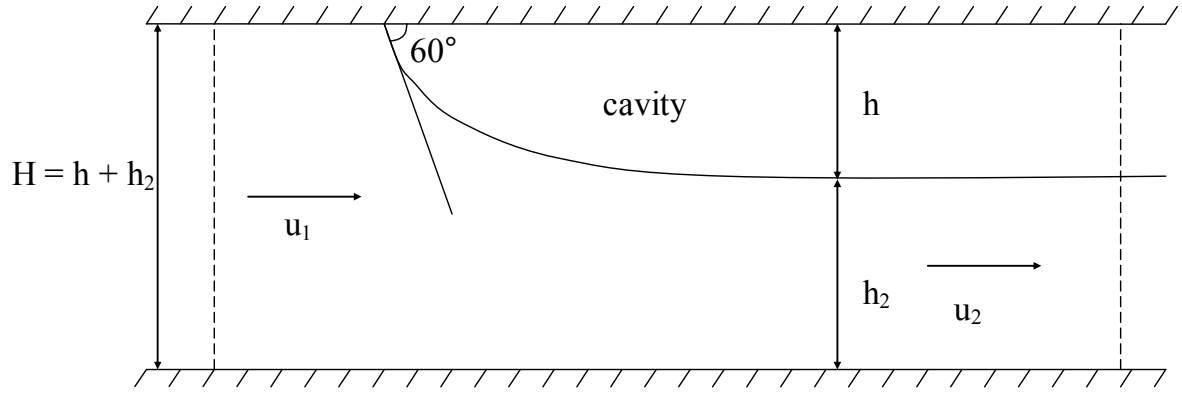

Figure 2-15: Schematic of a two-dimensional gravity current cavity flow. Dashed lines represent the control volume, which is moving with the gravity current head.

The frame of reference and control volume are selected to move with the gravity current head and conservation of mass and momentum are applied. In this frame of reference, the flow is steady and the gravity current is stationary, meaning the nose of the gravity current is a stagnation point. Therefore, Bernoulli's equation may be applied along the interface between the fluids, and the equations for conservation of mass, momentum and energy can be written as shown in Equation (2-45) to (2-47).

$$u_1 H = u_2 h_2 \qquad \text{mass} \qquad (2\text{-}45)$$

$$u_1^2 H + \beta_{initial} g H^2 = 2u_2^2 h_2 + \beta_{initial} g h_2^2 \qquad \text{momentum} \qquad (2\text{-}46)$$

$$v_2^2 = 2\beta_{initial} g (H - h_2) \qquad \text{energy} \qquad (2\text{-}47)$$

where: $u_1 =$ velocity of advancing fluid (equal to the front velocity in stationary frame of reference)

$u_2 =$ velocity of under flowing fluid

$h =$ depth of gravity current head

$h_2 =$ depth of under flowing fluid

$H =$ depth of ambient fluid

$\beta_{initial} =$ initial non-dimensional density difference (approx 1.0 for cavity flow)

These equations can be solved simultaneously by eliminating u_1 from the mass and momentum equations (Equations (2-45) and (2-46)) and u_2 from the momentum and energy equations (Equations (2-46) and (2-47)), giving the result in Equation (2-48). This result

predicts that the cavity will fill half the channel depth in steady energy conserving flows. The local Froude number for this type of flow can be calculated as $1/\sqrt{2}$, as shown in Equation (2-49).

$$h_2 = \frac{H}{2} = h \tag{2-48}$$

$$Fr_B = \frac{u_1}{\sqrt{\beta_{initial} g h}} = \frac{1}{\sqrt{2}} \tag{2-49}$$

The theoretical slope of the nose (the angle formed between the rigid surface and the top of the nose) for a rigid boundary gravity current has been calculated as 60° (Benjamin 1968), as indicated in Figure 2-15.

Flows for which the cavity fills more than half the channel depth are not possible unless energy is input into the flow (Benjamin 1968). In practical situations $h<H/2$, due to frictional energy losses (Simpson 1997).

By including an energy loss term in Bernoulli's equation, Benjamin (1968) also developed a theoretical relationship for the velocity of the gravity current front which incorporated energy losses. This relationship is based on the dimensionless gravity current depth and is presented in Equation (2-50). The non-dimensional gravity current depth is the height of the gravity current, h, divided by the total depth of ambient fluid, H, and is shown in Equation (2-52). Although this relationship was developed for cavity flows, the result also applies to Boussinesq flows. For Boussinesq flows the local Froude number is defined as shown in Equation (2-51). Benjamin (1968) demonstrated that the maximum energy dissipation would occur when $\phi = 0.347$, which corresponds to a local Froude number of 0.527.

$$\frac{u}{\sqrt{gH}} = \left(\frac{\beta_{initial}}{1-\beta_{initial}} \right)^{1/2} \left(\frac{(1-\phi)(2-\phi)}{1+\phi} \right)^{1/2} \tag{2-50}$$

$$Fr_B = \frac{u}{\sqrt{\beta_{initial} g h}} = \left(\frac{(1-\phi)(2-\phi)}{1+\phi} \right)^{1/2} \tag{2-51}$$

$$\phi = \frac{h}{H} \tag{2-52}$$

where: Fr_B = local Froude number proposed by Benjamin (1968)

u = front velocity

ϕ = dimensionless head height

Huppert and Simpson (1980) presented an empirical relationship for the local Froude number, based on the height just behind the elevated gravity current head, as shown in Equation (2-53). This work showed that Benjamin's (1968) relationship tends to over predict local Froude numbers for rigid boundary gravity currents.

$$Fr_{HS} = \frac{u}{\sqrt{\beta_{initial} g h_{HS}}} = \begin{cases} 1.19 & (\phi \le 0.075) \\ 0.5\phi^{-1/3} & (\phi > 0.075) \end{cases} \tag{2-53}$$

where: Fr_{HS} = local Froude number proposed by Huppert and Simpson (1980)

$h = h_{HS}$ = height of the current "just behind the head"

Rottman and Simpson (1983) proposed a theoretically derived relationship similar in form to that of Benjamin (1968), but with the introduction of the empirical parameter λ (see Equation (2-54)). When $\lambda^2 = 2$, the relationship is the same as that presented by Benjamin (1968). From their experiments, Rottman and Simpson (1983) suggested a best fit value of $\lambda^2 = 1$. The height was a theoretically defined tail depth, located behind the head.

$$Fr_{RS} = \frac{u}{\sqrt{\beta_{initial} g h_{RS}}} = \left(\frac{\lambda^2 (1-\phi)(2-\phi)}{2(1+\phi)} \right)^{1/2} \tag{2-54}$$

where: Fr_{RS} = local Froude number proposed by Rottman and Simpson (1983)

$h = h_{RS}$ = theoretically defined tail depth

λ^2 = empirical constant ~1

Shin et al. (2004) developed a new theory to define the local Froude number for lock exchange gravity current flows (see Equation (2-55)). Their theory predicts that energy dissipation is unimportant for fully turbulent flows and showed that long waves, travelling along the fluid interface, were responsible for transfer of energy and momentum between the light and heavy gravity currents. They suggested that this transfer controls the front velocity

and local Froude number of the current heads. The current height was defined as the dense fluid depth at the original lock gate position.

$$Fr_{SDL} = \frac{u}{\sqrt{\beta_{initial} g h}_{SDL}} = (1-\phi)^{1/2} \tag{2-55}$$

where: Fr_{SDL} = local Froude number proposed by Shin et al. (2004)

$h = h_{SDL}$ = height of the gravity current at the original lock position

A correlation for the local Froude number was also developed by Ungarish and Zemach (2005) and is shown in Equation (2-56). Their correlation was semi-empirical and represented a simplified compromise between existing correlations, weighted in favour of Rottman and Simpson's (1983) correlation for small values of ϕ, in accordance with experimental observations. The flow depth was defined as the height of the gravity current head.

$$Fr_{UZ} = \frac{u}{\sqrt{\beta_{initial} g h}_{UZ}} = (1+3\phi)^{-1/2} \tag{2-56}$$

where: Fr_{UZ} = local Froude number proposed by Ungarish and Zemach (2005)

$h = h_{UZ}$ = height of the gravity current head

The various correlations of local Froude number as functions flow depth, as predicted by Equations (2-51) to (2-55), are presented in Figure 2-16. The result of Shin et al. (2004) specified the flow depth to be at the original lock position, instead of at the gravity current head like the other researchers, but has been included here for comparison. The correlations of Huppert and Simpson (1980) and Rottman and Simpson (1983), define the flow depth just behind the head of the gravity current, which for lock releases in the constant velocity phase is approximately equal to the head height.

The differences in the various correlations for local Froude number, observed in Figure 2-16, are in part due to the inconsistency in the head height scale selected, and the difficulty in measuring the flow depth experimentally. A consistent and unambiguous measure of gravity current depth is needed to ensure consistency between various correlations. Recently, Marino

et al. (Marino et al. 2005) suggested that the head height may be determined unambiguously by vertically integrating the buoyancy excess or deficit and calculating an equivalent top-hat profile for the gravity current (this concept is explained in Section 2.5.9).

Two limits exist on the range of dimensionless gravity current depths. The first limit, of $\phi = 0$, represents a gravity current flowing in an infinitely deep ambient fluid. By fixing the height of the gravity current (h) and increasing the depth of ambient fluid (H), the ratio $\phi = h/H$ will approach zero. The second limit, of $\phi = 0.5$, represents a gravity current with no energy losses. For lock exchange flows, a value of $\phi = 0.5$ has been shown to conserve momentum, mass and energy (Benjamin 1968; Shin et al. 2004). It is believed values of $\phi > 0.5$ are not realisable in lock exchange flows without external energy input into the flow (Benjamin 1968; Marino et al. 2005; Shin et al. 2004).

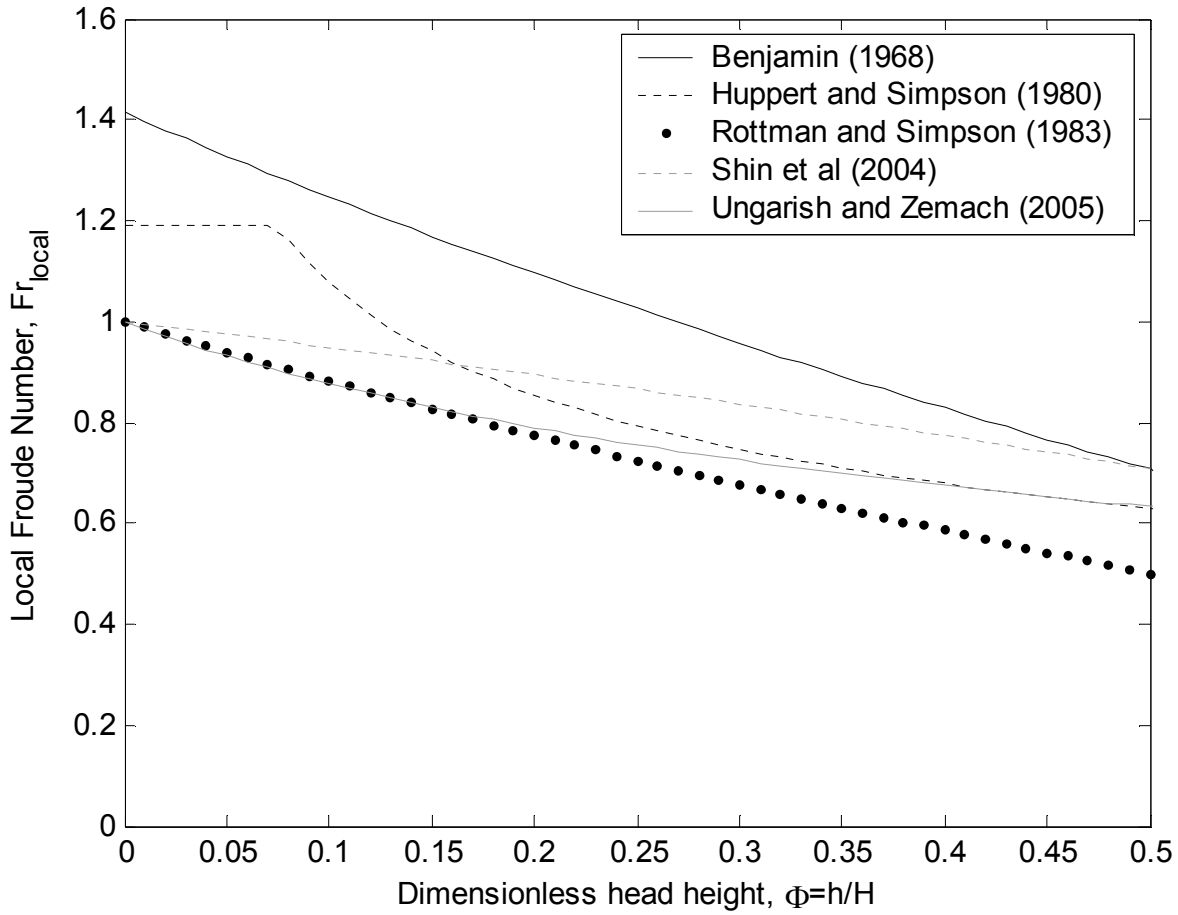

Figure 2-16: Plot of various correlations for local Froude number as a function of non-dimensional gravity current depth.

2.5.5 General Structure

Rigid boundary gravity currents propagate over solid surfaces. Typically, they are characterised by an elevated head, a raised nose, a series of advancing lobes and clefs at the front of the head, and billows rolling up and breaking off the head. Two length scales commonly used to define gravity currents are the head height and the lock depth, as defined in Figure 2-17. This figure depicts an idealised cross-section through the head of a fully turbulent gravity current propagating along a horizontal rigid boundary.

Gravity currents flowing along rigid boundaries develop an elevated nose, due to friction at the no-slip boundary. If the frame of reference is selected to move with the head, the nose of the gravity current is a stagnation point, so ambient fluid above this point will flow up over the head of the gravity current, while ambient fluid flowing below this point will be overrun and be mixed into the head of the flow (Simpson 1997). The shaded region in Figure 2-17 indicates fluid which will be overrun and entrained into the head of the gravity current as it advances.

The magnitude of the Reynolds number (Re) influences the shape and size of the head of the gravity current (Simpson 1997). The Reynolds number represents a ratio of the inertial forces to the viscous forces in the flow. For small Re the flow is laminar and dominated by viscous forces, while for large Re the flow is turbulent and dominated by inertial forces. For intermediate Reynolds numbers there is a gradual transition. For low Reynolds numbers flows (less than $Re \approx 10$), the head is small and only slightly elevated from the following gravity current, with minimal mixing (see Figure 2-18a). As the Reynolds number is increased, the gravity current approaches the limiting profile (for Re greater than ~1000) (Figure 2-18f), with an elevated, elongated head and increased mixing.

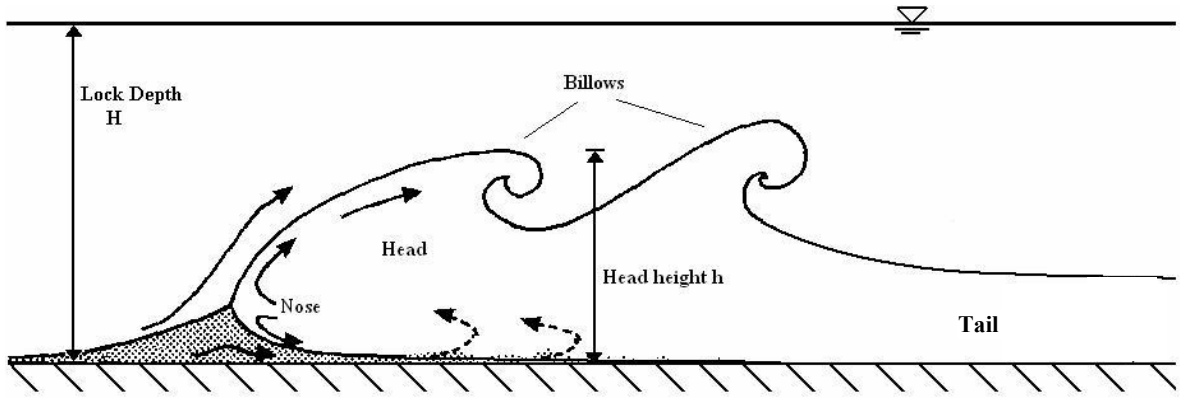

Figure 2-17: Cross-section through an idealised gravity current head. This figure is an extract from Simpson (1997) which has been modified.

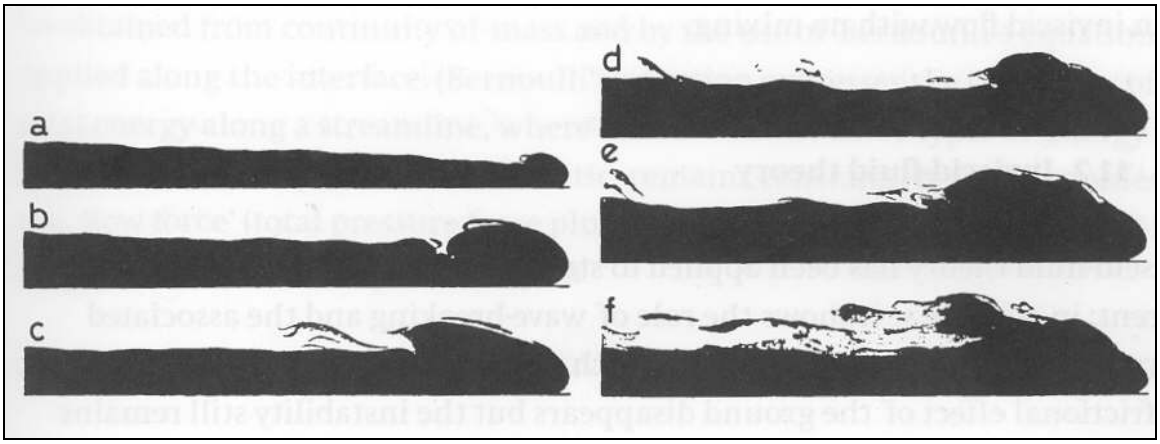

Figure 2-18: Shadow pictures of gravity current head profiles for a range of Reynolds numbers: (a) Re < 10 → (f) Re > 1000. This figure is an extract from Simpson (1997).

For large Reynolds numbers, viscous effects are unimportant and the flow becomes Reynolds number independent, meaning the flow becomes independent of viscous and diffusive effects (Linden 1999; Shin et al. 2004; Simpson 1997). The transition to Reynolds number independence occurs at a Re of approximately 1000, when the length scale is based on the compartment depth *H*, or approximately 500, when based on the gravity current head height (Simpson 1997). This Reynolds number independence has been observed in the similarity of the structure of atmospheric thunderstorm gravity currents ($\mathrm{Re} \sim 10^6$) to laboratory scale flows with Re of approximately 1000 (Simpson 1997).

The Reynolds number of backdraft gravity currents (for a typical full-scale structure with a compartment height of 3m) is approximately $5{,}000 < \mathrm{Re} < 50{,}000$ (Fleischmann 1994).

Therefore, fully turbulent small-scale saltwater gravity current flows (with Re > 1000), can be used to model full-scale backdraft gravity currents.

2.5.6 Bulk Characteristics

Gravity currents are often described by the bulk characteristics of the front of the flow. Typical bulk characteristics include the head height, the nose height, the nose angle, and the front velocity, which are described briefly below:

- The head height is a measure of the depth of the front of the gravity current, as shown in Figure 2-18. For lock exchange flows the head height is generally slightly less than half the lock depth.
- The furthermost point of rigid boundary gravity currents forms a raised nose, as shown in Figure 2-18. The nose forms due to the head of the gravity current over-running ambient fluid at the boundary. The nose is approximately $1/8^{th}$ the height of the raised head for high Reynolds number flows (Simpson 1997).
- The slope that the gravity current head forms with the rigid boundary has been found experimentally to be 45° (Britter and Simpson 1978).
- The Froude number of a gravity current flow is a dimensionless measure of the front velocity. For lock exchange gravity current with rigid upper and lower boundaries, the Froude number (using the lock depth as a length scale) has been found experimentally to be approximately 0.44 (Barr and Hassan 1963; Simpson 1997).

2.5.7 Mixing Processes

There are two main types of instability responsible for the mixing processes that occur in rigid boundary gravity currents (Simpson 1997). Both types of instability are illustrated in Figure 2-19 and are described below.

Billows are the main process by which surrounding ambient fluid is entrained into the gravity current (see Figure 2-19a) (Simpson 1997). They form in the region of high velocity shear above the front of the dense fluid and roll up the gravity current head like waves. The billows have been found to have the qualitative and quantitative properties of Kelvin-Helmholtz (K-H) billows, which are associated with the instability formed at the shear layer separating different density fluids flowing relative to one another (Simpson 1997).

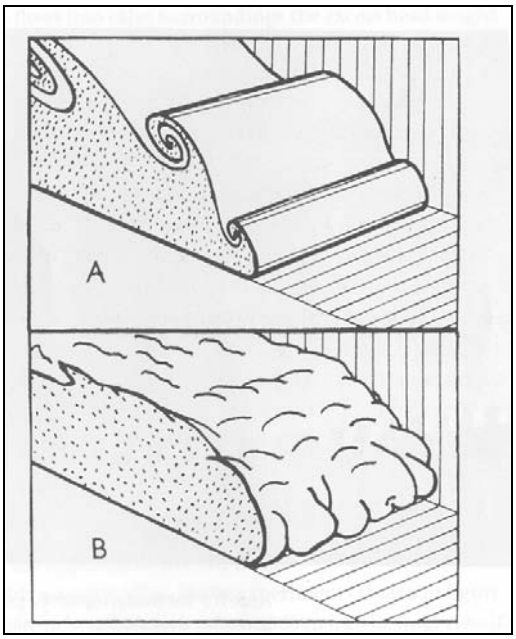

Figure 2-19: Two forms of instability at the head of a gravity current flowing along a surface: (a) billows (b) lobes and clefts. This figure is an extract from Simpson (1997).

Lobes and clefts are formed by the gravitational instability of ambient fluid that is over-run by the nose of the gravity current (see Figure 2-19b) (Simpson 1997). This was confirmed by experiments where ambient fluid over-run was prevented by a floor moving at the same speed as the head (Simpson, 1997). In these experiments, the lobes and clefts did not form and only the billows were visible.

The pattern of lobes and clefts within a gravity current constantly changes, but the total number of lobes and clefts has been found to remain approximately constant (Simpson 1997). Experiments show that lobes reach a maximum size, after which they collapse to form new lobes and clefts. The lobe size where collapse occurs is approximately twice the mean size, and is dependent on Re for Reynolds number in the range $400 < Re < 4000$ (Simpson 1997). At higher Reynolds numbers the mean lobe size is constant and has a value of approximately one quarter the head height (Simpson 1997).

As rigid boundary gravity currents flow, the leading edge forms a well-defined raised head. For high Reynolds number flows, the head is deeper than the following tail (Simpson 1997). The region immediately behind the head is an area of intense mixing (Simpson 1997), but mixing also occurs along the interface between the ambient and gravity current fluids further behind the head.

2.5.8 Internal Velocity Structure

Until recently, research into gravity currents focussed only on the bulk characteristics of gravity currents, without detailed measurements of the internal structure. However, recent advances in flow visualisation techniques have improved the understanding of the internal structure. A number of findings related to the internal velocity structure are summarised below.

Experiments by Kneller et al. (1999) confirmed fluid was entrained into rigid boundary gravity currents both beneath the nose and into the turbulent wake region behind the head.

The instantaneous fluid velocities immediately behind the gravity current head (both for rigid boundary and intrusive gravity current flows) have been found to be approximately 50% greater than the rate of advance of the head, while the mean velocities are approximately 30% greater (Kneller et al. 1999; Lowe et al. 2002). This indicates that tail fluid is being fed continuously into the head before being entrained into the turbulent wake region.

The stagnation point of rigid boundary gravity current flows (when the frame of reference is selected to move with the gravity current head) was shown to exist slightly below the gravity current nose (Thomas et al. 2003), not at the nose as previously thought (Simpson 1997).

The velocity profile from a vertical cross-section through the tail of the flow has been determined experimentally (Kneller et al. 1997; Kneller et al. 1999). The maximum internal velocity (in rigid boundary gravity currents with a free surface above) was shown to exist approximately $0.2h$ above the rigid boundary. The velocity profile was governed by the effects of the flow boundaries, and was found to fit a composite profile consisting of a logarithmic profile at the rigid boundary and a cumulative Gaussian profile in the shear layer, as shown in Figure 2-20. Similarly shaped velocity profiles were obtained experimentally by Zhu et al. (2006).

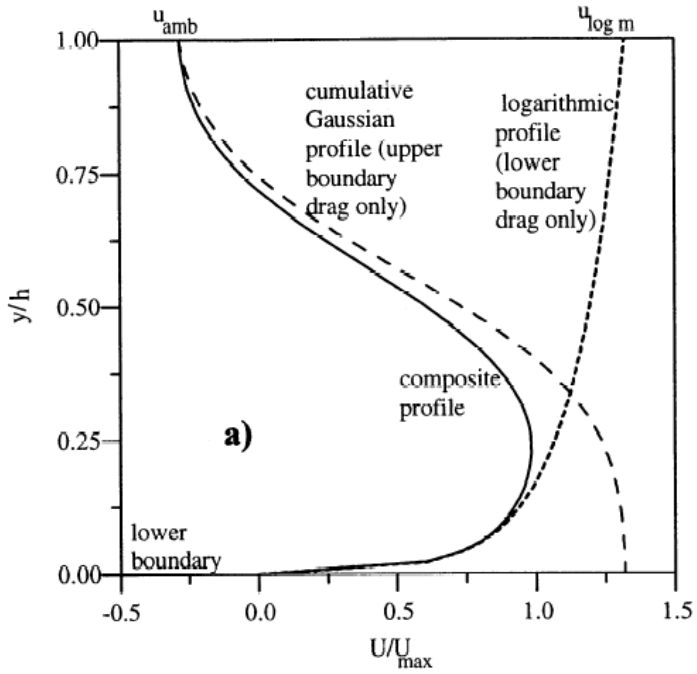

Figure 2-20: Rigid boundary gravity current velocity profile. This figure is an extract from Kneller et al. (1999).

Time-averaged quantities of quasi-steady gravity currents have been investigated by selecting a frame of reference moving with the gravity current head (Thomas et al. 2003). Time-averaged vorticity fields showed that vorticity was confined to the narrow interface between gravity currents and the ambient fluid, and also to regions near the rigid boundary. A similar pattern has been observed for the time-averaged strain rate. However, the strain rate at the nose was low and increased further up the head, in the region where billows develop.

The large vorticial eddies (billows), that form as a result of the Kelvin-Helmholtz instabilities at the shear layer between the gravity current and the opposing flow, have been shown to have approximately the same scale as the depth of the gravity current flow itself (Zhu et al. 2006).

In a static frame of reference, Kneller et al. (1999) found that mean motion in the gravity current head consisted of a single large vortex. Thomas et al. (2003) generated time-averaged streamlines for rigid boundary gravity currents in a frame of reference moving with the head, as shown in Figure 2-21, which showed two circulation cells in the head. These circulation cells were caused by the flow of fluid through the head towards the nose and the frictional effects from rigid boundary and the shear layer with the ambient fluid. Locations were found to be Reynolds number dependent.

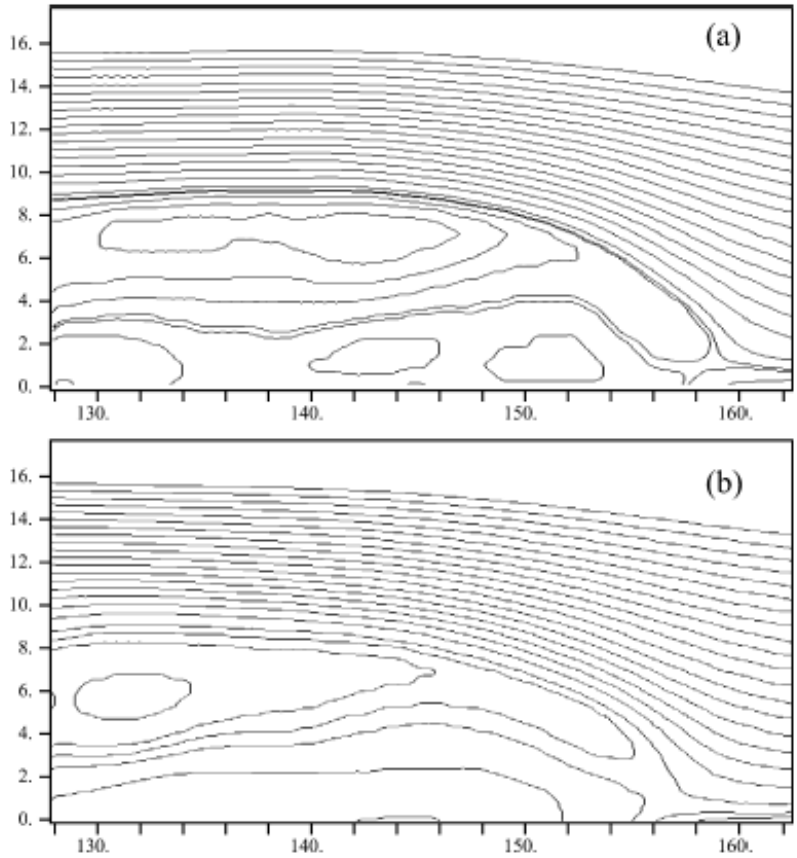

Figure 2-21: Streamlines from a rigid boundary gravity current of different Reynolds numbers: (a) $Re \approx 4000$ and (b) $Re \approx 1200$. This figure is an extract from Thomas et al. (2003).

2.5.9 Internal Concentration / Density Structure

The internal density structure of gravity currents has been investigated by a number of authors (Hacker et al. 1996; Marino et al. 2005; Shin et al. 2004). For low salt concentrations, the relative density, defined in Equation (2-57), is equal to the relative concentration and is the inverse of the dilution, so is a measure of the extent of mixing. Hacker et al (1996) noted that the knowledge of the internal concentration structure would be of critical importance to determine dilution rates and gas concentrations related to flammable limits.

$$R = \frac{\Delta\rho}{\Delta\rho_{initial}} = \frac{\beta}{\beta_{initial}} \qquad \text{Relative concentration / density} \qquad (2\text{-}57)$$

where: R = relative concentration/density

$\Delta\rho$ = density difference

$\Delta\rho_{initial}$ = initial fluid density difference

For full-depth lock release flows in the constant velocity phase, the gravity current consists mainly of the original density fluid and most of the mixing is confined to the shear interface between the current and the ambient fluid (Hacker et al. 1996).

Local Froude and Reynolds numbers are based on the gravity current head height. In the past this height has either been determined visually, by looking at the extent of dye mixing, or by selection of a representative density contour (Hacker et al. 1996). Both of which introduce some degree of ambiguity. The gravity current depth may be determined unambiguously through vertical integration of the buoyancy excess or deficit, as shown in Equation (2-58) (Marino et al. 2005).

$$g\Delta\rho_{initial}h(x,t) = g\int_0^H \Delta\rho(x,z,t)\,dz \tag{2-58}$$

where: $g\Delta\rho_{initial}h(x,t)$ = buoyancy excess or deficit at rigid boundary

g = gravity

$\Delta\rho_{initial}$ = initial density difference

$h(x,t)$ = equivalent gravity current height (assuming no mixing) at horizontal position x and time t

$\Delta\rho(x,z,t)$ = density difference at co-ordinate (x,z) at time t

H = total compartment height

By rearranging Equation (2-58), an expression for the equivalent gravity current height can be obtained. For a gravity current flow of freshwater (R=0%) flowing into an ambient of saltwater (R=100%), the equivalent head height is defined by Equation (2-59). The calculation effectively determines an equivalent top hat vertical density profile, assuming no mixing between the gravity current and ambient fluid, as shown in Figure 2-22. Using Equation (2-59), two-dimensional equivalent height profiles may be generated from concentration or density fields, as shown in Figure 2-23.

$$h(x,t) = \int_0^H \left[1 - R(x,z,t)\right]dz \tag{2-59}$$

where: R = relative concentration

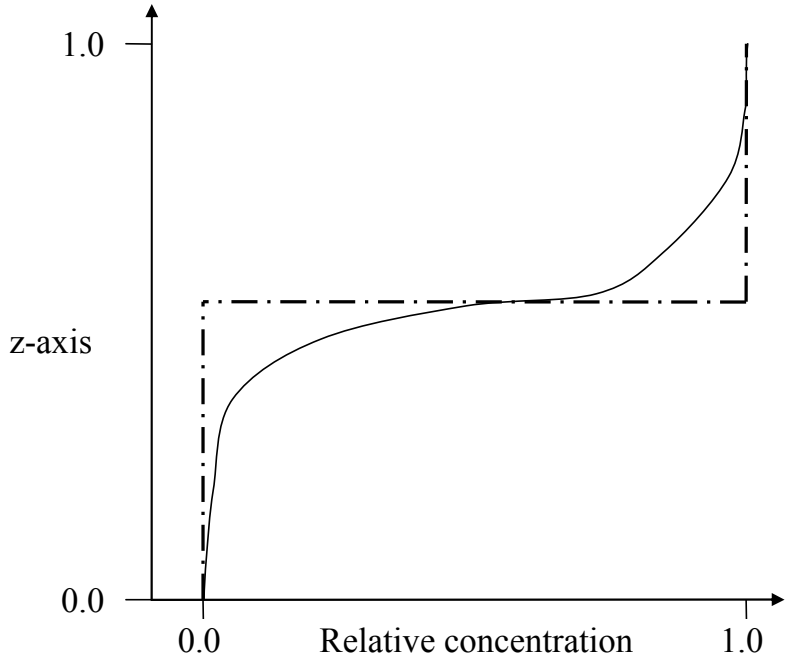

Figure 2-22: Illustration of the equivalent flow height. The solid line represents the actual relative concentration of the fluid with depth and the dash-dotted line represents the equivalent height.

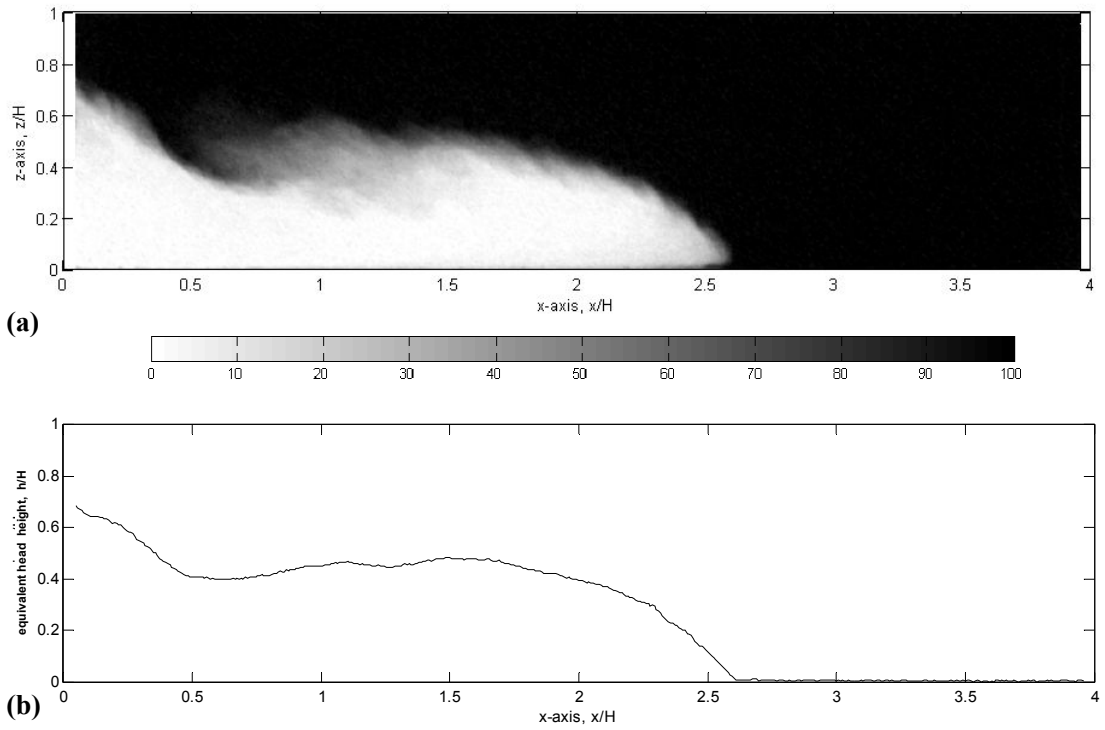

Figure 2-23: Schematic showing: (a) relative concentration/density field as percentage of compartment fluid, (b) corresponding equivalent height profile.

2.5.10 Review of Flow Characteristics

A review of the general flow characteristics typically used to characterise fully turbulent rigid boundary gravity currents is presented in Table 2-3. These characteristics apply to lock exchange gravity currents in the constant velocity phase, such as backdraft gravity currents. The experimental observations are for Boussinesq gravity current flows, and the inviscid flow theory of Benjamin (1968) applies to a flow with negligible viscous effects.

Table 2-3: Review of flow characteristics typical of Boussinesq rigid boundary gravity currents in the initial constant velocity phase. Equivalent values from inviscid flow theory (Benjamin 1968) are included for comparison.

Variable	Experimental Flows	Inviscid Flow Theory
Froude number	0.44	0.5
Local Froude number	0.65	0.707
Head height	<0.5H	0.5H
Nose height	1/8 of head height	No nose
Nose angle	45º	60º
Maximum internal velocity	1.5	1.0
Depth of maximum velocity	0.2 of head height	Uniform velocity
Mixing processes	Billows, lobes and clefts Two circulation cells	No mixing

2.6 Summary

This chapter has presented a review of literature relevant to gravity currents preceding backdraft. Gas flammability limits were discussed in Section 2.2. The feasibility of using scale saltwater modelling to replicate backdraft gravity currents was discussed in Section 2.3. A review of past research into gravity currents preceding backdrafts was presented in Section 2.4 and general flow characteristics of turbulent gravity currents were presented in Section 2.5.

The present study will apply both saltwater modelling techniques and computational fluid dynamics to investigate backdraft gravity currents in the Boussinesq limit. The following chapter provides detail of the computational model used to simulate these flows.

CHAPTER 3 NUMERICAL MODEL

3.1 Introduction

This chapter describes the computational fluid dynamics (CFD) fire simulation software Fire Dynamics Simulator Version 4 (FDS) (McGrattan 2005), which was developed at the National Institute of Standards and Technology (NIST) in the United States of America. The theoretical and mathematical basis of the hydrodynamic component of the model is presented in Section 3.2. A summary of previous model validation research is given in Section 3.3. For details of the heat transfer, flame spread, soot production and combustion components of FDS, the user is referred to the FDS Technical Reference Guide (Forney and McGrattan 2004). Detail of the historical development of FDS is provided in Appendix A.

3.2 Model Description

3.2.1 Fundamental Conservation Equations

Fire Dynamics Simulator (FDS) is a three-dimensional CFD model developed to simulate fire-driven flows. It numerically solves the conservation equations of mass, momentum, and energy for an expandable ideal gas mixture in the low Mach number limit. Therefore, the equations do not permit acoustic waves and the time step for the numerical solution is bounded by the flow speed, rather than the speed of sound. The gases are assumed to be Newtonian, which means the shear stress is linearly proportional to the strain rate (Street et al. 1996).

The governing equations for conservation of mass, momentum and energy, used in FDS, are presented in Equations (3-1) to (3-3) respectively (Forney and McGrattan 2004). They describe the low speed motion of gases, driven by chemical heat release and buoyancy forces and are based on the work of Rehm and Baum (1978).

The first term in the conservation of mass equation describes density changes with time, while the second term accounts for mass flowing into and out of the control volume (Street et al. 1996). For steady flow, the conservation of mass equation reduces to the continuity equation, which states flow into a control volume must equal the flow out.

$$\frac{\partial \rho}{\partial t} + \nabla \cdot \rho \bar{u} = 0 \tag{3-1}$$

The conservation of momentum equation is the fluid dynamics equivalent of Newton's second law of motion, which states that the sum of the forces acting on an object must equal its mass times its acceleration (Street et al. 1996). The first term represents the local acceleration and is an inertial term, which would be zero for a steady flow. The second is also an inertial term, and describes advective acceleration. The third term is the pressure gradient and the fourth term represents the effect of body forces (including the buoyancy force caused by gravity) acting on the flow. The last term represents viscous stresses, which act to diffuse momentum through the flow.

$$\frac{\partial}{\partial t}\left(\rho \bar{u}\right) + \nabla \cdot \rho \bar{u}\bar{u} + \nabla p = \rho \bar{f} + \nabla \cdot \tau_{ij} \tag{3-2}$$

The conservation of energy equation is based on the first law of thermodynamics, which (in the absence of any mass-energy conversion or electromagnetic effects) states that the energy in any process is conserved (Street et al. 1996). The left-hand side describes the net accumulation of energy within the control volume, while the right side describes the various gain and loss terms that lead to this energy accumulation.

$$\frac{\partial}{\partial t}\left(\rho h_{ent}\right) + \nabla \cdot \rho h_{ent} \bar{u} = \frac{DP}{Dt} + \dot{q}''' - \nabla \cdot \bar{q} + \tau_{ij} \cdot \nabla \bar{u} \tag{3-3}$$

The equation of state is required to relate the pressure, temperature, and density of the gas. For an ideal gas the relationship is known as the ideal gas law, which is presented in Equation (3-4).

$$P = \frac{\rho R T}{M} \tag{3-4}$$

where: $\rho = \text{density}$

$t = \text{time}$

$\bar{u} = \text{velocity}$

$P = \text{pressure}$

$\bar{f}$ = external force vector (gravity and drag)

τ_{ij} = viscous stress tensor

h_{ent} = sensible enthalpy

$\frac{D(\cdot)}{Dt} = \frac{\partial(\cdot)}{\partial t} + (\bar{u} \cdot \nabla)(\cdot)$ = derivative of a moving particle (Lagrangian derivative)

$\dot{q}'''$ = net heat gain from sources and sinks

$\nabla \cdot \bar{q}$ = conductive and radiative heat fluxes

R_g = universal gas constant

T = temperature

M = molecular weight of gas mixture

$\tau_{ij} \cdot \nabla \bar{u}$ = dissipation function

The equations for conservation of mass, momentum and energy are a coupled system of non-linear partial differential equations. The dependent variables appear in each equation and so the equations must be solved simultaneously. These equations are too complex to solve analytically, and so must be solved by numerical methods.

3.2.2 Isothermal, Incompressible Flows

The FDS model can be used to simulate buoyancy driven isothermal, incompressible flows (McGrattan 2004b). This reduces the number of equations that need to be solved and simplifies those that remain, resulting in a significant reduction in the computational demand. An application of this feature is to model fresh and saltwater exchange flows, where the effects of compressibility and heat transfer are unimportant, enabling direct comparison of numerical and experimental results for validation purposes.

3.2.3 Numerical Method

The model breaks the flow field up into a large number of cells and solves the governing equations at each. The larger the number of cells in a given flow field the more detailed the results. These cells are treated as control volumes and the flow of mass, momentum and energy across each boundary surface is calculated. The internal conditions, within each cell, are assumed to be uniform in space and only change with time.

Within FDS the partial derivatives of the conservation equations are approximated using second order finite differences, and the solution is updated in time using an explicit second order predictor-corrector scheme (Forney and McGrattan 2004). The numeric solver in FDS is based on fast Fourier transforms (FFT), which are less computationally demanding than conventional models (Klote and Milke 2002). A limitation of this approach is that computational cells must be rectangular with small aspect ratios, which means the x, y and z cell dimensions should be approximately equal. The numerical techniques are described in more detail by McGratten (2004a).

3.2.4 Turbulence Modelling

Most of the flows generated by fires are highly turbulent (Klote and Milke 2002). This is due to the relatively low viscosity of air and the large length scales at which these fluid flows occur. If the grid size is fine enough to capture all relevant length scales, a direct numerical simulation (DNS) may be used within FDS to simulate this turbulent mixing. In a DNS the turbulent eddies are calculated at all scales and the molecular terms (dynamic viscosity μ, thermal conductivity κ and material diffusivity D) are applied directly. As DNS makes no allowance for mixing processes on scales smaller than the cell size, a very fine grid must be selected to ensure realistic results are obtained. For most applications, including modelling of all fire scenarios and most 3D scenarios, accurate DNS calculations are not currently possible due to computational limitations (Cox and Kumar 2002). These limitations arise as the range of appropriate length scales is too large to calculate from a first principles analysis (Tieszen 2001). Combustion occurs on a scale of 1 mm or less (Baum 2000), while a typical residential scale fire and the resulting smoke flows, occur over scales of tens of metres.

In CFD modelling, turbulent effects that occur on scales smaller than the cell size cannot be simulated directly by the Navier-Stokes equations. So when the grid resolution is not fine enough to capture the mixing processes at all relevant scales, a turbulence model is required to account for the effects of sub grid scale turbulence.

Two types of turbulence modelling technique have been applied to CFD fire modelling: k-ε and large eddy simulation (LES). The k-ε turbulence model, which uses Reynolds averaged Navier-Stokes equations (RANS), is the most common and computes time-averaged turbulence variables (Cox and Kumar 2002; Nelson 2002). The LES model, calculates instantaneous values of large-scale turbulence directly from the governing equations, instead

of using time-averaged values, and approximates sub-grid-scale (SGS) turbulent motions (Baum 1994; Nelson 2002).

The turbulence model used within FDS is Large Eddy Simulation (LES). The LES technique is based on the fact that in turbulent flows the largest eddies account for the majority of the transport of momentum and energy and have the strongest influence on the mean flow and mixing (Baum 1994; Clement 2000). In LES, the motion of the large scale eddies is calculated directly from the governing equations, while the motions of small scale or sub grid scale (SGS) eddies, which cannot be resolved by the grid size, are approximated by an eddy-viscosity model. By default, the Smagorinsky SGS model is used in FDS. As the grid size is refined further, the solution should theoretically converge to a more and more accurate approximation of the governing equations.

The LES technique models molecular processes (viscosity μ, thermal conductivity κ, material diffusivity D) at scales smaller the cell size (Forney and McGrattan 2004). For this reason the dissipative terms μ, κ and D are modelled using surrogate expressions, which, in FDS, are based on the results of Smagorinsky (1963). The effect is to artificially increase the dissipative terms to account for the SGS mixing, turbulence effects, and eddies.

The Smagorinsky SGS model is represented by Equations (3-5) to (3-7) (Forney and McGrattan 2004). In LES, the actual fluid viscosity, which is specified by the user, becomes the lower bound for the Smagorinsky viscosity (Equation (3-5)) (Forney and McGrattan 2004). The Prandtl number is used to relate the viscosity to the fluid conductivity (Equation (3-6)) and the Schmidt number is used to relate the viscosity to the fluid diffusivity (Equation (3-7)). The viscosity, diffusivity, Prandtl number and Schmidt number used by FDS are turbulent values, which are properties of the flow and not actual fluid properties. The turbulent Prandtl number and the turbulent Schmidt number are specified by the user and are assumed to be constant.

$$\mu_{LES} = \max\left[\mu, \rho(Cs\Delta)^2 |S|\right] \tag{3-5}$$

$$k_{LES} = \frac{\mu_{LES} c_p}{\mathrm{Pr}_{turbulent}} \tag{3-6}$$

$$(\rho D)_{l,LES} = \frac{\mu_{LES}}{Sc_{turbulent}} \tag{3-7}$$

where: μ_{LES} = Smagorinsky viscosity

k_{LES} = Smagorinsky conductivity

μ = fluid viscosity

ρ = fluid density

C_s = empirical Smagorinsky constant

$\Delta = \sqrt[3]{\Delta_x \Delta_y \Delta_z}$ = characteristic length of grid cell

$|S|$ = magnitude of the stress tensor

c_p = specific heat capacity

$\mathrm{Pr}_{turbulent}$ = turbulent Prandtl number

D = diffusivity

$Sc_{turbulent}$ = turbulent Schmidt number

The square of the magnitude of the stress tensor is presented in Equation (3-8) (Klote and Milke 2002), where *u, v* and *w* represent the velocity components in the *x, y* and *z* directions respectively.

$$|S|^2 = 2\left(\frac{\partial u}{\partial x}\right)^2 + 2\left(\frac{\partial v}{\partial y}\right)^2 + 2\left(\frac{\partial w}{\partial z}\right)^2 + \left(\frac{\partial u}{\partial y} + \frac{\partial v}{\partial x}\right)^2 + \left(\frac{\partial u}{\partial z} + \frac{\partial w}{\partial x}\right)^2 + \left(\frac{\partial v}{\partial z} + \frac{\partial w}{\partial y}\right)^2 \tag{3-8}$$

In FDS the default value of the empirical constant C_s is 0.20 (Forney and McGrattan 2004). The most appropriate value of C_s has more to do with the differencing scheme of the convective terms than it does with any physical phenomenon (McGrattan 2004a). Different values for C_s have been suggested, but LES results have been found to be relatively insensitive to minor changes in C_s (Tannehill et al. 1997).

3.2.5 Velocity Boundary Condition

The velocity boundary condition (VBC) controls the extent to which a fluid sticks to a solid surface. Theoretically, the velocity at a solid surface will be zero and increase rapidly through a narrow region known as the boundary layer. However, for most practical applications, the

numerical grid is too coarse to accurately resolve the boundary layer (McGrattan 2004b). Therefore, a velocity boundary condition parameter (VBC) has been included in the model, allowing the velocity at the wall to be set to a fraction of the value in the cell adjacent to the wall. The VBC parameter has the most influence on regions of the flow field close to rigid boundaries.

The VBC parameter ranges from VBC=-1, which represents a no-slip boundary condition, to VBC=1, which represents a free-slip boundary condition (McGrattan 2004b). A no-slip boundary condition is appropriate for direct numerical simulations (DNS), where the boundary layer is accurately resolved. For large eddy simulations (LES), which typically involve coarser grids, values of the VBC parameter between -1 and 1 can be used to represent partial slip boundary conditions, where the velocity at the boundary is a fraction of the velocity in the adjacent cell. FDS has a default value of VBC=0.5 for LES simulations.

3.2.6 Model Sensitivity

The results of any computer simulation are sensitive to the input parameters used. The user must perform a sensitivity study to determine the effect of varying individual parameters. In a sensitivity analysis, the value of various inputs are changed systematically to determine the effect on the model results. Typically, the grid size is the most important parameter defined by the user (McGrattan 2004a).

3.3 Previous Validation Work

Previous validation research, carried out over the last 25 years, has been used to validate various aspects of the FDS model. The objective of any validation work is to determine the accuracy of individual components of the model, and to asses the relative contribution of each element to the final accuracy of the simulations. It is not feasible to completely validate every aspect of the FDS model in a single piece of research. Therefore, past research has generally focussed on the validation of individual components of the model for a given set of scenarios. All validation research contributes to a model's development by identifying its strengths and weaknesses.

3.3.1 Bulk Characteristics of Saltwater Flows

The results of FDS simulations have been compared to the bulk characteristics of saltwater flows. Typical bulk flow characteristics such as front position, front velocity and overall flow dimensions are easily quantified by adding dye to saltwater flows, but they unfortunately give no quantitative measure of the internal flow structure.

Early validation work compared results of two-dimensional inviscid simulations of salt-water plumes to saltwater experiments (Baum et al. 1982). Both experimental and numerical results displayed a constant rate of plume decent until it reached the floor. However, the simulations reached rate of fall approximately 20% to 50% faster than the experimental data. Given that the grid resolution was very coarse the approximation was reasonable.

Further comparisons to saltwater flows were made for more detailed simulations. Due to computational requirements, only two-dimensional simulations were possible, but the grid resolutions were improved. Simulations of rigid boundary gravity currents showed that the simulations successfully predicted the front position of the gravity current with time, and the overall characteristics of the flow (Baum et al. 1995; McGrattan et al. 1994). Gravity current simulations, including heat transfer effects, showed that the speed of the gravity current front was reduced by heat loss (and the resulting buoyancy loss), in agreement with experiment (Rehm et al. 1997).

Two-dimensional and three-dimensional numerical simulations of backdraft gravity currents have been compared to saltwater experiments (Fleischmann 1994; Fleischmann and McGrattan 1999; Weng and Fan 2002). Further detail of this research was presented in the previous chapter (Literature Review).

3.3.2 Internal Flow Structure of Saltwater Flows

Clement (2000) compared experimental and numerical results of the internal flow structure of saltwater plumes, with the aim of validating the hydrodynamic component of the FDS model. Saltwater experiments, which were scaled to represent typical fire induced flows within residential buildings, were visualised with laser induced fluorescence (LIF). This system generated concentration fields and dilution contour fields in two-dimensional slices through the flow. Experimental results were compared directly to those from three-dimensional numerical simulations generated with version 1.0 of FDS. The validation focussed on time-

averaged results (for which the turbulent fluctuations are smoothed out), and compared experimental and numerical cross-sections through the flow. Some key findings of this research are outlined below:

- The numerical simulations were found to be highly grid dependent, but convergence was generally obtained through grid refinement. A maximum grid size, of 2% of the fire compartment height, was recommended for the simulation of fire induced smoke flows within multi-compartment residential scale buildings.
- Comparisons of numerical and experimental data demonstrated the difficulty in modelling the transition to turbulence in a spill plume, and concluded that the grid resolution was not fine enough to correctly capture this effect.
- Numerical simulations of a fire plume and ceiling flow demonstrated that the accuracy of FDS was generally very good. However, some flow characteristics observed in the saltwater experiments were not resolved in the numerical simulations. In particular the transit times of the ceiling jet, in the initial stages of the flow, were under predicted by FDS (velocities were over predicted) when compared to the experimental flows.

3.3.3 Isolated Fire plumes

The experimental fire plume correlations of McCaffrey (1979) were compared to numerical simulations of isolated fire plumes from FDS (Baum et al. 1996; Baum et al. 1997). These simulations were complex as they involved the hydrodynamic, combustion and heat transfer components of the model. The simulations showed close agreement with time averaged plume centreline temperatures and velocities and were able to accurately resolve the Gaussian distribution of temperature and velocity for cross-sections through the flow.

3.3.4 Full-scale fire scenarios

The simulation of full-scale, realistic fire scenarios is of course the ultimate aim of the FDS model. Extensive research has been carried out to validate FDS simulating full-scale fire scenarios. These fire scenarios are unsteady in time and involve fires burning within compartments, making detailed comparisons difficult because of the number of parameters that need to be assessed.

Flow visualisation, in fire scenarios, is difficult due to the harsh environment (Klote and Milke 2002). Typically, only global values or isolated point measurements of flow properties and heat transfer effects are possible.

The most comprehensive validation work completed to date compared a range of fire experiments and numerical simulations (U.S. Nuclear Regulatory Commission and Electric Power Research Institute 2006). The experimental geometries were relatively simple, but were varied to include large scale warehouses and multi-room enclosures, containing small to large heat release rate (HRR) fires. Zone-models, which are based on empirical relationships, were also investigated as part of the overall study. The research found that the FDS performed well when compared with the experiments, but the results were not significantly better than the zone-models. The associated computational cost of solving the governing equations in FDS may be many orders of magnitude greater than that of the zone-models. However, as FDS solves the transport equations instead of relying on empirical correlations, it is a much more predictive model and can be used in complex configurations, not suited to the use of zone models.

Other research into the performance of FDS to simulate full-scale fire scenarios is available in the literature. A summary of FDS validation research is presented in the FDS Technical Reference Guide (McGrattan 2004a).

3.4 Summary

In this chapter details of the CFD model Fire Dynamics Simulator (FDS) have been presented. Section 3.2 described the hydrodynamic component of model, while Section 3.3 discussed past validation research.

In Chapter 4, the experimental techniques used to simulate and visualise backdraft gravity currents are discussed, then Chapter 5 explains how FDS was used to simulate these experimental flows to enable a direct comparison of the experimental and numerical results.

CHAPTER 4 EXPERIMENTAL METHODS

4.1 Introduction

This chapter describes the experimental methods used in the saltwater modelling experiments, which were designed to replicate backdraft gravity current flows. A general description of the experimental setup is presented in Section 4.2. The light attenuation (LA) technique, which generates width-integrated concentration fields, is described in Section 4.3, and particle tracking velocimetry (PTV), which generates 2D velocity fields, is described in Section 4.4.

4.2 Experimental Setup

The experiments in the present study were carried out were carried out with salt and fresh water at the Fluid Mechanics Laboratory at the University of Canterbury in Christchurch, New Zealand. The feasibility of using salt and fresh water flows to replicate buoyancy driven backdraft gravity currents was discussed in the previous chapter.

4.2.1 Flume

The flume used in all of the experiments was 5.0m long, 0.40m deep and 0.252m wide. The walls were constructed of 18mm thick transparent Perspex, to facilitate flow visualisation. The flume was located in a dark room, which prevented the entry of any ambient light.

The sides of the flume were connected, at the top, with regularly spaced steel ties to resist hydrostatic pressures and prevent lateral movement. This ensured flume walls remained parallel as the flume was filled. The flume was mounted on a rigid steel framed truss, which could be tilted to enable surfaces to be levelled.

A lock-exchange arrangement was used in the experiments. The use of a simple lock gate setup was appropriate as backdraft research has indicated that, prior to ventilation, compartment conditions are relatively uniform (Fleischmann 1994; Gottuk et al. 1999). The orientation of the experiments was inverted compared to that of backdraft gravity currents. Saltwater represented buoyant hot gases trapped in a fire compartment, while freshwater represented cool dense ambient air. Removal of the lock gate allowed an exchange flow to develop and simulated compartment ventilation.

An elevated Perspex section was fitted in one half of the flume and an 11mm thick Perspex lid was suspended from the top of the flume. This created an elevated rectangular compartment, which replicated a typical fire compartment. In cross-section, the compartment was 0.252m high x 0.252m wide, which was a scaled version of the 2.5m wide x 2.5m high and 3.6m long compartment typically used for full-scale fire testing (International Organization for Standardization 1993).

A schematic of the experimental flume setup is presented in Figure 4-1, while a schematic of the gravity current flow that developed during the experiment is presented in Figure 4-2.

Near the middle of the flume, the elevated section was separated from the rest of the flume by two adjacent vertical stainless steel lock gates (represented by the dashed line in Figure 4-1). The elevated section was filled with salt water, while the other side of the flume was filled with fresh water. The lock gates were sealed on all sides by foam tape to prevent leakage. A schematic of these lock gates is provided in Figure 4-3.

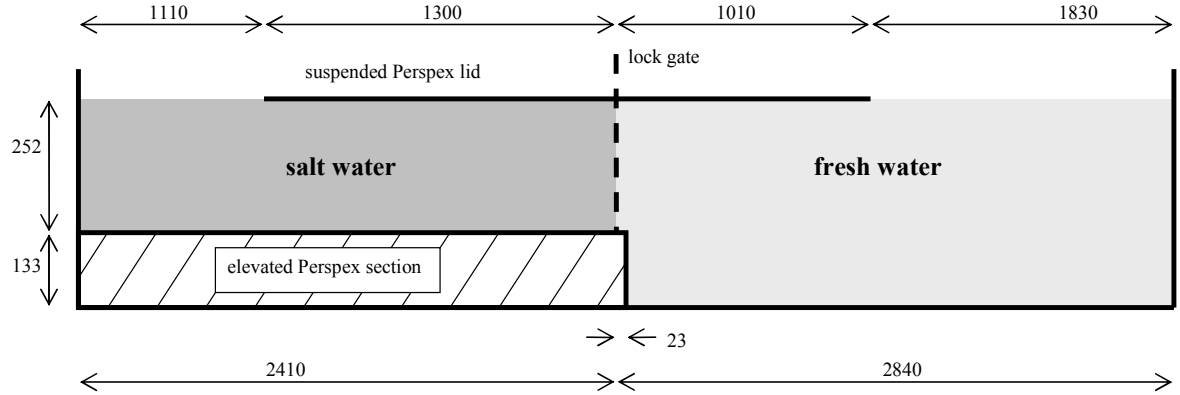

Figure 4-1: Side elevation of experimental flume setup. The dotted line represents the location of the lock gate. All dimensions are in mm and are taken from the inside face of the flume walls. Not to scale.

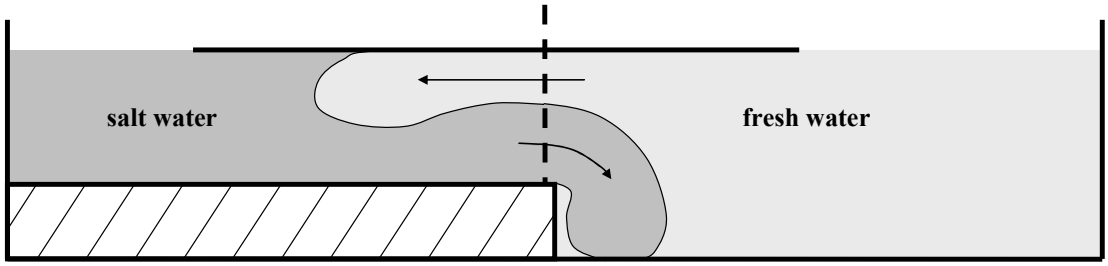

Figure 4-2: Side elevation of the lock exchange flow after removal of the lock gate. The dotted line represents the location of the lock gate. After lock gate removal, fresh water forms a gravity current flowing along the suspended Perspex lid.

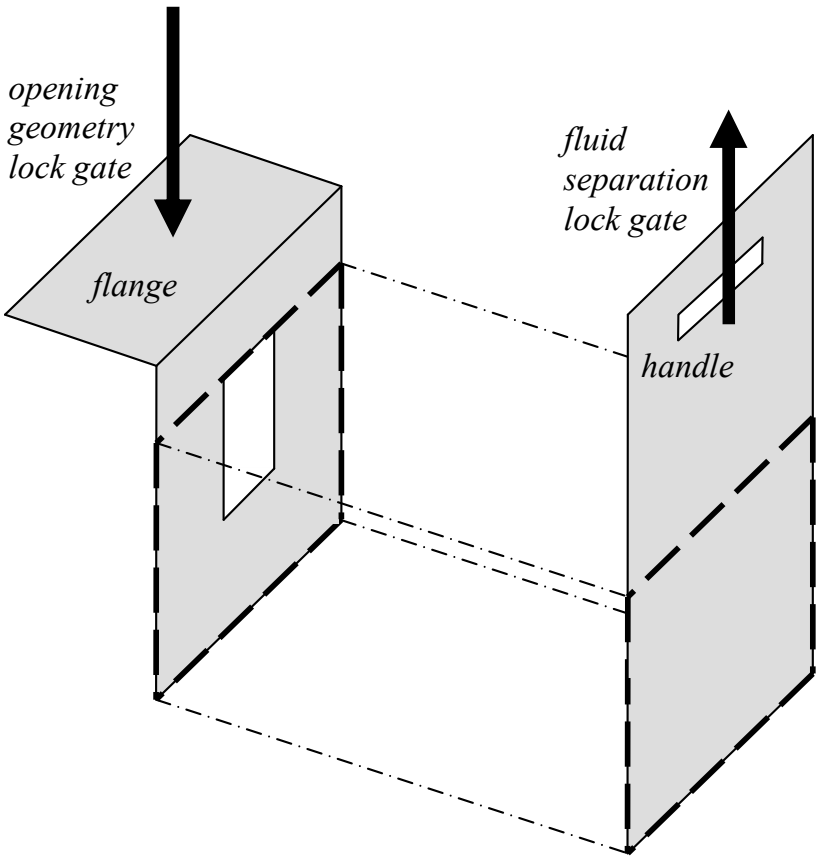

Figure 4-3: Schematic of a typical opening geometry lock gate and the fluid separation lock gate. The bold dashed lines indicate a cross-section through the compartment. (NOTE: The dash-dot lines indicate how the gates fit together, not a physical separation).

The first gate replicated the desired compartment opening geometry (*opening geometry lock gate* in Figure 4-3), and was clamped in place by a flange to prevent movement. The second lock gate completely sealed off the two sections of the flume (*fluid separation lock gate* in Figure 4-3), separating the salt and fresh water. By pulling a handle, the *fluid separation gate* was rapidly removed to start each experiment. The gates were lubricated to reduce friction and assist rapid gate removal. The different geometries used for the *opening geometry lock gate* are described in Section 4.2.3.

To allow access for mixing and bubble removal, no end wall was included on the end of the saltwater compartment, and the suspended Perspex lid only extended 1.3m (approximately five lock depths) into the elevated saltwater compartment and 1.01m (approximately four lock depths) into the other end of the flume. The effect on the gravity current motion of having a free-surface instead of a rigid boundary further from the lock gate was assumed to be

negligible, because only the initial period of flow, which occurred adjacent to the rigid boundary, was of interest. Also, as gravity currents are a type of exchange flow, ambient fluid motion occurs only in the regions already passed by, or in the immediate vicinity of, the head of the propagating current.

4.2.2 Procedure

Before each experiment, the lock gates were removed and the flume was completely filled with fresh water. The flume was then left overnight, so that the water adjusted to room temperature and de-aerated. During the de-aeration process, air dissolved in the water formed bubbles on the solid flume surfaces. These bubbles were removed prior to each experiment so that they would not interfere with the fluid flow or the flow visualisation. Allowing the water temperature to adjust to a steady state prevented temperature differentials developing throughout the flume and also prevented temperature changes over time, during both the light attenuation calibration process (see Section 4.3.3) and the experiments. Temperatures on both sides of the lock were monitored using mercury thermometers to ensure they stayed within +/- 0.2°C.

After allowing the water temperature to adjust, the lock gates were lowered into position and salt was mixed with the water in the elevated section of the flume. The salt used in the experiments was standard sodium chloride (NaCl). The quantities of salt required to obtain the required density difference were calculated based on the tabulated data in the CRC Handbook of Chemistry and Physics (Frederikse and Lide 1997). The salt mass, of approximately 1000g, was measured with scales accurate to 0.1g and then manually mixed into the flume. The target dimensionless density difference was selected to ensure Reynolds number independence. A value of approximately $\beta_{initial} = 0.005$ was used for all experiments, except those with a window opening geometry, which required a dimensionless density difference of approximately $\beta_{initial} = 0.04$ to generate fully turbulent gravity current flows. The density of the fluid on both sides of the lock gates was sampled and analysed using an Anton Parr DMA60 density meter with a DMA602 measuring cell, which was accurate to 0.04kg/m^3 (Clement 2000), or 0.004%.

Additional substances, dependent on the flow visualisation technique being employed, were also mixed with the flume water. For the light attenuation (LA) experiments (described in

Section 4.3) a red dye of a known concentration was mixed uniformly with the saltwater only, while in the particle tracking velocimetry (PTV) experiments (described in Section 4.4) a known concentration of fine particles was mixed uniformly throughout the entire flume (salt and fresh water).

The flume water was left for approximately five minutes prior to the start of each experiment, for ambient turbulent motions to diminish. The experiments were started by rapidly lifting the *fluid separation lock gate* out of the flume. This allowed an exchange flow to develop between the fresh and saltwater, as shown in Figure 4-2. The dense saltwater flowed out and over the edge of the elevated section of the flume, simulating hot gas escaping a ventilated compartment, and the fresh water flowing into the compartment along the Perspex lid, simulating a backdraft gravity current.

4.2.3 Opening Geometries

A number of different opening geometries were investigated in the experiments and a separate *opening geometry lock gate* was constructed for each. These gates were made from 0.9mm thick stainless steel sheeting. The steel was extended above the level of the compartment, forming a flange, which was used to clamp the gate into position (see Figure 4-3).

Compartment ventilation, which is required to form backdraft gravity currents, commonly occurs as doors and windows are opened by fire fighters, or as glass windows fracture due to the effects of heat (Fleischmann and McGrattan 1999; Hume 2005). The experimental compartment opening geometries were chosen to reflect this and included: a fully open end wall, a horizontal step, a vertical slot, a door and a window. The last four of these opening geometries are illustrated in Figure 4-4. Past researchers have investigated similar compartment openings (Fleischmann and McGrattan 1999).

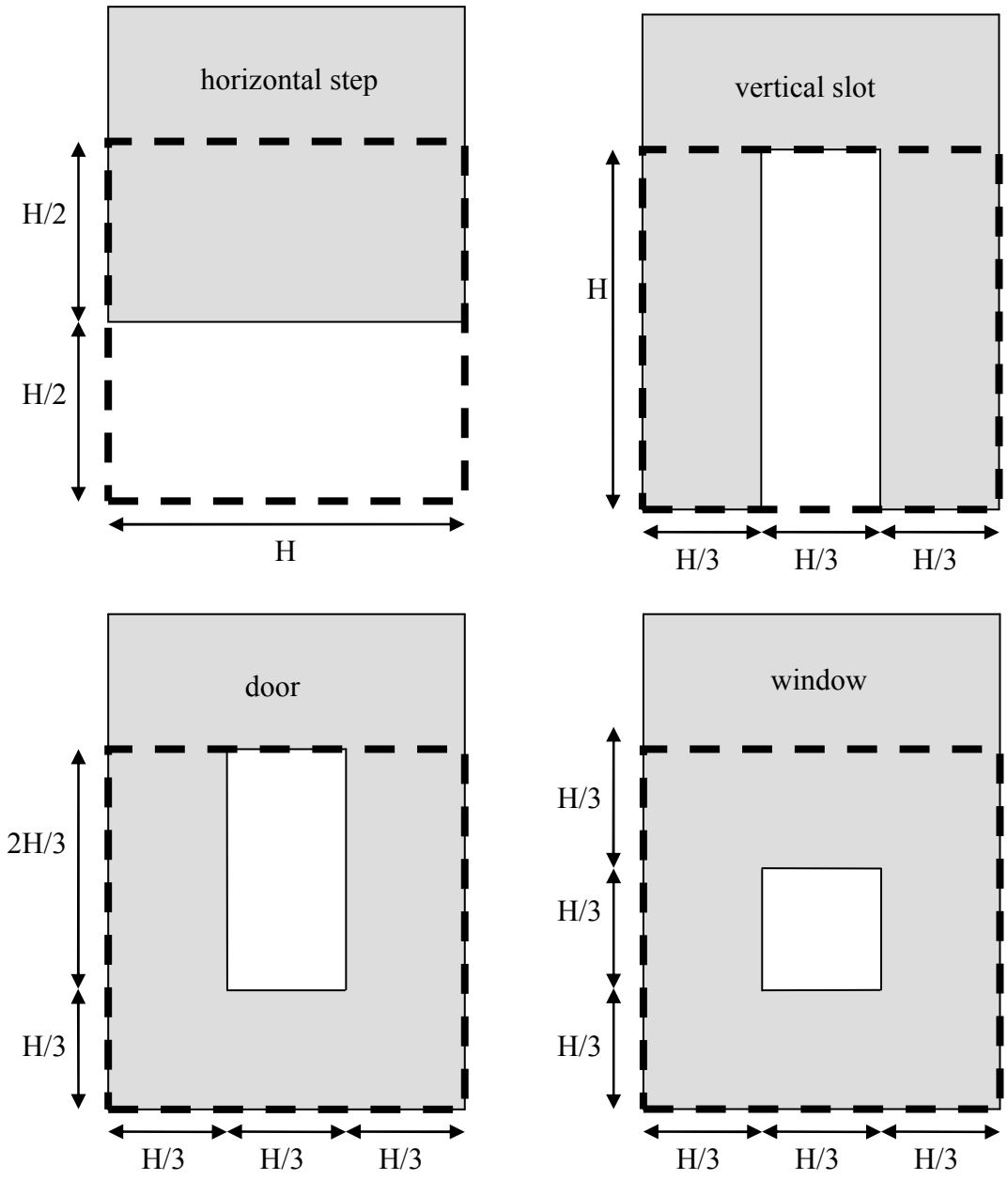

Figure 4-4: Schematic showing the geometry of four *opening geometry lock gates* used in the experiments. The dotted line represents a cross-section through the compartment, the shaded area represents the lock gate, and the white rectangles represent holes cut in the lock gate. The compartment height H=252mm.

The opening geometries were selected to represent real compartment opening geometries, but were inverted to match the orientation of the saltwater experiments. The horizontal step represents a full width window, which reaches from wall to wall. The vertical slot opening represents a full height door, reaching from the floor to the ceiling. The door opening represents a typical door, which does not reach all the way to the ceiling. The window represents a small window centred on a wall.

In addition to the four compartment opening geometries shown in Figure 4-4 above, an experiment was conducted without an *opening geometry lock gate*, which represented a fully open end wall. The reason for using this geometry was to generate data for comparison to past research, providing validation of, and improve confidence in, the experimental techniques being employed.

4.3 Light Attenuation

The internal concentrations within backdraft gravity currents are important because they provide detail of the location and evolution of flammable gas mixtures. In the past, concentrations have been determined from sampling probes inserted in the flow. However, with advances in digital imaging, non-intrusive techniques such as light attenuation (LA) may be used to provide full spatial and temporal resolution of concentrations. The LA technique was adopted in this research and is explained below.

4.3.1 Theory

Light attenuation (LA) is a non-intrusive flow visualisation technique that can be used to obtain width integrated 2D concentration fields. Dye is introduced to the flow and, based on the intensity of light transmitted, the dye concentration can be determined. The technique is non-intrusive, meaning it does not physically interfere with, or alter, the flow. These concentration fields provide detail of the internal structure and mixing occurring within fluid flows. Densities caused by dissolved salts can be determined as they are linearly proportional to the concentration (for low concentrations).

A uniform white light source is directed through the dyed fluid and all other sources of light are eliminated. As the light travels through obstructions and interfaces, the intensity is attenuated by absorption, reflection and distance. Absorption occurs as light travels through transparent substances (including air, Perspex, glass, water and dye), reflection occurs at the interfaces of these substances and attenuation occurs with distance as the light rays diverge. The difference between the intensity of light passing through a dyed and an un-dyed fluid is due to attenuation by the dye. Therefore, if the relationship between light attenuation and dye concentration is known, the light intensity can be used as a measure of the dye concentration.

One of the first applications of the light attenuation technique was to investigate two-dimensional lock exchange gravity currents (Hacker et al. 1996). In these experiments, it was assumed that light attenuation was linearly related to the dye concentration, as shown in Equation (4-1).

$$c = c_0 f\left(\frac{I_0}{I}\right) \tag{4-1}$$

where: c = mean across-channel dye concentration

c_0 = reference dye concentration

f = calibration constant (assumed linear)

I = light intensity with dye in fluid

I_0 = reference light intensity (with no dye in fluid)

A more advanced relationship was developed by Cenedese and Dalziel (1998), who used absorption theory to show that the intensity of light passing through a dyed fluid will decay exponentially with the integrated dye concentration, as shown in Equation (4-2). The optical thickness, *d*, describes this exponential light intensity decay rate. The derivation of this relationship is included in Appendix B.

$$ch_f = a\ln\left(\frac{I_0}{I}\right) = ad \tag{4-2}$$

$$d = \ln\left(\frac{I_0}{I}\right) \tag{4-3}$$

where: ch_f = integrated dye concentration

c = concentration of dyed fluid

h_f = width of dyed fluid

a = constant

d = optical thickness of the fluid

This relationship is valid for low integrated dye concentrations (Cenedese and Dalziel 1998; Kikkert 2006). However, at higher integrated dye concentrations the relationship becomes invalid, as illustrated in Figure 4-5. The transitional integrated dye concentration where this equation becomes invalid can be determined by incrementally adding small amounts of dye.

To optimise the resolution of the light attenuation technique, the maximum integrated dye concentration should approach, but not exceed, the transition concentration. When no dye is present in the fluid, $I = I_0$ and $c = 0$, which defines the origin in Figure 4-5.

If the maximum dye concentration $c_{\max}$ is known and the corresponding optical thickness is measured, then any other dye concentration can be determined as a fraction of the maximum concentration, as shown in Equation (4-4). The width of the dyed fluid (h_f) was assumed to remain constant, eliminating any dependence on this parameter.

$$R = \frac{c}{c_{\max}} = \frac{\ln\left(\frac{I_0}{I}\right)}{\ln\left(\frac{I_0}{I_{\max}}\right)} = \frac{d}{d_{\max}} \tag{4-4}$$

where: $R =$ relative concentration / relative density

$c_{\max} =$ maximum fluid dye concentration

$I_{\max} =$ light intensity for maximum fluid dye concentration

$d_{\max} = \ln\left(\frac{I_0}{I_{\max}}\right) =$ maximum optical thickness (with maximum dye)

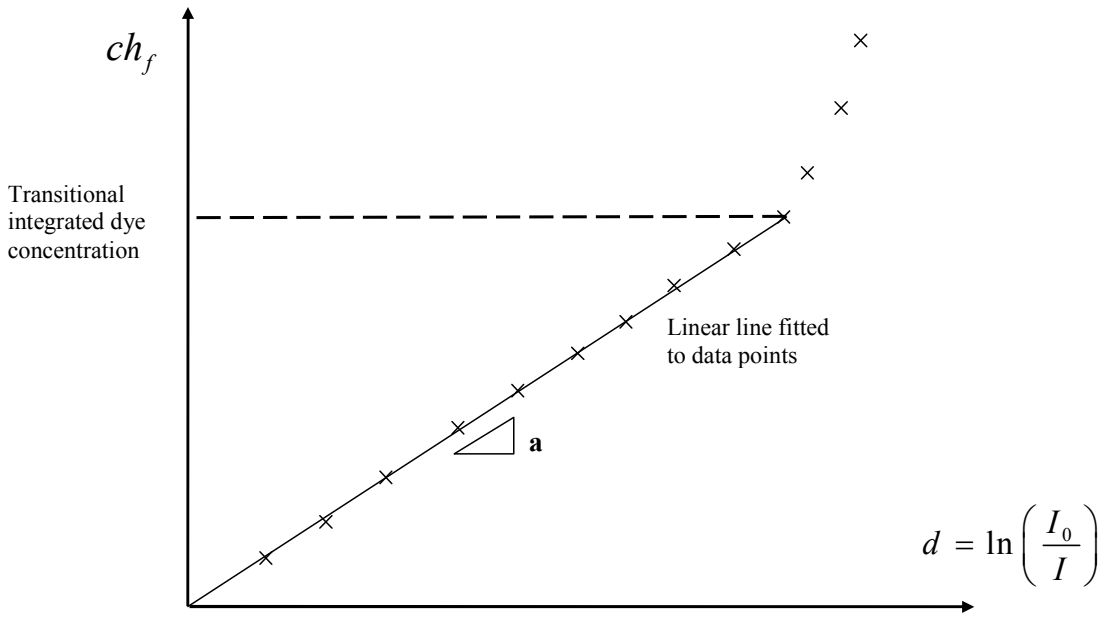

Figure 4-5: Diagram showing the relationship between integrated dye concentration and optical thickness.

The relative concentration R is equal to the relative density for low salt concentrations and is effectively a measure of the level of mixing that a fluid has undergone. Fluid with the maximum concentration of dye has a relative concentration of 1.0, while the un-dyed ambient fluid has a relative concentration of 0.0. A relative concentration between 0.0 and 1.0 indicates mixed fluid. The Relative concentration may also be expressed as a percentage.

The inverse of the relative concentration is the dilution of the dyed fluid. A dilution of 1.0 indicates undiluted fluid, while a dilution of infinity indicates ambient fluid.

$$S = \frac{1}{R} \tag{4-5}$$

where: $S = \text{dilution}$

The LA process is illustrated graphically in Figure 4-6, which shows how the relative concentration may be determined from the light intensity once the relationship between the two is known.

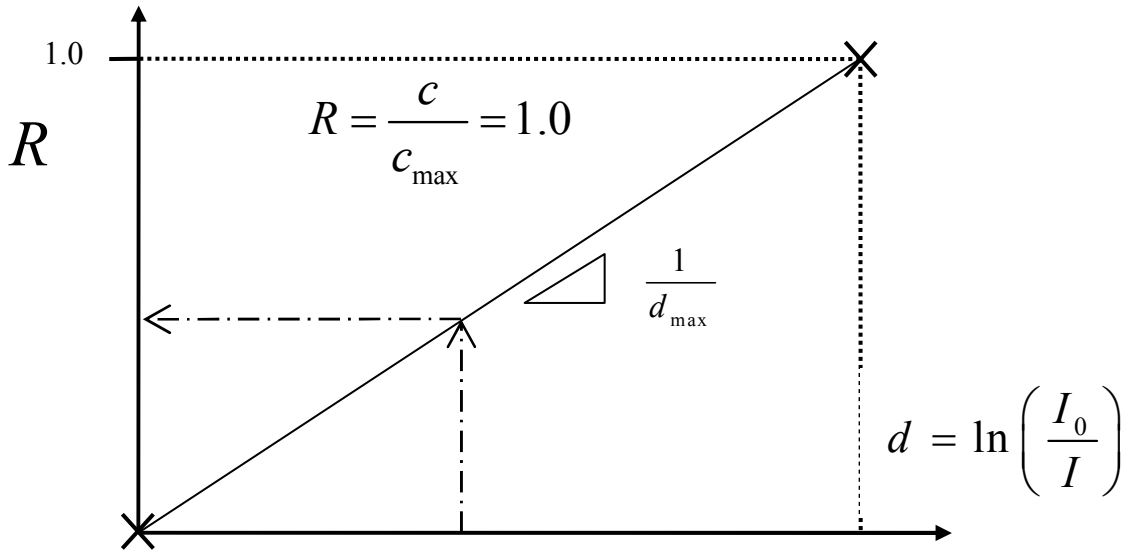

Figure 4-6: Diagram of light attenuation process. The dash-dotted line illustrates how the relative dye concentration may be determined from the optical thickness (which is calculated from light intensity). The dotted line corresponds to the maximum relative dye concentration. The solid line represents the relationship in Equation (4-4).

Cenedese and Dalziel (1998) found that the level of light attenuation was a function of light wavelength as well as dye concentration. When exposed to white light, they found that red organic dye had a region of constant response at a wavelength of approximately $510\eta m$, which corresponds to green light. Green light can be selected either by placing a suitably coloured filter over the camera lens, or by only using results from the green gun of a digital camera and discarding the intensities from the blue and red guns.

Using red dye and the attenuation of green light, Kikkert (2006) found that the optical thickness was also dependent on temperature and background light intensity. The temperature effects may be eliminated by allowing the fluids to reach steady state temperatures prior to the experiment. Temporal background light intensity effects may be minimised by allowing lights to fully heat up prior to the experiment, and time-averaging the data where possible. Spatial variations in background light intensity may be eliminated by carrying out pixel by pixel field calibrations, effectively applying Equation (4-4), separately, at every pixel in the digital image.

If the precautions mentioned above are followed, the relationship between green light optical thickness and relative red dye concentration, suggested by Equation (4-4), is valid.

4.3.2 Experimental Equipment

The light attenuation experiments were carried out in the flume described in Section 4.2. The lighting and data capture setup used in these experiments is illustrated in Figure 4-7.

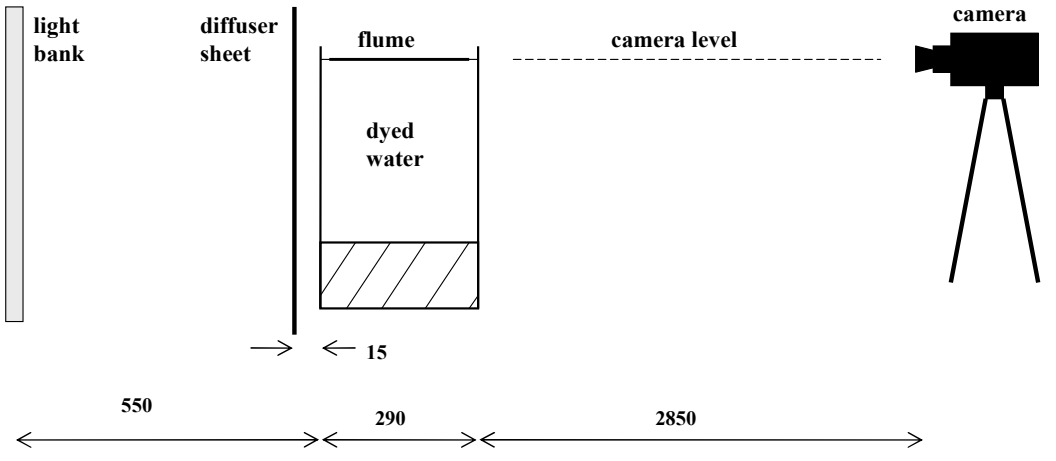

Figure 4-7: End elevation of lighting and camera setup for light attenuation experiments. Dimensions are in mm and are taken from the outside face of the flume walls. Not to scale.

A red organic food dye was used to trace the flow. The dye was Carmoisine Powder (colour #25070 with a corresponding food additive code No. 122) manufactured by Formula Foods. Calibration experiments carried out by Kikkert (2006) showed that the dye did not react with NaCl salt and that aging effects were minimal.

A light bank of 24 vertically orientated fluorescent tube lights, spaced at 60mm centres, illuminated the flow. The light bank was positioned parallel to the flume, 550mm from the outside surface. A light diffuser sheet, made of 2mm thick translucent Perspex, was positioned between the light bank and flume, 15mm from the face of the flume. The diffuser acted to spread the light, creating a relatively uniform light intensity field. Blackout sheeting was positioned around the edge of the light bank and above and below the diffuser sheet to reduce the amount of reflected light reaching the camera.

The camera used for the LA experiments was a Jai CV-M7^{+} CL. The camera recorded digital 8 bit colour images at 24 frames per second, but only the light intensities from the green gun were used in the analysis. The frame resolution was 1268 by 1024 pixels and the intensities at each pixel ranged from zero to 255. The maximum number of frames that could be captured in an experiment was limited to 1142 by the size of the RAM in the data logging computer. All camera settings were manually adjustable and not altered during each experiment. Exposure and gain levels were adjusted so that the maximum light intensity level was slightly below saturation.

The camera was fixed on a tripod and positioned orthogonal to, and 2.85m from, the side of the flume. It was centred on a point 0.5m (approximately two lock depths) into the saltwater compartment from the lock gate and level with the suspended Perspex lid. The total field of view extended laterally 0.5m (approximately two lock depths) either side of this point and vertically down to the rigid bottom boundary. The camera location is shown graphically in Figure 4-7 and Figure 4-8.

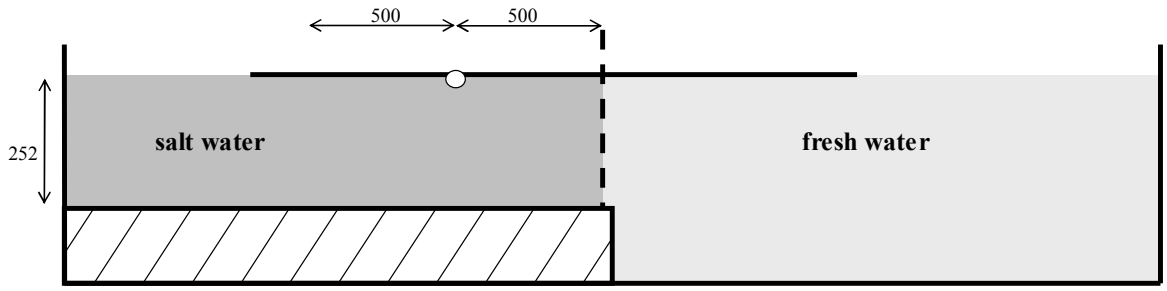

Figure 4-8: End elevation showing camera view and the centred position. The white circle represents the centre of view of the camera. Not to scale. All dimensions in mm.

4.3.3 Calibration

Calibration experiments were carried out in the flume described in Section 4.2. The purpose of the calibration experiments was to establish the validity of the linear relationship between the green light optical thickness and integrated red dye concentration suggested by Equation (4-2) and to establish the transitional integrated red dye concentration where this linear relationship was invalid (see Figure 4-5).

Previous calibration experiments had shown temperature changes of the order of 1ºC, significantly affected the level of light attenuation (Kikkert 2006). Therefore, temperature differences were monitored to ensure they were less than +/- 0.2ºC. As required, cooling blocks and heating coils were used to control the temperature.

A concentrated solution of red dye was created by mixing Carmoisine Powder with fresh water. Approximately 3.8g of Carmoisine Powder, measured with scales accurate to 0.01g, was added to two litres of water at 20ºC, measured with scales accurate to 0.1g. A 5mL pipette was used to incrementally add small volumes of this concentrated dye solution to the flume.

After adding each increment, the dye was mixed uniformly and a sequence of digital images was captured. Each sequence of digital images was time-averaged, eliminating the effects of temporal light intensity fluctuations.

The integrated red dye concentration was plotted against the green light optical thickness for individual pixels in the digital image. The relationship was linear for integrated red dye

concentrations lower than a transitional integrated concentration of approximately of $0.12 \, g/m^3 \, m$, as shown in Figure 4-9, confirming the linear relationship suggested by Equation (4-2). For clarity, only the maximum and minimum intensity pixels from the image are plotted in this figure, but other pixels showed similar results. A straight line, fitted from the origin to the transitional integrated dye concentration, matched experimental results with less than 5% error for an individual pixel (see Figure 4-9 (b)). The slope of this line was dependent on the background light intensity, but this was accounted for through pixel by pixel calibrations.

A separate calibration experiment was also carried out to ensure that salt (NaCl) did not significantly affect the linear nature of the relationship between green light optical thickness and integrated red dye concentration. Salt and the red dye were added incrementally and mixed uniformly in the flume water. The total of approximately 1kg of salt was added to the saltwater compartment side of the lock, corresponding to a density difference of $\beta \sim 0.005$. The volumetric increase due to adding salt was accounted for using tabulated data in the CRC Handbook of Chemistry and Physics (Frederikse and Lide 1997). The results, presented in Figure 4-10, indicate that effect of the salt was not significant, with maximum errors in predicted dye concentration were again less than 5%. The addition of salt altered the slope of the lines presented in Figure 4-9 (b) and Figure 4-10 (b), but again this was accounted for with pixel by pixel field calibrations prior to each experiment.

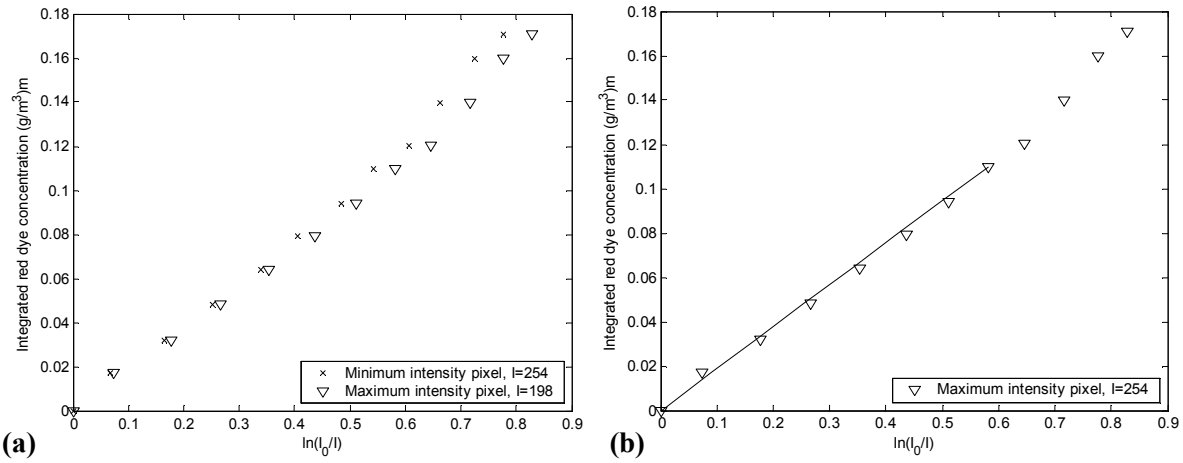

Figure 4-9: Typical plot of green light optical thickness versus integrated red dye concentration from calibration experiment with red dye, but no salt: (a) typical experimental data points, (b) linear line fitted from the origin to the transitional concentration.

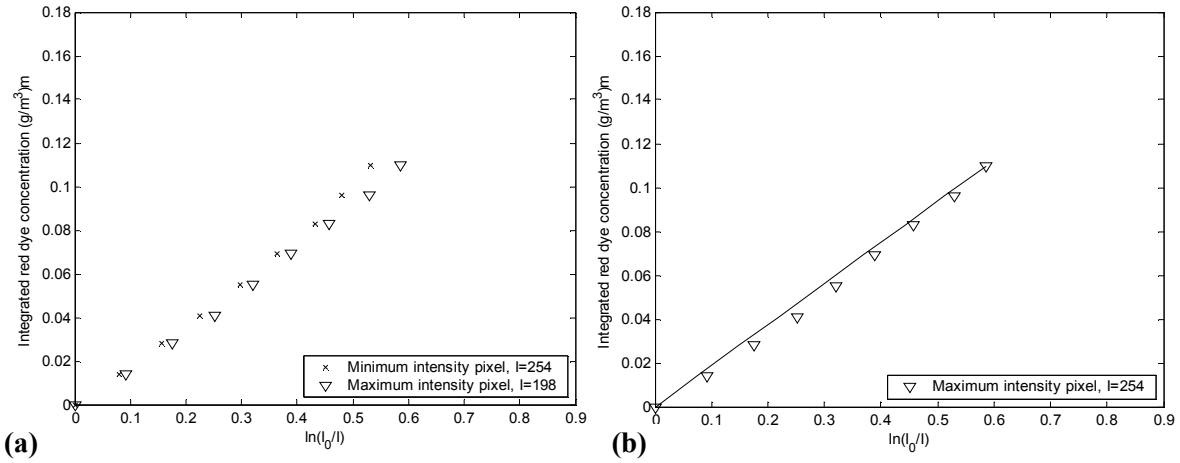

Figure 4-10: Typical plot of green light optical thickness versus integrated red dye concentration from calibration experiment with red dye and salt (NaCl): (a) typical experimental dataset, (b) straight line fitted from the origin to the transitional concentration.

To ensure that the transitional integrated red dye concentration (0.12 $g/m^3 m$) was not exceeded, a maximum integrated red dye concentration of 0.11 $g/m^3 m$ was used in the experimental flows.

4.3.4 Data Capture

The typical procedure used to capture data in the LA experiments is outlined below:

- The light bank was turned on and all ambient sources of light were eliminated.
- A scale ruler was temporarily inserted down the centre of the flume, to determine a length scale for the subsequent analysis.
- Camera settings were manually adjusted so maximum green light intensities were slightly below saturation (255).
- A field calibration was carried out prior to each experiment. The field calibration defined the origin and the maximum dye concentration / optical thickness in Figure 4-6 for every pixel in the image. An image sequence was taken of the fresh water (with no dye or salt), to act as a reference point for the minimum dye concentration. After mixing red dye and salt uniformly, a second image sequence was taken to act as a reference point for the maximum dye concentration. Typical field calibration image sequences were approximately 100 frames in length.

- The flume water was left undisturbed for approximately five minutes prior to each experiment, to allow ambient fluid motions to decay.
- The *fluid separation lock gate* was removed rapidly, allowing an exchange flow to develop. The lock gate was visible in the corner of the camera view, so the exact time of removal could be determined.
- An experimental digital image sequence was captured. Typical experimental image sequences were between 600 and 1100 frames in length.

4.3.5 Data Processing

Analysis of the digital images captured in the light attenuation experiments required calculations at individual pixels. With typical laboratory experiments involving hundreds of images and each image containing thousands of pixels, the process was computationally demanding. The computer software ImageStream version 5.0 (Nokes 2006d), a software package developed specifically for processing of digital images from fluid mechanics experiments, was employed to automate the process. Details of the software design and capabilities can be found in the system theory and design manual (Nokes 2006e) and the user's guide (Nokes 2006f).

The process used to analyse the data is outlined below:

- The field-calibration image sequence of freshwater was time-averaged, creating a "freshwater" image. The field-calibration image sequence with the maximum dye concentration was also time-averaged, creating a "maximum dye" image. The time-averaging eliminated errors associated with temporal fluctuations in light intensity from the field-calibration images.

- The optical thickness for the maximum dye concentration was calculated at every pixel using Equation (4-6), the green light intensities in the "maximum dye" image, $I(x,z)$, and the green light intensities from the "freshwater" image, $I_0(x,z)$.

$$d_{\max}(x,z) = \ln\left(\frac{I_0(x,z)}{I(x,z)}\right) \tag{4-6}$$

where: (x,z) = pixel co-ordinate

- The optical thickness was calculated at each pixel of each frame in the experimental image sequence, using Equation (4-7), the green light intensities in the experimental frame, $I(x,z,t)$, and the green light intensities in the "fresh water" image, $I_0(x,z)$.

$$d(x,z,t) = \ln\left(\frac{I_0(x,z)}{I(x,z,t)}\right) \tag{4-7}$$

where: (x,z,t) = pixel co-ordinate (x,z) at time t

- The relative concentration was calculated at each pixel in each frame in the experimental image sequence using Equation (4-8), which is the ratio of the optical thickness in the experimental frame, $d(x,z,t)$, to the maximum optical thickness (with the maximum dye concentration), $d_{\max}(x,z)$.

$$R(x,z,t) = \frac{d(x,z,t)}{d_{\max}(x,z)} \tag{4-8}$$

- Finally, a relative concentration field was created for each experimental frame using a pseudo colour scale to represent the magnitude of the relative concentration. The relative concentration represented the fraction of saltwater in the mixture and was expressed as a percentage: 0% = freshwater and 100% = saltwater.

Typical images from an experiment with the horizontal step opening, trimmed to include only the flow region ($0.0H < x < 4.0H$, $0.0H < z < 1.0H$), are shown below. Figure 4-11 and Figure 4-12 are time-averaged colour images taken as part of the field calibration process immediately prior to the experiment. Figure 4-13 shows an instantaneous colour image taken midway through the experiment. Figure 4-14 shows the experimental image converted to a width-integrated relative concentration field based on the green light intensities.

Figure 4-11: Time averaged colour image from field calibration before addition of dye and salt.

Figure 4-12: Time averaged colour image from field calibration after addition of dye and salt.

Figure 4-13: Instantaneous colour image taken midway through the experiment.

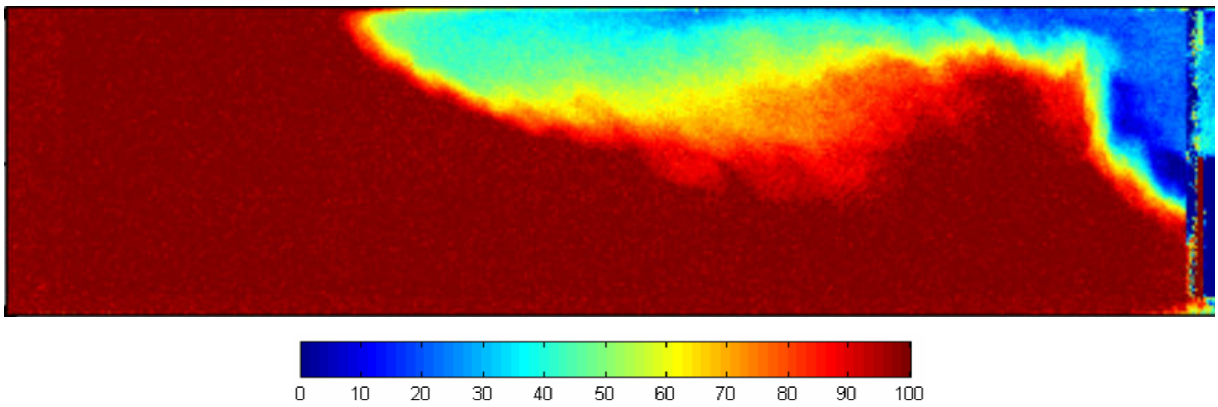

Figure 4-14: Instantaneous false colour plot showing the relative concentration field. Dark red (100) represents salt water and dark blue (0) represents fresh water. Scale is expressed as a percentage of saltwater.

4.3.6 Accuracy

The errors associated with the experimental relative concentration fields produced by the LA analysis are discussed below.

Time Scales

The time scales used in the experiments were based on the capture rate of the digital camera (24 frames per second) and introduced a time-scale error of +/- $^{1}/_{24}$ seconds.

The lock gate was removed over a maximum period of half a second (a time which was determined directly from the experimental image sequences). The experiment was assumed to start halfway through the lock-gate removal. Therefore, it was estimated that the error associated with the experimental start time was less than ¼ of a second.

Length Scales

Length scales were estimated using a one metre scale, placed in the centre of the flume. For each experiment this scale was used to generate length scale estimates to the nearest pixel (approximately 1 millimetre) +/-0.004H.

Parallax

An error associated with the experimental setup was parallax. Parallax occurs due to the viewing angle of the camera changing for different parts of the flume, as shown in Figure 4-15 and Figure 4-16, which distorts the image. Increasing the separation distance between the flume and camera reduces this error. Therefore, to minimise the effects of parallax, the camera was located as far as possible from the side of the flume (at a distance of 2.85m), which resulted in a maximum viewing angle of approximately 10 degrees.

Consider a relatively two-dimensional gravity current moving as a slug of fluid with no internal mixing, as shown in the plan view in Figure 4-17 (b). Two different viewing positions are considered, (1) at an angle to the flume and (2) perpendicular to the flow. The apparent relative concentration versus the distance down the flume for these viewing positions is plotted in Figure 4-17 (a). The relative concentration (R) is 0% within the gravity current and 100% in the ambient fluid and length scales are measured along the centre of the flume.

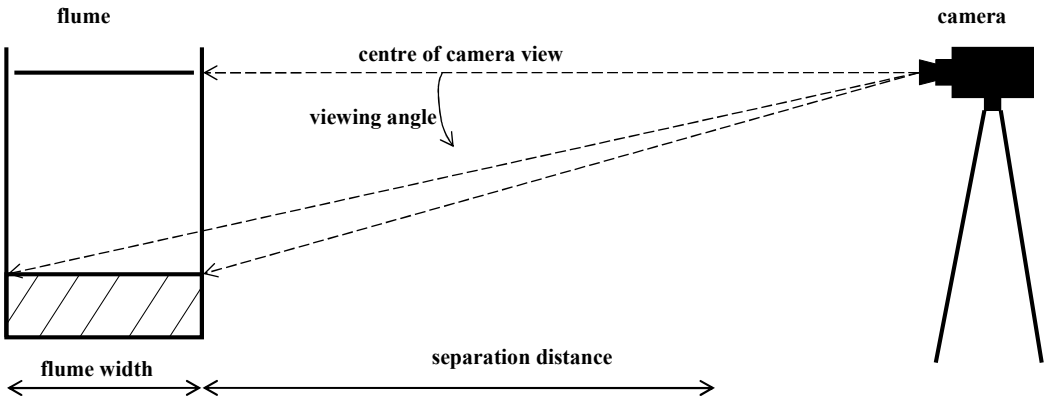

Figure 4-15: End elevation of flume showing the source of parallax errors

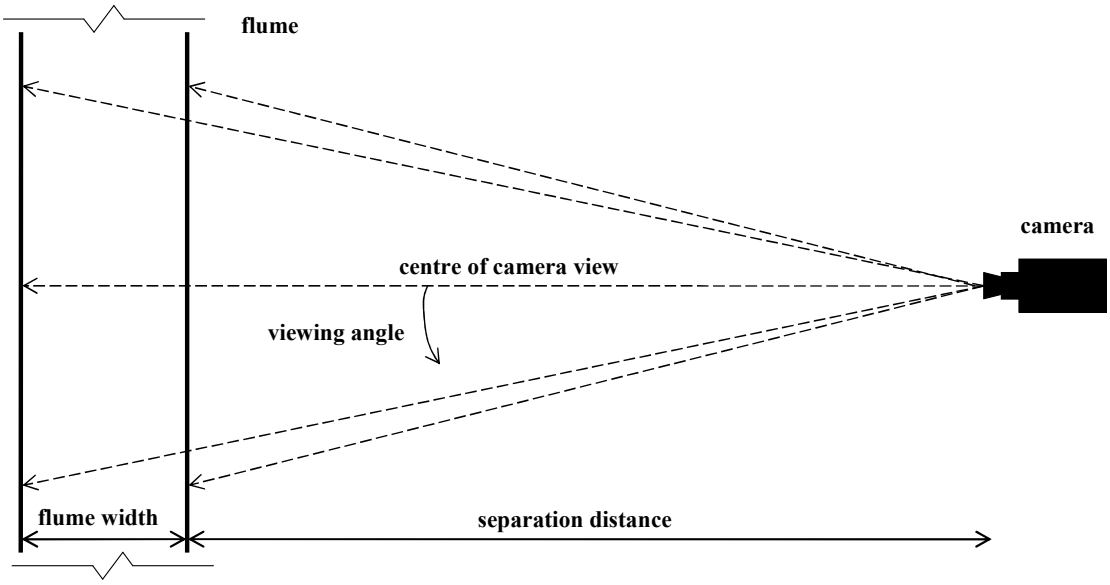

Figure 4-16: Plan view of flume showing the source of parallax errors. The dotted lines represent light paths.

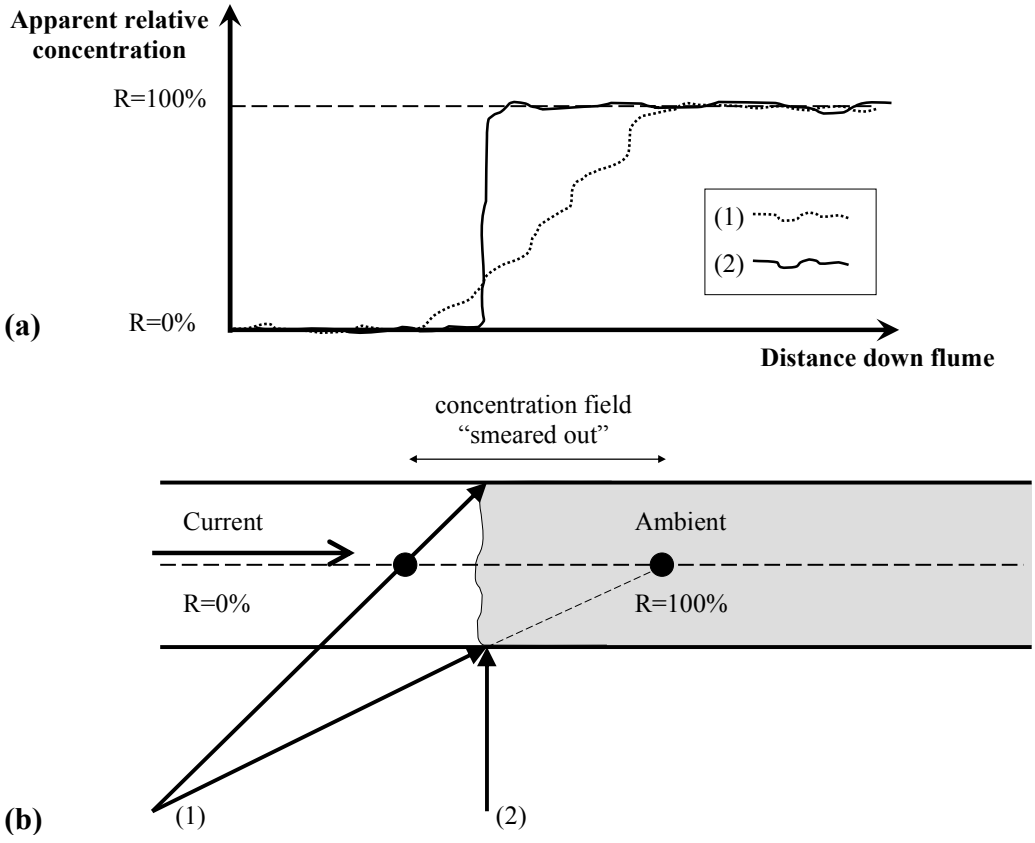

Figure 4-17: Schematic showing the effect of parallax on the concentration field: (a) width averaged relative concentration versus distance down the flume, (b) plan view of flume with showing a relatively two-dimensional flow moving left to right and the interface with the ambient fluid.

When looking from position (2), there is a distinct interface between the current and the ambient fluid. However, when looking from (1) there appears to be a band of mixing at the front of the flow, even though the current is moving as a slug of fluid. Therefore, the concentration fields from LA would have no error directly in front of the camera, but at the edges of the camera view (where the viewing angle was largest) concentration interfaces in depth integrated concentration fields would appear to be "smeared out", increasing the apparent extent of mixing (see Figure 4-17). The maximum width of this concentration field "smearing" was determined from trigonometry to be approximately 0.16H.

The "smearing" also introduced errors to the bulk characteristics of the flow, such as the front position and Froude number. The front position was defined at the nose of the flow to be 85% of the compartment fluid concentration. For a two-dimensional gravity current with no internal mixing, the maximum possible error in front position was calculated from trigonometry to be 0.06H. The front position would be over-estimated in the initial stages of the flow and underestimated in the later stages. For a typical gravity current flow, the maximum error in Froude number would be approximately 4%. The Froude number would be underestimated in the initial stages of the flow and overestimated in the later stages.

Another effect of parallax was to distort length scales at image edges, where the flume was located 1.02 times further away from the camera than at the centre. The length scale was averaged across the field of view of the camera. Therefore, using trigonometry, parallax introduced a maximum length scale error of approximately +/- 1% to the edges of the image.

Lighting System

The lighting system used in the experiments had random light intensity fluctuations, which introduced temporal fluctuations in the relative concentrations at individual pixels. The variations were random in nature, so were eliminated from the calibration process by time averaging, but could not be removed from the experimental flows as they were unsteady. The typical variation for a single pixel with a uniform mixture of dye is shown in Figure 4-18. Other pixels throughout the experimental images showed similar magnitude fluctuations.

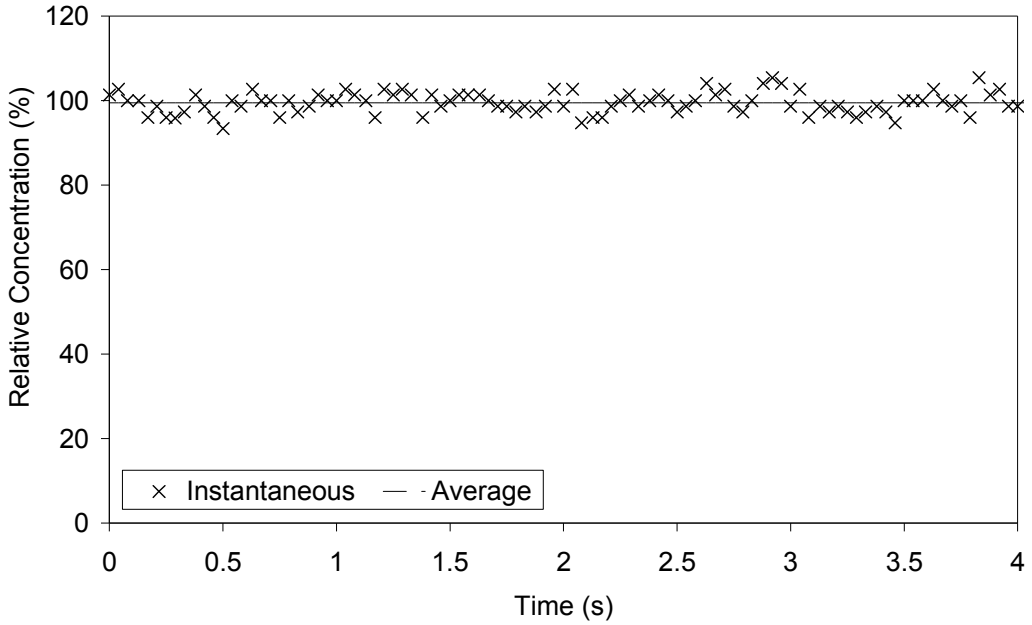

Figure 4-18: Typical temporal fluctuation in relative concentration for a single pixel.

The standard deviation of the temporal fluctuation in relative concentration was approximately 2.5% and the estimated maximum error was approximately +/-6%.

Spatial variations in the lighting system were eliminated through the pixel by pixel field calibration process.

Assumed Green Light Attenuation Relationship

It was assumed in Equation (4-2) that the relationship between relative concentration and green light optical thickness was linear for low red dye concentrations. From the calibration experiments described in Section 4.3.3, the largest error associated with this assumption was approximately +/-5%.

4.4 Particle Tracking Velocimetry

The internal velocity structures of backdraft gravity currents can further the understanding of the dynamics of these flows. With recent advances in digital imaging, the velocities of fluid flows are now commonly determined by particle tracking velocimetry (PTV) and particle image velocimetry (PIV). Unlike many of the older techniques, they provide full spatial and temporal resolution of internal velocity structure and are non-intrusive.

A description of the theory behind the particle tracking velocimetry (PTV) flow visualisation technique is presented in Section 4.4.1. For further general information about the PTV technique the reader is referred to the work of Nokes (2006b).

4.4.1 Theory

Particle tracking velocimetry (PTV) is a non-intrusive flow visualisation technique that can be used to obtain two-dimensional velocity fields, by using digital photography to track the motion of small particles suspended in the flow. The flow is seeded with fine particles and illuminated by a thin light sheet. A high speed digital video camera, positioned orthogonal to this light sheet, records the flow. Individual particles are tracked from frame to frame and particle velocities are calculated based on the particle displacement and time step between frames. Particle velocities are then interpolated onto a rectangular grid, producing a time series of two-dimensional velocity fields.

The PTV technique is similar in some respects to particle image velocimetry (PIV). Both techniques produce a time series of velocity fields from digital images of flows seeded with particles and have been applied to the study of gravity current flows (Thomas et al. 2003; Zhu et al. 2006). However, the main difference is that in PIV the velocities are calculated by the cross-correlation of light intensities for selected regions of the flow, whereas PTV tracks the motion of individual particles. As some spatial averaging occurs in PIV, areas with high velocity gradients may be resolved better by a PTV analysis (Plew 2005).

4.4.2 Experimental Equipment

The PTV experiments were conducted in the flume described in Section 4.2. The experimental configuration is illustrated in Figure 4-19 and Figure 4-20. All water in the flume was uniformly seeded with small particles prior to the addition of any salt. A vertically orientated white light source was positioned above the flume, illuminating all particles in a thin vertical slice though the centre of the flume. Blackout curtains were placed behind the flume, providing a dark background to contrast with the illuminated particles. A high speed camera, positioned orthogonal to the side of the flume, was used to capture images of the flow.

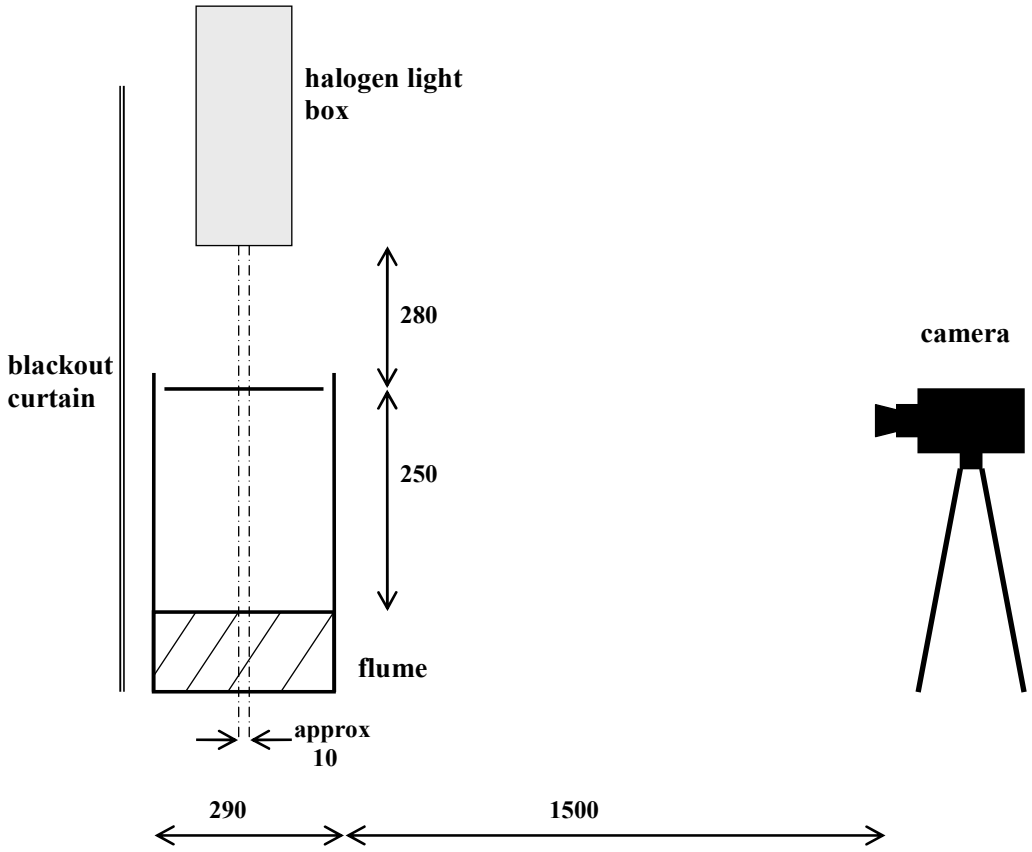

Figure 4-19: End elevation of experimental setup for PTV experiments. The dot-dash line represents the edge of the white light sheet. All dimensions in mm. Not to scale.

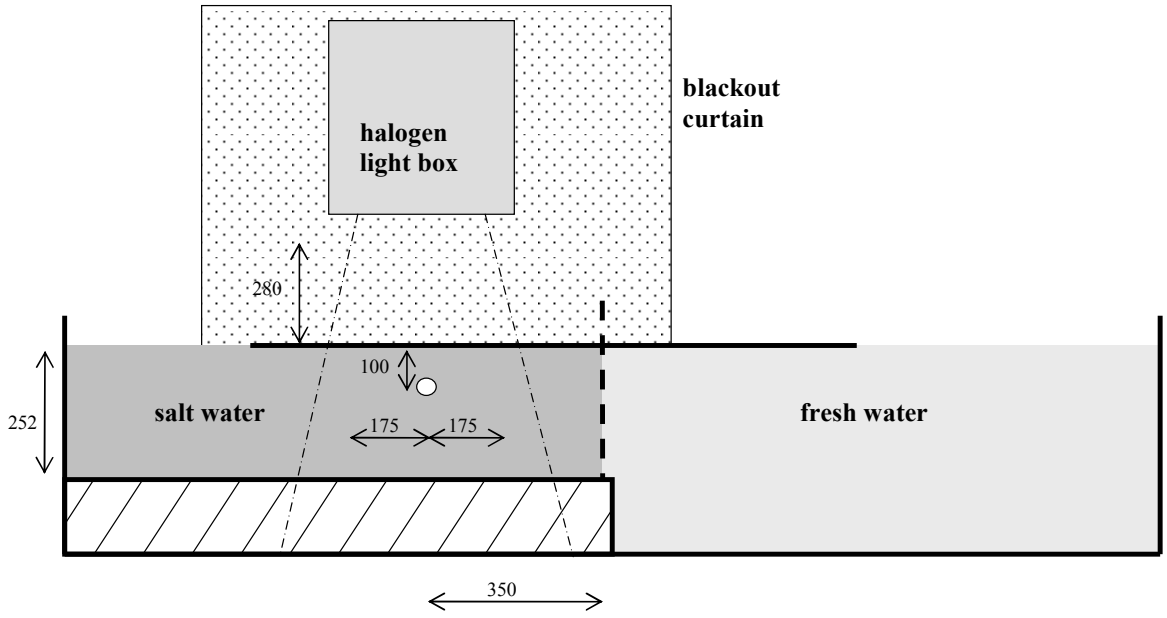

Figure 4-20: Side elevation of the experimental setup for PTV experiments. The dot-dash line represents the edge of the white light sheet. The white circle represents the centre of view of the camera. All dimensions in mm. Not to scale.

A black and white Jai CV-M4^{+} CL camera, capable of recording 8-bit black and white images at 24 frames per second, was used in the experiments. The frame resolution was 1268 by 1024 pixels, with pixel intensities ranging from zero to 255. The size of the RAM in the data logging computer restricted the maximum number of frames per experiment to 1142. The camera settings were adjusted manually to capture the desired number of particles per frame and were kept constant during each experiment.

The camera was located on a tri-pod 1500mm from, and orthogonal to, the side of the flume, as shown in Figure 4-19 and Figure 4-20. The camera was centred on a point 350mm into the saltwater compartment from the lock gate and 100mm below the suspended Perspex lid. The total field of view extended vertically between the upper and lower rigid boundaries and laterally 200mm either side of the central point.

The light sheet used to illuminate particles needed to have a high intensity, so that particles could be easily identified. Two different light sources that may be used for PTV work are high-intensity halogen bulbs, and laser light sheets (Nokes 2006b). A halogen based lighting system was selected due to its ease of use and significant cost advantages over laser based systems.

A light box containing a linear 2kW white halogen bulb was used to produce a thin white light sheet. The halogen bulb, approximately 300mm long and 10mm in diameter, was positioned near the rear of the box, as shown in Figure 4-21. A thin light sheet was produced by passing the light through two 400mm long parallel slits (the first slit was 12mm thick and the second was 6mm thick). The light sheet was approximately 10mm thick as it passed through the flow. Due to the significant amount of heat produced by the 2kW Halogen bulb, two fans were used to drive cool air over the bulb and prevent overheating.

It was important that the particles used to seed the flow act as tracers that accurately represented the velocity of the fluid around them. The selection of particle size had to ensure that particles were small enough to respond rapidly to fluid movement, but large enough so they could be identified by their reflected light.

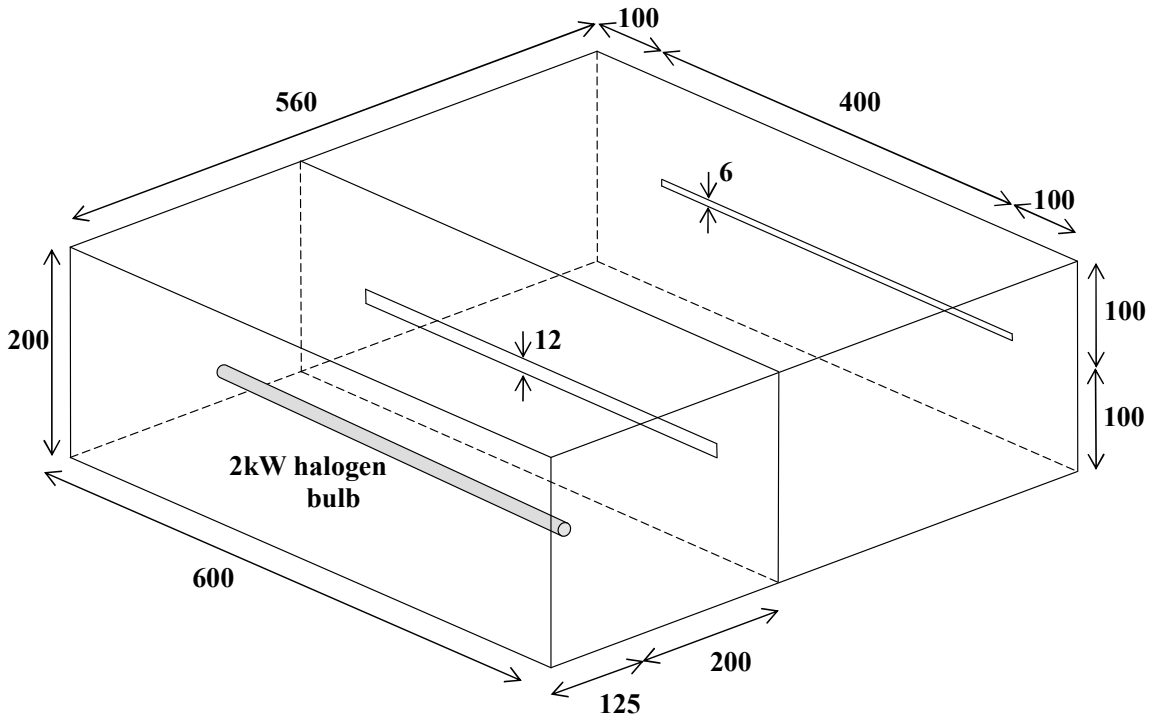

Figure 4-21: Isometric diagram of halogen light box used as a light source for PTV experiments. All dimensions in mm. Not to scale.

For water based flows, small particles of Pliolite VT resin are commonly used to seed the flow (Ballard 2004; Nokes 2006b; Plew 2005; Thomas et al. 2003). This material has a density approximately 3% greater than that of water and, when finely ground (to approx 200μm in diameter), particles fall velocities have a negligible impact on the characteristics of the flow and may be ignored for laboratory scale flows with short time scales (Nokes 2006b). The particles used in the experiments were Pliolite VT resin, which was ground to a sieve size diameter between 180μm and 250μm.

The surface tension effects of water make it difficult to introduce such fine particles. To overcome this difficulty, the particles were first added to a small amount of surfactant/water mixture, which reduced the surface tension effects of the water (Nokes 2006b), before being introduced to the flume water.

4.4.3 Data Capture

The typical procedure used to capture data in the PTV experiments is outlined below.

- The tracer particles were mixed uniformly through the flume and salt was mixed with water on the elevated compartment side of the lock gate.

- A scale ruler, temporarily inserted into the centre of the flume, was used to determine a length scale for the use in the subsequent analysis.
- The halogen light box was turned on and all other sources of light were eliminated.
- Exposure and gain levels on the digital camera were adjusted to allow the optimal number of particles to be identified (~ 1,500).
- The flume water was left undisturbed for approximately five minutes prior to the start of each experiment to allow ambient fluid motions to decay.
- A sequence of images was captured for each experiment. Typical experimental image sequences were 600 to 1100 frames in length.
- As the lock gate was not in the field of view of the camera, a pulse of light from a light emitting diode (LED) was used to determine the time of gate removal.

4.4.4 Data Processing

A PTV analysis involves three steps: particle identification, particle matching and velocity field interpolation. Although relatively simple in principle, the process of identifying thousands of individual particles in each frame, matching them between hundreds frames and interpolating velocity fields, is both complex and computationally demanding. FluidStream Version 6.03 (Nokes 2006a), a software package developed specifically for particle tracking velocimetry, was used for analysing the image sequences. Details of the software design and capabilities can be found in the system theory and design manual (Nokes 2006b) and the user's guide (Nokes 2006c).

Particle Identification

Once a sequence of images was captured, individual particles were identified in each frame. The *Gaussian absolute algorithm* was used to determine the location and size of particles, based on the light intensities within the image. The algorithm assumes that the light intensity across a particle is normally distributed. It searches the image for pixels with a local maximum intensity greater than a user-specified maximum. Adjacent pixels with intensities greater then the user-specified threshold intensity are assumed to be part of the particle. Finally, a Gaussian intensity profile is fitted in the x and y directions on either side of the local maximum, allowing the particle's location to be identified with sub-pixel accuracy. A typical experimental frame showing all identified particles is shown in Figure 4-22.

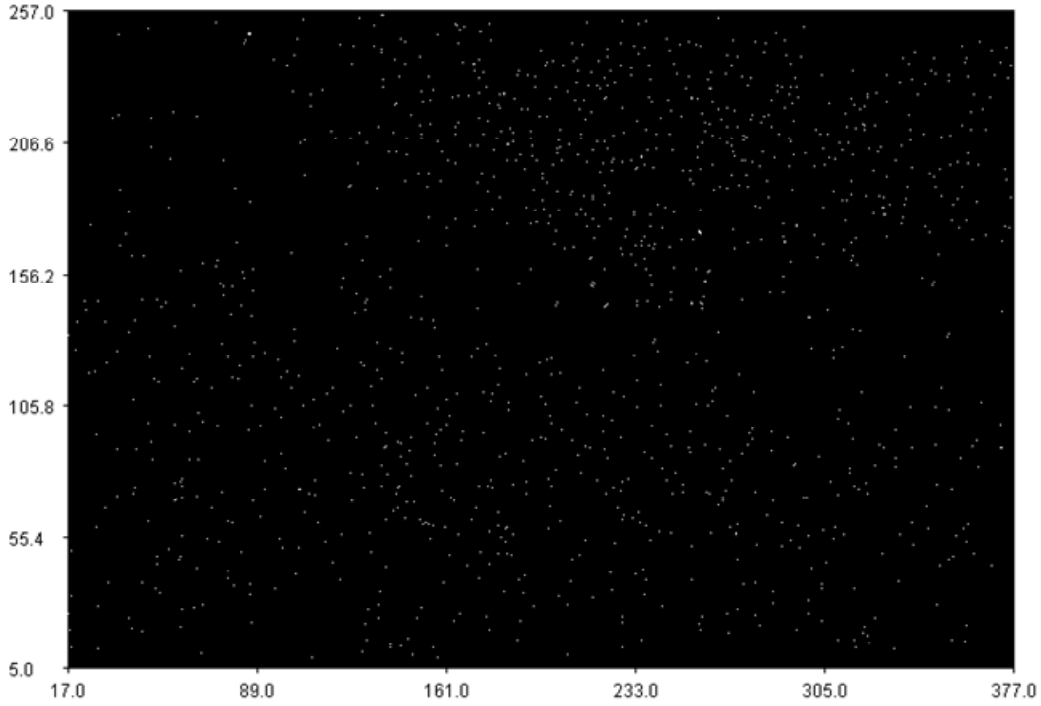

Figure 4-22: Typical image showing particles identified from an experiment. Particles represented by white dots. Scale of the axis is mm.

Particle Matching

In the particle matching process, the identified particles were matched from frame to frame. For each particle in the frame, a number of candidate particle matches were identified within a specified region in the next frame. A cost was calculated for each of these potential candidate particle matches, the lower the cost the better the match. The purpose of a costing strategy or algorithm is to generate costs so that correct matches have much lower costs than incorrect matches. A user defined maximum matching cost (MMC) allowed matches with costs above this threshold to be ignored. Careful selection of the MMC improves the accuracy of the PTV analysis (Nokes 2006e).

Finally, the *auction* algorithm was used to calculate the optimal solution. This algorithm determines the particle matches that give the lowest overall cost. This means individual particles may not necessarily be matched to the candidate particle with the lowest cost or even matched at all, but the overall cost is minimised and an optimal overall solution is obtained.

Four costing algorithms were utilised in this research: the *adjacency costing*, the *local velocity costing*, the *distance costing*, the *path length costing*. A brief description of these costing

algorithms is provided below. Further information on these and other possible costing strategies can be found in the Fluid Stream system theory manual (Nokes 2006b) and user's guide (Nokes 2006c).

The *adjacency costing* and *distance costing* are state based costings. A state based costing only requires information about the state (the location, size and intensity) of particles in each frame. The *adjacency costing* is designed to measure the degree to which particle patterns surrounding particle 1 in the first frame correspond to the same pattern surrounding particle 2 in the second frame. The cost calculated by the *distance costing* is proportional to the distance between particle 1 in the first frame and particle 2 in the second. Therefore, the cost will be lowest for particles that are closest together.

The *local velocity costing* and *path length costing* are matching based costings. A matching based costing is more complex and relies on existing particle matches. For this reason the matching process must be started by a state based costing before matching based costings may be used. The *local velocity costing* uses estimates of particle velocities surrounding particle 1 to estimate its position in the next frame. The cost is based on the difference between the estimated displacement between frames and that associated with a particular match. For the *path length costing*, the cost is inversely proportional to the number of particles in the path created by matching two particles, the shorter the path the higher the cost. Therefore, it can be used to eliminate short paths, which are often erroneous.

Velocity Field Interpolation

The particle velocities were calculated from the displacement of particles and the time step between frames. As the particles were randomly distributed throughout the flow, the velocities were particle-centred, providing velocity estimates at a random set of locations within the frame.

To produce a more useful velocity field, velocities were interpolated onto a regularly spaced grid using Thessian triangulation. Interpolation triangles were formed from adjacent particles, as shown in Figure 4-23(a). A rectangular grid was overlaid onto the flow field and the velocity at a grid point was estimated from the particle velocities at the corners of the triangle in which the grid point was located, as shown in Figure 4-23(b). If the grid point did not fall within an interpolation triangle, the velocity at that grid point was undefined. More details on

this, and other possible velocity field interpolations schemes, are available in the Fluid Stream system theory manual (Nokes 2006b). A typical experimental velocity field is shown in Figure 4-24.

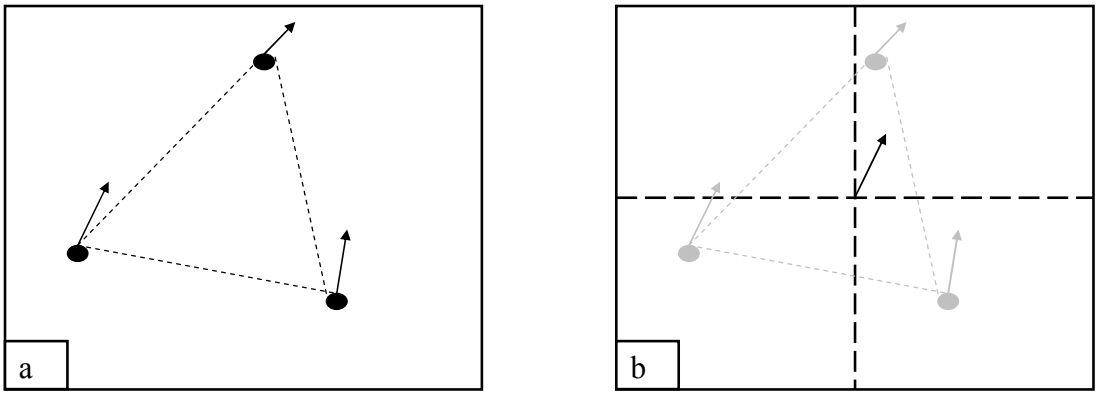

Figure 4-23: Velocity field interpolation by Thiessan triangulation: (a) randomly distributed particle velocities and the interpolation triangle, (b) rectangular grid and interpolated velocity. Arrows represent velocity vectors. Dots represent particles.

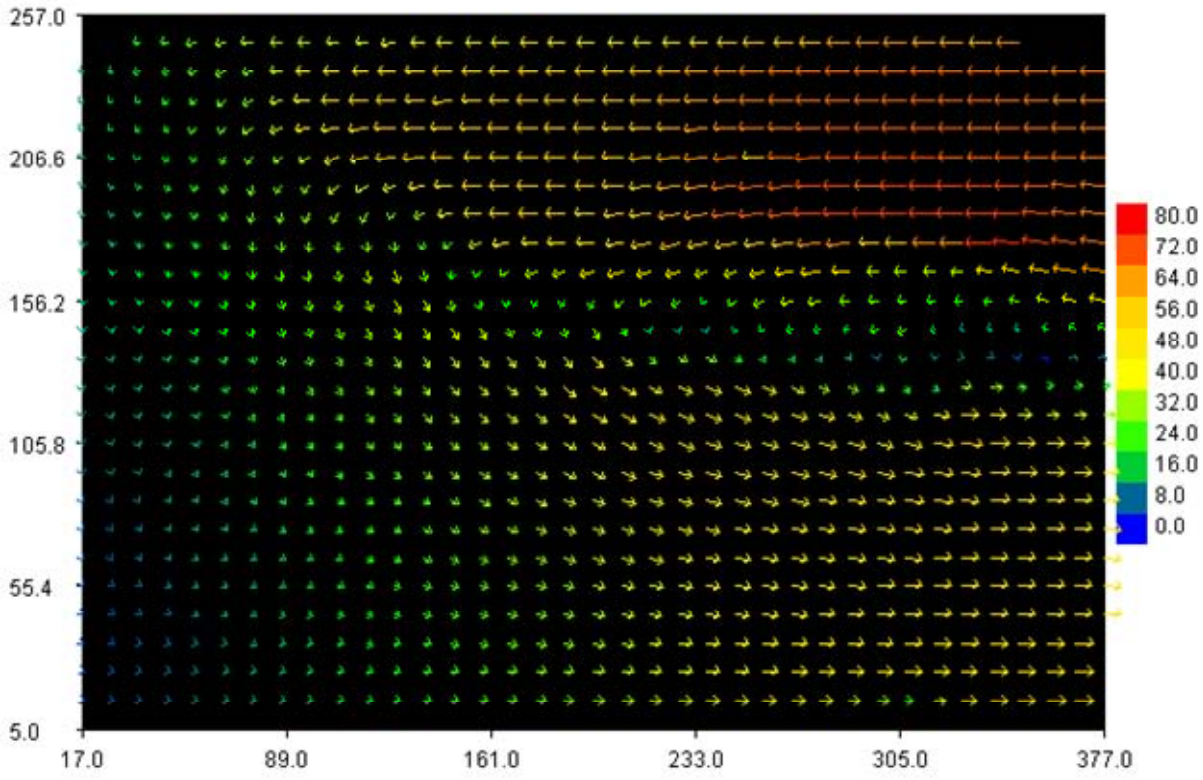

Figure 4-24: Typical experimental velocity field for the full opening geometry, which was generated on a rectangular 10mm grid. Axis are in mm. Velocities are in mm/s.

4.4.5 Resolution

The resolution obtained by a PTV analysis depends on the frame rate of the camera and the density of particle seeding. The aim of this section is to quantify these factors and to determine the resolution of the generated velocity fields.

The spatial resolution of the velocity fields was controlled by particle seeding density. The target particle seeding was approximately 1500 particles per frame, which represented a compromise between spatial resolution and computational demand. Typically the analysis focussed on an area approximately 250mm x 350mm in size. Therefore, the average spatial resolution of particle velocity estimates was approximately 10mm, or 0.04H.

The temporal resolution of the velocity fields was limited by the camera frame rate, of 24 frames per second.

4.4.6 Accuracy

The errors associated with the experimental velocity fields produced by the PTV analysis are discussed below.

Ambient Fluid Motion

Immediately prior to the start of each experiment, the flume water was left undisturbed for five minutes to allow ambient fluid motions to decay. If the fluid was left longer, too many particles would settle out of the flow. Even after leaving the fluid for approximately five minutes, some oscillatory ambient fluid motion was still observed. The maximum ambient motion was of the order of +/- 4% of the bulk front velocity of the gravity current flows.

Temporal Scale

The frame rate of the digital camera was used to create time scales, so errors were limited to the frame rate of +/- $^{1}/_{24}$ seconds.

The process of gate removal took a maximum time of half a second, and was signalled by a pulse of light from an LED. The experiment was assumed to begin halfway through this gate removal process, which took approximately 0.5s. Therefore, it was estimated that the error associated with the experimental start time was less than ¼ of a second.

Spatial Scale

Length scales were estimated off a 350mm scale rule, placed in the centre of the flume. The length scale was estimated to the nearest pixel ($^1/_3$mm), so the associated spatial scale error was approximately +/-0.013H.

Parallax

The length scales at the image edges were distorted by parallax, as these areas were located further from the camera than the centre of the image. The maximum distance between the camera and the centre of the flume was 1.05 the distance directly in front of the camera. As the length scale was averaged across the width of the experimental image, the maximum error introduced to the spatial scale was approximately 2.5%.

Particle Identification

Using the *Gaussian absolute algorithm*, particle locations were determined with an accuracy of at least one quarter of a pixel (Nokes 2006c). Spatial scales were approximately 0.31mm/pixel and particle movement was of the order of 2mm per frame, so the corresponding error in velocity estimates was approximately +/-4.0 %.

Particle Matching

The particle matching process can introduce errors by generating incorrect particle matches. However, incorrect matches were largely eliminated by visual inspection and careful use of the matching algorithms described in Section 4.4.4.

4.5 Summary

This chapter has described the experimental procedure and visualisation techniques used to investigate gravity currents prior to backdraft. Section 4.2 presented details of the experimental flume used to conduct the experiments, while Sections 4.3 and 4.4 explained the light attenuation (LA) and particle tracking velocimetry (PTV) flow visualisation techniques respectively. Detail was provided about the theory, implementation and accuracy of these techniques.

The following chapter describes how the CFD model Fire Dynamics Simulator version 4 (FDS) was used to numerically simulate the experimental flows.

CHAPTER 5 NUMERICAL METHODS

5.1 Introduction

The computer software Fire Dynamics Simulator Version 4.06 (FDS) was used to generate numerical simulations of the experimental saltwater flows discussed in the previous chapter. The inputs specified in these simulations are outlined in Section 5.2 below. The sensitivity analysis, presented in Section 5.4, discusses the sensitivity of the model to variations in the input parameters.

5.2 Specifications

The initial conditions and boundary conditions used in FDS simulations are specified by the user. The specifications used in this research are discussed below and a sample input file is included in Appendix A.

The simulations were run on a computer with a Pentium 4, 3.4GHz processor and 2 GB of RAM. The simulation run times varied from less than 30s, for the coarsest grid, to approximately 18 hours, for the finest grid.

5.2.1 Miscellaneous Parameters

A number of miscellaneous parameters were set, which determined global properties in the numerical simulations.

- The flow was assumed to be isothermal and incompressible. Heat transfer effects were assumed to be negligible as the experimental flows were driven only by differences in salt (NaCl) concentration. Compressibility effects were assumed to be unimportant due to the high modulus of elasticity of water and the relatively small forces and velocities involved in the flows.
- Gravity was assumed to be oriented vertically downwards, with a magnitude of 9.805m/s^2 (see Figure 5-1).
- The ambient fluid, located outside the computational domain, was assumed to be fresh water.
- The total simulation time was adjusted for the different opening geometries so that the gravity current of fresh water reached the end of the domain before the simulation ended.

- The FDS default value of the Smagorinsky constant, $C_s = 0.2$, was used for the turbulence modelling (McGrattan 2004b). Large eddy simulation (LES) has been found to be relatively insensitive to this parameter (Tannehill et al. 1997), so it was not investigated in the sensitivity analysis in Section 5.4.
- The initial value of the time step was a function of the typical grid dimension divided by a characteristic flow velocity, as shown in Equation (5-1) (McGrattan 2004b). During the calculation, the time step was automatically adjusted, based on two limiting criteria. The first criterion, the Courant-Friedrichs-Lewy (CFL) condition, is significant when convective transport dominates diffusive transport and ensures that the time step is smaller than the time required for a parcel of fluid to cross a grid cell. Secondly, the Von Neumann criterion places limits on the time step due to the diffusive transport terms and is important for fine grid resolution simulations or direct numerical simulations (DNS). More detail about these criteria can be found in the FDS Technical Reference Guide (McGrattan 2004a).

$$\Delta t_{initial} = \frac{5(\delta_x \delta_y \delta_z)^{1/3}}{\sqrt{gH}} \tag{5-1}$$

where: $\Delta t_{initial} =$ initial time step

$\delta_x =$ cell-size in the x-direction

$\delta_y =$ cell-size in the y-direction

$\delta_z =$ cell size in the z-direction

$g =$ gravity

$H =$ height of the computational domain

5.2.2 Geometry and Boundary Conditions

A rectangular computational domain was used in the simulations, as shown in Figure 5-1 and Figure 5-2.

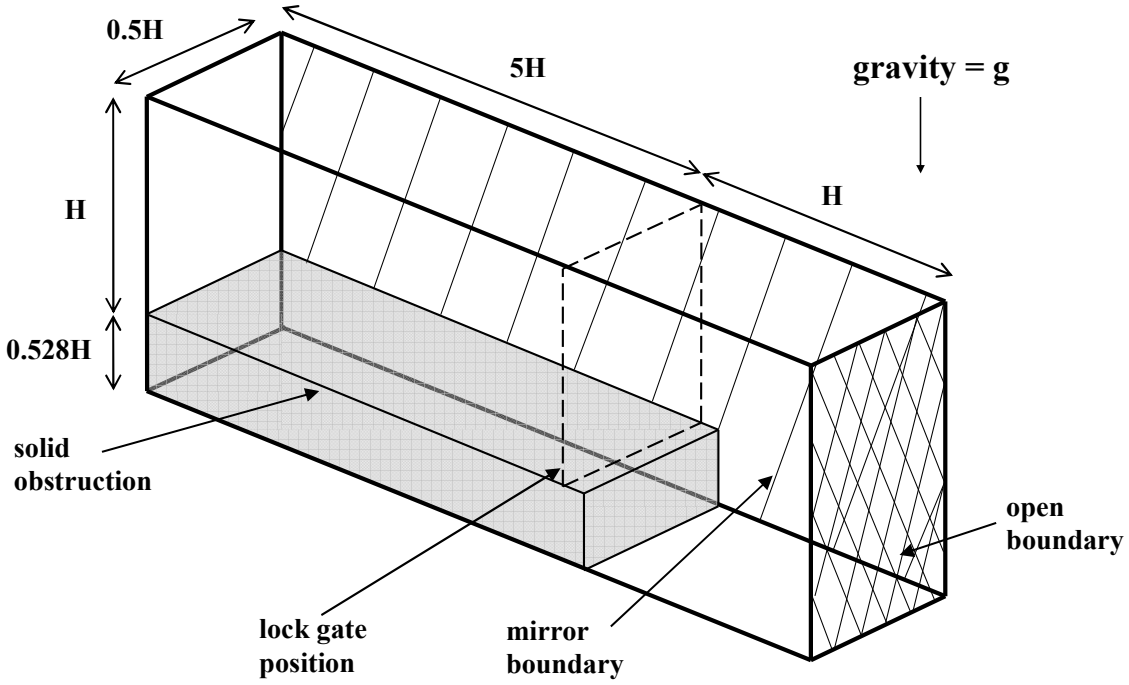

Figure 5-1: Perspective drawing of the computational domain used in the numerical simulations. The striped face is a plane of symmetry. The hashed face is an open boundary. The grey surface is a solid obstruction. The dashed lines represent the initial fluid separation. H=0.252m.

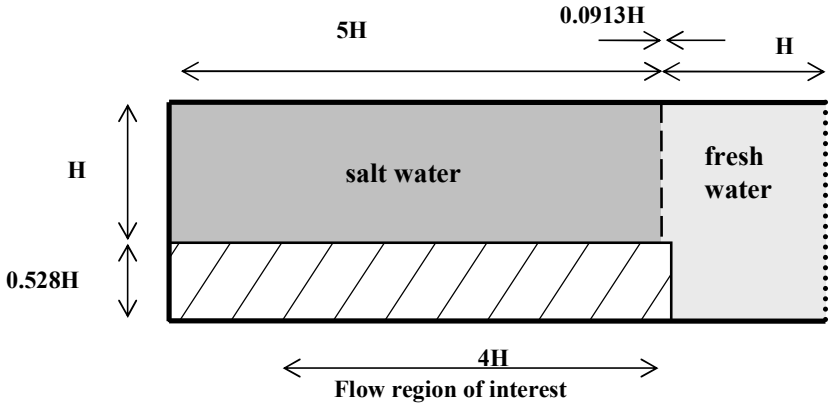

Figure 5-2: Side elevation of computational domain. The solid bold line indicates a rigid boundary and the extent of the computational domain. The dotted line indicates an open boundary condition. The dashed line represents the lock gate location. The striped region represents a solid obstruction. H=0.252m.

The computational domain was divided into a number of grid cells. For these simulations the cells were kept close as close as possible to cubes. Increasing the number of cells improves the resolution of the simulations, but also increases the computational requirement. The number of cells in each direction of the numerical grid was selected to be of the form $2^l 3^m 5^n$

(where *l*, *m* and *n* are integers).This allowed the number of cells in each direction to be factored down to 2's 3's and 5's, which improves the computational efficiency of the numerical solver (McGrattan 2004b). The sensitivity analysis, discussed in Section 5.4.1, demonstrated that grid independence was achieved when cells were H/100 in size. Therefore, a grid size of H/100 was used in the final simulations.

To match the experimental configuration, a solid obstruction was located in the bottom left of the computational domain and a thin obstruction was used to represent the opening geometry lock gate, as shown in Figure 5-1. Different thin obstructions were used to represent the different experimental opening geometries.

Only part of the experimental flume was modelled, to limit the computational demand for each simulation. The vertical extent of the computational domain was approximately 1.53*H*, matching that of the experimental flume, however the horizontal limits were only extended 5*H* from the lock gate into the saltwater compartment and 1*H* in the other direction. The effect of reducing the domain size was investigated in the sensitivity analysis in Section 5.4.4.

A plane of symmetry, or mirror boundary, was positioned on an entire face of the computational domain, as shown in Figure 5-1, halving the computation demand. From a numerical point of view, a plane of symmetry is a no-flux, free-slip boundary (McGrattan 2004b).

An open boundary was specified at one end of the computational domain, a distance H from the initial fluid separation (see the hashed face in Figure 5-1). This open boundary allowed salt water to flow out of the compartment and fresh water to flow in.

All other boundaries in the domain were solid boundaries. These surfaces were assigned a velocity boundary condition (VBC), which controls the extent to which fluid sticks to the boundary. The sensitivity analysis, discussed in Section 5.4.2, demonstrated that a quarter-slip boundary condition, VBC=-0.5, provided the closest match to experiment and was therefore used in the final simulations.

5.2.3 Fluid Specifications

Saltwater was specified to the left of the lock gate and fresh water was specified everywhere else, as shown in Figure 5-2. These fluids were assumed to be initially uniformly mixed and at rest, but an exchange flow developed between the fluids during the simulation.

The specified fresh water density and dynamic viscosity were based on tabulated data from Street (1996) for water at 20ºC, as shown in Table 5-1. To match the experiments a dimensionless density difference of $\beta_{initial} = 0.005$ was used in the simulations, except those involving the window opening geometry, which required a density difference of $\beta_{initial} = 0.04$ to generate fully turbulent gravity current flows.

FDS uses the Smagorinsky sub-grid scale turbulence model. Therefore, the viscosity, diffusivity and Schmidt number used in the model are turbulent values, not those of the actual fluid. The actual dynamic viscosity, shown in Table 5-1, serves as a lower bound estimate of the turbulent fluid viscosity. Due to the low salt concentrations involved, the dynamic viscosity was assumed to be the same for fresh and salt water.

The Schmidt number relates the fluid viscosity to the mass diffusivity, as shown in Equation (5-2). For sodium chloride (NaCl) in water, the Schmidt number is approximately $Sc = 700$ (Frederikse and Lide 1997; Street et al. 1996) (based on a mass diffusivity of $D = 1.5 \times 10^{-9} m^2/s$ and a kinematic viscosity of $\nu = 1.003 \times 10^{-6} m^2/s$ at 20ºC). Much higher than the turbulent Schmidt number of the order of $Sc_{turbulent} \sim 1.0$ suggested by the sensitivity analysis in Section 5.4.3.

$$Sc = \frac{\nu}{D} = \frac{\mu}{\rho D} \tag{5-2}$$

where: Sc = fluid Schmidt number
D = mass diffusivity
ν = kinematic viscosity
ρ = density
μ = dynamic viscosity

A summary of the fluid properties input into FDS is presented in Table 5-1 below.

Table 5-1: Summary of the fluid properties used in FDS simulations.

	Fresh water	Salt water
density, ρ (kg/m^3)	998.2	1003.2
lower bound dynamic estimate of viscosity, μ (kg/m/s)	1.002×10^{-3}	1.002×10^{-3}
turbulent Schmidt number, $Sc_{turbulent}$	1.0	

5.3 Outputs

Fire Dynamics Simulator (FDS) can output a variety of variables which are specified by the user. Results may be output either at single cells, at every cell in the computational domain, or in two-dimensional slices. Sequences of two-dimensional (2D) velocity field slices and concentration field slices were generated at intervals of approximately one second, providing sequences between 20 and 30 frames long. To enable direct comparison with the saltwater experiments the two-dimensional concentration fields were width-integrated. To supplement the experimental data, mass-flow rates through the compartment openings, horizontal relative concentration slices through the gravity current flows and point velocity measurements were also produced.

5.4 Sensitivity Analysis

A sensitivity analysis was carried out to determine how sensitive model results were to systematic changes in the input parameters. The input parameters investigated were: the grid size, the velocity boundary condition, the turbulent Schmidt number, the effect of reducing the computational domain. The sensitivity analysis was carried out using only the full compartment opening geometry, so other opening geometries were not modelled until the completion of the sensitivity analysis.

As part of the sensitivity analysis a number of bulk characteristics for the front of the gravity current flows were assessed: the front position versus time, the head height and the Froude number (or dimensionless velocity). Definitions of these parameters are included in the Analysis chapter. The bulk characteristics did not change significantly with time for front positions greater than approximately $x \sim 2.5H$, allowing average bulk front characteristics to be calculated. In addition, the orientation was inverted to match the practical problem being simulated.

5.4.1 Grid Size

The grid size is important as it defines the spatial resolution of the numerical simulation. In general, reducing the grid size improves the resolution of the numerical solution to the governing equations (McGrattan 2004a). A grid size sensitivity analysis involves systematically refining the numerical grid until the output quantities do not change appreciably with subsequent refinements.

To investigate grid dependence, the height of the saltwater compartment (H) was divided into 12, 25, 50, 75 or 100 cells, with other dimensions scaling accordingly to ensure the cells were approximately cubic, as shown in Table 5-2. Further grid refinement was not possible due to computer hardware constraints.

The grid size sensitivity was investigated with a half-slip boundary condition (VBC=0.0), a turbulent Schmidt number of 1.0, and with the reduced computational domain (see Section 5.4.2 to Section 5.4.4 for detail on these parameters).

Boundary Layer Thickness

The gravity current flows generated in both the numerical simulations and experiments were fully turbulent. However, at physical boundaries, frictional effects are important, due to the presence of a boundary layer (Street et al. 1996). A turbulent boundary layer, with a viscous sub-layer, would develop and act to retard the flow close to the boundary.

To estimate the magnitude the turbulent and viscous boundary layers, for comparison with the grid sizes modelled in FDS, a uniform velocity flow, passing over a flat plate and through a pipe, will be considered. The turbulent boundary layer and viscous sub-layer that would develop for such flows is illustrated in Figure 5-3. The dimensions of interest are the turbulent boundary layer thickness (δ) and the viscous sub-layer thickness (δ_v).

Table 5-2: Detail of different grid sizes used in sensitivity analysis.

Number of cells in H	Grid Size (H)	Grid Size (mm)	Number of Cells in Domain
12	0.083	21.0	9,000
25	0.040	10.1	72,000
50	0.020	5.0	560,000
75	0.013	3.4	2,160,000
100	0.010	2.5	4,500,000

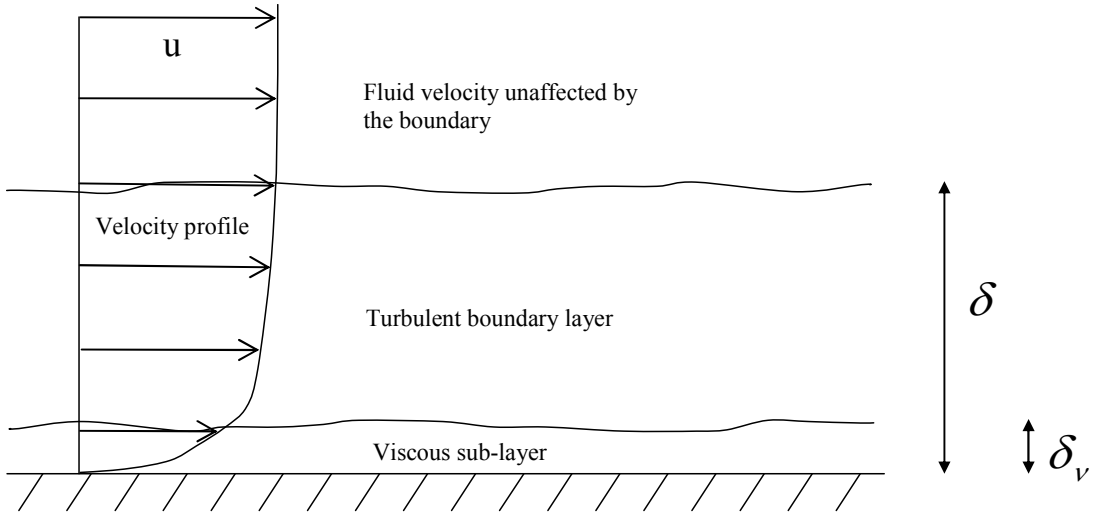

Figure 5-3: Turbulent boundary layer for uniform velocity flow over a flat plate

The gravity current flows being considered in this research travel a maximum distance of approximately four compartment depths (H). Therefore, to give an indication of the growth of the boundary layer, the thicknesses will be estimated at locations 2H and 4H from the compartment opening.

The approximate turbulent boundary layer thickness, for uniform flow over a flat plate, can be approximated from Equation (5-3) (Street et al. 1996). Due to the 0.2 power, the estimated boundary layer thickness is only weakly dependent on the flow velocity.

$$\delta = \frac{0.38x}{\mathrm{Re}_x^{0.2}} \tag{5-3}$$

where: $\delta =$ boundary layer thickness

x = distance downstream from leading edge of plate

$\mathrm{Re}_x = \frac{ux}{\nu}$ = Reynolds number based on distance from leading edge

u = flow velocity

ν = fluid viscosity

The flow velocity of a gravity current front can be estimated from Equation (5-4). Past research suggests a typical Froude number of 0.44 for rigid boundary gravity currents (Barr and Hassan 1963; Simpson 1997).

$$u \sim U = Fr\sqrt{\beta_{initial} g H} \tag{5-4}$$

where: Fr = Froude number

$\beta_{initial}$ = initial density difference

g = gravity

H = compartment / lock depth

For the gravity current flows being investigated, the initial density difference was 0.5%, the lock depth was 0.252m and, using Equation (5-4), the front velocity may be estimated as 0.049m/s. Therefore, at locations 0.5m and 1m from the lock gate, the turbulent boundary layer thickness was estimated as 25mm and 44mm respectively (0.10H and 0.17H).

The thickness of the viscous boundary layer region for a uniform flow over a flat plate may be estimated from Equation (5-5) and Equation (5-6) (Pope 2000).

$$\delta_\upsilon = 5\left(\frac{\nu}{\upsilon^*}\right) \tag{5-5}$$

$$\upsilon^* = \sqrt{\frac{\tau_0}{\rho}} \tag{5-6}$$

where: δ_υ = viscous sub-layer thickness

ν = fluid kinematic viscosity

υ^* = friction velocity

τ_0 = boundary shear stress

ρ = fluid density

For a turbulent boundary layer developing on a flat plate, the boundary shear stress can be calculated from Equation (5-7) (Street et al. 1996).

$$\tau_0 = \frac{0.03\rho U^2}{\mathrm{Re}_x^{0.2}} \tag{5-7}$$

At locations 2H and 4H from the lock gate, the viscous sub-layer thickness was estimated as 1.6mm and 1.7mm (0.0065H and 0.0069H).

The turbulent boundary layer and viscous sub-layer thicknesses at distances 2H and 4H from the compartment opening are summarised in Table 5-3.

The smallest grid size, 0.01H, is approximately the same order of magnitude as the viscous sub-layer, but an order of magnitude smaller than the turbulent boundary layer. Therefore, it is expected that, even for simulations generated using the finest possible grid size, the turbulent boundary layer will be accurately resolved, but the viscous sub-layer will not. This also has an influence on the selection of an appropriate velocity boundary slip condition, in Section 5.4.2.

Bulk Front Characteristics

The sensitivity of the bulk characteristics of the gravity current front to changes in the grid size was investigated by comparing the results of simulations with different grid sizes.

The propagation of the gravity current front was plotted for the different grid sizes, as shown in Figure 5-4. The finer grid resolutions (0.02H, 0.013H and 0.01H) gave very similar results. Compared to the finer resolutions, the coarser grid resolutions (0.083H and 0.04H) were found to slightly overestimate the front position, especially in the initial stages of the flow. In general, when the grid size was reduced below 0.02H, the front position versus time was relatively grid independent.

Table 5-3: Approximate boundary layer thicknesses for a turbulent gravity current

Distance from compartment opening	**0.5m (~2H)**	**1.0m (~4H)**
Turbulent boundary layer thickness	25mm (0.10H)	44mm (0.17H)
Viscous sub-layer thickness	1.6mm (0.0065H)	1.7mm (0.0069H)

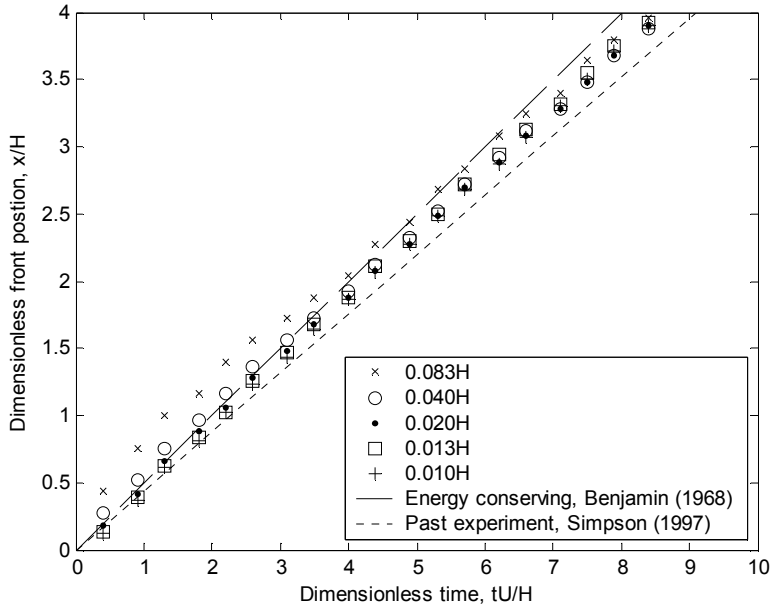

Figure 5-4: Dimensionless plot of numerical gravity current front position versus time for different grid sizes

Other bulk front characteristics investigated included the head height, Froude number and local Froude number, which are plotted Figure 5-5 (a), (c) and (e) respectively. For all three variables the results from the finer grids (0.02H, 0.013H and 0.01H) were relatively similar, but those from the coarser grid sizes (0.083H and 0.04H) were different. For the finer grid resolutions, the head height and local Froude number were found to be initially relatively unsteady, but converge to a quasi-steady value after approximately $x = 2.5H$. This trend is associated with the stabilisation and development of the gravity current head in the initial period of flow. The averages of these variables from this quasi-steady phase, are plotted against the grid resolution in Figure 5-5 (b), (d) and (f) respectively.

The graphs of the average variables indicate converge as the grid size is reduced. However, even at the finer grids (0.013H and 0.01H), some variability with grid size is apparent. Due to the computational restraints associated with this investigation, the grid size could not be refined further to determine if the observed variations were related to the grid size or the unsteady turbulent nature of the flow.

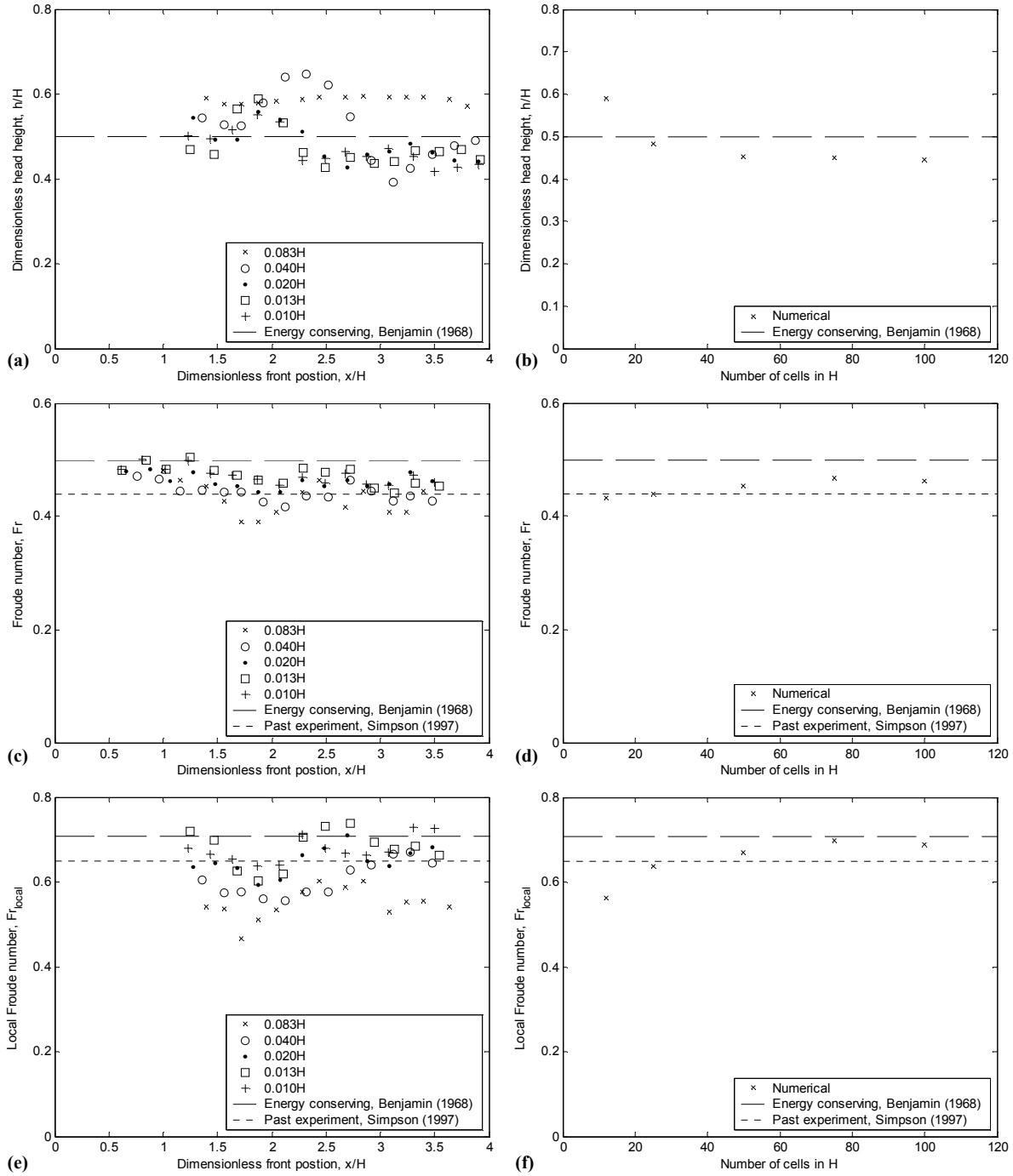

Figure 5-5: Plots of numerical bulk characteristics and average bulk characteristics for different grid sizes: (a, b) head height, (c, d) Froude number, (e, f) local Froude number.

Internal Mixing

To compare the resolution of the concentration structure, two-dimensional (2D) relative concentration fields from the mirror boundary were compared. Typical slices, all taken 17.2s after the start of the simulation, are shown in Figure 5-6 (a) to (e). Two-dimensional slices, and not width-integrated slices, were investigated to avoid smoothing of the turbulent

structure, which would have made assessment of the effects of grid resolution more difficult. The orientation of these slices was inverted to match that of backdraft gravity currents.

Visual inspection of these relative concentration fields indicates a strong dependence on grid size. The coarsest grid (0.083H) size resolves almost none of the turbulent structure, but more detail becomes visible as the grid is refined. Large billows become visible at a grid size of 0.04H and a raised nose is resolved at a grid size of 0.013H. A definite increase in resolution occurs as the cell size is reduced from 0.02H to 0.013H, but much less change is evident as the cell size is further reduced to 0.01H. This indicates that, at least qualitatively, grid independence is achieved for grid resolutions of approximately 0.01H.

Selected Grid Size

These results suggested that a grid size of 0.01H should be used in the final simulations to achieve grid independence.

5.4.2 Velocity Boundary Condition

The velocity boundary condition (VBC) parameter is used by FDS to control how much the fluid sticks to a solid boundary. A VBC of -1 represents a no-slip boundary, where the velocity at the boundary is zero, while a VBC of 1 represents a full-slip or frictionless boundary, where the velocity at the boundary is the same as in the adjacent cell. An intermediate value of VBC specifies a partial-slip condition, where the velocity at the wall is a fraction of the value at the adjacent cell, which is useful when the numerical grid is too coarse to accurately resolve the boundary layer (McGrattan 2004b).

To investigate the sensitivity of FDS to the VBC parameter, simulations were run with a range of different VBC values. A summary of the VBC parameters investigated is provided in Table 5-4. These simulations were carried out with a grid size of 0.01H, a turbulent Schmidt number of 1.0 and the reduced computational domain.

Table 5-4: Summary of the different velocity boundary slip conditions investigated.

VBC parameter	Full-slip	Three-quarter slip	Half-slip	Quarter-slip	No-slip
	1.0	0.5	0.0	-0.5	-1.0

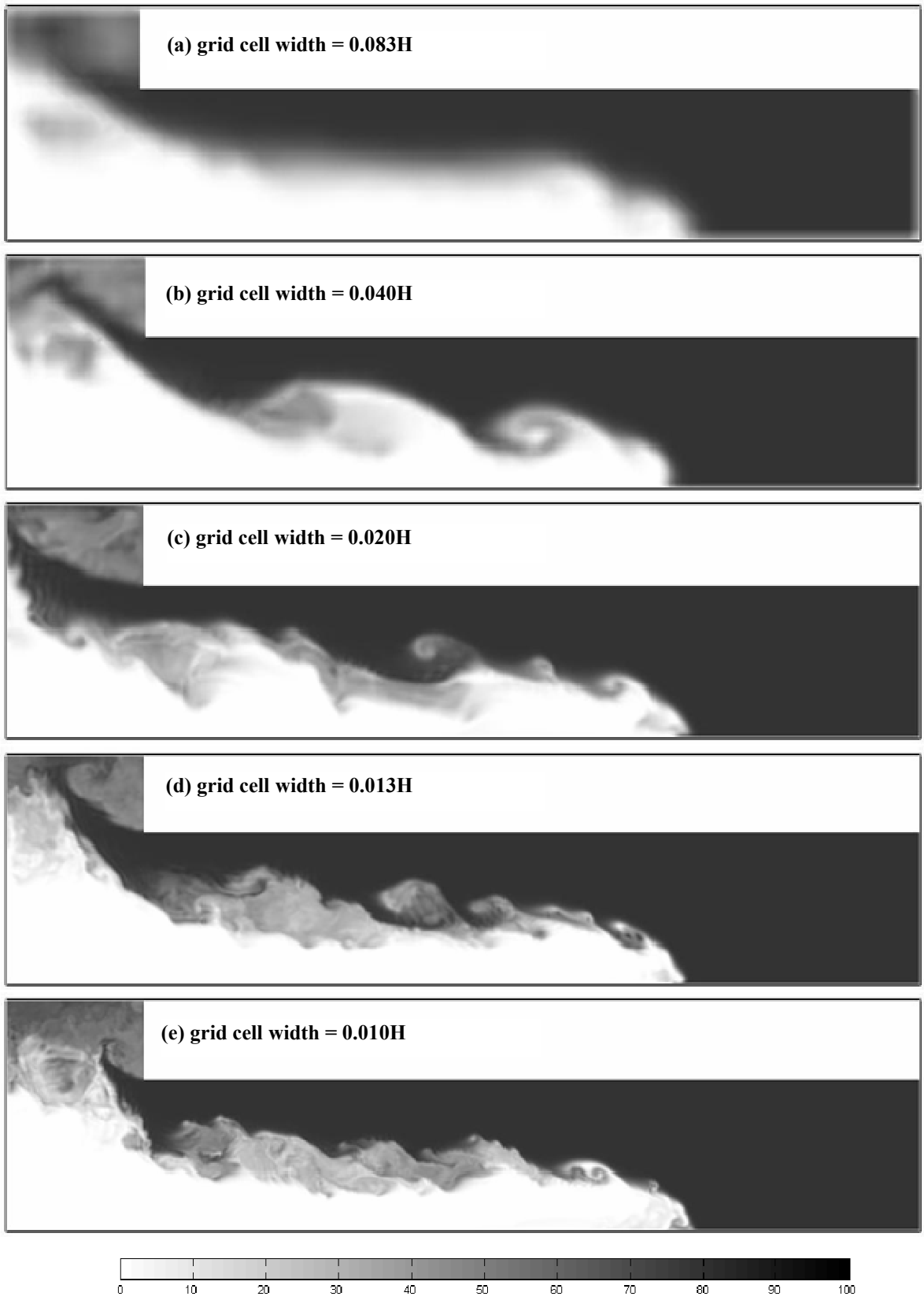

Figure 5-6: Numerical two-dimensional relative concentration fields for different grid sizes at time=17.2s. Black represents saltwater and white represents fresh water. The white rectangle in the top right hand corner represents a solid obstruction. The orientation has been inverted.

Bulk Front Characteristics

The propagation of the front of the gravity currents was plotted for different values of the VBC parameter, as shown in Figure 5-7. Decreasing the VBC parameter effectively increased the friction experienced at physical boundaries. Therefore, the front propagated more slowly with the no-slip boundary condition (VBC=-1.0) than with a full-slip boundary condition (VBC=1.0). The front propagation in the full-slip boundary simulation was very close to the theoretical energy conserving value of Benjamin (1968), while the no-slip and quarter-slip (VBC=-0.5) simulations were closer to the experimental result from Simpson (1997).

Additional bulk front characteristics investigated were the head height, the Froude number and the local Froude number, which are shown in Figure 5-8 (a), (c) and (e), while the average values were plotted against the VBC parameter in Figure 5-8 (b), (d) and (f). These parameters were relatively insensitive to the VBC. The average values of these parameters are also independent of the VBC, except for the full-slip and three-quarter-slip conditions, which under-predicted head height and over-predicted the Froude and local Froude numbers.

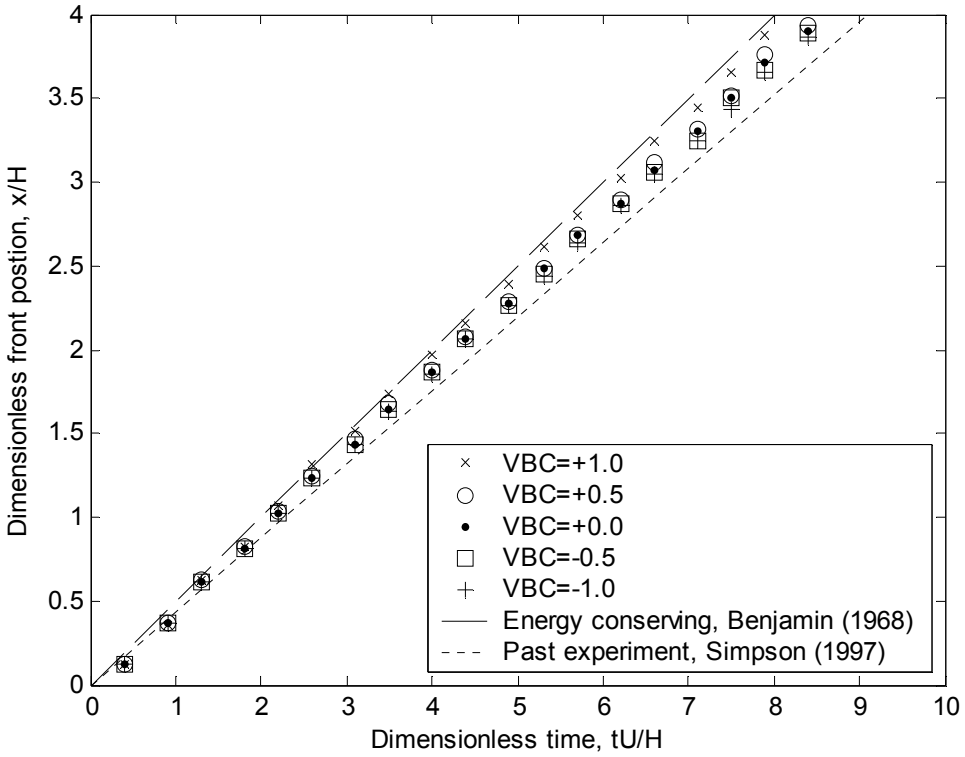

Figure 5-7: Dimensionless plot of numerical gravity current front position versus time for different velocity boundary condition parameters (VBC).

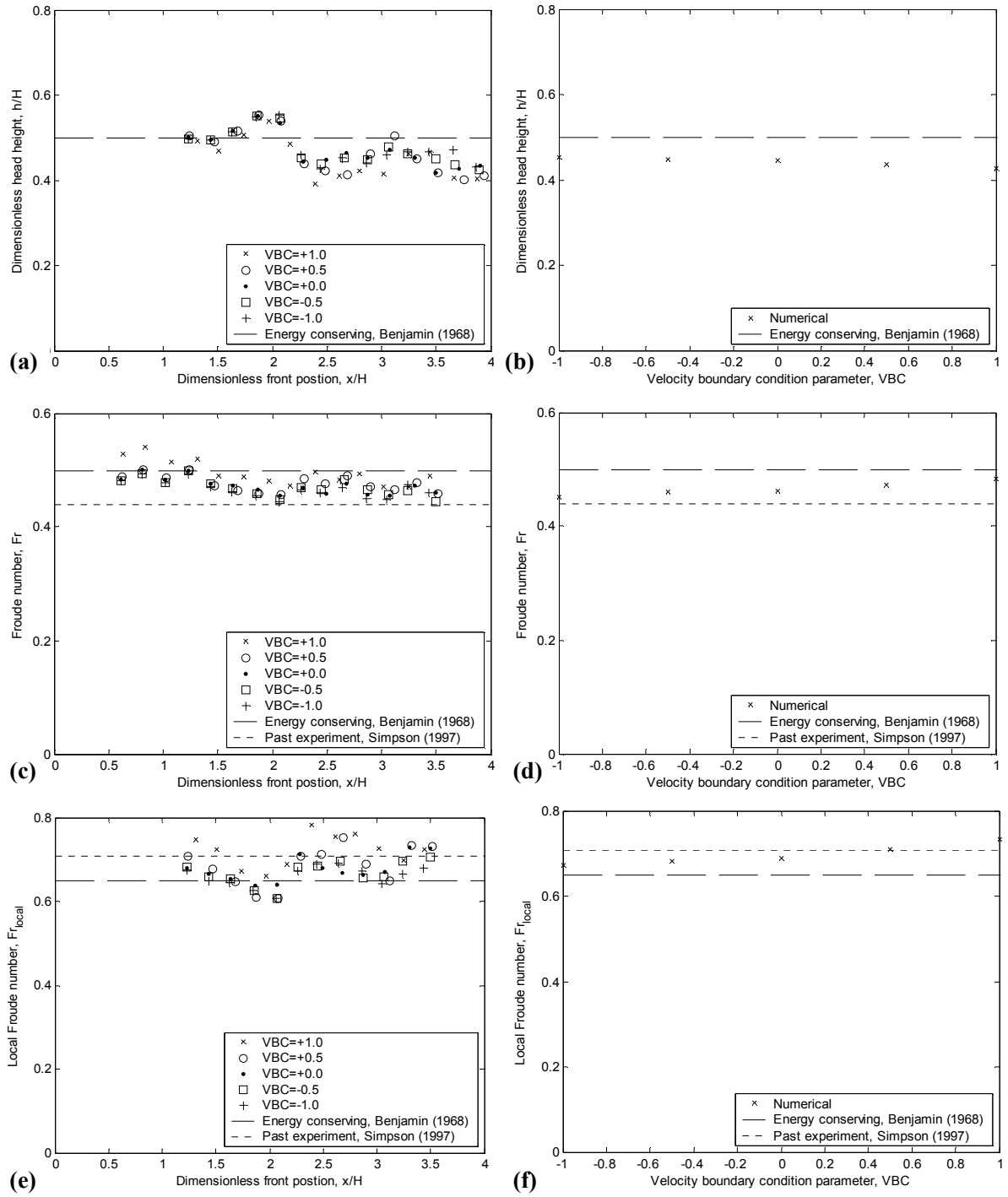

Figure 5-8: Plots of numerical bulk front characteristics of gravity current for different velocity boundary condition parameters (VBC): (a, b) head height, (c, d) Froude number, (e, f) local Froude number.

Internal Relative Concentration

The sensitivity of the relative concentration field to the VBC parameter was investigated by a direct comparison to experimental results. The analysis focused on the flow at the head of the gravity current, as this is where any differences in the frictional effects at the rigid boundary were apparent. Typical relative concentration fields created at a front position of

approximately 3H (where the shape of the front did not change significantly with time) as shown in Figure 5-9. Width-integrated fields were investigated instead of 2D fields, as they allowed the average (across channel) effect of the friction to be studied and enabled a direct comparison of experimental and numerical results.

A typical experimental width-integrated relative concentration field, is shown in Figure 5-10. The head of the gravity current was found to have a raised nose, indicating overrun of ambient saltwater fluid and a uniform thickness mixed layer was located above a relatively uniform region of freshwater. No billow structures were visible.

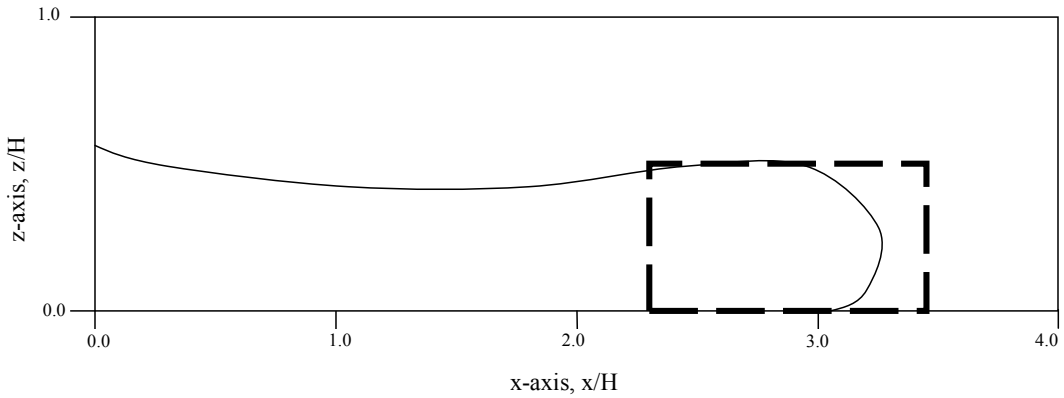

Figure 5-9: Area where the nose relative concentration fields were investigated, represented by bold dashed line. The orientation is inverted.

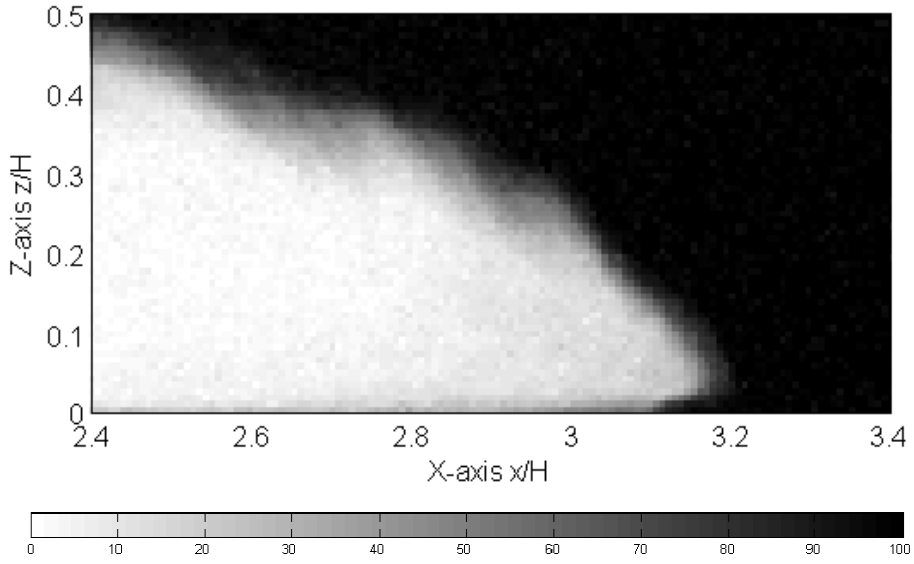

Figure 5-10: Width-integrated experimental relative concentration fields at front of gravity current. Black represents saltwater and white represents fresh water. The orientation is inverted.

Typical width averaged mixing profiles generated from the FDS simulations with different VBC parameters are presented in Figure 5-11 (a) to (e).

The full-slip VBC did not match the experimental result. In these simulations, no raised nose existed, so no ambient fluid was overrun and no lobe and cleft formation occurred. The flow was relatively two-dimensional, with the mixing due only to the Kelvin-Helmholtz (K-H) billows. Unlike the experiment, these billows were relatively coherent at the front of the current, as shown in Figure 5-11 (a). These billows broke down more slowly than in the experiment and were still visible at distances exceeding 1.5 compartment depths (H) behind the front.

The billow structure, visible in the concentration fields, was less coherent in the simulations with a three-quarter-slip and half-slip VBC, which indicated that increasing the friction at the boundary increased the level of out of plane mixing. The raised nose, seen in the experiment, was starting to become visible.

The concentration fields with quarter-slip and no-slip VBC were very similar to those from experiment. No billow structures were visible, a raised nose was evident, and the slope of the head was comparable.

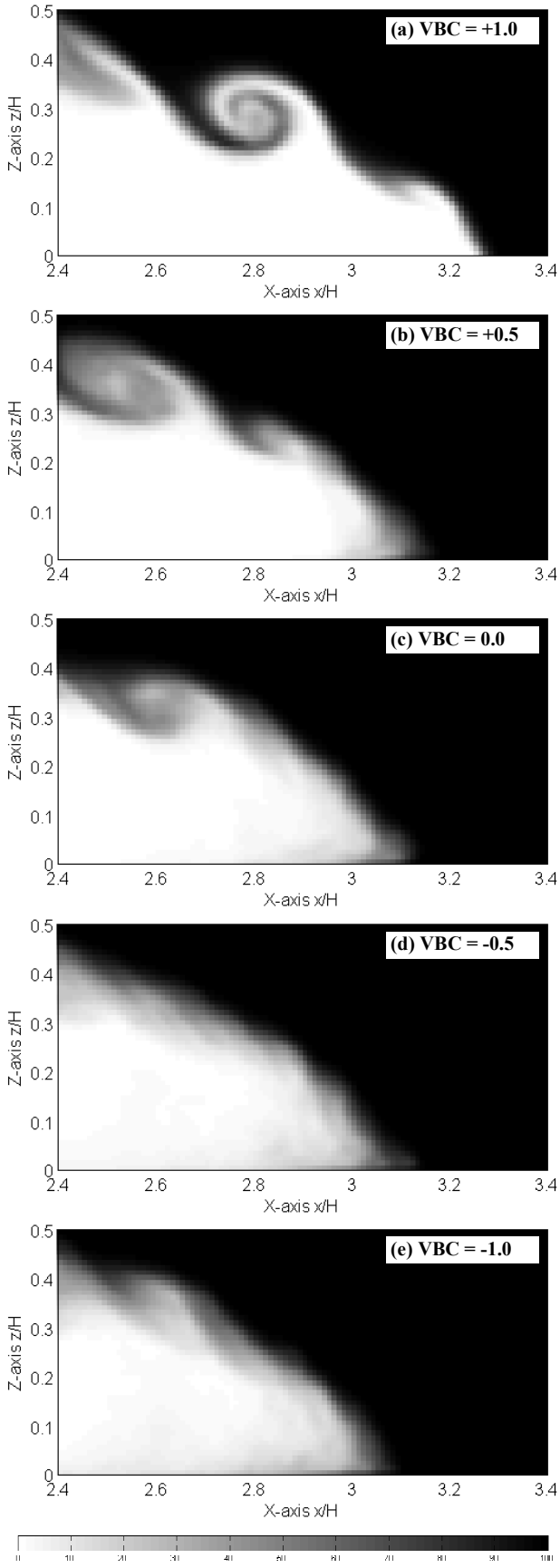

Figure 5-11: Width-integrated numerical relative concentration fields at front of gravity current for VBC parameters. Black represents saltwater and white represents fresh water. The orientation is inverted.

Internal Velocity

Two-dimensional velocity fields (from a slice along the mirror boundary) were used to create velocity profiles for the tail of the flow, as shown in Figure 5-12. The equivalent experimental result from the present study was included for comparison. These profiles were generated when the front had reached approximately $x \sim 3.5H$ (at a time of $t^* \sim 7.5$) and were spatially averaged over a width of approximately $0.2H$, from $1.3H < x < 1.5H$, to reduce the effects of turbulent fluctuations on the velocity fields. This region was situated approximately halfway between the inflow and the head of the current, and was selected as the spatial velocity gradients were minimal. Only horizontal velocities were investigated, as they were found to be an order of magnitude larger than the vertical velocities.

Kneller (1999) proposed the tail velocity profile shown in Figure 5-13 to match experimental rigid boundary gravity currents with a free-surface above. The profile was scaled vertically by the gravity current depth, h, which for rigid boundary flows is approximately half the compartment height (h ~ 0.5H) (Simpson 1997).

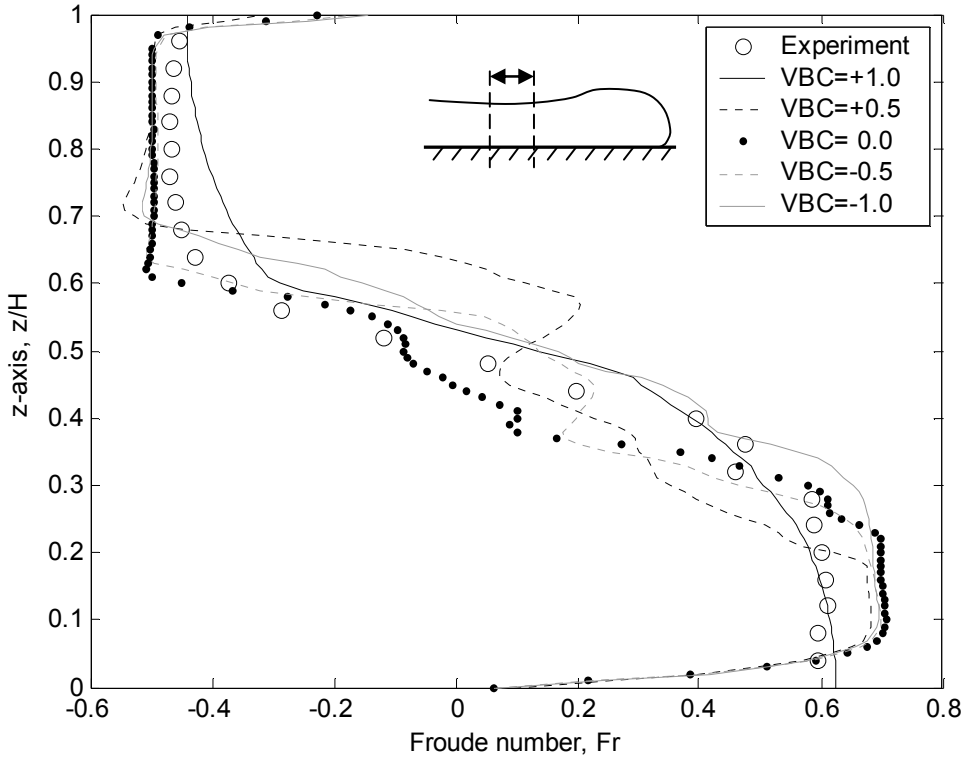

Figure 5-12: Horizontal velocity versus depth for different VBC parameters and from experiment. Velocities are averaged in time and space. Inverted orientation. Positive indicates a flow into the compartment, while negative indicates a flow out of the compartment.

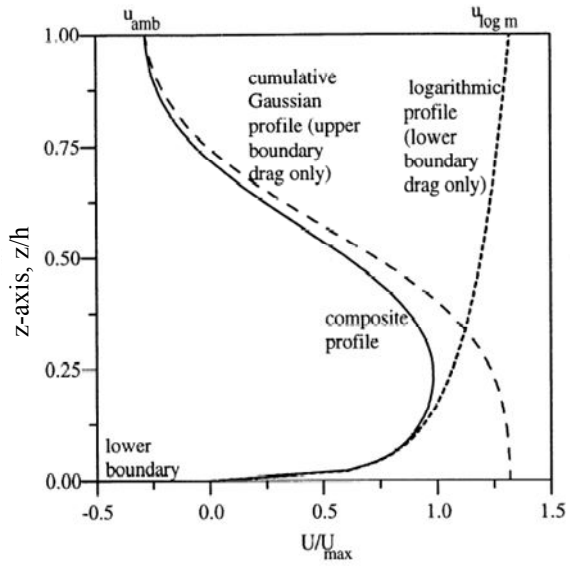

Figure 5-13: Suggested velocity profile for tail of rigid boundary gravity currents with a free surface above. This figure is an extract from Kneller et al. (1999).

For the full-slip boundary condition, where VBC=1.0, no friction was experienced at rigid boundaries and the flow velocity at the boundary was the same as the adjacent fluid. The velocity profile did not match Kneller's (1999) profile, especially close to the boundaries.

The other four simulations, involving three-quarter-slip (VBC= 0.5), half-slip (VBC= 0.0), quarter-slip (VBC = -0.5) and no-slip (VBC = -1.0) boundary conditions, had profiles that were similar to both the experimental profile generated in the present study and that proposed by Kneller (1999). The effects of turbulence were evident through the central region of the flow. All profiles slightly over estimated the maximum velocities, when compared to the experimental result. The flow was retarded at the upper and lower rigid boundaries, which reduced the velocities in these regions. The location of maximum velocity occurred at between $0.10H < z < 0.20H$, compared to $z \sim 0.10H$ ($z \sim 0.2h$) from Kneller (1999). The velocity at mid-depth was approximately zero, due to the counter-flow opposing the gravity current, and an internal mixing region of approximately 0.5H existed, where the velocity changed rapidly with depth. Overall, these velocity profiles suggest the quarter-slip and no-slip VBC parameters show the closest fit to the experimental profile.

Suggested VBC Parameter

The bulk front characteristics, concentration profiles and velocity profiles suggest that a velocity boundary condition of VBC=-0.5, or -1.0 would be appropriate. However, as the grid

size (0.01H) was the same order of magnitude as the viscous boundary layer (see Section 5.4.1), it will not be resolved, so a no-slip boundary condition was believed to be inappropriate. Therefore, a quarter-slip boundary condition (VBC=-0.5) was suggested for further simulations.

5.4.3 Turbulent Schmidt number

The Schmidt number is a ratio of the viscosity to the mass diffusivity. The larger the Schmidt number, the slower mass will be diffused in the flow. The FDS model requires the user to specify a turbulent Schmidt number ($Sc_{turbulent}$), which is a function of the flow and the fluid.

When non-dimensionalised, the governing equations used by FDS have an inverse and coupled dependence on both the Schmidt and Reynolds numbers (Clement 2000). The gravity current flows being simulated are fully turbulent, with Re >> 1, so the flows should be relatively insensitive to the Sc, so long as it is the correct order of magnitude.

Various values of Schmidt number are proposed in the literature. Clement (2000) used FDS to simulate turbulent saltwater flows and found that the turbulent Sc needed to be of the order of unity to achieve satisfactory results. This result is close to the turbulent Schmidt number of 0.7, proposed by Yimer (2002), for CFD modelling of turbulent axi-symmetric free-jet flows of air. In addition, Pope (2000) suggests that the turbulent Prandtl number (which describes heat diffusion and so is analogous to the Schmidt number) should be approximately 1.0, and Reynolds (1976) suggests that the turbulent Schmidt and turbulent Prandtl numbers are of the order of unity (from experiments involving turbulent jets in various fluids).

In this study, the sensitivity of the FDS model to different Schmidt numbers was investigated by running simulations with Schmidt numbers of 0.1, 1, 10 and 100. In these simulations the grid size was 0.01H, the velocity boundary condition was quarter-slip (VBC=-0.5) and the reduced computational domain was used. Front propagation was found to be independent of Schmidt number over this range. Two-dimensional slices through the relative concentration fields were compared for different Schmidt numbers. Typical images are plotted in Figure 5-14 (a) to (d) for a time 17.2s after the start of the simulation. For $Sc_{turbulent} = 0.1$, the flow had a smoothed appearance, indicating excessive diffusion, while for turbulent Schmidt numbers of 10 and 100 the concentration fields had a discontinuous checkerboard appearance.

Using an intermediate value for the Schmidt number of 1.0, the flow had a realistic appearance, which agreed with the findings from literature discussed above. Therefore, a value of the turbulent Schmidt number of 1.0 is suggested for further simulations.

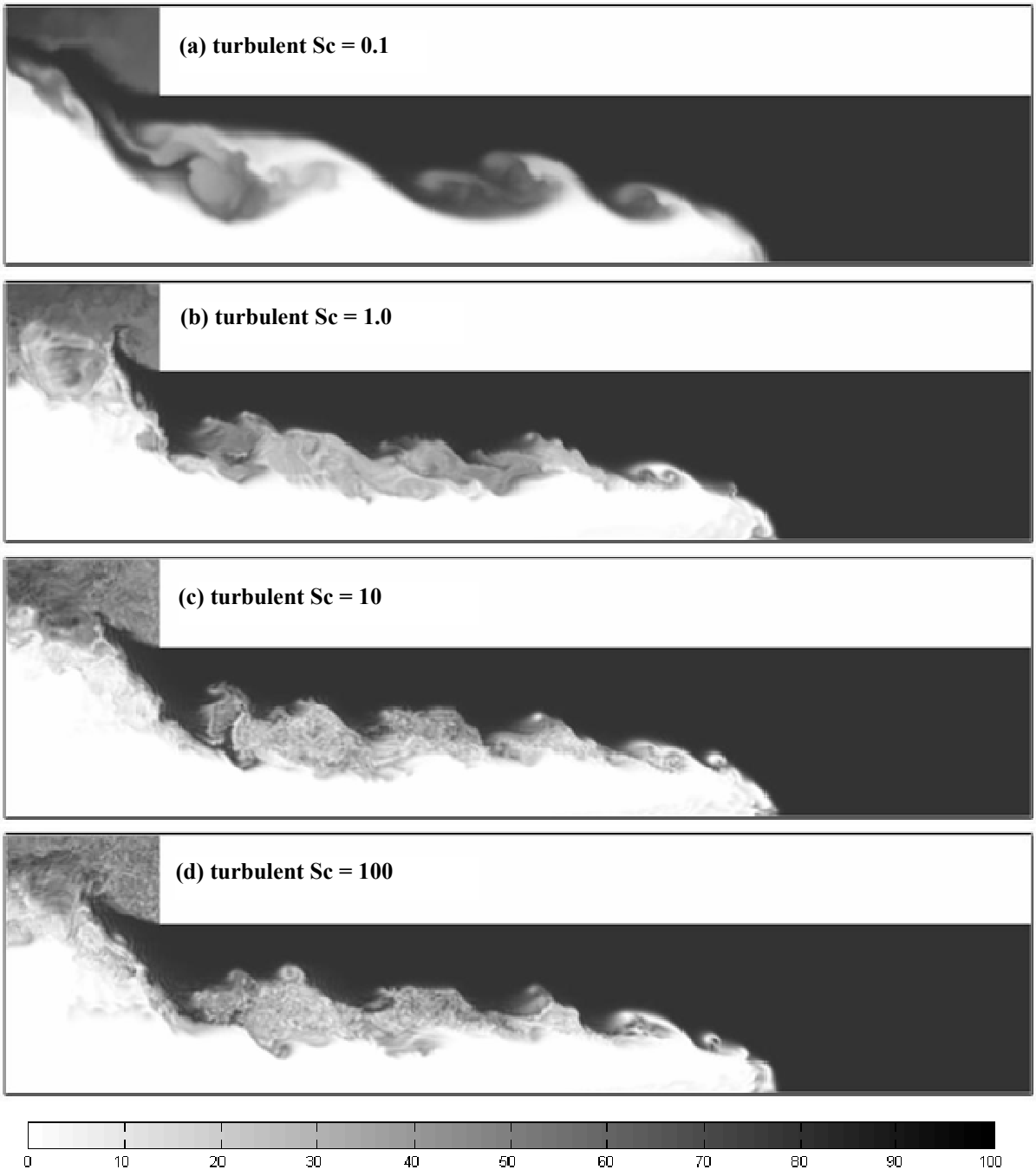

Figure 5-14: Two-dimensional numerical relative concentration field from mirror boundary for different turbulent Schmidt numbers at time=17.2s. The white rectangle in the top right hand corner represents a solid obstruction. Black represents saltwater and white represents freshwater. The orientation is inverted.

5.4.4 Reduced Computational Domain

The number of grid-cells that can be modelled in any simulation is limited by the computer's RAM capacity. Therefore, to achieve the finest grid possible with the available hardware, it was necessary to model only part of the flow and not the entire experimental flume.

To investigate the effect of reducing the extent of the numerical domain, the results of a reduced domain, shown in Figure 5-15, were compared to the results from an extended domain, shown in Figure 5-16. The extended domain was one compartment depth (H) longer on either end than the reduced domain. Due to RAM limitations, these simulations were carried out using the second finest grid size (0.013H). A quarter-slip velocity boundary condition (VBC=-0.5) and a turbulent Schmidt number of 1.0 were also used.

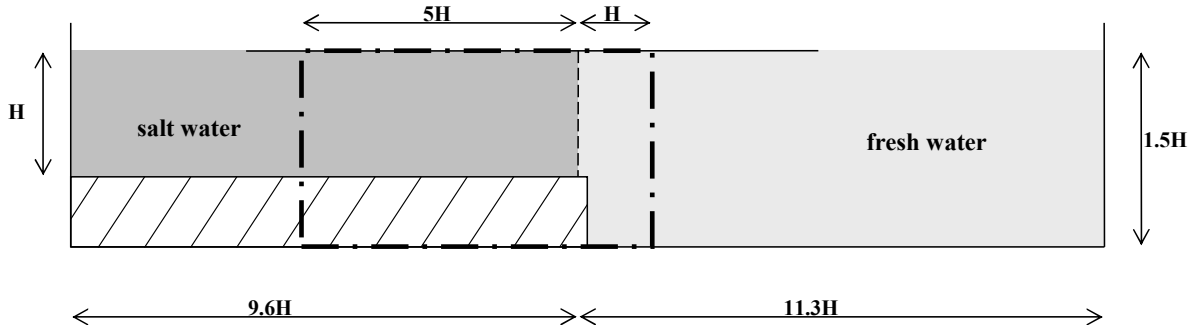

Figure 5-15: Side elevation of experimental flume setup. The bold dash-dotted line indicates the extent of the computational domain modelled from the reduced domain simulation.

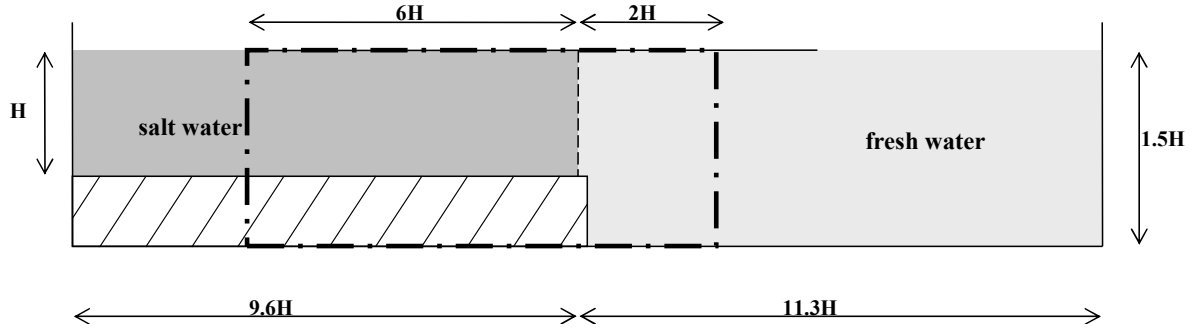

Figure 5-16: Side elevation of experimental flume setup. The bold dash-dotted line indicates the extent of the computational domain modelled from the extended domain simulation.

Bulk Front Characteristics

The bulk front characteristics of the gravity current from the reduced domain were compared to those from the extended domain. The front propagation, Froude numbers and local Froude numbers, shown in Figure 5-17 (a), (c) and (d) respectively, were almost identical for both simulations. The head height, shown in Figure 5-17 (b), showed some slightly larger variations especially in the initial stages of the flow, where the flow is collapsing and stabilising. The differences that do exist are attributed to the unsteady turbulent nature of the flows being simulated. These differences are random in nature, meaning that the reduced domain is not consistently over-predicting or under-predicting these variables. Therefore, overall, no significant difference exists between the bulk flow characteristics of the two simulations.

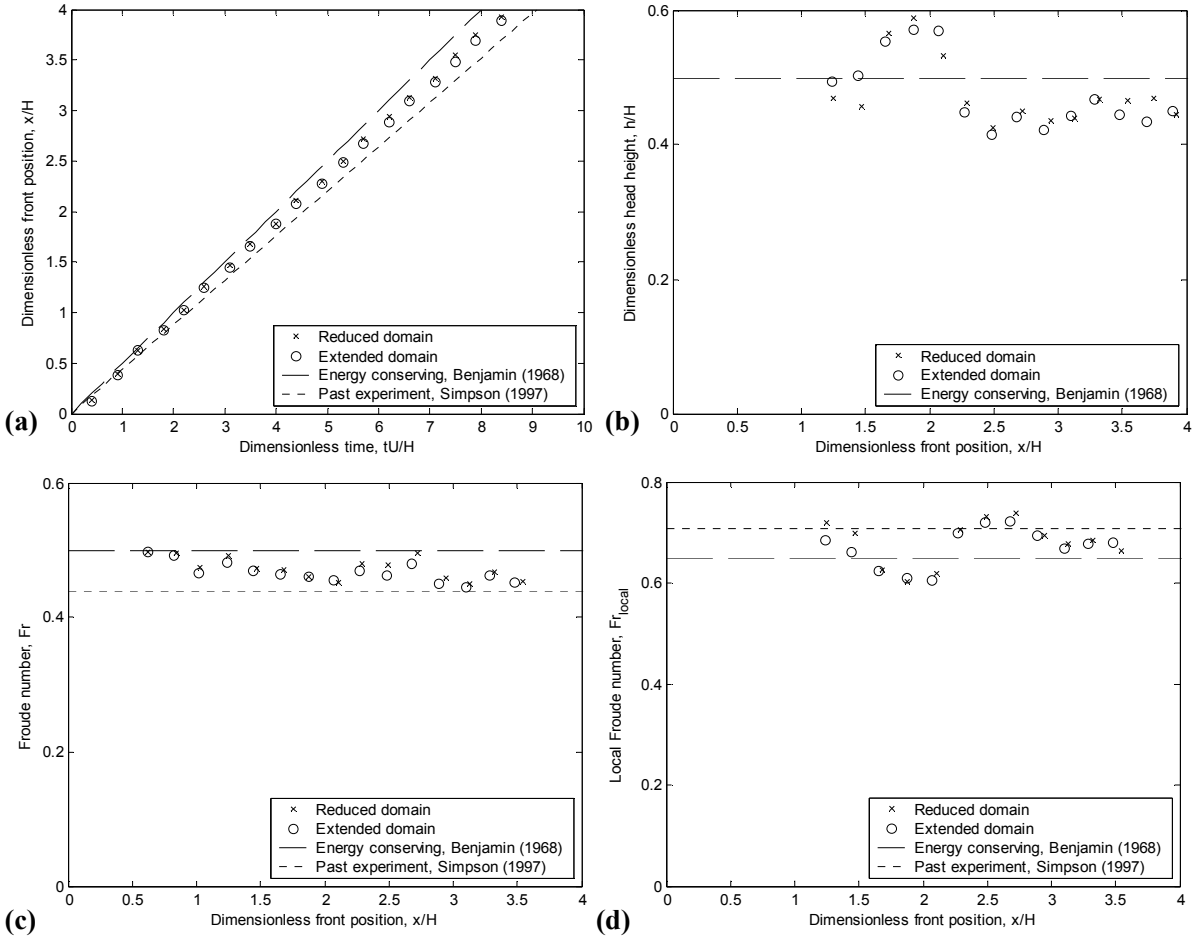

Figure 5-17: Bulk front characteristics of gravity current for the reduced and extended numerical domains: (a) Front propagation, (b) head height, (c) Froude number, (d) local Froude number.

Internal Mixing

The internal structure of the gravity currents was investigated qualitatively by comparing width-integrated relative concentration fields. The width-integrated fields for the two domains were similar in shape, and the mixed layer similar in shape and thickness. Typical width-integrated relative concentration fields are presented in Figure 5-18. In these plots, the nose of the flow from the reduced domain appears to be different in shape to that from the extended domain, but this is due to the unsteady formation of lobes and clefts at the front of the flow and is not apparent at earlier and later stages in the flow.

Suggested Domain Extent

Reducing the computational domain boundary was shown to have no significant quantitative effect on the bulk characteristics and no qualitative effect on the internal concentration structure. The slight differences that existed were attributed to the unsteady turbulent nature of the flows. Therefore, it was suggested that the reduced size computational domain was suitable to be used for further simulations.

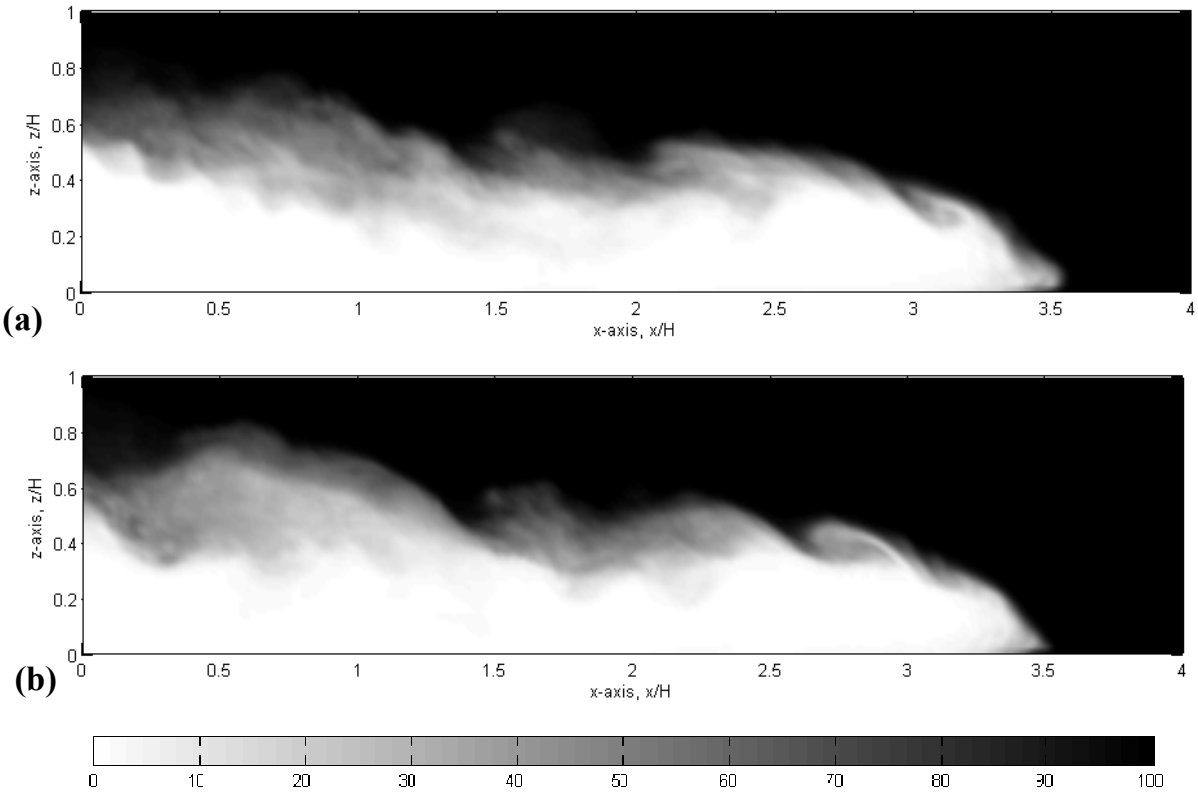

Figure 5-18: Width-integrated numerical relative concentration fields from mirror boundary at time=17.2s: (a) reduced domain (b) extended domain. Black represents saltwater and white represents freshwater. The orientation is inverted.

5.5 Summary

This chapter outlined how the computer software FDS was used to simulate the experimental gravity current flows described in the previous chapter. In Section 5.2 the input specifications used in the simulations were summarised, while Section 5.3 discussed the model outputs. Section 5.4, presented the sensitivity analysis, which was carried out to determine the models sensitivity to changes in various input parameters.

CHAPTER 6 ANALYSIS

6.1 Introduction

The analysis methods used to process the experimental and numerical results are presented below. A consistent method of analysis was adopted so that results could be compared directly. The co-ordinate system is presented in Section 6.2, while the dimensionless variables used in the Results chapter are outlined in Section 6.3. In Section 6.4, definitions of the bulk front characteristics, including head height, front position, and front velocity, are presented. Finally, Section 6.5 outlines how flammable regions, for typical backdraft gravity currents, were determined from the relative concentration fields.

6.2 Co-ordinate System

The spatial co-ordinate system used to interpret the results of the experiments and numerical simulations is presented in Figure 6-1. The origin was located at the top corner of the saltwater compartment opening, the z-axis was positive down (in the direction of gravity) and the x-axis was positive down the length of the saltwater compartment. In this frame of reference, the gravity current flows from left to right along a lower rigid boundary, as shown in Figure 6-2, matching the orientation of backdraft gravity currents.

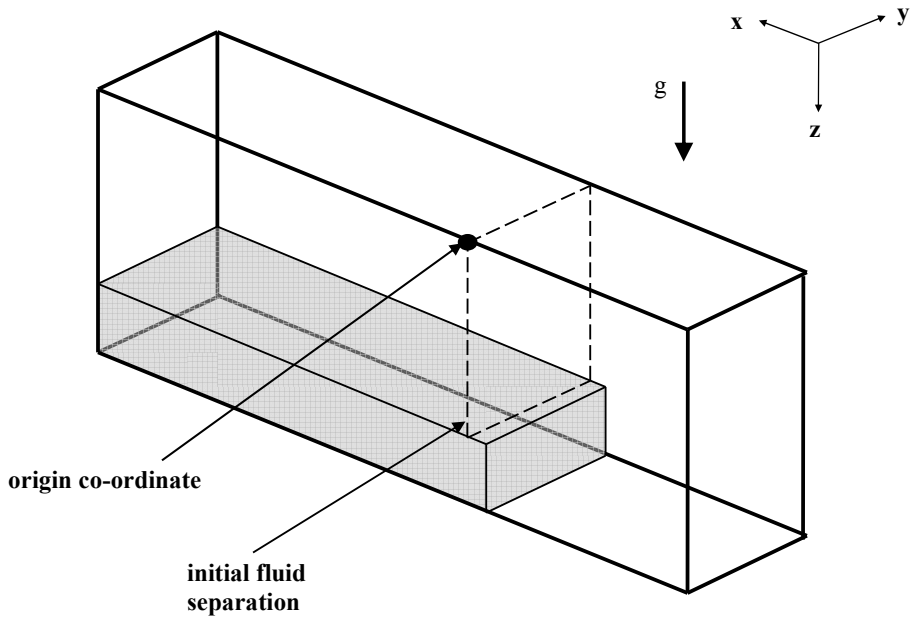

Figure 6-1: Schematic showing the orientation of the spatial co-ordinate system.

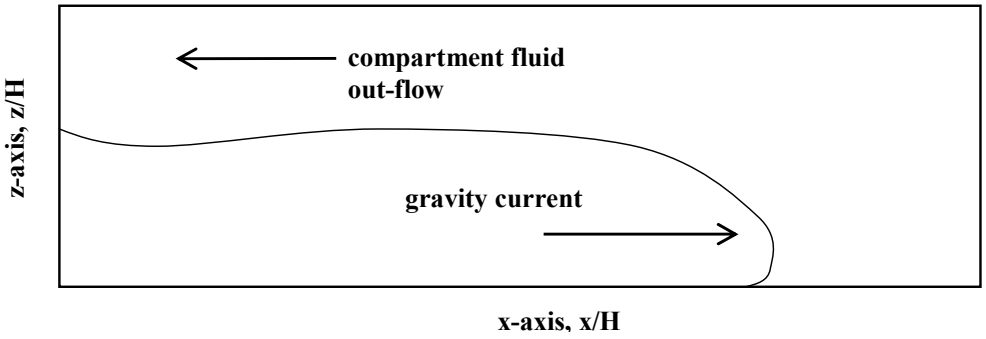

Figure 6-2: Schematic of gravity current flow once the data was re-orientated.

6.3 Non-dimensional Variables

The non-dimensional variables used in the Results section are defined in Equations (6-1) to (6-7) below (these equations were developed in Literature Review chapter).

$$x^* = \frac{x}{H}$$ dimensionless distance (6-1)

$$\phi = \frac{h}{H}$$ dimensionless head height (6-2)

$$t^* = \frac{t\sqrt{\beta_{initial} gH}}{H}$$ dimensionless time (6-3)

$$Fr = \frac{u}{\sqrt{\beta_{initial} gH}}$$ Froude number (6-4)

$$Fr_{local} = \frac{u}{\sqrt{\beta_{initial} gh}}$$ local Froude number (6-5)

$$\mathrm{Re}_{local} = \frac{uh}{\nu}$$ local Reynolds number (6-6)

$$R = \frac{\Delta\rho}{\Delta\rho_{initial}} = \frac{\beta}{\beta_{initial}}$$ relative concentration
0% = ambient fluid (fresh water)
100% = compartment fluid (salt water) (6-7)

6.4 Bulk Front Characteristics

The bulk front characteristics investigated in the present study were the head height, the front position and the front velocity. These parameters were all derived from the relative concentration fields using the methods explained below.

The experimental and numerical concentration fields, from which the bulk front characteristics were derived, were spaced at intervals of $t^* = 0.44$ for the full, horizontal step, vertical slot and door opening geometries and $t^* = 1.2$ for the window opening geometry. The time required for the head of the gravity current to reach $x^* = 4H$ was opening geometry dependent, ranging from $t^* = 8$ (full opening geometry) to $t^* = 22$ (window opening geometry). Generating the numerical concentration fields more frequently was not practical from a data processing point of view.

6.4.1 Head Height

Gravity current head heights were determined from the relative concentration field. First, equivalent height profiles were generated from concentration fields, by vertically integrating the relative concentration/density (see Equation (6-8)), providing an unambiguous measure of gravity current depth (Marino et al. 2005). A typical relative concentration field and the corresponding equivalent height profile are shown in Figure 6-3.

$$h(x,t) = \int_0^H \left[1 - R(x,z,t)\right] dz \tag{6-8}$$

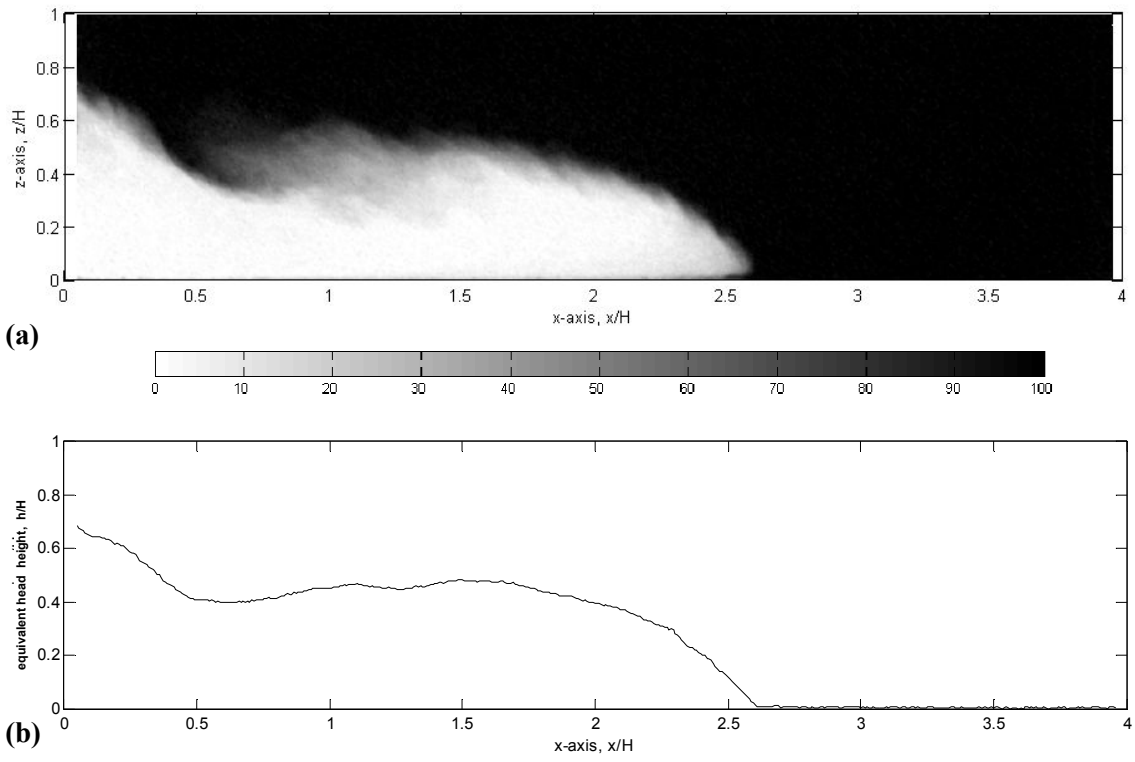

Figure 6-3: Instantaneous plots from an experiment with a full opening: (a) width-integrated relative concentration field, (b) the corresponding equivalent height profile.

The head height was defined as the depth of the equivalent height profile a specified distance behind the front/nose of the gravity current, as illustrated in Figure 6-4. The gravity currents from the different opening geometries varied in shape and size, so a different *averaging width* and *head-nose distance* (see Figure 6-4) was specified for each opening, as shown in Table 6-1. The *head-nose distance* was the distance between the nose/front of the flow and the deepest section of the equivalent height profile. This distance was determined from time-sequences of equivalent height profiles for each of the different opening geometries. The *averaging width* spatially averaged the effects of any turbulent fluctuations or experimental error in the equivalent height profile. Spatial gradients in the equivalent height profile were found to be minimal over the *averaging width*.

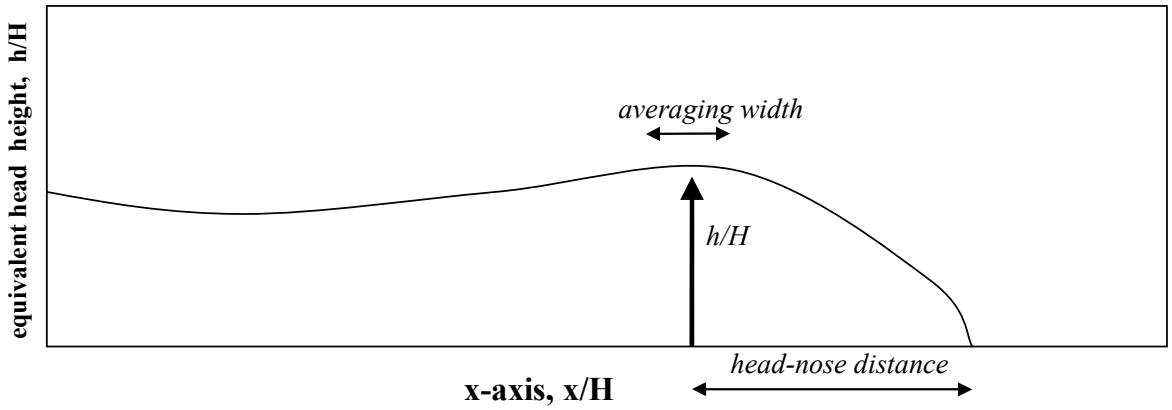

Figure 6-4: Illustration showing how equivalent head heights were determined from equivalent height profiles.

Table 6-1: Definitions of *averaging width* and *head-nose distance* used to determine equivalent head heights for the difference opening geometries.

Opening Geometry	*head-nose distance*	*averaging width*
Full opening	1.0H	0.25H
Horizontal Step	0.8H	0.2H
Vertical Slot	0.6H	0.2H
Door	0.6H	0.2H
Window	0.5H	0.2H

6.4.2 Front Position

The front position was defined as the point where a horizontal line at $z = 0.05H$ intercepted the 85% relative concentration contour line, as illustrated in Figure 6-5. The line was located at $z = 0.05H$, because this was the approximate height of the nose of the gravity current flows, which represents the foremost point of the gravity current head. The choice of the 85% contour was somewhat arbitrary. However, due to the high concentration gradient through the nose region, contours of 75% and 95% were shown to only slightly offset the front position versus time plots. Higher contour values were not investigated, because background "noise" in the experimental concentration fields was of the order of 5% and may have caused erroneous front position predictions.

As a check of the accuracy of this method, another method was also used to determine the front position. In the second method, the front position was specified as the foremost point of the equivalent height profile, as illustrated in Figure 6-6. Both definitions of front position generated consistent results. Therefore, for clarity, only the results using the first method were used.

6.4.3 Front Velocity

The front velocity was determined from the plots of front position versus time. The velocity of the gravity current front at each point was defined as the gradient of a first order polynomial fit through five points on the distance versus time plot, as shown in Figure 6-7.

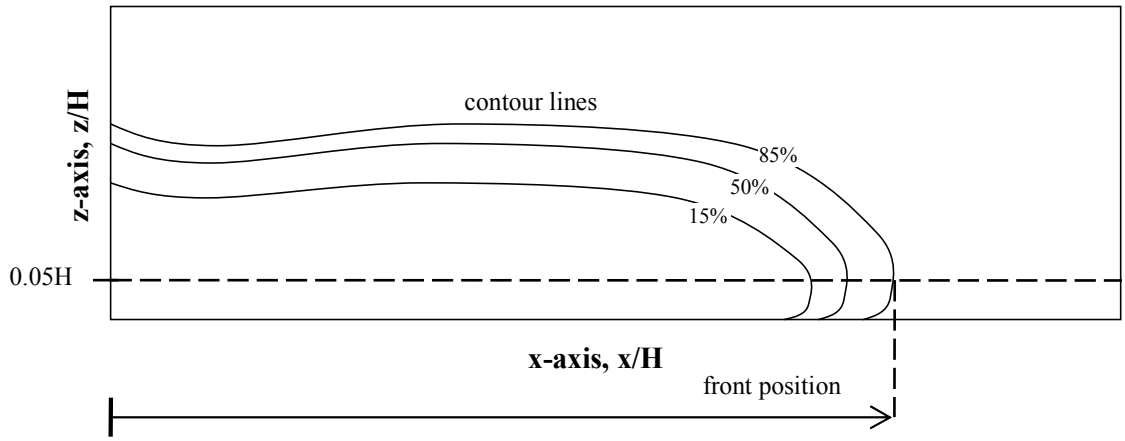

Figure 6-5: Illustration showing how front position was determined from a relative concentration field.

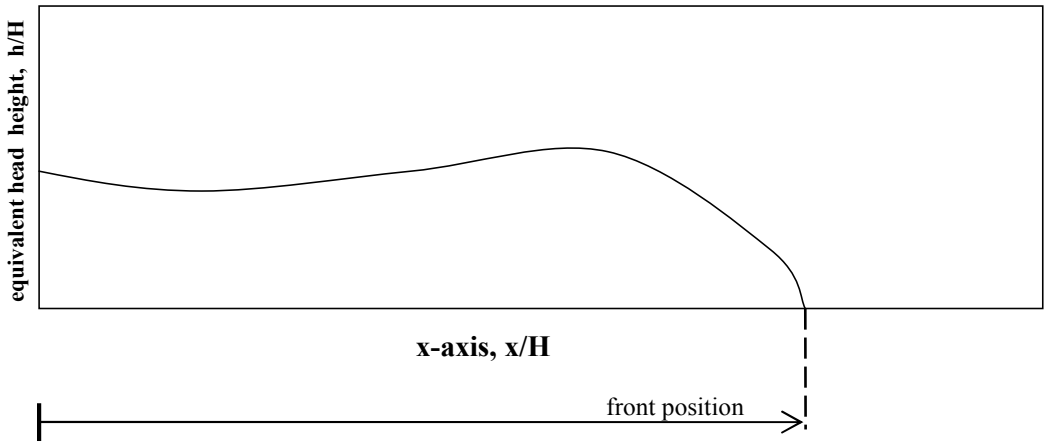

Figure 6-6: Diagram illustrating how front positions were determined from equivalent height profiles.

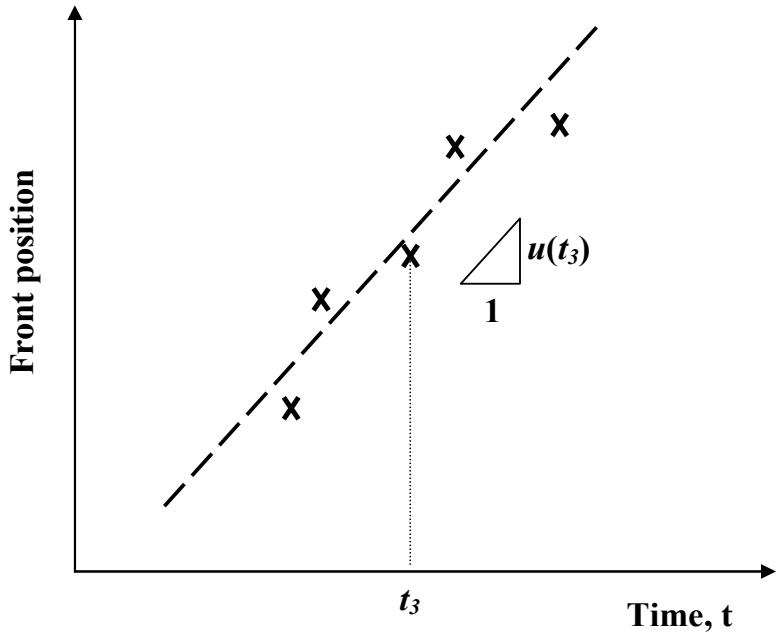

Figure 6-7: Schematic showing how the front velocity was defined.

6.5 Flammable Regions

The flammable region within gravity currents preceding backdrafts are of interest as they will ignite if exposed to an ignition source. Relative concentration fields were used to determine which regions of the flow would correspond to flammable gas mixtures. A methane fuel was selected, because experimental gas composition data was readily available in the literature, from past backdraft experiments. First, typical compartment initial conditions, from experiments which resulted in backdraft, were determined. Then methane flammability limits were used to determine the range of relative concentrations corresponding to flammable gas mixtures. These steps are described in detail below.

Initial Conditions

Fleischmann (1994) generated experimental backdrafts with a methane fuel. A summary of the range of the measured initial mass fractions that resulted in backdrafts is presented in Table 6-2. The average of these ranges was assumed to be representative.

The mass fractions of water and nitrogen were not measured and volume fractions were not provided. Therefore, an iterative process was used to convert the mass fractions to volume fractions, and to predict mass and volume fractions of water and nitrogen. The water volume fraction was assumed, from stoichiometry, to be two times the sum of the volume fractions of carbon dioxide and carbon monoxide. The mass fraction of nitrogen was adjusted to provide a total mass fraction of unity. The initial experimental volume fractions are shown in Table 6-3.

Table 6-2: Experimental initial gas mass fractions which resulted in backdrafts (Fleischmann 1994).

Fuel	Range of mass fractions	Average mass fraction
Methane (CH_4)	0.10 – 0.30	0.20
Oxygen (O_2)	0.05 – 0.12	0.09
Carbon dioxide (CO_2)	0.03 – 0.05	0.04
Carbon monoxide (CO)	0.00 – 0.01	0.005

Table 6-3: Average experimental initial mass and volume fractions which resulted in backdraft. Values in brackets were measured experimentally, other values have been calculated.

Component	Mass Fraction	Volume Fraction
Methane (CH_4)	(0.20)	0.30
Carbon monoxide (CO)	(0.005)	0.00
Oxygen (O_2)	(0.09)	0.07
Nitrogen (N_2)	0.61	0.53
Carbon dioxide (CO_2)	(0.04)	0.02
Water (H_2O)	0.05	0.06

The inert components (carbon dioxide, water and nitrogen) were converted to an equivalent volume of nitrogen, based on the ratio of their specific heats to that of nitrogen (Shore 1996) and a combined fuel volume was calculated by summing those of methane and carbon dioxide.

The upper flammability limit (UFL) and lower flammability limit (LFL) of methane and carbon dioxide in air and pure oxygen are shown in Table 6-4 (Beyler 2002; Perry et al. 1997). The flammable limits of a composite gas mixture may be approximated using Le Chatelier's Rule (Beyler 2002; Perry et al. 1997), which is shown in Equation (6-9). However, as the volume of carbon monoxide fuel was much smaller than the volume of methane (ratio of carbon dioxide to methane of approximately 1%), the flammable limits of the composite mixture of methane and carbon dioxide are almost identical to those for methane, as shown in Table 6-4. Therefore, all fuel was assumed to be methane. The initial experimental gas composition may now be represented as an equivalent mixture of methane, oxygen and nitrogen, as shown in Table 6-5.

$$FL_{comp} = \frac{100}{\sum \frac{C_i}{FL_i}} \tag{6-9}$$

where: FL_{comp} = composite flammable limit

FL_i = component flammable limit

C_i = component fraction of total fuel

Table 6-4: Flammable limits for methane, carbon monoxide and composite fuel mixture. Expressed as volume fractions.

Limit	Methane (CH_4)	Carbon monoxide (CO)	Composite (~ 99% CH_4, 1%CO)	Graph
UFL (air)	14	74	14.1	**C**
LFL (air)	5.3	12.5	5.3	**D**
UFL (O_2)	61	-	-	**A**
LFL (O_2)	5.1	-	-	**B**

Table 6-5: Equivalent initial volume fractions.

Component	Volume Fraction
Methane (CH4)	0.31
Oxygen (O2)	0.07
Nitrogen (N2)	0.63

Flammability Diagram for Methane

The flammability diagram for methane, shown in Figure 6-8, was constructed from the flammable limits and the stoichiometric equation for methane, using the approach described by Mashuga et al (1998) and Shore (1996). This is a two-axis flammability plot, where the oxygen volume fraction is not explicitly shown, but may be determined from the concentrations of fuel and nitrogen. The air line represents all possible concentrations of fuel and air. The stoichiometric line represents all stoichiometric combinations of methane and oxygen. The flammable limits for combustion in air were plotted on the air line (points C and D), while the limits for combustion in pure oxygen were plotted on the vertical axis (points A and B) (see Table 6-4 for numerical values of points A to D). The minimum oxygen concentration (MOC) (point E) was assumed to be located at the intersection of a horizontal line passing through the LFL (air) and the stoichiometric line (Shore 1996). The flammability envelope was constructed by connecting points with straight lines, B→ D→ E → C → A (Shore 1996).

The maximum experimental temperature, prior to ventilation and backdraft, was approximately 300ºC, while ambient temperatures were approximately 20ºC (Fleischmann 1994). Therefore, a mixture of ambient and compartment gases would be approximately 150ºC. The associated change in the magnitude of the flammability limits, as the temperature is increased from ambient to 150ºC, is less than 10% (Shore 1996), so temperature effects were ignored.

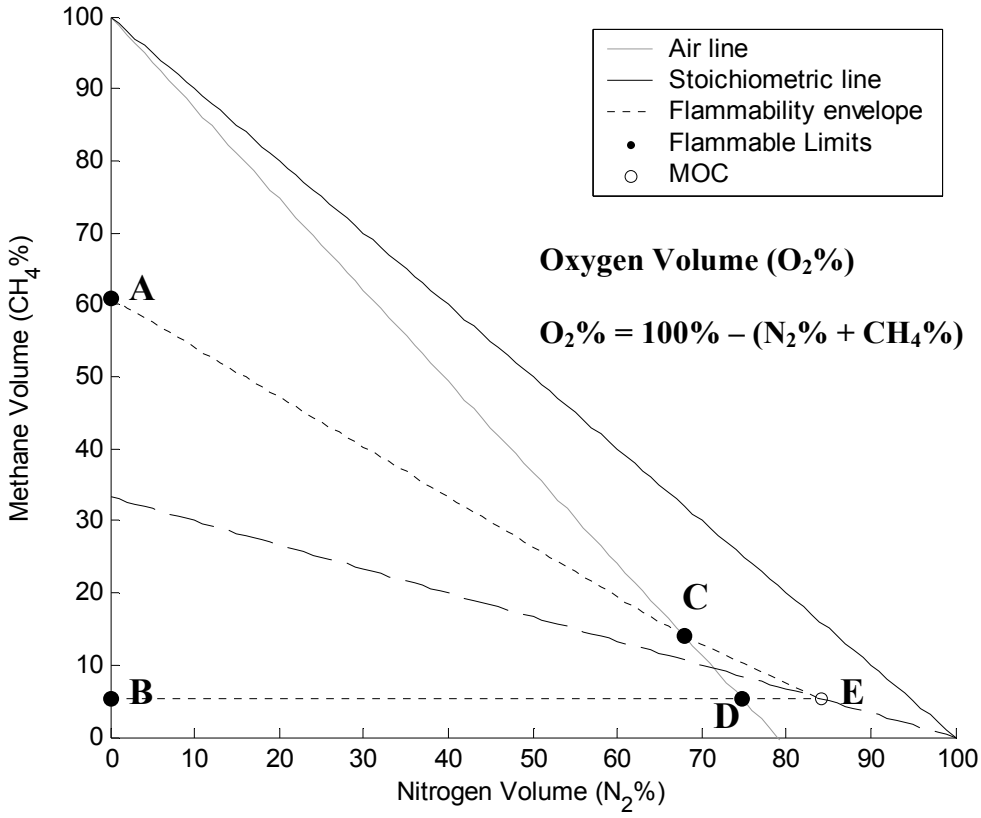

Figure 6-8: Flammability diagram for methane.

Flammable Relative Concentrations

The initial experimental gas composition (from Table 6-5) is represented by the square symbol on the methane flammability diagram in Figure 6-9. The black dot on the nitrogen axis represents fresh air (nitrogen volume fraction ~ 79%). All possible mixtures of compartment gases and fresh air are represented by the ventilation line, a straight line connecting these points. Flammable gas mixtures are predicted for relative concentrations between 17% and 37%, where the ventilation line falls within the flammability envelope. Using this result, the volume of flammable gases can be estimated from the width-integrated relative concentration fields as the area within the concentration field where the concentrations falls within the flammability limits $17\% < R < 37\%$.

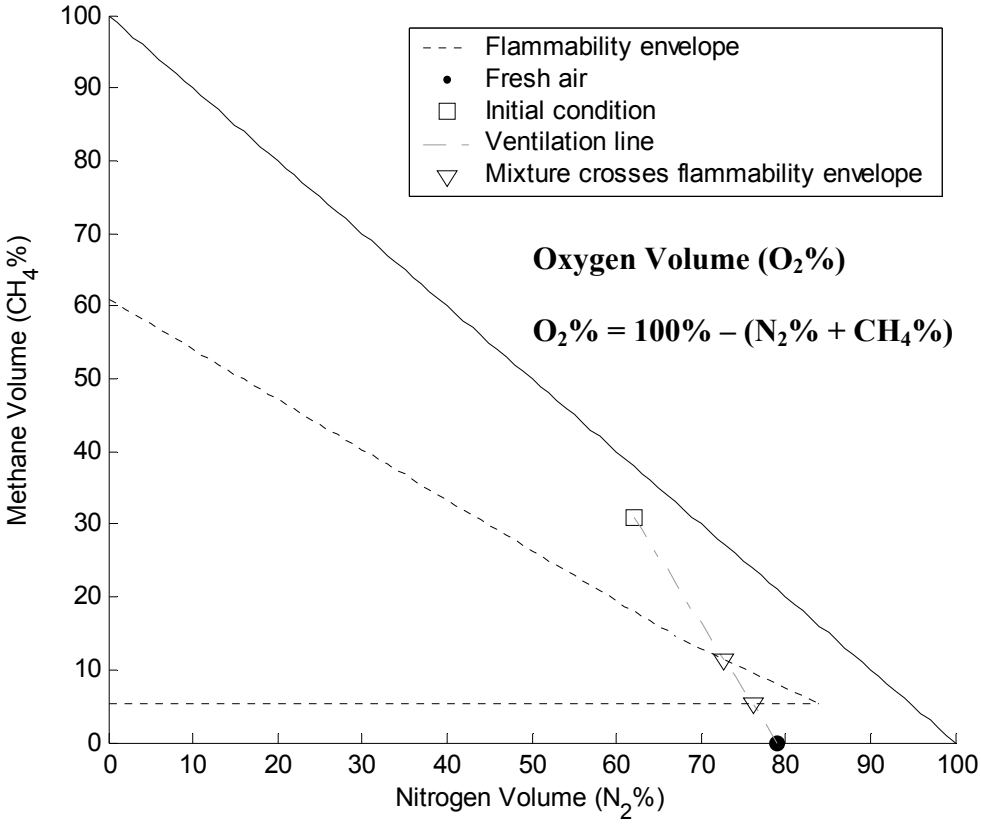

Figure 6-9: Compartment ventilation line superimposed on the flammability diagram for methane.

6.6 Summary

This chapter has outlined the procedures used to analyse the experimental and numerical data. Section 6.2 introduced the co-ordinate system used to interpret the data, while Section 6.3 outlined the scaling equations used to non-dimensionalise the results. Definitions for the bulk front characteristics were introduced in Section 6.4. Finally, Section 6.5 described how flammable regions were determined from the width-integrated concentration fields.

CHAPTER 7 RESULTS AND DISCUSSION

7.1 Introduction

The aim of this chapter is to quantify the effect of different compartment opening geometries on backdraft gravity currents and to validate the ability of the CFD model FDS to simulate these flows. Results of experimental and numerical modelling are presented for five different compartment opening geometries. All of the flows were Boussinesq, with density differences less than 5%, and fully turbulent, with local Reynolds numbers greater than the limiting value of 500 (Simpson 1997).

General observations of the flows generated by each of the different compartment openings are presented in Section 7.2. In Section 7.3, the bulk front characteristics of the experimental and numerical flows are presented and compared. Section 7.4 analyses the mass flux through the compartment openings and within the head of the gravity currents. The internal relative concentrations within the gravity current flows are examined in Section 7.5. Finally, the internal velocity structure of the flows is investigated in Section 7.6.

7.2 General Observations

General qualitative observations for each of the different opening geometries are presented the sub-sections below. The mixing processes evident within these flows were consistent with those suggested by Simpson (1997) and Fleischmann (1994). Billows formed at the front of the gravity currents and rolled up and broke off the head, and lobes and clefts formed due to the gravitational instability of ambient fluid over-run by the gravity current nose. However, two additional mixing processes were also evident, both of which generated large amounts of mixing in the initial stages of the flows. The first was a plume, which formed as the flow passed over the vertical drop for the horizontal step and window opening geometries. The second was lateral spreading, which occurred as the flow spread laterally after passing through narrow openings such as the vertical slot, door and window opening geometries.

7.2.1 Full Opening

A time sequence of relative concentration fields for the full opening geometry is shown in Figure 7-1 (a). As the compartment was ventilated, an exchange flow developed with freshwater flowing in along the lower boundary and saltwater flowing out of the compartment along the upper boundary (note this description assumes the flow is inverted in order to match the practical problem being simulated). At a front position of approximately 0.5H, the front of the freshwater flow had formed a small head, which was slightly higher than the following fluid. For front positions between $0.5H < x < 2.0H$, as freshwater continued to flow into the compartment, the size of the head increased and billows were visible forming just behind the head. For front positions greater than approximately 2.0H, the head size and shape did not change significantly and the structure of the head matched the descriptions from the literature: a raised nose with a height approximately $1/8^{th}$ the head height, a head angle of approximately 45º, a mixed zone above the tail region behind the head and a tail and head of similar depth (Simpson 1997). Throughout the flow, mixing within the head region was confined to the narrow interface between the gravity current and the counter-flowing compartment fluid above. For front positions less than approximately 2.0H, billow structures were visible behind the head before they broke down into three-dimensional turbulence. However, when the front position had reached approximately 2.0H, coherent billow structures were not visible anywhere in the flow and they were instead replaced by a relatively thick band of mixing.

7.2.2 Horizontal Step Opening

A time sequence of relative concentration fields for the horizontal step opening geometry is presented in Figure 7-1 (b). After the lock gate was removed, freshwater dropped towards the lower boundary as a plume and the initial momentum gained from this vertical drop caused the freshwater fluid to rapidly spread horizontally into the compartment. This generated large amounts of mixing, so practically no undiluted freshwater entered the tail of the gravity current. At a front position of approximately 1.0H, a gravity current head had developed at the leading edge of this flow. For front positions greater than approximately 1.5H, an internal hydraulic jump was located between $0.5H < x < 1.0H$ and was believed to be caused by friction from the lower boundary slowing the fluid. The height of the head and hydraulic jump was much greater than the height of the tail immediately adjacent to the inflow. For front positions greater than approximately 2.5H, the shape of the head did not change appreciably with time and the visual depth was only slightly less than that for the full opening. For front positions greater than approximately 2.5H, the turbulent tail region was thin near the compartment opening, but thickened further into the compartment, where it was the same depth as the head. Throughout the flow, two-dimensional billow structures were not visible due to out of plane motions generated by the opening, but a thick band of mixing shed continuously off the head and indicated the presence of three-dimensional turbulence.

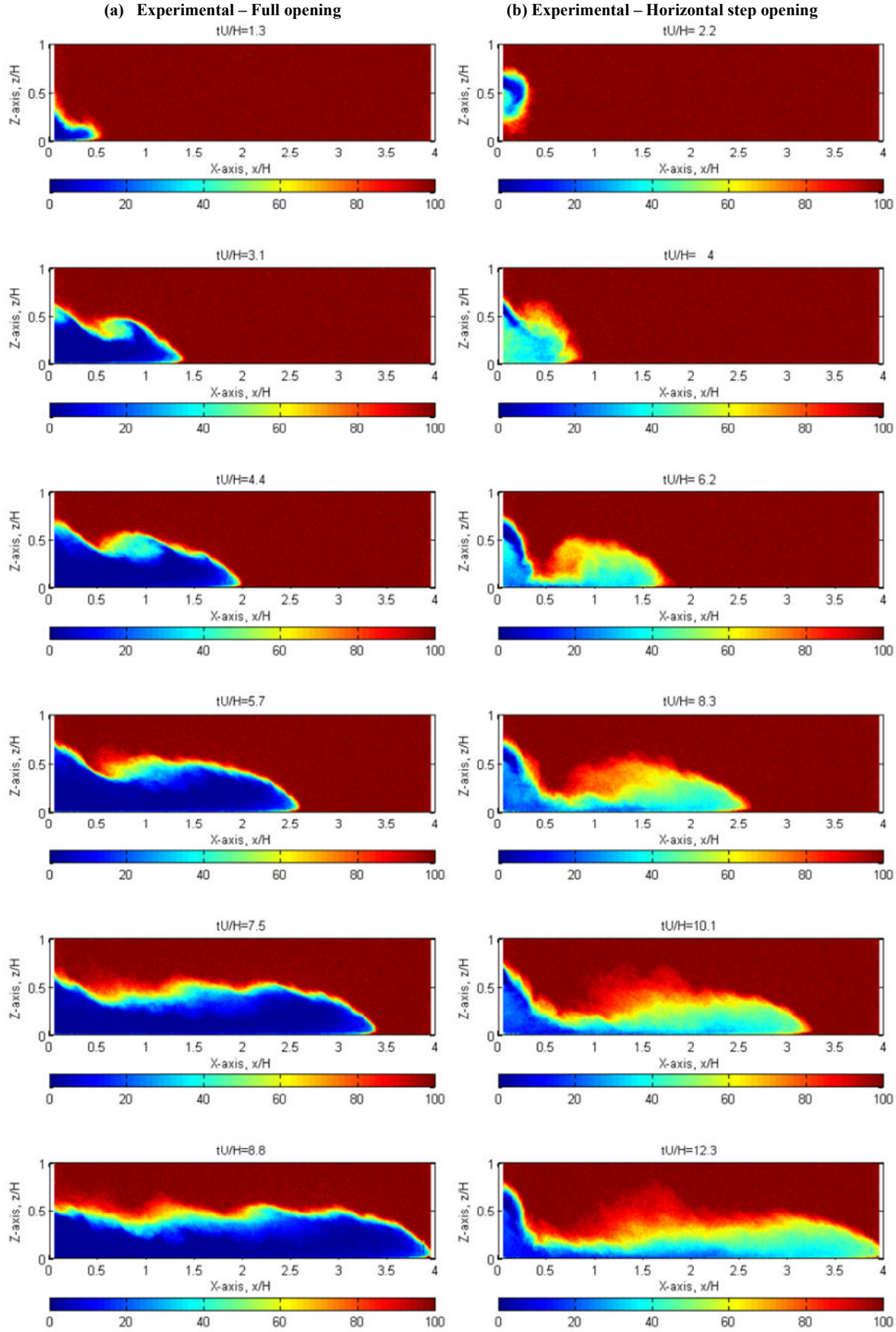

Figure 7-1: Experimental width-integrated relative concentration fields: (a) full opening geometry (b) horizontal step opening geometry. 0% indicates freshwater, 100% indicates saltwater.

7.2.3 Vertical Slot Opening

A time sequence of relative concentration fields for the vertical slot opening geometry is presented in Figure 7-2 (a). Upon removal of the lock gate, freshwater flowed into the compartment and spread laterally, causing significant mixing and dilution, but less than that observed for the horizontal step opening. A clearly defined head, with a depth elevated above the tail region which followed, became visible when the front reached approximately $1.0H$, after the flow had spread laterally and reached the compartment sidewalls. The size of the head continued to increase gradually, but did not change substantially for front positions greater than approximately $2.0H$. At all stages in the flow, the visual height of the head and the tail were significantly smaller than those generated by the full and horizontal step openings, due to a combination of a reduced opening area, which allowed less fluid to enter the compartment, and reduced turbulent mixing (when compared to the horizontal step opening). Two-dimensional billow structures were not visible at any stage, due to the out of plane motions generated by the initial lateral spreading at the start of the flow. Throughout the flow, the mixing layer in the head and tail regions extended to the lower boundary and the horizontal concentration gradients in the tail of the flow were minimal.

7.2.4 Door Opening

A time sequence of relative concentration fields for the door opening geometry is shown in Figure 7-2 (b).The time sequences of concentration fields for the door opening showed similar trends to those observed for the vertical slot opening, but the height of the gravity current flow was reduced by the reduced opening area.

7.2.5 Window Opening

A time sequence of relative concentration fields for the window opening geometry is shown in Figure 7-3. As fluid flowed through the window opening a plume formed, which was much smaller than that for the horizontal opening, because the opening area was reduced. After the plume reached the lower boundary, fluid spread laterally to the sidewalls and flowed lengthways into the compartment. Unlike the horizontal step opening, no hydraulic jump was visible adjacent to the inflow. Significantly more mixing and dilution occurred than for any of the other opening geometries and the fluid within the gravity current contained more saltwater than freshwater. For front positions greater than approximately $1.5H$, a distinctive raised head developed and was followed by a thinner tail region. The head shape and size did not change significantly for front positions greater than approximately $2.0H$.

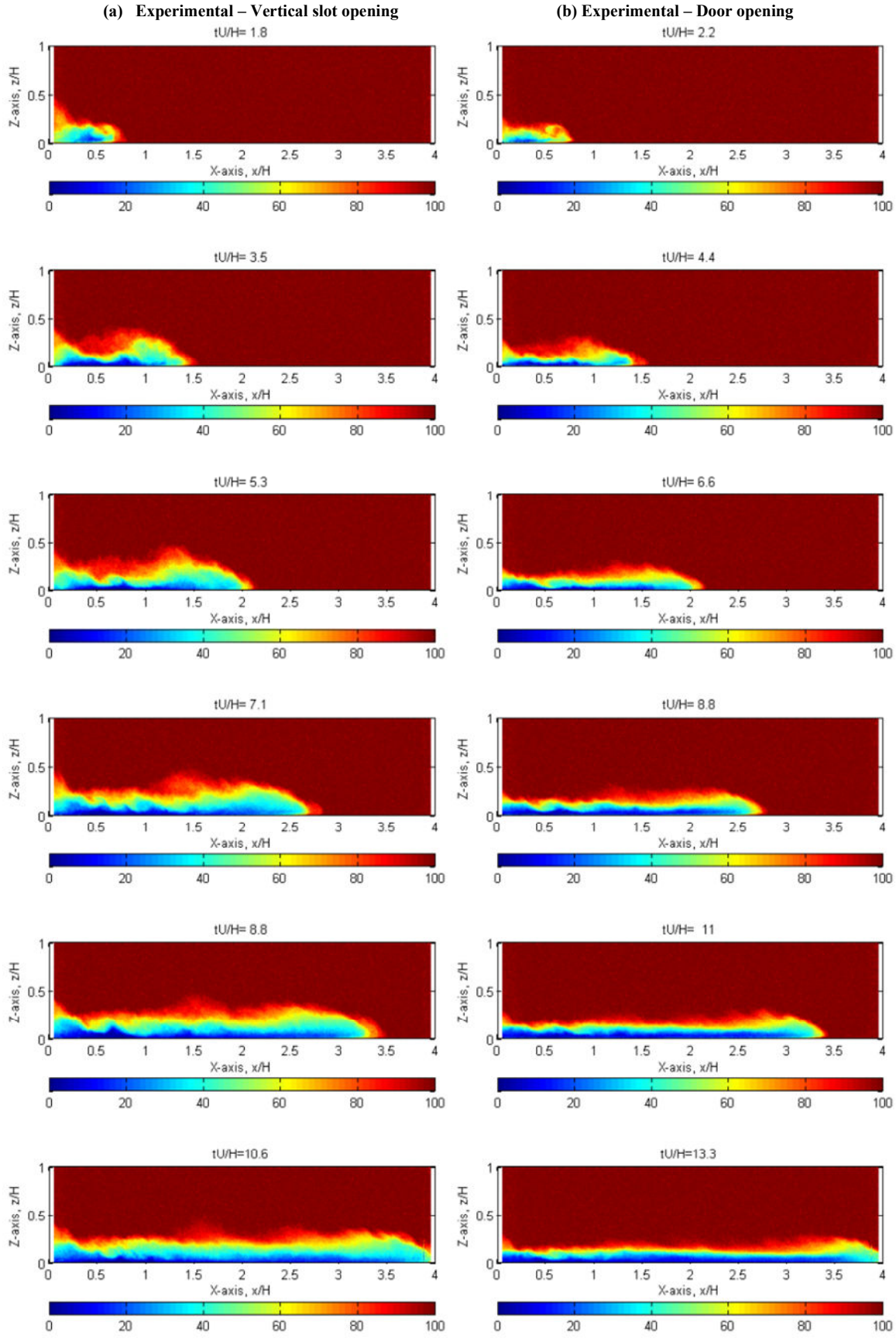

Figure 7-2: Experimental width-integrated relative concentration fields: (a) vertical slot opening geometry (b) door opening geometry. 0% indicates freshwater, 100% indicates saltwater.

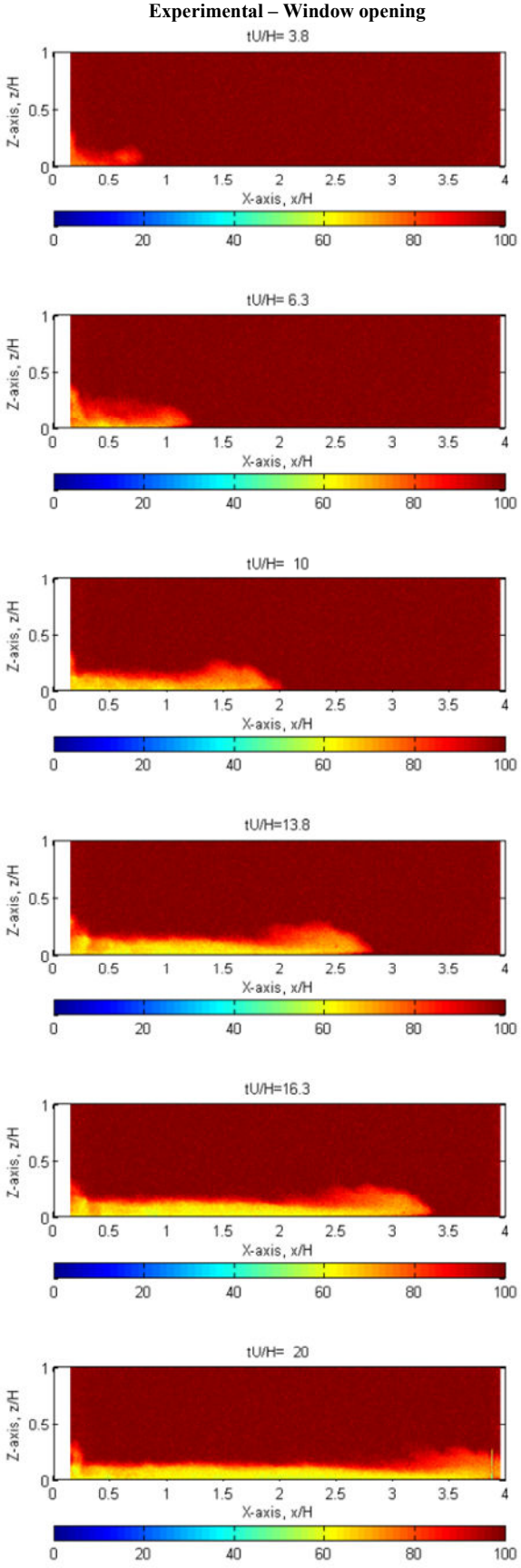

Figure 7-3: Experimental width-integrated relative concentration fields for the window opening geometry. 0% indicates freshwater, 100% indicates saltwater.

7.3 Bulk Front Characteristics

A number of bulk characteristics related to the front of the gravity current flows were investigated, including the front position, the front velocity and the head height. The front position and Froude numbers are important for backdrafts because they determine the speed of propagation of the gravity current flow, which in turn determines when flammable gases will reach ignition sources. The head of a gravity current is one of the most important features of gravity current flows and it is generally believed that the behaviour of the head will influence the entire gravity current (Ballard 2004).

To put the experimental results into context, the accuracy of the experimental technique used to generate the bulk characteristics is reviewed in Section 7.3.1 and the experimental variability of the bulk front characteristics is discussed in Section 7.3.2 (from repeated experiments with the same opening geometry). The bulk front characteristics are described for each of the opening geometries in Sections 7.3.3 to 7.3.7. Average bulk characteristics are presented and discussed in Section 7.3.8. Finally, in Section 7.3.9, comparisons are made between the results of the present study and experimental results and models from the literature.

7.3.1 Experimental Accuracy

Limitations associated with the accuracy of the experimental flow visualisation technique should be taken into account before interpreting experimental results or comparing experimental and numerical results. These limitations were described in the Experimental Methods chapter and the effects on the bulk front characteristics are summarised below. In general, these represent the maximum possible errors and occur at the edges of the flow region (where $x \sim 0.0H$ or $x \sim 4.0H$).

- The maximum error in length scales was approximately 1%.
- The maximum error in front position was approximately $0.06H$.
- The maximum error in Froude number was approximately 4%.

7.3.2 Experimental Variability

Turbulent flows are a random phenomena (Pope 2000). As the gravity currents investigated in this study are unsteady and fully turbulent, instantaneous results are not expected to be entirely repeatable and some variability is expected, but the amount of scatter should be

comparable between repeated experiments. For example, turbulent eddies and billows will form at slightly different times and locations between experimental runs. If temporal or spatial gradients are negligible, then the respective temporal or spatial averages should also be repeatable.

The experiments with full and horizontal step opening geometries were repeated, to assess the experimental variability of the bulk front characteristics. Knowing the magnitude of any inherent variability in these flows will give a benchmark on which to assess the accuracy of the numerical results. If the differences between the experimental and numerical data are similar to those between the repeated experiments, then it would suggest that the numerical model is realistically predicting the experimental flows. However, if the differences between the experimental and numerical flows are larger, it would suggest that there is some fundamental difference between the experimental and numerical flows. The bulk characteristics investigated for these repeated opening flows are presented in Figure 7-4 and discussed below.

Front Position

For both the full and horizontal step openings, a slight offset existed in the propagation of the front for the repeated experimental runs (Figure 7-4(a)). The maximum magnitude of the offset was approximately 0.5 dimensionless time units. Differences between experimental runs were larger for the horizontal step than for the full opening, due to the increased turbulence generated by the step opening.

Froude Number

For both opening geometries, the Froude number was repeatable for front positions greater than $1.0H$, but less repeatable at smaller front positions (Figure 7-4(b)). The maximum difference in Froude number between experimental runs was approximately 0.15 and occurred in the initial stages of the horizontal step opening flow. The large initial differences in the horizontal step Froude number were associated with the rapid changes of front velocity that occurred as the inflow plume reached the lower boundary and spread horizontally.

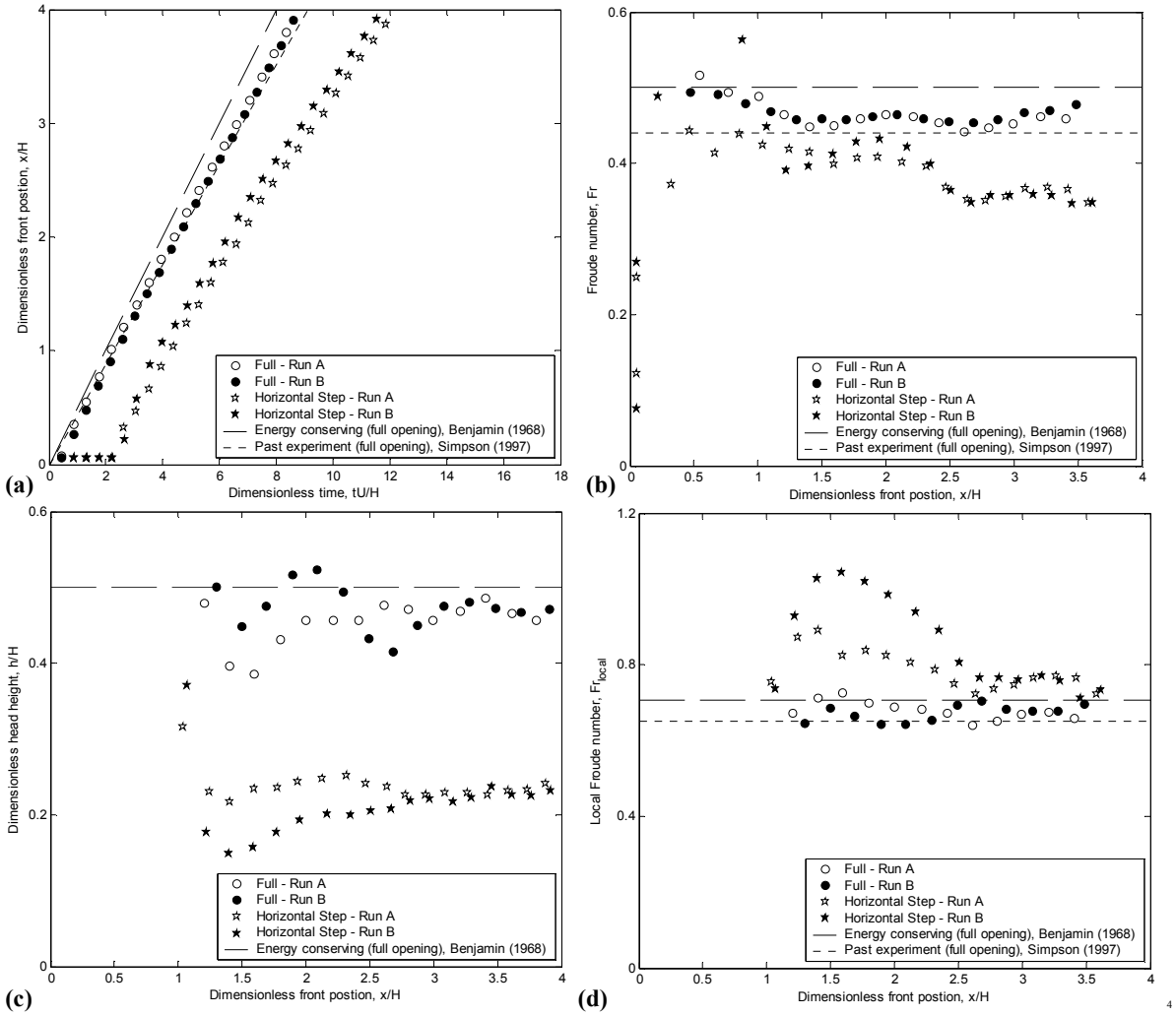

Figure 7-4: Experimental front bulk front characteristics for repeated experimental runs: (a) front position versus time, (b) Froude number versus front position, (c) head height versus front position, (d) local Froude number versus front position.

Head Height

For both opening geometries, the head height (Figure 7-4(c)) showed poor repeatability when the front position was less than 3.0H, but good repeatability at larger front positions. The maximum difference between experimental runs was approximately 0.07H. These variations were associated with the initial growth of the gravity current head. In the initial stages of flow the head was small, but it gradually increased in size with time (see Section 7.2.2).

Local Froude Number

The local Froude number (Figure 7-4(d)) exhibited the similar trends to both the head height and the Froude number, upon which it is based. The local Froude number was repeatable for

front positions greater than $3.0H$ and the maximum difference in local Froude number between experimental runs was approximately 0.22.

Average Bulk Front Characteristics

The bulk front characteristics were averaged for front positions greater than approximately $3.0H$, where they all remained relatively constant with time, see Table 7-1.

7.3.3 Full Opening

The experimental and numerical bulk front characteristics for the full opening geometry are presented in Figure 7-5. After removal of the lock gate the flow entered the constant-velocity phase (Simpson 1997), with the Froude number not changing substantially with time for front positions greater than $1.5H$. After some initial fluctuations, the head height and local Froude numbers remained reasonably constant for front positions greater than $2.5H$, with the Froude number slightly less than the energy conserving value of $Fr = 0.50$ from Benjamin (1968), but close to the experimental value of $Fr = 0.44$ from Simpson (1997). The initial variability was associated with the development of the head, which initially increased in size, but converged to a head height close to the energy conserving value of Benjamin (1968) for front positions greater than $2.0H$, as shown in Figure 7-6 (a) and (b).

Table 7-1: Average front bulk front characteristics for the repeated experimental runs.

Opening Geometry	Experimental Run	Head height $\phi = \frac{h}{H}$	Froude number Fr	Local Froude number Fr_{local}
Full	A	0.47	0.46	0.67
	B	0.46	0.46	0.68
	Difference	Less than 1%	1%	2%
Horizontal Step	A	0.23	0.36	0.75
	B	0.23	0.36	0.75
	Difference	3%	Less than 1%	less than 1%

Experimental and numerical results were similar, with variations similar to those obtained from the repeated experimental runs. Head heights and Froude numbers converged for front positions greater than approximately 3.0*H* and 1.0*H* respectively. However, for front positions less than 2.0*H*, the numerical simulation over predicted the head height with an error greater than the 0.07*H* error from the repeated experimental runs. When the numerical head heights were plotted against the results from both experimental runs (see Figure 7-7), they were slightly greater than the head heights for Run B. Therefore, the numerical and experimental bulk front characteristics were found to be in close agreement, with errors similar to those from the repeated experimental runs.

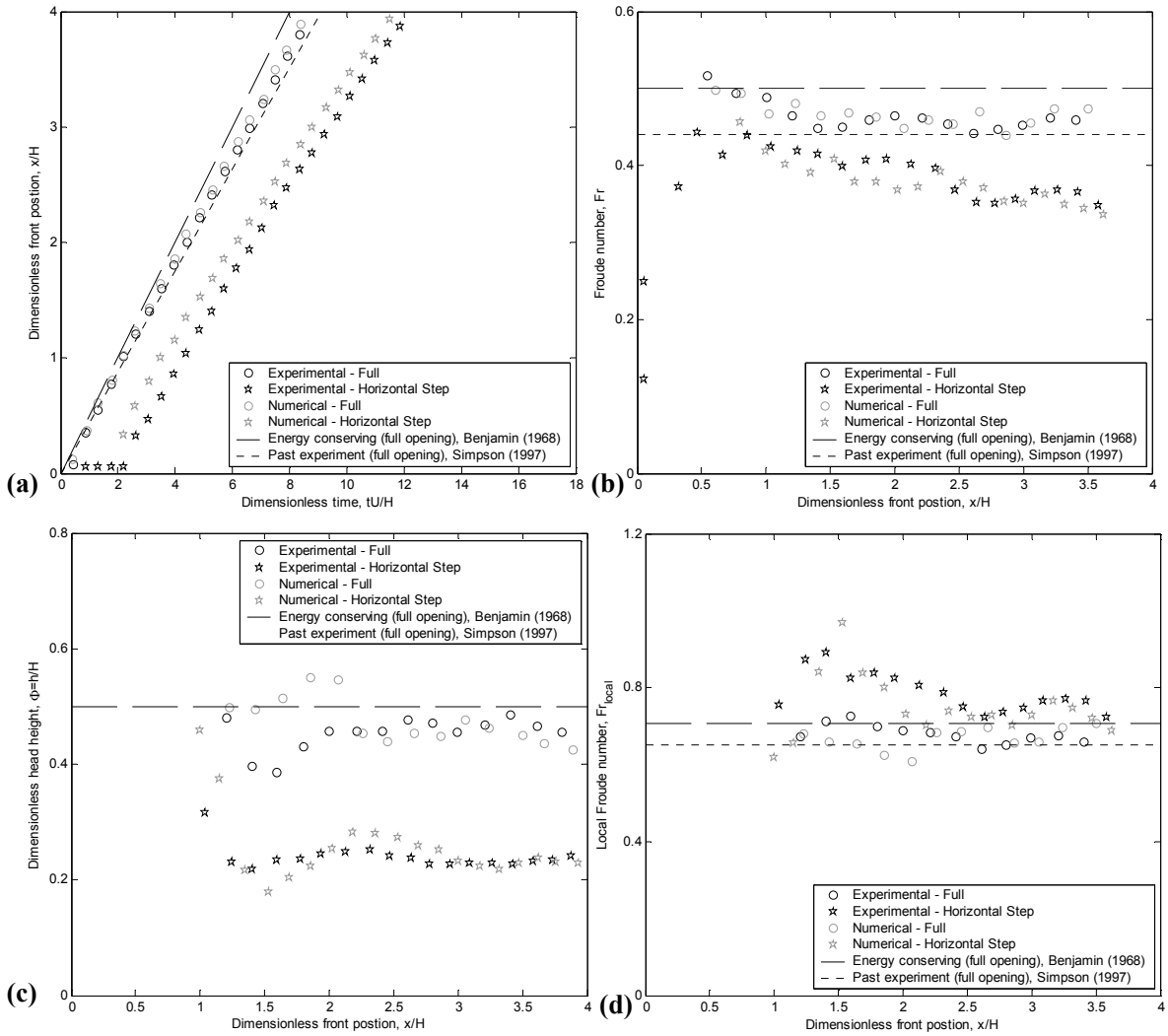

Figure 7-5: Bulk front characteristics for full and horizontal step opening geometries: (a) distance versus time, (b) head height versus front position, (c) Froude number versus front position, (d) local Froude number versus front position.

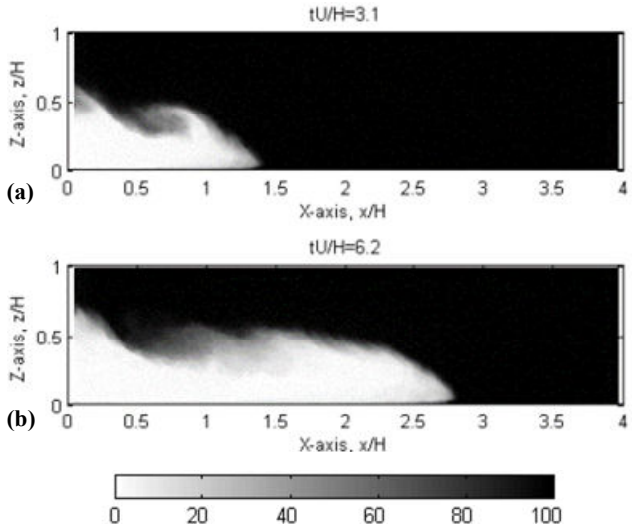

Figure 7-6: Experimental width-integrated relative concentration fields for the full opening geometry at different times.

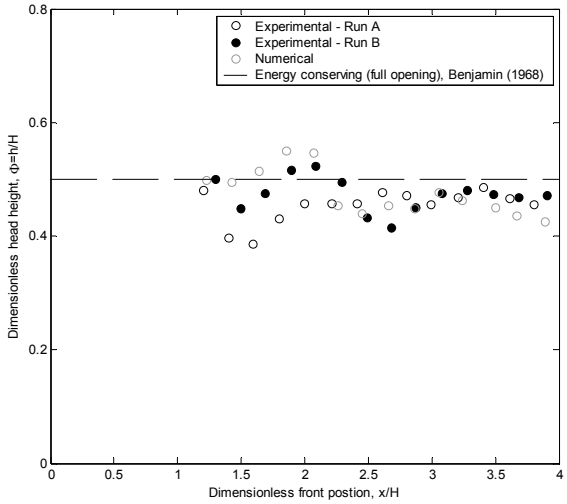

Figure 7-7: Experimental and numerical head height versus front position for the full opening.

7.3.4 Horizontal Step Opening

The bulk front characteristics for the horizontal step opening are presented in Figure 7-5. The flow took approximately two dimensionless time units to drop to the lower boundary and begin spreading horizontally into the compartment, which explains the initial delay in front propagation. The head height initially grew in size, reaching a peak at approximately 2.2*H*, before decreasing as the head flattened and widened, as seen in Figure 7-8 (a) and (b).

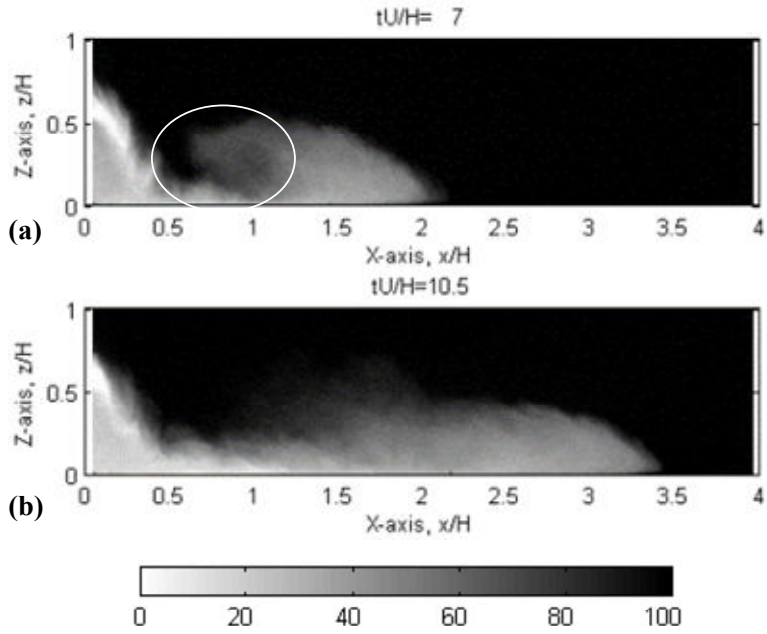

Figure 7-8: Experimental width-integrated relative concentration fields for the horizontal step opening geometry at different front positions. (a) momentum driven flow, (b) buoyancy driven flow.

The initial Froude number for the flow was approximately 0.4, but at a front position of approximately 2.5*H*, there was an abrupt reduction to a Froude number of approximately 0.36. For front positions greater than approximately 2.5*H*, temporal changes in the Froude and local Froude numbers were insignificant. The decrease in Froude number was attributed to a transition from a momentum driven flow to one driven by buoyancy. As the flow dropped over the horizontal step it formed a plume and formed a super-critical flow at the lower boundary, but as the front continued to propagate away from the opening, friction and turbulence slowed the front causing a hydraulic jump adjacent to the inflow. This hydraulic jump is circled Figure 7-8 (a). At a front position of approximately 2.5*H*, dissipation of this initial momentum resulted in a transition to a flow driven by buoyancy forces (from the density differences between the gravity current and compartment fluids).

For front positions greater than approximately 3.0*H* and 2.5*H* respectively, the experimental and numerical head heights and Froude numbers converged. However, in the initial stages of the flow, the offsets between the experimental and numerical front positions were larger than the offsets from the repeated experiments. The numerical front positions are plotted against the results from both of the repeated experiments, in Figure 7-9. The numerical front position was found to diverge from the results of both experimental runs for dimensionless times in the

range $2 < t^* < 6$, but match the experimental front position for Run B at larger times. Over the same period, front positions from both experimental runs were consistent. This indicates that the numerical simulation over predicted the speed of establishment of the gravity current head.

7.3.5 Vertical Slot Opening

The bulk front characteristics for the vertical slot opening are presented in Figure 7-10. The initial Froude and local Froude numbers were high, as the undiluted freshwater flowed into the compartment, but reduced with the velocity (for front positions less than 2.0*H*), as the flow spread laterally and reached the compartment side walls. The initial decrease in velocity occurred because the flow was spread out over a larger width, three times wider than the original opening. Over the same period as the velocity decreased, the head height showed an initial growth phase. For front positions greater than 2.0*H*, the head height did not change appreciably with time, but the Froude and local Froude numbers continued to fluctuate significantly.

A comparison of the experimental and numerical results showed that they varied significantly in the initial stages of the flow, but converged later in the flow. The heat heights were similar for front positions greater than 2.5*H* and the experimental and numerical Froude and local Froude numbers were essentially the same for front positions greater than approximately 3.0*H*.

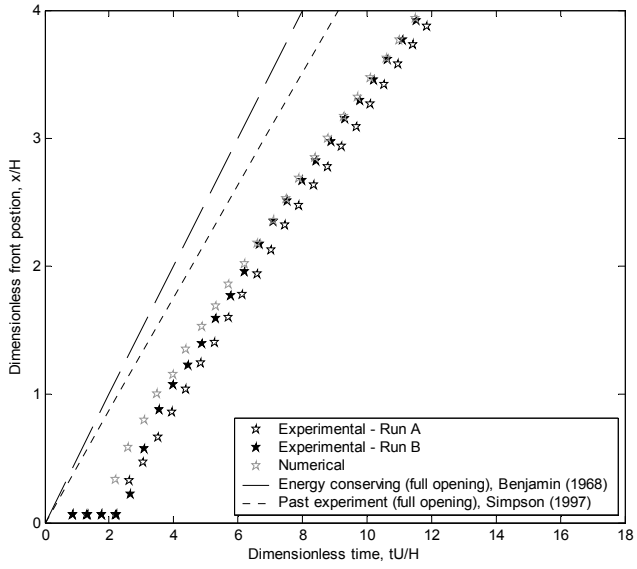

Figure 7-9: Experimental and numerical distance versus time plot for the horizontal step opening.

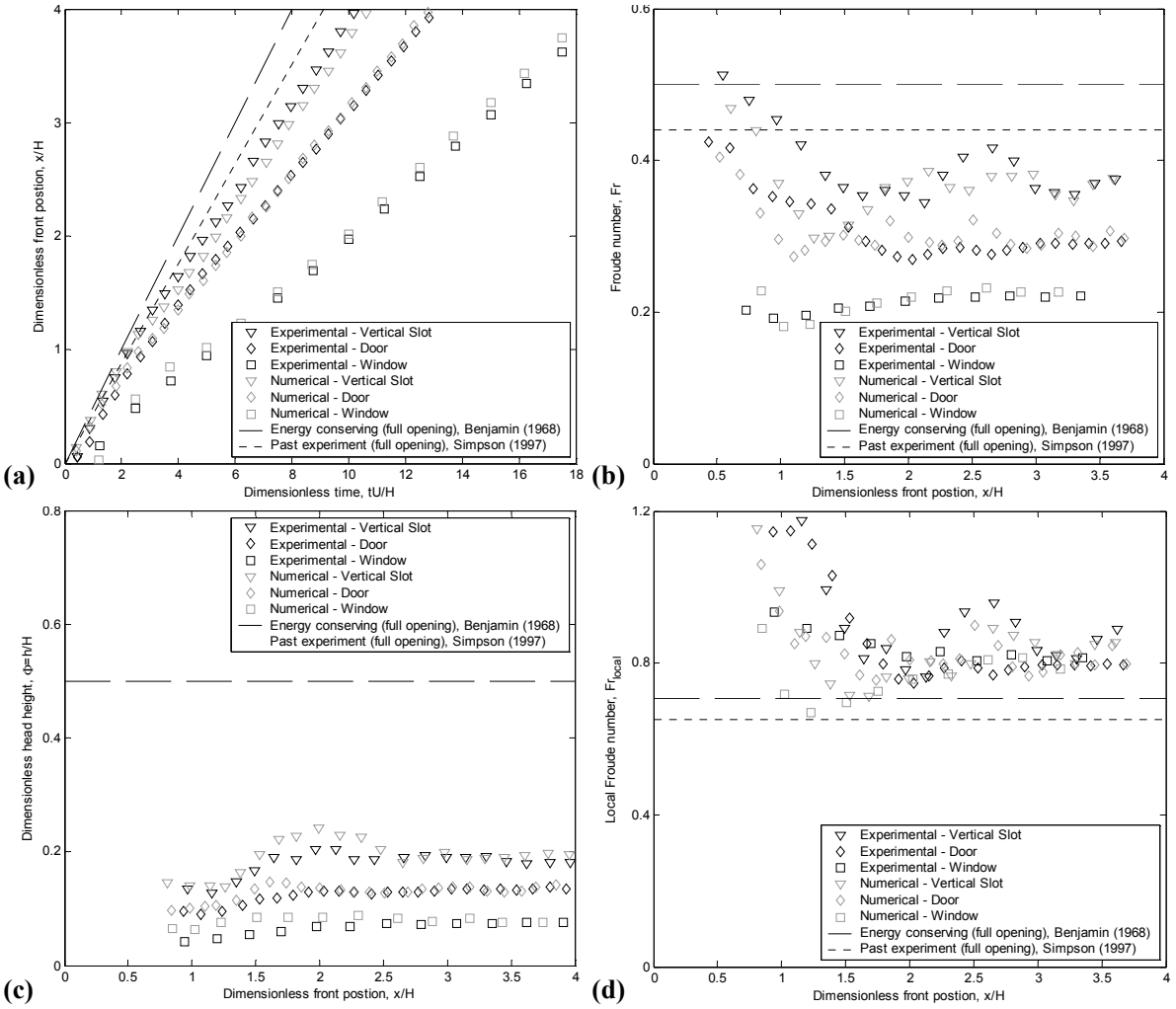

Figure 7-10: Bulk front characteristics for vertical slot, door and window opening geometries: (a) distance versus time, (b) head height versus front position, (c) Froude number versus front position, (d) local Froude number versus front position.

7.3.6 Door Opening

The bulk front characteristics for the door opening exhibited similar trends to those from the vertical slot opening and are also presented in Figure 7-10. However, the magnitudes of the bulk characteristics were reduced, due to the decreased area of the door opening. The reduced opening area reduced the flow of freshwater through the opening, which reduced the head height, as shown in Figure 7-11. This in turn reduced resulting buoyancy forces and therefore reduced the velocity of the front of the flow. The head heights and Froude numbers did not change significantly for front positions greater than 2.0*H* and 3.0*H* respectively, which also corresponded to the convergence of the experimental and numerical results.

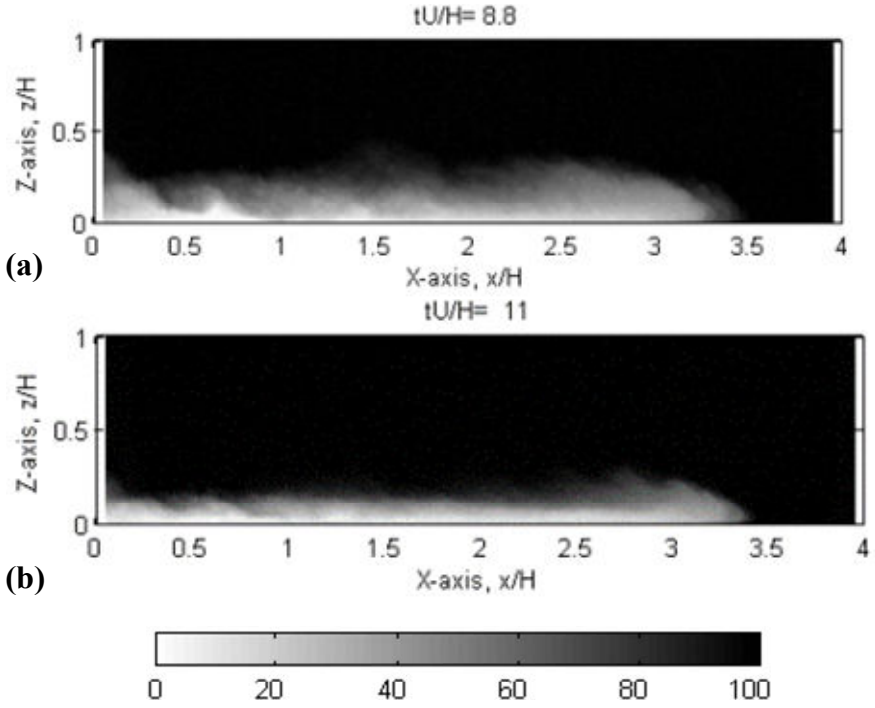

Figure 7-11: Experimental width-integrated relative concentration fields for different openings geometries: (a) vertical slot, (b) door.

7.3.7 Window Opening

The bulk front characteristics for the window opening are also presented in Figure 7-10. The gravity current had relatively constant Froude and local Froude numbers for front positions greater than 2.0*H*. The head height initially increased slightly, but remained relatively constant for front positions greater than 2.5*H*. The Froude and local Froude numbers had smaller magnitude fluctuations than the Froude and local Froude numbers from the vertical slot and door openings.

No hydraulic jump was evident adjacent to the opening and no transition from a momentum driven flow to a buoyancy driven flow was observed. This indicated that the momentum initially gained from the plume was rapidly dissipated through turbulence as the flow spread laterally to the compartment side walls.

The experimental and numerical head heights and Froude numbers were relatively consistent front positions greater than approximately 2.5*H* and 1.5*H* respectively.

7.3.8 Average Bulk Front Characteristics

In general, the bulk front characteristics for all opening geometries did not change significantly with time for front positions greater than approximately $x = 3.0H$, therefore the bulk characteristics were averaged over this period, as shown in Table 7-2. The exceptions were the Froude and local Froude numbers from the vertical slot opening, which continued to fluctuate (see Section 7.3.5). However, they were also averaged to allow a comparison with the other opening geometries. A number of trends were apparent in the average bulk front characteristics data and are discussed below.

In general, Froude numbers were dependent on the area of the opening geometry. Therefore, the length of the delay between ventilation and ignition of backdrafts depends not only on the location of the ignition source and initial compartment temperature, but also on the opening geometry. The larger opening geometries tended to produce faster gravity currents, because they allowed more freshwater to flow into the compartment, creating larger buoyancy forces to drive the flow.

Table 7-2: Summary of the average experimental and numerical bulk front characteristics: EXP - indicates experimental results, FDS – indicates numerical results.

Opening Geometry	Density Difference β	Head height $\phi = \frac{h}{H}$		Froude number Fr		Local Froude number Fr_{local}		Local Reynolds number Re_{local}	
		EXP	FDS	EXP	FDS	EXP	FDS	EXP	FDS
Full	0.0050	0.47	0.45	0.46	0.46	0.67	0.68	6220	5970
Horizontal Step	0.0050	0.23	0.23	0.36	0.35	0.75	0.73	2330	2320
Vertical Slot	0.0050	0.19	0.19	0.37	0.37	0.86	0.86	2020	2000
Door	0.0050	0.13	0.14	0.29	0.30	0.79	0.81	1040	1100
Window	0.0400	0.07	0.08	0.22	0.23	0.79	0.82	1220	1490

The average local Froude numbers, which use head height as a length scale, were similar for all opening geometries, ranging from $0.67 < Fr_{local} < 0.87$. As discussed in Section 7.3.9, when the local Froude number was plotted against heat height, all points collapsed onto a single curve, which indicated that the local buoyancy conditions at the head of gravity currents were driving the flow.

The head heights were opening geometry dependent, with the larger area openings generating larger head heights. This occurred because larger openings allowed more fluid to flow into the compartment as discussed in Section 7.4.

The percentage differences between the experimental and numerical bulk front characteristics are presented in Table 7-3. The percentage differences for the full and horizontal step openings were similar to those from the repeated experimental runs (see Table 7-1), which indicates that the numerical simulations from FDS successfully replicated the average bulk characteristics of these flows.

The numerical simulation for the window opening had errors of approximately 8% in both the head height and Froude number, which were significantly larger than the corresponding errors associated with the other opening geometries. It is likely that these errors were, at least partially, associated with the reduced scale of the gravity current flows generated by the window opening. Compared to the other flows, the window opening gravity currents travelled slower and were smaller, which meant similar magnitude errors would result in slightly larger percentage errors. In addition, in the numerical simulations for the window opening, fewer grid cells were available to resolve the flow than for an equivalent larger scale flow, which effectively reduced the grid resolution of the window opening geometry simulations.

Table 7-3: Percentage differences between experimental and numerical bulk front characteristics (relative to experimental results) for different opening geometries.

Opening Geometry	Head height $\phi = \frac{h}{H}$	Froude number Fr	Local Froude number Fr_{local}
Full	-3%	less than 1%	1%
Horizontal Step	less than 1%	-2%	-2%
Vertical Slot	3%	less than 1%	-1%
Door	2%	3%	3%
Window	8%	8%	3%

7.3.9 Comparison to Literature

This section compares the average bulk front characteristics to the results of past experiments and also to theoretical models in the literature.

The average Froude number for the full opening, $Fr = 0.46$, was lower than the energy conserving value of $Fr = 0.5$ from Benjamin (1968), but slightly higher than the experimental value of $Fr = 0.44$ from Simpson (1997) and Fleischmann (1994). The average Froude number for the window opening was $Fr = 0.22$, which is in agreement with the Froude number of $Fr = 0.22$ obtained by Fleischmann (1994) for the same opening geometry.

The average head heights for the full and window openings were $\Phi = 0.47$ and $\Phi = 0.07$ respectively. These values were lower than the corresponding experimental results of Fleischmann (1994), who reported $\Phi = 0.50$ for the full opening and $\Phi = 0.29$ for the window opening.

The reason for the discrepancy in head heights between the present study and past research was the difference in definition of head height. The definition of the head height in the present study follows the work of Marino et al. (2005) and was based on the equivalent height of the gravity current, assuming no mixing and a top hat concentration/density profile to conserve buoyancy. The head height was measured as the deepest section of the equivalent height profile in the head of the flow. Typically, in the past, the head height has either been determined visually, by looking at the extent of the dye, or by selection of a representative concentration/density contour. For flows with little internal mixing (like the full opening),

head heights based on the equivalent height profile and visual inspection will be similar, but for flows with significant levels of internal mixing and dilution (such as those generated by the window opening geometry), the equivalent height measurement will be much smaller than that obtained from visual inspection.

The models discussed below were either developed from simple lock release flows, without three dimensional openings or vertical drops to promote mixing, or were developed empirically and disregarded internal mixing. Past researchers have measured the height of the flow in a variety of locations. The model proposed by Shin et al (2004) is not comparable to the present study because it uses a different length scale. The models of Huppert and Simpson (1980) and Rottman and Simpson (1983), define the flow depth in the tail region "just behind the head". In the constant velocity phase, the head region of simple lock release flows consists mainly of unmixed fluid, with a thin mixing layer located above (see Figure 7-1 (a)). Ungarish and Zemach (2005) define the head height through the deepest part of the head of the flow, which is consistent with the present study. Therefore, the equivalent head heights determined in this study are comparable.

The average local Froude numbers and head heights for the different openings were compared to models from the literature (Benjamin 1968; Huppert and Simpson 1980; Rottman and Simpson 1983; Ungarish and Zemach 2005), as shown in Figure 7-12. The best fit occurs with the model of Ungarish and Zemach (2005), which was semi-empirical and represented a compromise between existing models and experimental observations and has been reproduced in Equation (7-1) below. The general trend is an almost linear decrease in local Froude number as the corresponding equivalent head height is increased. The numerical and experimental values from the present study are also in close agreement. It should be noted that the results for the vertical slot opening were still fluctuating, but were included for comparison (see Section 7.3.5).

$$Fr_{UZ} = (1+3\phi)^{-1/2} \tag{7-1}$$

where: $Fr_{UZ} =$ local Froude number proposed by Ungarish and Zemach (2005)

$\phi =$ dimensionless head height

The fact that the local Froude numbers and head heights for the significantly different opening geometries collapse onto a single curve indicates that, once the flows propagated away from the opening (and reached a front position of approximately 3.0H), the local Froude number, and therefore also the front velocity, of the gravity current head was governed directly by the local buoyancy conditions. The initial conditions, opening geometry and any initial lateral spreading or vertical drops only influence the local Froude number of the flow indirectly, as they affect mixing in the flow which in turn influences the local buoyancy conditions at the gravity current head. This result highlights the relevance of defining the gravity current head height based on conservation of buoyancy (βgh) and the equivalent flow depth.

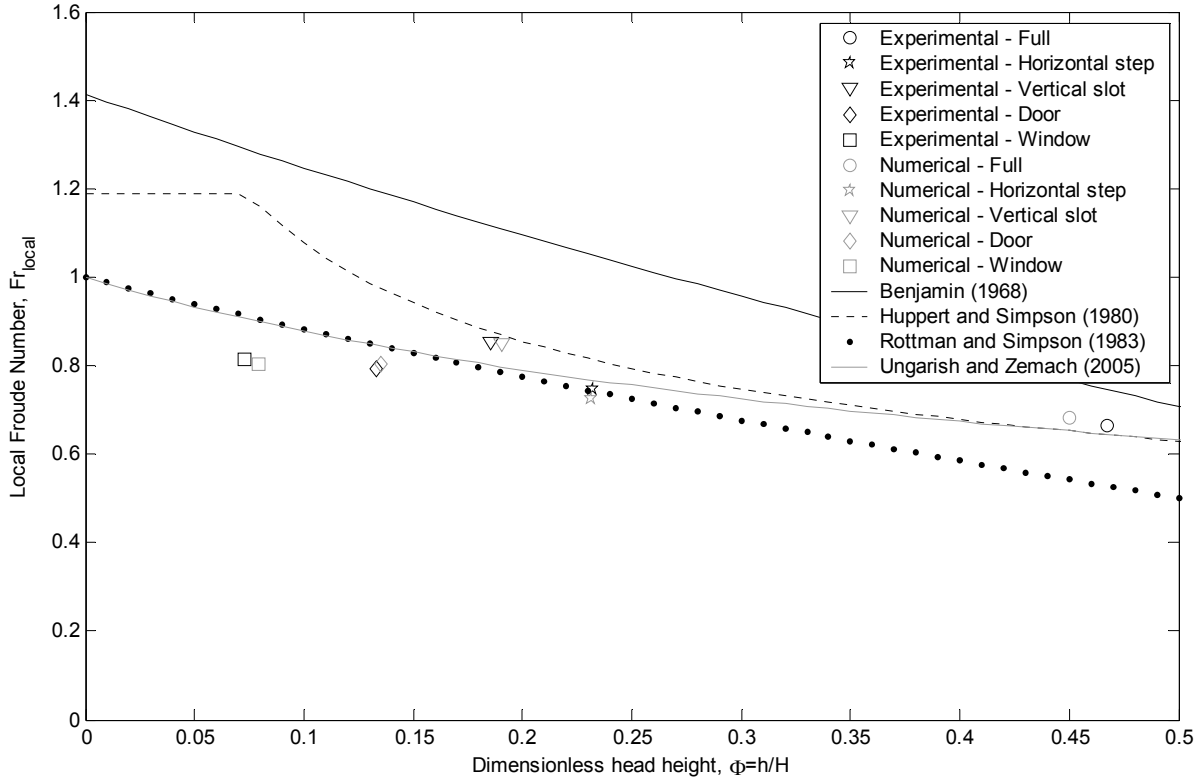

Figure 7-12: Average experimental and numerical local Froude numbers and head heights.

7.4 Mass Flux

The mass flow-rates (fluxes) were investigated both through the compartment openings and within the gravity current. In Section 7.4.1, the numerical mass fluxes through the compartment openings are compared with empirical correlations from literature. The ratios of the mass fluxes through the compartment openings and the within the head of the gravity currents are calculated and discussed in Section 7.4.2.

7.4.1 Compartment Opening Mass Flux

The compartment opening mass flux was investigated for the numerical simulations. Corresponding experimental values were not measured in the present study and so comparison of the numerical mass fluxes was made to an empirical value from literature. These mass fluxes are important in backdraft gravity currents because they determine the rate at which fluid from outside the compartment (required to create flammable mixtures and drive the gravity current flow) is supplied to the gravity current. The discharge coefficient, or dimensionless flow-rate, accounts for streamline contraction through openings and was calculated from Equation (7-2) (Brown and Solvason 1962; Linden 1999). This discharge coefficient assumes a steady mass flow-rate. The discharge coefficient was plotted against time for each of the compartment opening geometries, as shown in Figure 7-13.

$$C_Q = \frac{Q_{mass}}{\Delta\rho \frac{1}{3} A \left(\beta_{initial} g H_o\right)^{\frac{1}{2}}} \tag{7-2}$$

where: C_Q = dimensionless inflow or discharge coefficient

Q_{mass} = mass inflow rate (mass flux)

A = area of rectangular compartment opening

H_o = compartment opening height

$\beta_{initial} g = g'$ = reduced gravity

$\Delta\rho$ = density difference

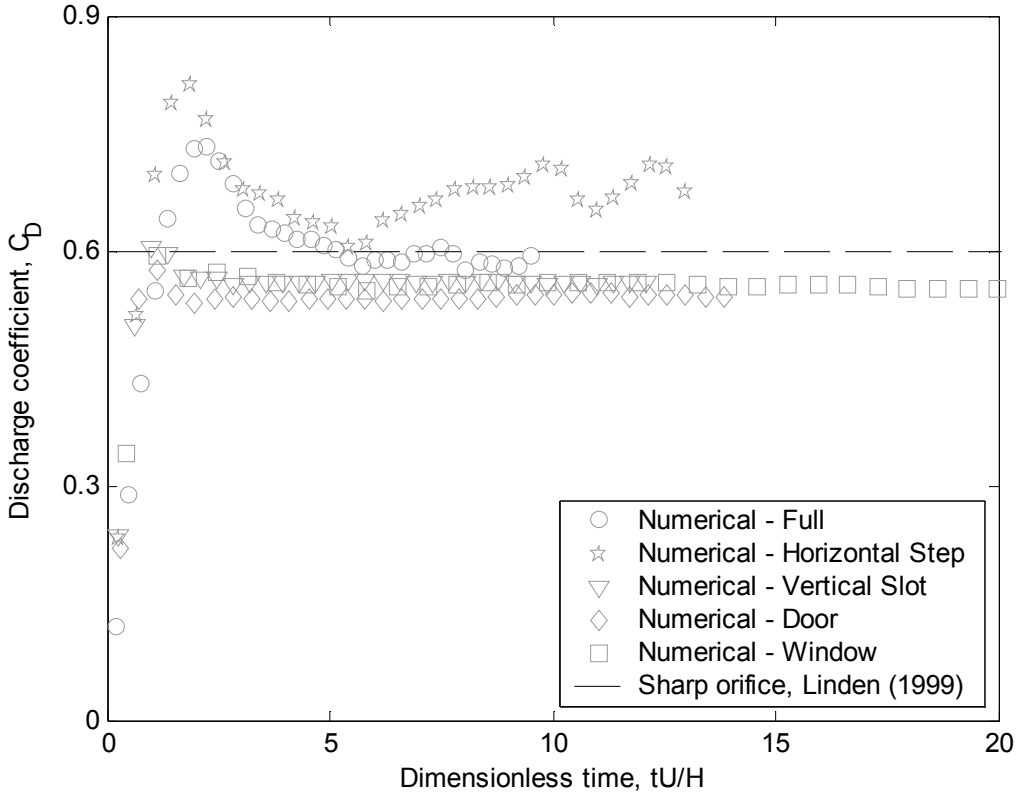

Figure 7-13: Plot of numerical discharge coefficient versus time for different opening geometries.

The fluctuations in the discharge coefficient were greatest for the horizontal step opening. Analysis of the concentration fields showed these fluctuations were associated with billows shedding periodically off the interface between the inflowing and out-flowing fluids and being carried through the compartment opening. A typical billow structure is shown in the two-dimensional relative concentration field in Figure 7-14, and corresponds to the fluctuation in the discharge coefficient in Figure 7-13 at a time of approximately $t^* = 11$. A longer period of flow would need to be analysed to determine whether the inflow for the horizontal step opening would reach a steady state. For the other opening geometries, these billows formed within the compartment, and so had a less significant influence on the compartment opening mass flux.

After initially fluctuating, the discharge coefficients for the other opening geometries (full, vertical slot, door and window) reached a steady state, which indicates that they supply a constant flux of fluid into the tail of the gravity current. In a backdraft situation this would correspond to a constant supply of oxygen to the compartment. The average discharge coefficients are presented in Table 7-4 and are relatively independent of opening geometry

and similar to the value of $C_Q = 0.60$, suggested by Linden (1999) for sharp edged orifices. For comparison, the horizontal step discharge coefficients, which did not reach a steady state, were also averaged for times greater than $t^* = 8$.

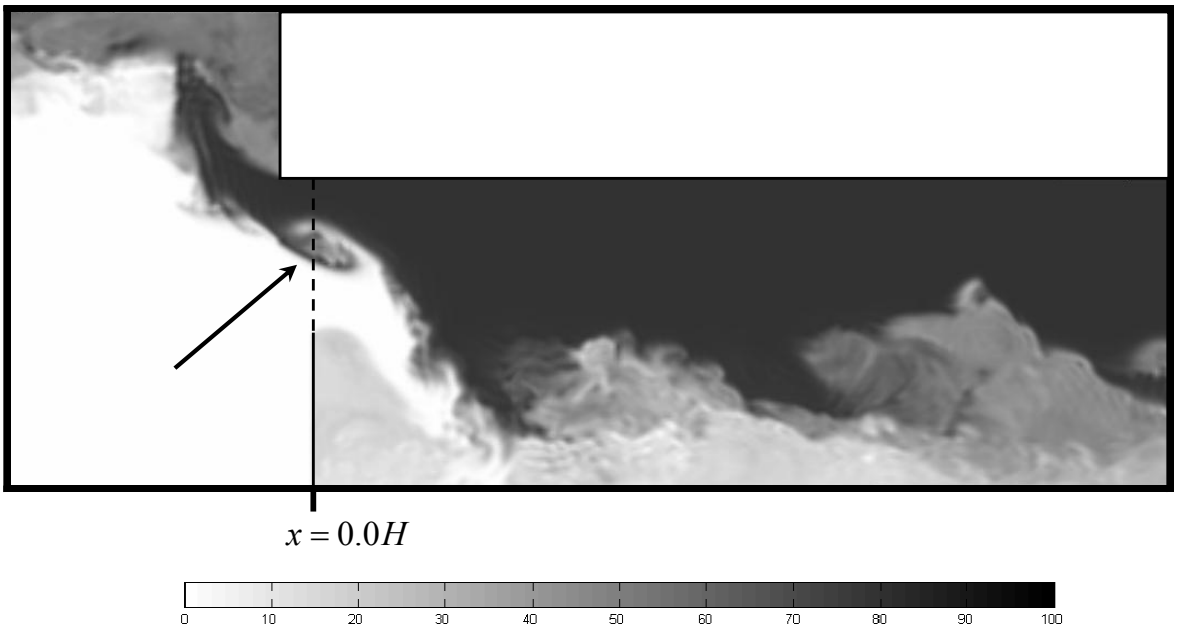

Figure 7-14: Numerical two-dimensional relative concentration field from mid-width for horizontal step opening geometry at time $t^* = 11$. Dashed line indicates opening and arrow indicates the location of a billow forming within the opening.

Table 7-4: Average numerical discharge coefficients for different opening geometries.

Opening Geometry	**Full**	**Horizontal Step**	**Vertical Slot**	**Door**	**Window**
Average Discharge Coefficient	0.59	0.68	0.56	0.54	0.55

7.4.2 Gravity Current Mass Flux

The gravity current head heights were found to be strongly opening geometry dependent, with the larger area openings generating larger head heights, as outlined in Section 7.3.8. To further investigate the correlation between opening geometry and head height, the ratio between mass flux through the compartment opening was compared to the mass flux at the head of the gravity current.

As discussed in Section 7.4.1, the steady state mass flux through a rectangular compartment opening may be calculated from Equation (7-2) (Brown and Solvason 1962; Linden 1999).

The gravity current front was assumed to flow along the compartment boundary as a two-dimensional slug of fluid with no internal mixing and no raised head. The height of the flow was based on the head height, which is calculated from the equivalent depth of unmixed fluid to conserve buoyancy. The mass flux of the gravity current head was approximated from the average head height, compartment width, average front velocity and initial density difference, as shown in Equation (7-3) below. This equation can be expanded to include the non-dimensional parameters for head height and velocity, as shown in Equation (7-4). The definitions of the relevant compartment opening and compartment dimensions are shown schematically in Figure 7-15 below.

$$Q_{mass(gc)} = hWu\Delta\rho \tag{7-3}$$

$$Q_{mass(gc)} = \Phi(HW)Fr\sqrt{\beta_{initial}gh}\Delta\rho \tag{7-4}$$

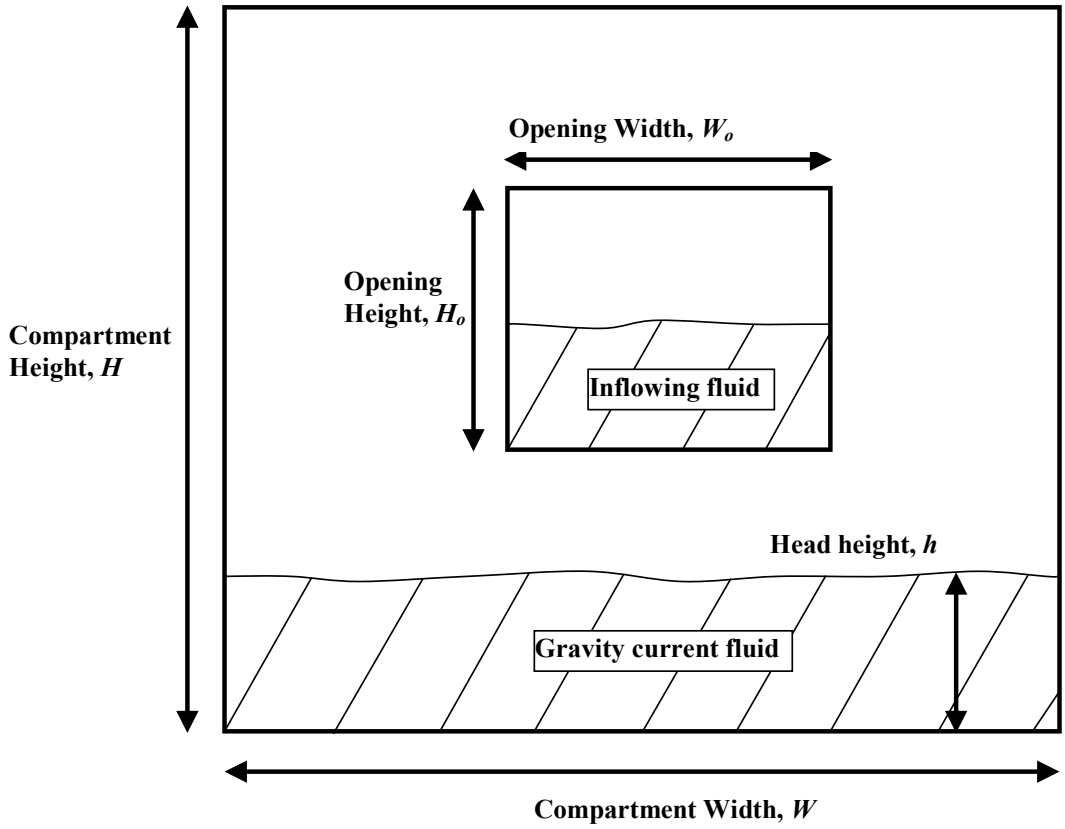

Figure 7-15: Schematic of the end elevation of the compartment with a window opening and fluid moving as a slug of fluid with no internal mixing.

The ratio of the mass flux in the gravity current to the mass flux through the compartment opening can be calculated as shown in Equation (7-5). The dimensionless equation shows a dependence on the area of the opening, with larger openings allowing more fluid to flow into the compartment, and an inverse square root dependence on the height of the compartment openings, which is due to the square root relationship in the buoyancy terms used to generate the ratio. The flux ratio is also dependent on the dimensionless heat height, Froude number of the gravity current head and the dimensionless discharge coefficient at the compartment opening inflow.

$$\frac{Q_{mass(gc)}}{Q_{mass}} = \frac{3\Phi Fr}{C_Q}\sqrt{\frac{H}{H_o}}\frac{HW}{H_oW_o} \tag{7-5}$$

As the flow is assumed to be incompressible, approximately steady state and have no sources or sinks, the flow into the compartment opening should be approximately equal to the flow at the gravity current head, so the flux ratio is expected to be approximately equal to 1.0.

The actual values of the flux ratio are shown in Table 7-5 for both the numerical and experimental flows. These flux ratios were based on the average gravity current conditions (discussed in Section 7.3.8) and the empirical value for the discharge coefficient of sharp edged orifices, $C_Q = 0.60$ (Linden 1999).

The flux ratios for both the experimental and numerical results for all openings were greater than 1.0. From an initial inspection this would appear to suggest that the flow of dense fluid in the gravity current head was greater than the flow of dense fluid into the compartment. However, an assumption used to generate the flux ratios was that the gravity current moved as a slug of fluid, whereas in reality some of the dense fluid from the nose either formed into billows that rolled up and broke off the head or was slowed by friction at the lower boundary and entrained below the nose. Therefore some of the fluid which was included in the equivalent head height measurement would have been advancing along the compartment at a lower velocity than the gravity current head and therefore the mass flux would have been slightly overestimated by Equation (7-3), which explains why the flux ratios were greater than 1.0.

The horizontal step and window opening geometries had flux ratios that were significantly higher than the other opening geometries. This is believed to be associated with the increased level of mixing and turbulence generated as the flows dropped vertically through the openings. This mixing in turn caused a larger fraction of the gravity current fluid to form as billows at the head of the gravity current. This phenomenon was apparent from the pronounced raised heads at the front of the gravity currents for the horizontal step and window openings, which were not evident for the other opening geometries (see Figure 7-1, Figure 7-2 and Figure 7-3).

The experimental and numerical flux ratios were generally consistent, except for the window opening geometry, which showed significantly more variation than the other opening geometries (differences in flux ratio of approximately 0.2 compared to 0.06 or less for the other opening geometries). The differences associated with the experimental and numerical results for the window opening geometry are discussed in detail in Section 7.3.8.

Table 7-5: Ratio of mass flux at the gravity current head to mass flux at compartment opening for different opening geometries.

	Opening Geometry				
	Full	**Horizontal Step**	**Vertical Slot**	**Door**	**Window**
Experimental	1.08	1.17	1.05	1.06	1.22
Numerical	1.04	1.14	1.05	1.12	1.42

7.5 Internal Concentration Structure

The internal concentration structure of the gravity current flows was investigated. The concentration structure is a measure of the extent of mixing and may be used to determine the location of flammable mixtures within backdraft gravity currents.

In Section 7.5.1, the accuracy of the experimental techniques used to determine the internal concentration structure is summarised. Section 7.5.2 outlines the experimental variability of the internal concentration structure (from repeated experiments with the same opening geometry). The across channel two-dimensionality of the gravity current flows is investigated in Section 7.5.3. The internal concentration fields are described in Section 7.5.4 and concentration profiles are compared in Section 7.5.5. Finally, Section 7.5.6 determines the flow regions that represent flammable gas mixtures in backdraft gravity currents.

7.5.1 Experimental Accuracy

Limitations associated with the experimental flow visualisation technique should be considered when interpreting the experimental results and when comparing them to numerical results. These limitations were described in the Experimental Methods chapter and the effects on the width integrated relative concentration field are summarised below.

- The maximum error in length scale was approximately 1%.
- Concentration interfaces were "smeared" out, by parallax, over a maximum width of approximately 0.16H. The error was greatest at the extremes of the flow region ($x \sim 0.0H$ or $x \sim 4.0H$) and zero at $x = 2.0H$.
- The maximum random error in relative concentration was approximately $R = 6\%$ and was caused by the lighting system.
- The maximum relative concentration error associated with assumed relationship between light attenuation and dye concentration was approximately $R = 5\%$.

7.5.2 Experimental Variability

Variability was inherent in the experimental flows, due to their turbulent nature and any slight variations in the initial conditions. To determine the variability of the internal concentrations, results from repeated experiments were compared. This provided a benchmark from which to compare the experimental and numerical results. For clarity, only the results from experimental Run A were compared to the numerical results later in Section 7.5.

Concentration Fields

The magnitude of the differences between time-sequences of width-averaged relative concentration fields for the repeated experimental flows are plotted in Figure 7-16 (the differences are represented by shaded regions). The magnitude of the differences varied throughout the flow field, with the largest differences near the inflow and at the nose of the flows. The differences at the nose were associated with offsets in the front position between experimental runs, which were identified in Section 7.3.2, and the unsteady formation of lobes and clefts. The variability throughout the body of the gravity currents were of more significance and were associated with the turbulent nature of the flow. These differences are probably associated with billows forming at slightly different times and locations in repeated experimental runs. For the full opening, the differences were largely located at the mid-depth of the compartment, but the differences for the horizontal step opening were randomly distributed throughout the body of the flow, due to the increased turbulent mixing.

Concentration Profiles

Vertical concentration profiles were generated for the head and tail of the flow (as outlined in Section 7.5.5) and are presented in Figure 7-17 (a) and (b) respectively. For both opening geometries, the repeated concentration profiles through the head of the flow were nearly identical. However, the repeated profiles through the tail of the flow showed significant variations. The larger differences in the tail of the flows were probably associated with the turbulent eddies shedding from the gravity current head at different times in repeated runs.

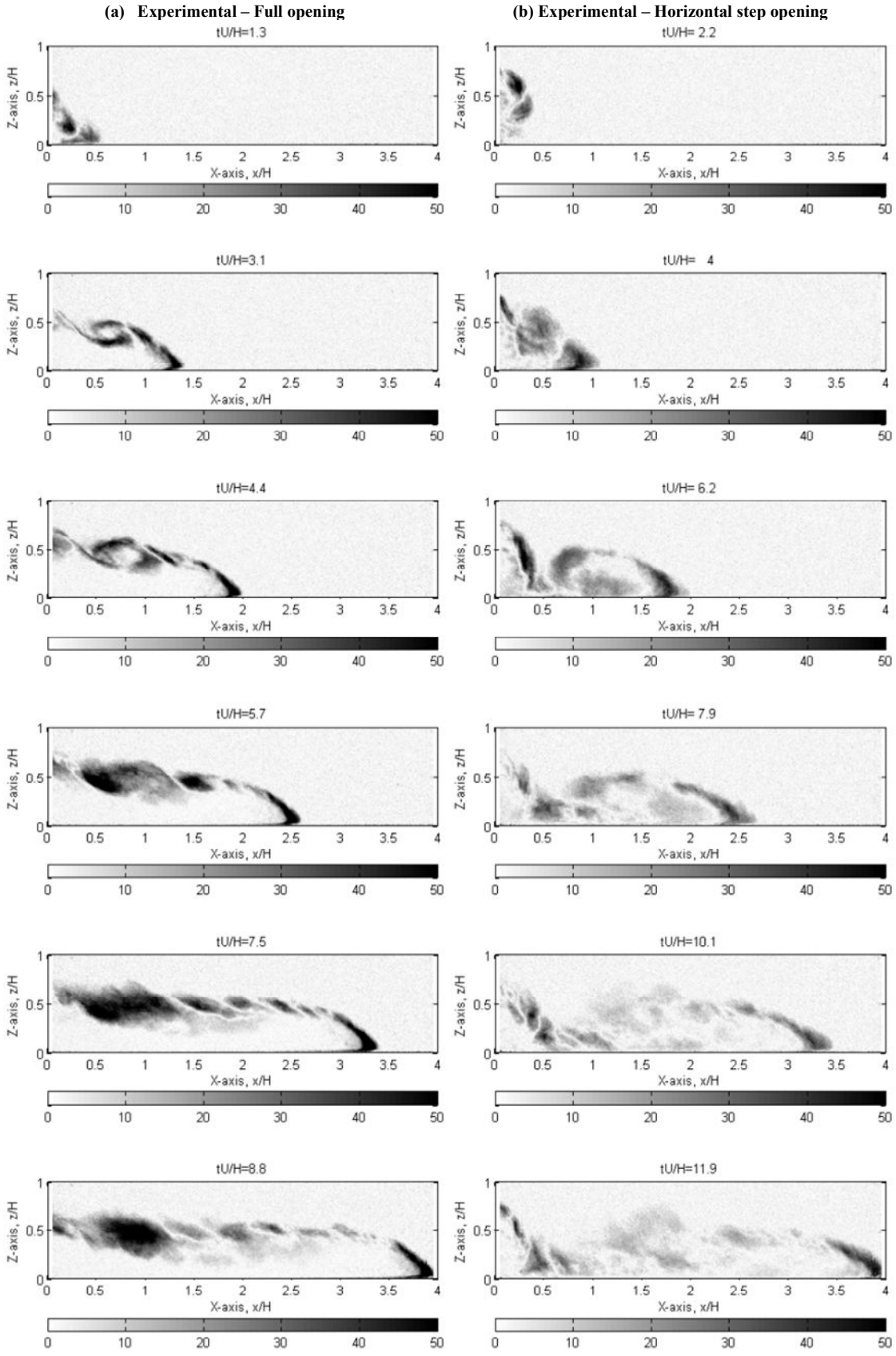

Figure 7-16: Magnitude of the difference in relative concentration between width-integrated relative concentration fields from repeated experimental runs: (a) full opening geometry (b) horizontal step opening geometry.

Flammable Regions

The relative concentration fields were used to predict the volume of regions within the flow which would correlate to flammable mixtures, (as outlined in Section 7.5.6). The flammable volumes were plotted against time, as shown in Figure 7-18. For both opening geometries, the flammable volumes increased almost linearly and the results from repeated experimental runs were consistent. Fluctuations in the flammable volumes occurred due to turbulence and were larger for the horizontal step opening than for the full opening. The maximum difference between repeated experimental runs was approximately $0.06H^3$.

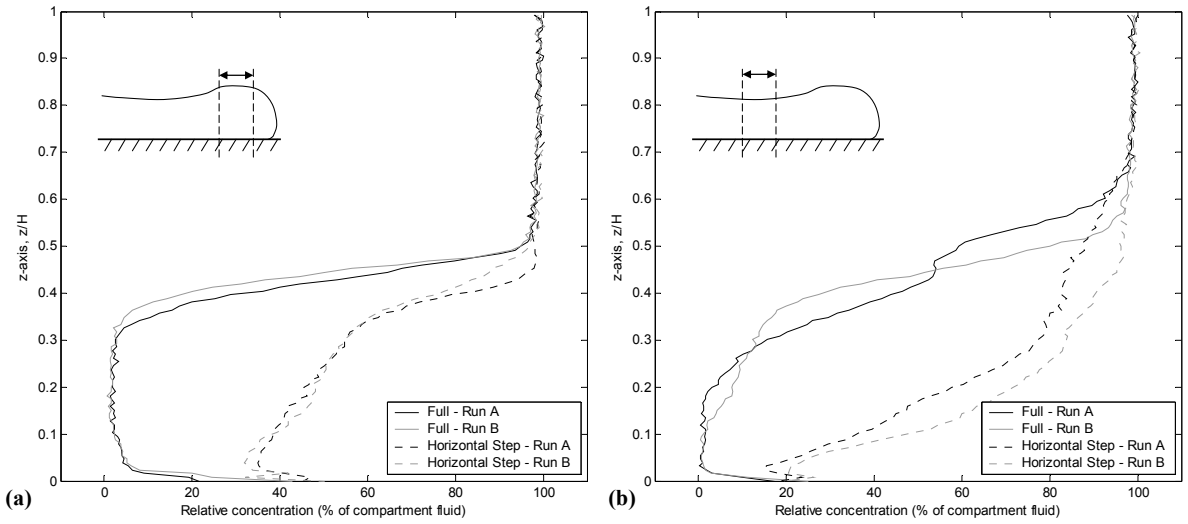

Figure 7-17: Width-integrated relative concentration profiles for repeated runs: (a) head of flow, (b) tail of flow. 0% indicates freshwater, 100% indicates saltwater.

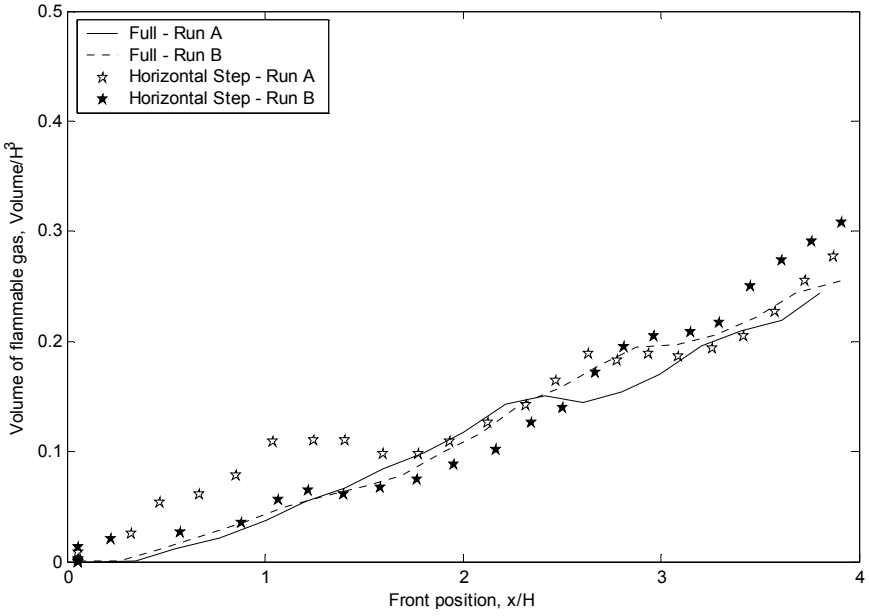

Figure 7-18: Volume of flammable region versus time from the repeated experimental runs.

7.5.3 Two dimensionality

To investigate the two-dimensionality of the flows, time-sequences of relative concentration contour lines were created for each opening, as shown in Figure 7-19. These time-sequences show a plan view (looking down on the flow from above). Due to experimental limitations, these time-sequences were only produced for the numerical simulations. The contours were created from a horizontal concentration slice at $z = 0.05H$, which corresponded to the approximate height of the nose or fore-most point of the flow. A relative concentration of $R = 85\%$ was selected to represent the front the flow. Due to the high concentration gradients through the nose region of the flow, the contours at relative concentrations of 80% and 90% demonstrated the same trends as those for the 85% contour, but were slightly offset spatially.

The contour time-sequences for the full and horizontal step openings were initially completely two-dimensional. As the flows propagated, out of plane motions (in the y-direction) developed within the flow causing perturbations, but the profiles remained predominantly two-dimensional. The influence of boundary friction was apparent near the sidewalls, where curvature of the concentration contours indicated the presence of boundary layers.

The time-sequences produced by the vertical slot, door and window openings were initially three-dimensional, with a half-circle shaped contours indicating the flows were spreading radially. However, once the gravity current flows reached the compartment side-walls, they became predominantly two-dimensional. The transition to a predominantly two-dimensional flow occurred once the front position was greater than approximately 1.5-2.0H. This agrees with the findings of Fleischmann (1994), who investigated the gravity current flows produced by a similar range of three-dimensional opening geometries and found that the flows were largely two-dimensional after the front reached approximately 1.5H.

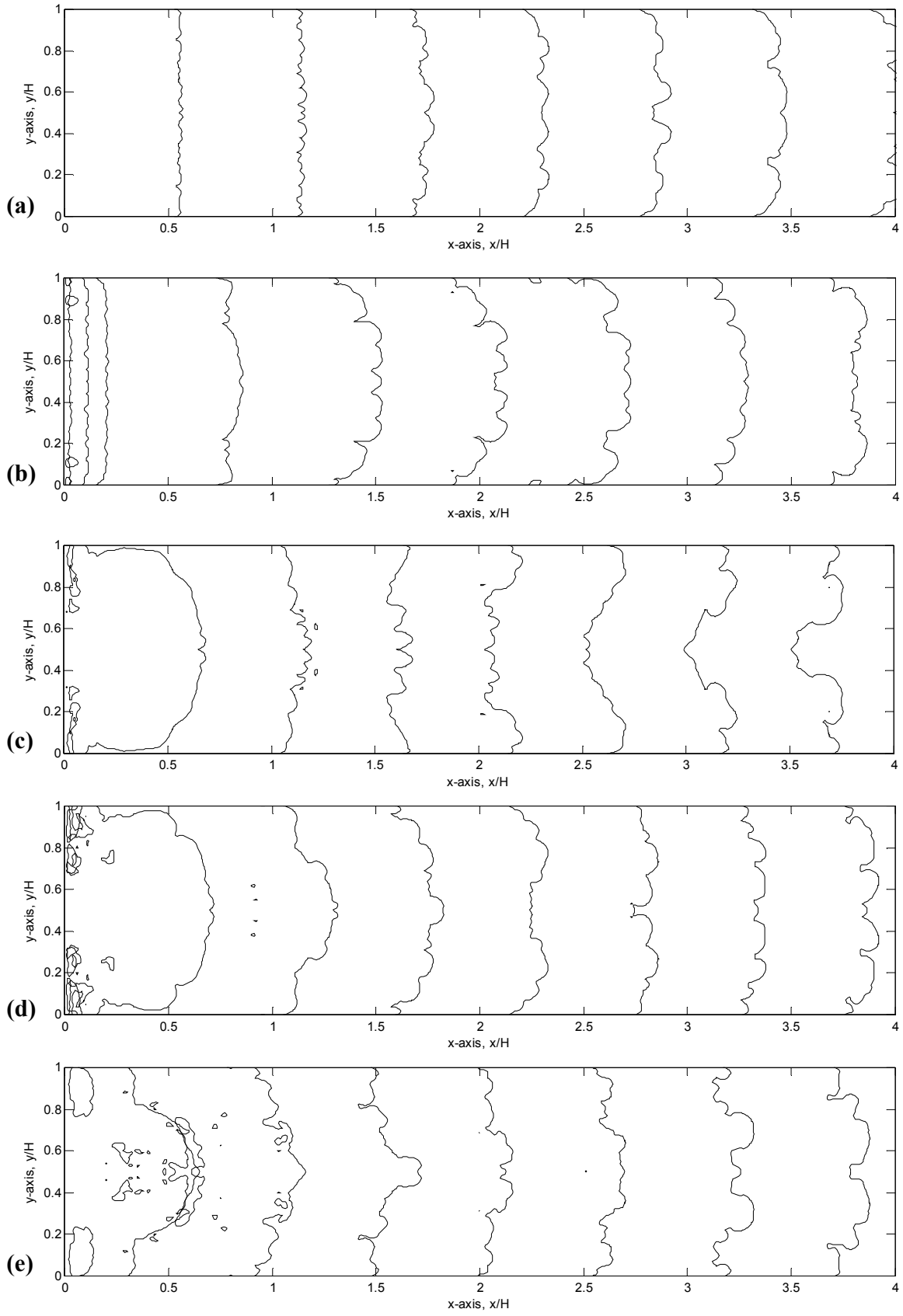

Figure 7-19: Plan view of time-sequences of numerical simulation relative concentration contours ($R = 85\%$) representing the gravity current front for different opening geometries: (a) full, (b) horizontal step, (c) vertical slot, (d) door, (e) window.

7.5.4 Concentration Fields

Time sequences of experimental width-integrated relative concentration fields for the different opening geometries were presented along with a general discussion of the gravity current flows in Section 7.2. The equivalent time sequences from the numerical simulations are presented alongside the experimental ones in Appendix C. Typical instantaneous concentration fields from these sequences, generated when the front of the flow reached approximately $x = 3.5H$, are presented in Figure 7-20 and Figure 7-21 for the experimental and numerical flows respectively. The front position of $x = 3.5H$ was selected as it enabled the head of the flow and a large portion of the tail to be visualised in a single frame. Relative concentrations are expressed as a percentage of saltwater (0% indicates freshwater, 100% indicates saltwater). It should be noted that the spatial extent of the experimental concentration fields was slightly less than $0.0H < x < 4.0H$. Time-sequences showing the magnitude of the differences between the experimental and numerical concentration fields were produced for the different opening geometries and are presented in Appendix C.

In general, the experimental and numerical concentration fields were qualitatively similar, but the concentration fields in the numerical simulation appeared slightly lumpier. The numerical simulation used LES, which directly solves for the large scale eddies, but models turbulence on scales smaller than the numerical grid with an eddy-viscosity model. This lumpiness in the numerical concentration fields was believed to have been due to the unresolved sub-grid scale eddies.

To investigate the time-varying nature of the flows, concentration field time-histories were generated. A horizontal slice, at $z = 0.05H$, was made through the concentration field at every frame. The height of $z = 0.05H$ was selected as it was the approximate height of the nose or foremost point of the gravity current head. These slices were plotted on a distance versus time plot, as shown in Figure 7-22, and enabled temporal concentration changes to be assessed. Due to data processing limitations, it was not practical to produce numerical concentration field time-histories.

A discussion of the concentration fields for the different opening geometries is presented below and differences between the experimental and numerical flows, specific to individual compartment openings, are discussed.

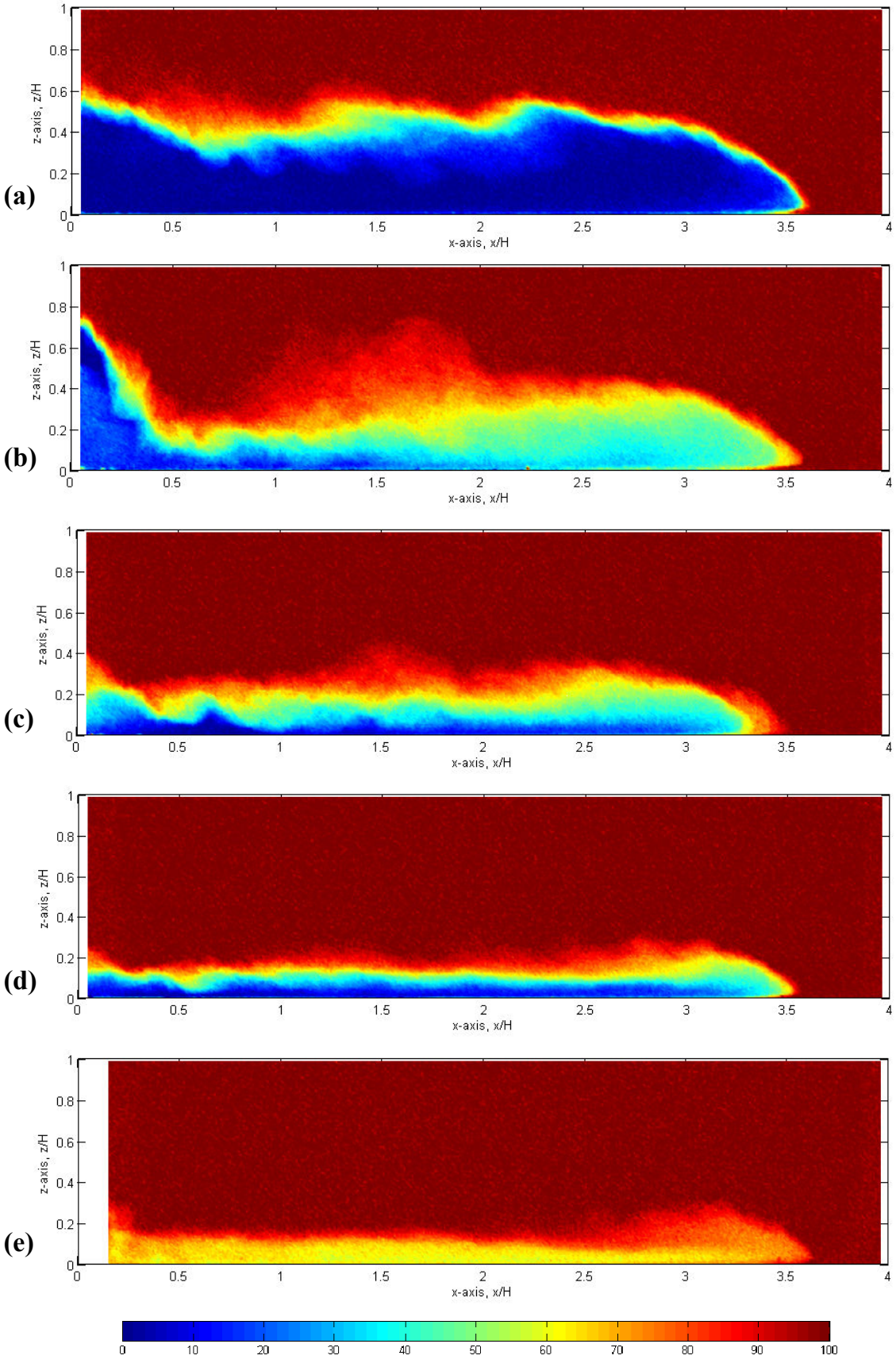

Figure 7-20: Typical experimental width-integrated relative concentration fields for different opening geometries: (a) full, (b) horizontal step, (c) vertical slot, (d) door, (e) window.

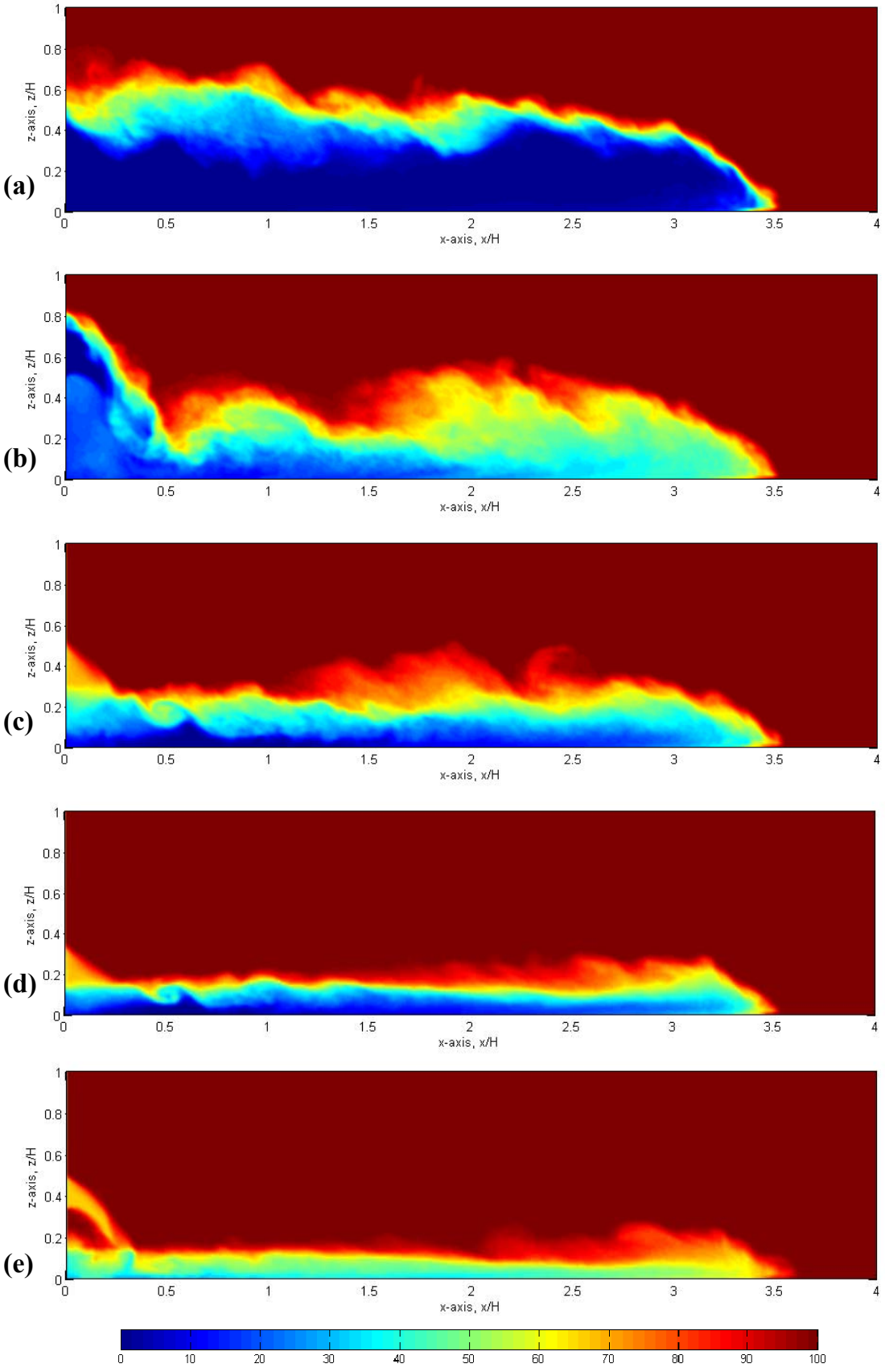

Figure 7-21: Typical numerical width-integrated relative concentration fields for different opening geometries: (a) full, (b) horizontal step, (c) vertical slot, (d) door, (e) window.

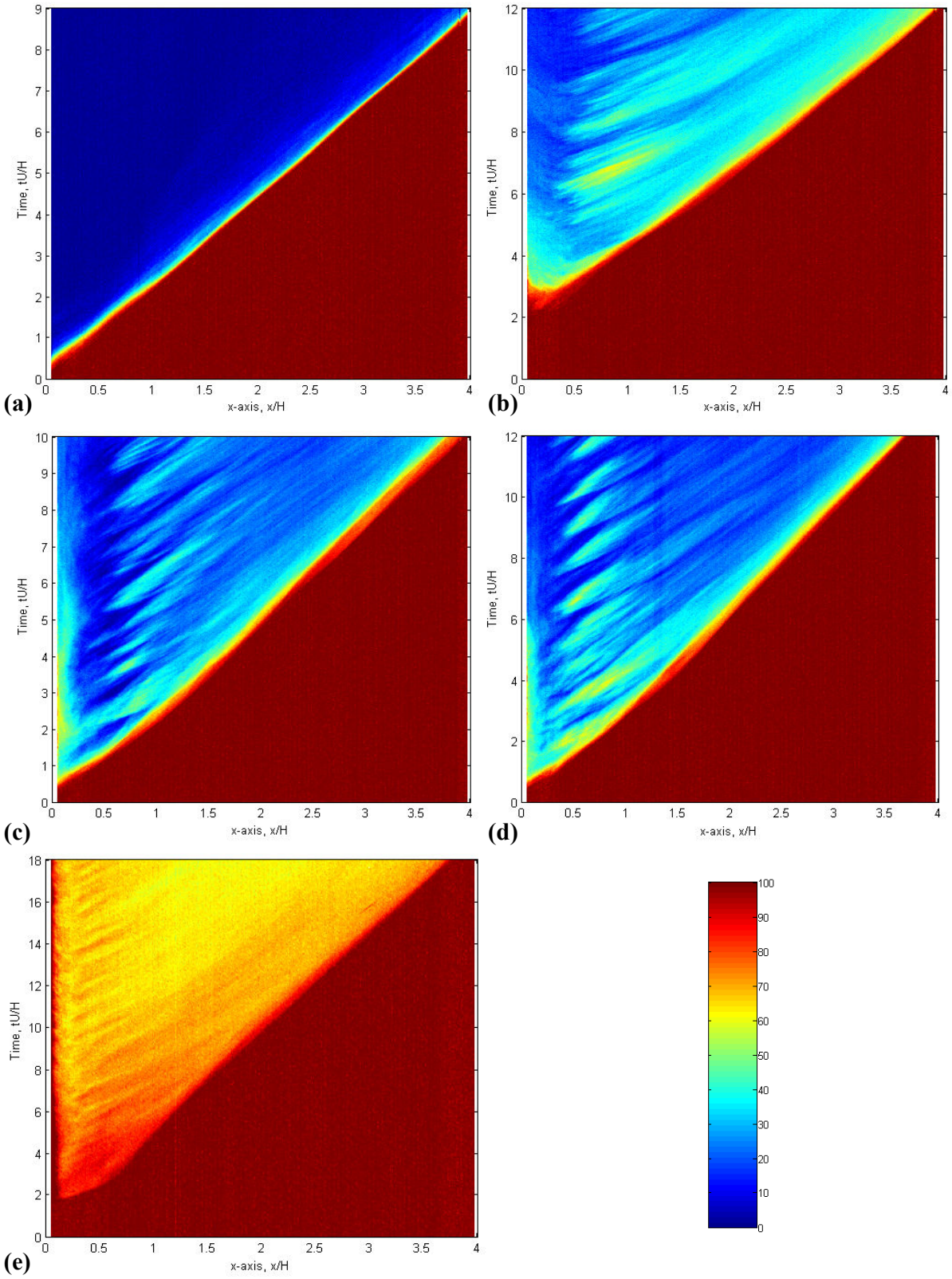

Figure 7-22: Experimental width-integrated concentration field time-history on a plot of horizontal distance versus time for repeated runs: (a) full, (b) horizontal step, (c) vertical slot, (d) door, (e) window.

Full Opening

For the full opening geometry, the head size increased for front positions less than approximately 2.0H, but remained relatively unchanged for the remainder of the flow. The typical structure of the head for front positions greater than approximately 2.0H can be observed in Figure 7-20 (a) and Figure 7-21 (a) for the experimental and numerical flows respectively. The mixed region at the nose in Figure 7-21 (a) was not visible earlier and later in the flow and was associated with lobes and clefts forming at the nose.

The head and tail concentration fields of the gravity current may be divided vertically into three distinct layers: a lower layer of unmixed gravity current fluid, a counter-flowing upper layer of unmixed compartment fluid and a central mixed region. The mixing within this central region was primarily caused by billows, which formed at, and broke off, the head.

The time-history concentration field for the flow is shown in Figure 7-22 (a). A distinctive interface existed between the gravity current fluid and the compartment fluid. The gravity current fluid (to the left of the interface) consists almost entirely of unmixed freshwater. The uniform slope of the interface represents the relatively constant velocity of the gravity current front, in agreement with the findings in Section 7.3.3.

In the numerical simulations, billow structures remained coherent in the width-averaged concentration fields longer than in the experiment, as shown in Figure 7-23. Relatively coherent billows were visible behind the head until the front had reached approximately $x = 1.5H$, in the experimental flow, and $x = 2.0H$, in the numerical flow. Billows break down into three-dimensional turbulence as the result of out of plane motions. These out of plane motions are enhanced by boundary friction and lobes and clefts, which are formed by the gravitational instability of ambient fluid that is over-run by the nose of the gravity current (Simpson 1997), but may also develop naturally, without boundary friction, once the billows have evolved far enough (Lowe et al. 2002). The reason the numerical simulations under-predicted billow breakdown was believed to be due to slight irregularities, or perturbations, in the experimental initial conditions, which would have enhanced billow breakdown. These irregularities obviously cannot be modeled by the numerical simulations. The issue of billow breakdown was not apparent for the other opening geometries, because the turbulent out of plane motions generated by the respective openings dominated those which developed naturally within the flow.

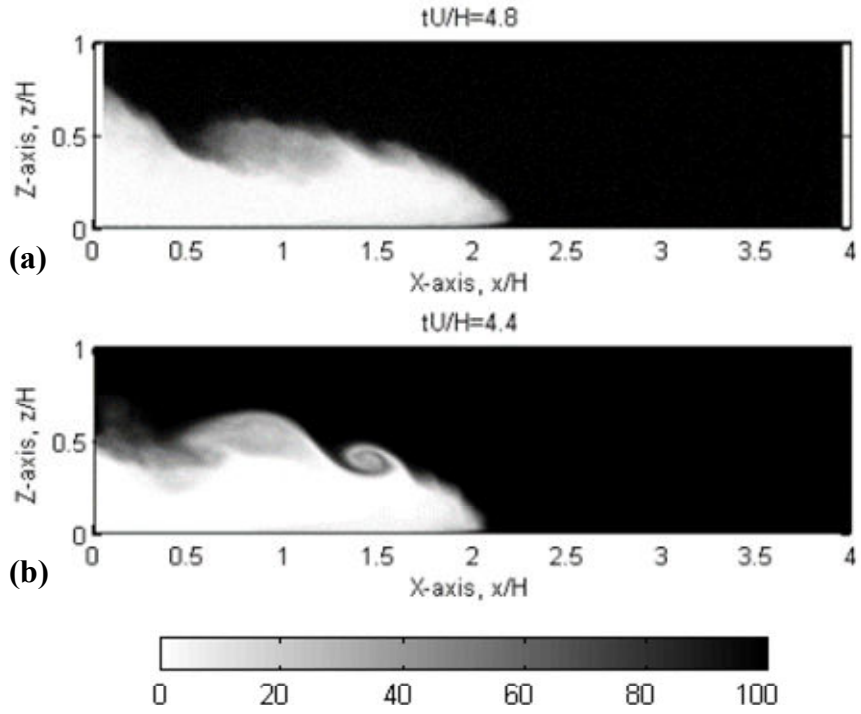

Figure 7-23: Width-integrated relative concentration fields for the full opening geometry: (a) experimental, (b) numerical.

The magnitude of the differences in the experimental and numerical concentration fields (shown in Appendix C) were larger than those from the repeated experimental runs for front positions less than approximately 2.0H, but similar at larger front positions. This indicates that in the later stages of the flow, the numerical simulation was accurately replicating the concentration fields. The large initial differences were probably associated with the slow breakdown of numerical billows (discussed above). The differences were the greatest at the nose and adjacent to the inflow. In the body of the flow, the differences were confined to the turbulent region at mid-depth of the compartment.

Horizontal Step

The shape and size of the head of the horizontal step gravity current did not change significantly for front positions greater than approximately 2.5H and the general shape of the head can be seen in Figure 7-20 (b) and Figure 7-21 (b) for the experimental and numerical flows respectively. The horizontal step flows were highly turbulent and billows which formed on the inflow plume were found to have a large impact on the concentration field at later stages in the flow. The experimental mixed region located above the tail of the flow in Figure 7-20 (b) between $1.0H < x < 2.0H$ (reproduced in Figure 7-24 (b)), was caused by a

billow which shed off the plume as it formed, as shown in Figure 7-24 (a). This billow was not visible in the repeated experimental run. In the numerical concentration field in Figure 7-21 (b), the thickness of the tail of the gravity current was over predicted for $0.5H < x < 1.5H$ (reproduced in Figure 7-25 (b)). The increased mixing was generated by a single billow, which was formed at the interface between the inflowing and out-flowing fluids and was swept into the compartment, as shown in Figure 7-25 (a). Therefore, these mixed regions were assumed to be associated with the turbulent nature of the flow.

The mixing layer within the head and tail of the gravity currents extended to the lower compartment boundary. This was caused by the turbulent mixing which occurred in the initial period of collapse, as the flow dropped over the step. The increased mixing meant that the visual depth of the gravity current was only slightly smaller than that for the full opening, despite the fact that the opening was half the area.

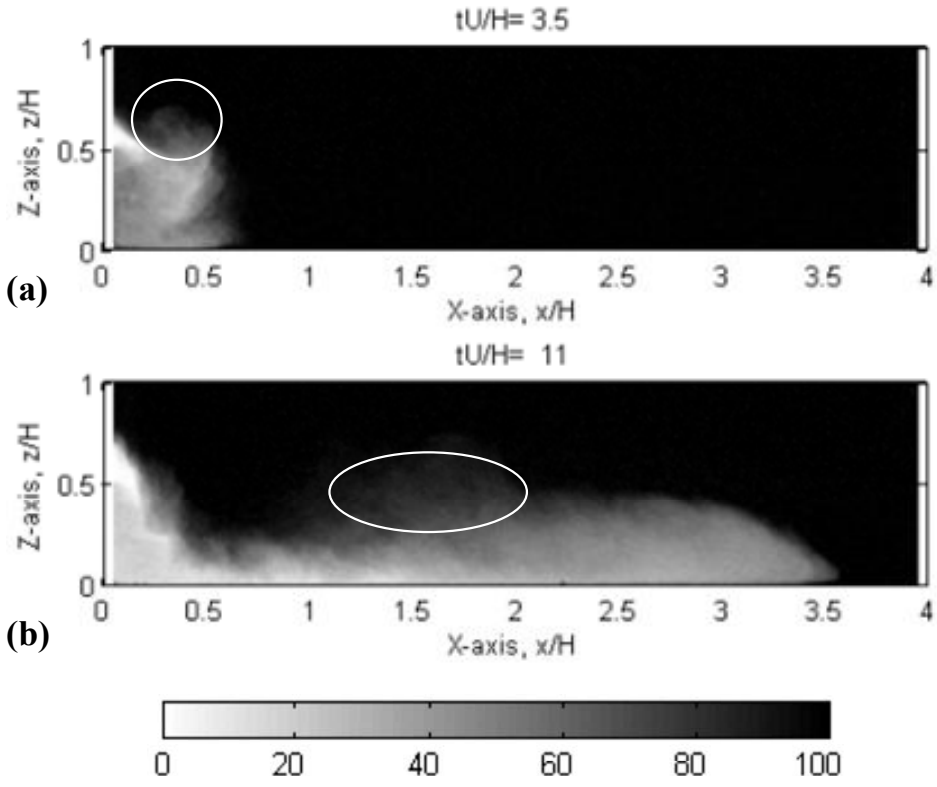

Figure 7-24: Experimental width-integrated relative concentration fields for the horizontal step opening geometry for different times.

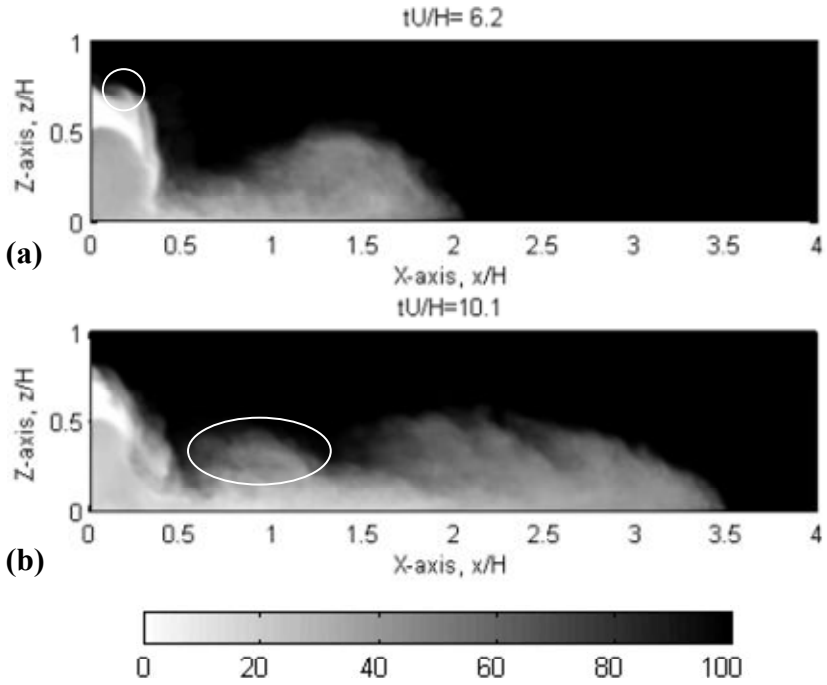

Figure 7-25: Numerical width-integrated relative concentration fields for the horizontal step opening geometry for different times.

The evolution of the internal structure can be seen in the time-history concentration field in Figure 7-22 (b) and again shows a distinct interface between the gravity current fluid and the compartment fluid with a relatively uniform slope. To the left of the interface, regularly spaced streaks are visible in the concentration field. These streaks were caused by billows that formed regularly along the interface between the inflowing and out-flowing fluid (on the top of the plume). As they were carried into the compartment, they temporarily enhanced the mixing in the tail of the gravity current. These billows were broken up by three-dimensional turbulence as they were swept further into the compartment, which explains why the streaks are smeared out and become less distinctive at distances greater than approximately $x = 1.5H$.

The magnitudes of the differences between the experimental and numerical concentration fields (from Appendix C) were significantly greater in the initial stages of the flow than those from the repeated experiments. This occurred because the numerical simulation over predicted the speed of establishment of the head (as found in Section 7.3.4). For front positions greater than approximately 2.5*H*, the differences within the body of the flow were similar to, but slightly greater than, those from the repeated experimental runs.

Vertical Slot

At front positions greater than approximately $2.0H$, the head shape was relatively constant, and had the typical shape shown in Figure 7-20 (c) and Figure 7-21 (c) for the experimental and numerical flows respectively. The gravity current was approximately half the size of those generated by the full and horizontal step opening geometries. The reduced size was associated with the reduced opening area and decreased level of turbulent mixing. The mixing layer was a similar thickness in the head and tail regions and extended down to the lower boundary due to the turbulence that was generated as the flow spread laterally through the opening.

The time-history concentration field for the vertical slot is shown in Figure 7-22 (c). The interface between the gravity current fluid and compartment fluid initially curved upwards as the front decelerated. The relatively uniform slope, for distances greater than $x = 2.0H$, showed that the front velocity was nearly constant for this period. Regularly spaced streaks were again evident in the time-history concentration field as shown in Figure 7-26 (a).

The magnitude of differences between the experimental and numerical concentration fields (see Appendix C) were distributed randomly throughout the body of the flow at all stages and did not appear to change magnitude significantly as the flow propagated.

Door

The shape of the gravity current was similar to that generated by the vertical slot opening, but the size of the gravity current was reduced due to the reduced opening area, as shown in Figure 7-20 (d) and Figure 7-21 (d) for the experimental and numerical flows respectively. The time-history concentration field, shown in Figure 7-22 (d), also showed similar trends to those for the vertical slot opening. The streaks were thicker, because, although the billows were of similar size to those from the vertical slot opening, they were carried down closer to the lower boundary, due to the reduced scale of the flow, as shown in Figure 7-26. The magnitude of the differences between the experimental and numerical concentration fields (shown in Appendix C) were again randomly distributed throughout the flow.

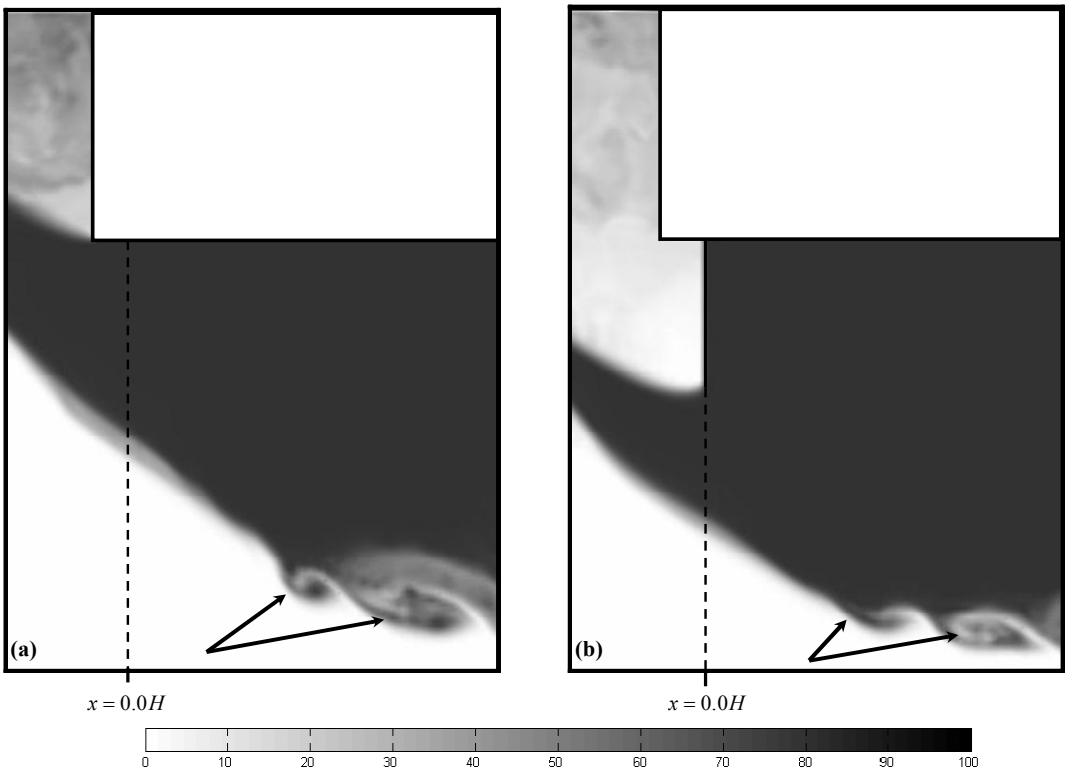

Figure 7-26: Numerical two-dimensional relative concentration field from mid-width of flow for: (a) vertical slot opening, (b) door opening. The arrows indicate billows forming at the interface of the inflowing and out flowing fluids.

Window

The shape and size of the head did not change significantly for front positions greater than approximately $2.0H$, and had the typical structure observed in Figure 7-20 (e) and Figure 7-21 (e) for experimental and numerical flows respectively. The extent of mixing within the flow was greater than that generated by all the other opening geometries, which was due to the combination of the flow dropping vertically and spreading laterally. The mixed layer extended to the lower boundary throughout the flow and the minimum relative concentration within the flow was approximately $R = 60\%$.

The experimental time-history concentration field for the flow is shown in Figure 7-22 (e) and highlights the level of mixing compared to the other opening geometries. The streaks, caused by billows forming on the top of the plume fluid, were less apparent than those for the other opening geometries, due to the reduced scale of the billows forming at the inflow.

The experimental and numerical relative concentration fields were qualitatively similar, but the concentrations near the rigid boundary appeared to be over-predicted by the numerical simulation. The differences between the experimental and numerical concentration fields were relatively uniform, instead of being randomly distributed through the flow like the other openings. These differences were either associated with an error in the experimental technique, an error in the numerical technique (such as insufficient grid resolution), or some fundamental difference between the experimental and numerical flows.

Limitations on the accuracy of the light attenuation flow visualisation technique may have contributed to the observed differences for the window opening geometry, as discussed below:

- For the window opening, extra salt was required to increase the density difference and ensure the flow was fully turbulent (the window opening had a density difference of $\beta = 0.04$ compared to $\beta = 0.005$ for the other opening geometries). Experimentally, the greater salt concentrations increased the level of light refraction, which occurred as the fresh and salt water mixed. This may have influenced the accuracy of the light attenuation flow visualisation technique and hence reduced the accuracy of the experimental concentration results to some extent.

- The window opening geometry gravity current flow was significantly more three-dimensional flow than the flows for the other opening geometries. This may have reduced the accuracy of the light attenuation flow visualisation technique, which uses line of sight averaging techniques to determine the internal concentration structure.

- Although outside the scope of the present investigation, further experiments using alternative flow visualisation techniques, such as laser induced fluorescence (LIF), could be investigated to determine if errors associated with the experimental technique contributed to the observed differences for the window geometry gravity currents.

The smaller scale of the window geometry flow may have reduced the accuracy of the numerical model. The reduced size of the window geometry gravity current resulted in fewer grid cells to resolve the flow than for an equivalent larger scale flow, such as the gravity current for the full opening geometry. This effectively reduced the grid resolution of the

window opening geometry simulations and may have also contributed to the observed differences (as discussed in Section 7.3.8). The grid resolutions could not be reduced further in the present study due to limitations in computational resources. However, as part of a future study, adadditional numerical simulations of the window geometry flow could be completed to investigate whether the grid resolution contributed to the observed differences.

There were, however, two findings that tend to suggest that there was some fundamental difference between the experimental and numerical flows. For the window opening, the numerical simulation substantially over-predicted the front Froude number and hence front velocity (by approximately 8%, see Section 7.3.8), which was confirmed from visual inspection of the concentration fields in Appendix C. This indicates that the buoyancy forces which drove the numerical flow were over-predicted. The second point was that, for the window opening, the experimental and numerical local Froude numbers were consistent with each other, with the different opening geometries and with literature (as shown in Figure 7-12). This indicates that the experimental local buoyancy and therefore relative concentrations were accurate.

7.5.5 Concentration Profiles

Relative concentration profiles were created from vertical slices through the concentration fields. These profiles were generated when the front had reached approximately $3.5H$ and were spatially averaged over a width of approximately $0.2H$. Spatial averaging reduced the effects of random errors associated with the experimental technique, but did not significantly alter the shape of the concentration profiles, as shown in Figure 7-27, which compares un-averaged and averaged profiles for the head and tail of the flow for the horizontal step opening. The head concentration profiles were generated from the deepest section of the head, at the locations shown in Table 7-6. The tail region, from $1.3H < x < 1.5H$, was located approximately halfway between the inflow and the head of the current, where the horizontal concentration gradients were minimal (see Figure 7-20 and Figure 7-21). The head and tail concentration profiles are presented in Figure 7-28 and Figure 7-29 respectively.

Table 7-6: Summary of regions used to determine the head concentration profiles for the different compartment opening geometries.

Opening Geometry	Averaging limits for x-axis (x/H)	
	Minimum	Maximum
Full	2.8	3.0
Horizontal Step	2.7	2.9
Vertical Slot	2.8	3.0
Door	3.1	3.3
Window	3.1	3.3

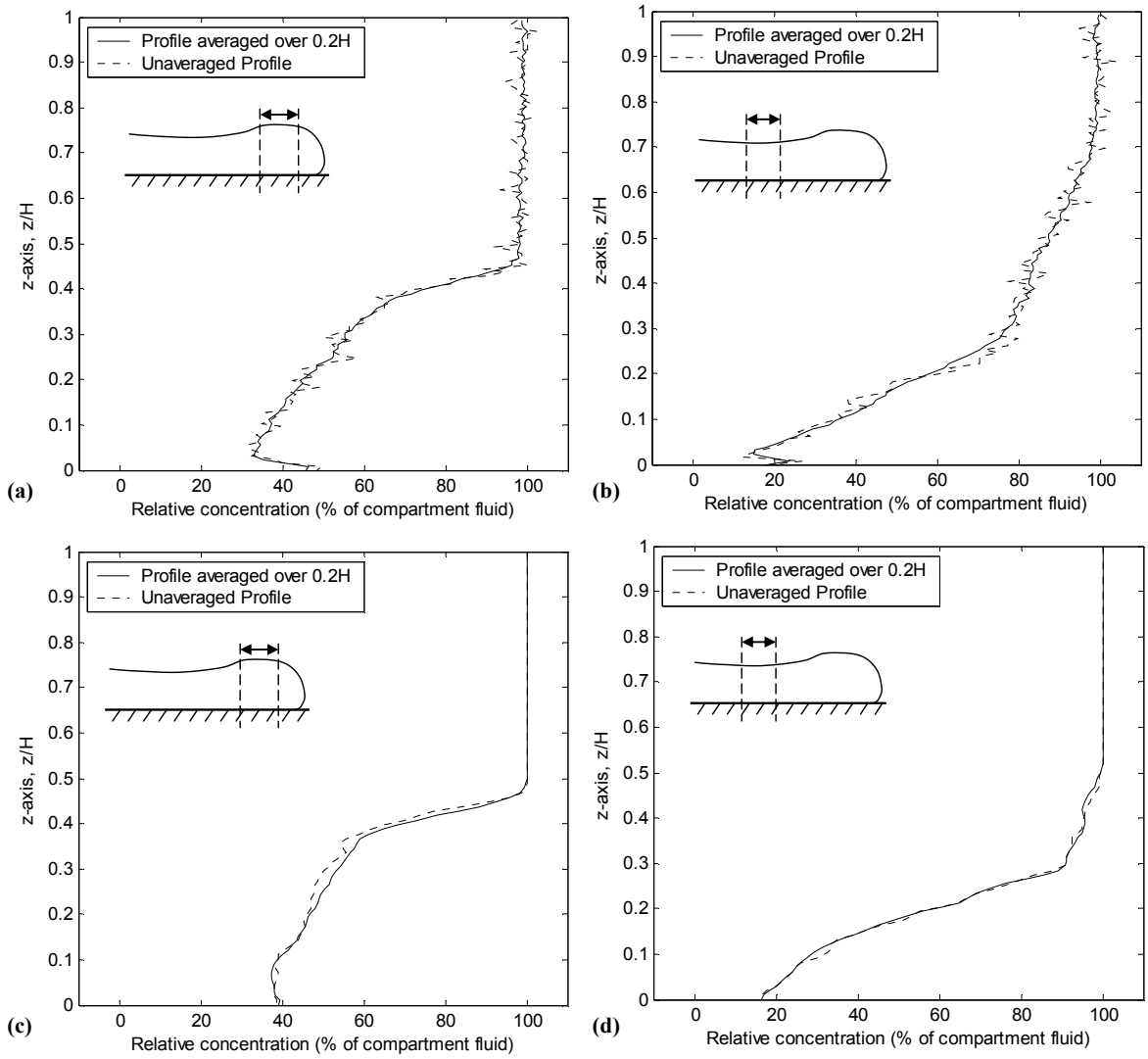

Figure 7-27: Spatially averaged and un-averaged width-integrated relative concentration profiles for horizontal step opening: (a) experimental – head, (b) experimental – tail, (c) numerical - head (d) numerical – tail.

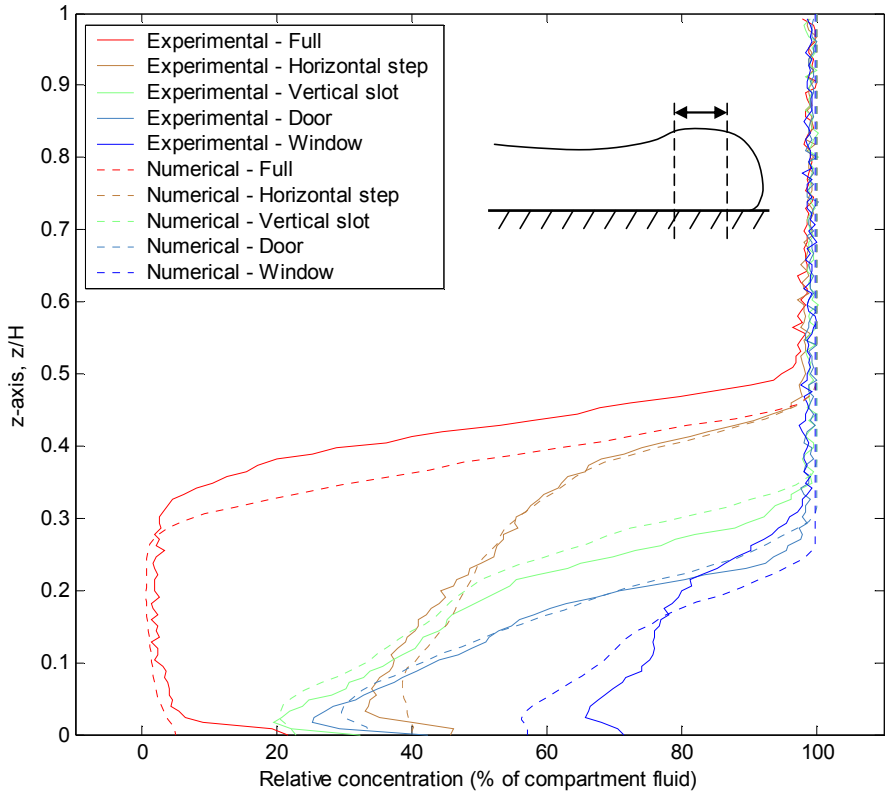

Figure 7-28: Experimental and numerical head width-integrated relative concentration profiles for different opening geometries.

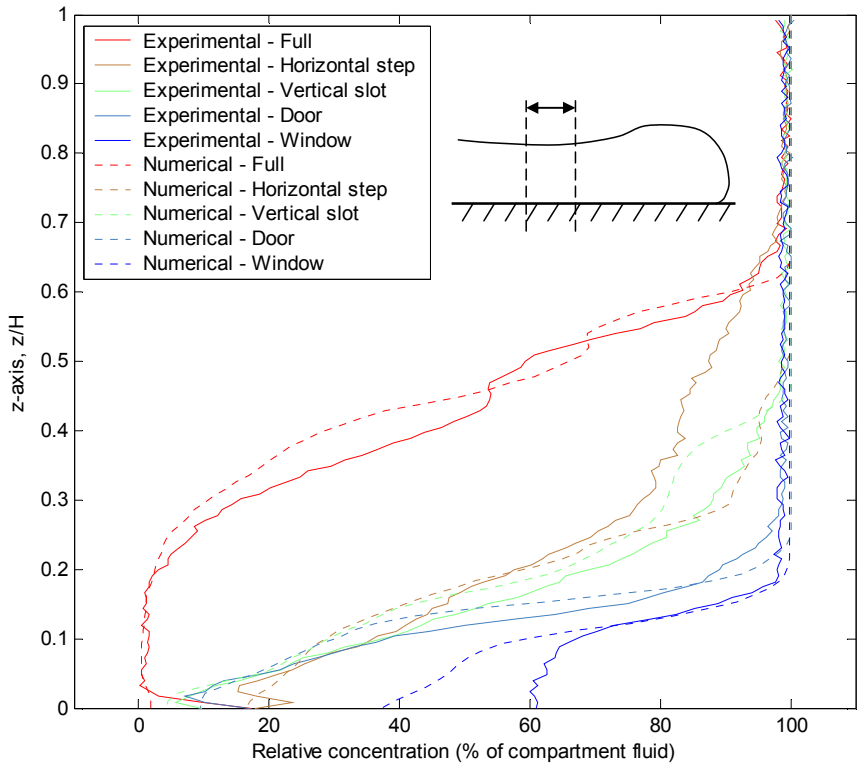

Figure 7-29: Experimental and numerical tail width-integrated relative concentration profiles for different opening geometries.

The head and tail concentration profiles highlight the differences between the flows generated by the various opening geometries. The full opening consists of lower and upper layers of unmixed fluid and a central mixed region approximately $0.2H$ thick. The other opening geometries have a counter-flow of unmixed compartment fluid, but the mixed region extends down to the lower boundary. The differences in the concentration profiles were associated with the opening geometries themselves, which cause varying amounts of turbulent mixing (due to either a vertical drop or lateral spreading).

In general, the shapes of the experimental and numerical head concentration profiles for all opening geometries were similar, with differences due to the turbulent nature of the flow. The differences for the full and horizontal step openings were similar to those from the repeated experiments (see Section 7.5.2). However, the numerical simulation for the window opening, overestimated the relative concentration close to the lower boundary ($0.0H < z < 0.1H$), as discussed in Section 7.5.4).

7.5.6 Flammable Regions

The range of relative concentrations that would represent flammable mixtures in backdraft gravity currents depends on the fuel type, the temperature and the initial conditions. However, to gain a quantitative insight as to where flammable regions would exist, typical initial conditions from past backdraft experiments were investigated. Assuming methane gas fuel and using the initial experimental gas mass fractions from Fleischmann (1994), relative concentrations between 17% and 37% were shown to correlate to flammable gas mixtures. Details of this calculation were presented in the Analysis chapter.

Location

Time-sequences of relative concentration fields were used to predict the location and extent of regions which correlate to flammable mixtures in backdraft gravity currents. Experimental and numerical time sequences of predicted flammable regions are presented in Appendix C. Typical frames from these sequences, generated when the front of the flow had travelled approximately 3.5H, are presented in Figure 7-30 and Figure 7-31 respectively. These flammable regions were width averaged, which means that for the three-dimensional openings they are only valid for front positions greater than approximately 1.5-2.0H, where the flows were predominantly two-dimensional (as found in Section 7.5.3).

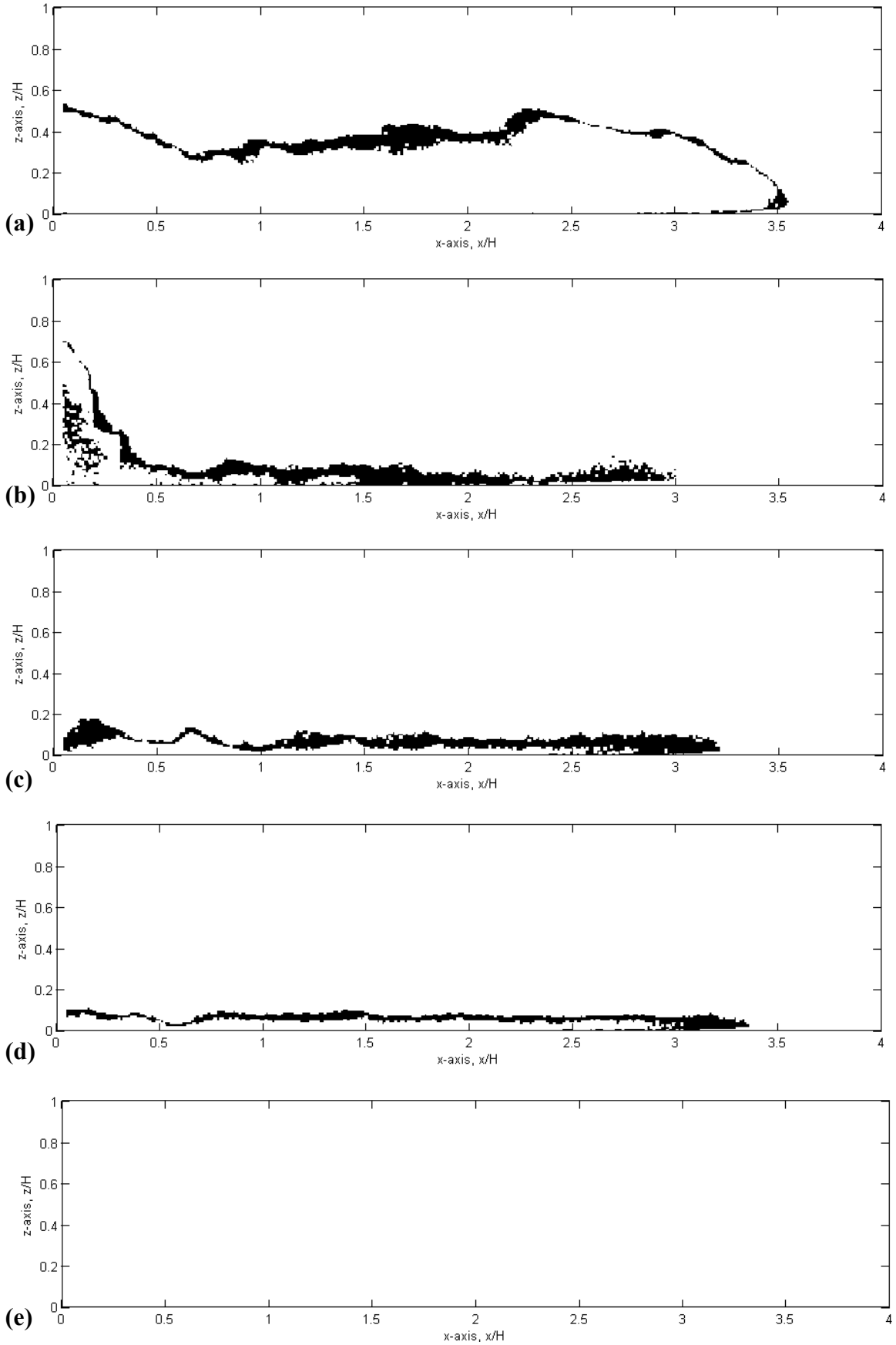

Figure 7-30: Instantaneous plot of the experimental flammable region for different opening geometries: (a) full, (b) horizontal step, (c) vertical slot, (d) door, (e) window.

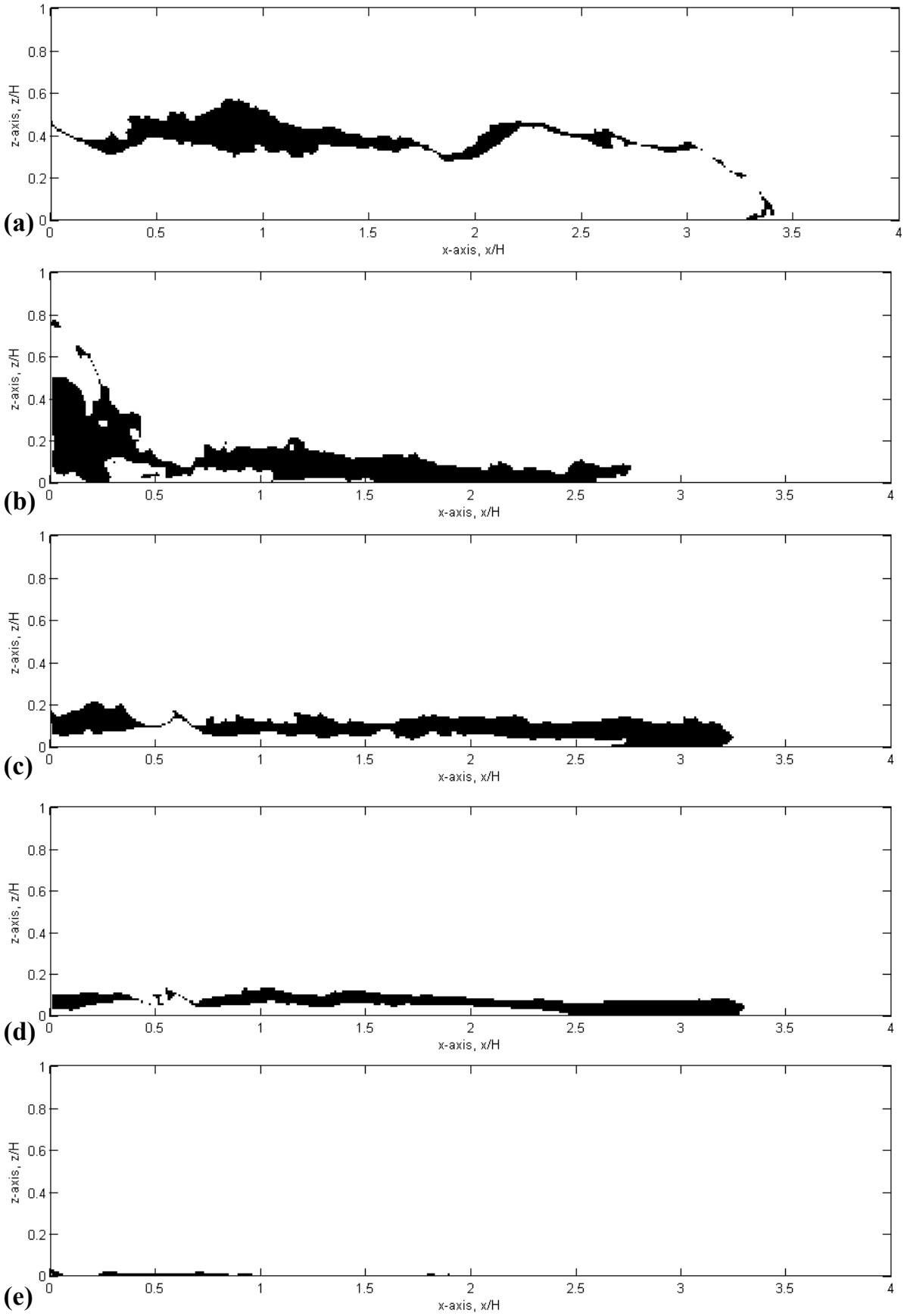

Figure 7-31: Instantaneous plot of the numerical flammable region for different opening geometries: (a) full, (b) horizontal step, (c) vertical slot, (d) door, (e) window.

The flammable region for all opening geometries was located within a thin band. Generally, the flammable region was slightly thicker in the tail region, due to the increased turbulent mixing. For the full opening, most of the flammable layer existed at mid-height of the compartment, but curved around the head of the flow, reaching the solid boundary near the nose. For the horizontal step, vertical slot and door openings, the flammable region was located at, or close to, the lower boundary. Ignition sources, such as smoldering embers, are likely to exist at ground level. As the full opening geometry flammable region was only located near the ground at the nose of the flow (instead of throughout the body of the flow as observed for the horizontal step, vertical slot and door openings opening), the flammable mixture the full opening geometry may be more difficult to ignite.

The experimental flammable region for the window opening geometry was virtually non-existent. The compartment gases remained fuel rich (oxygen lean), needing more oxygen to become flammable. The gas mixtures did not cross the flammability envelope, staying within the shaded region in Figure 7-32. Therefore, for the initial conditions selected, backdraft ignition would not occur (or would be difficult) over the period of time investigated.

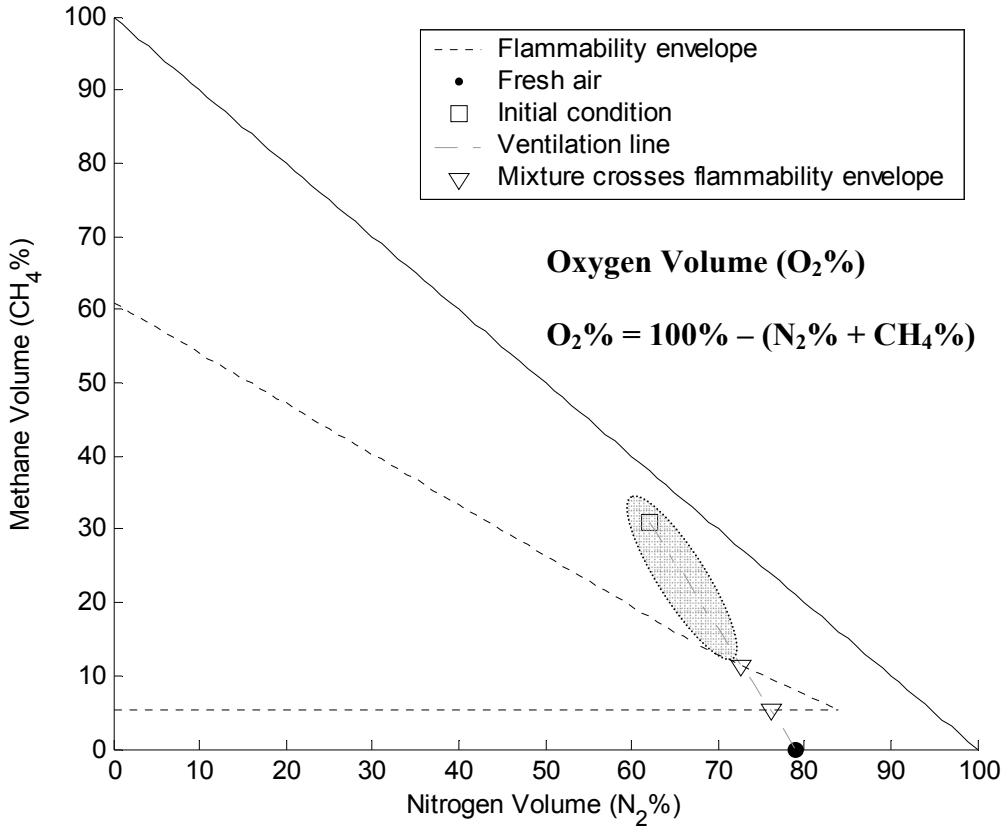

Figure 7-32: Compartment ventilation line superimposed on the flammability diagram for methane. Shaded region indicates fuel rich gas mixtures for the initial conditions from Fleischmann (1994).

For the window geometry, as heated gases continued to flow out of the compartment, the gravity current would eventually reflect off the back wall and a lower layer of fresh air and upper layer of compartment gases would develop. The interface between these layers could potentially be flammable, so a backdraft with delayed ignition would still be possible. The experimental results of Fleischmann (1994) indicated that, in general, ignition of backdrafts for the window opening did not occur until after the gravity current had reflected off the compartment end wall.

The results of the present study indicate that firefighters should ventilate potential backdraft compartments through the smallest hole possible, thus keeping the compartment gas mixtures fuel rich (oxygen lean) in order to prevent the formation of flammable mixtures, at least temporarily. Application of water, or other extinguishing agents, through the opening could then be used to eliminate possible ignition sources, cool gas mixtures and further dilute the fuel mass fractions, without the risk of backdraft. The cutting extinguisher, a fire-fighting tool developed for such a purpose, may be used to "cut" a small hole through doors and walls and spray water to cool gases and extinguish ignition sources (Gojkovic and Bengtsson 2001).

The locations of experimental and numerical flammable regions were comparable, but the thickness of the numerical flammable regions was consistently greater than those from experiment. This issue is discussed further in the following paragraphs.

Flammable Volumes

Volumes of the potential flammable regions were created from the predicted flammable regions and are plotted in Figure 7-33. The flammable volumes were calculated between the limits $0.2H < x < 3.8H$, to avoid gaps in the experimental data associated with the experimental setup (camera viewing angles and lock gates). For all of the opening geometries, the flammable volume increased approximately linearly with time. However, some fluctuations from this linear trend existed. These fluctuations were associated with the turbulent nature of the flow and were more significant for the horizontal step opening due to the increased turbulence generated by that opening.

The flammable region volumes were opening geometry dependent, with the horizontal step compartment opening producing the largest volume of flammable gases and the window opening produced little or no flammable gases, as discussed earlier.

A comparison of the numerical and experimental results indicates that the numerical simulation consistently over-predicted the volume of flammable regions present within the flow. The magnitude of the differences varied with time, due to turbulent fluctuations. For the full and horizontal opening geometries, the variations between the experimental and numerical volumes were larger than those from the repeated experimental runs (approximately $0.06H^3$, from Section 7.5.2). Therefore, the numerical simulation over-predicted the extent of mixing for the range of relative concentrations correlating to flammable regions ($17\% < R < 37\%$). The ratio of the numerical and experimental flammable volumes was investigated for front positions greater than approximately $1.5H$, where the flows were predominantly two-dimensional (as shown in Section 7.5.3), and the maximum and minimum ratios for each opening are presented in Table 7-7 (these ratios were not applicable to the window opening, because no experimental flammable region was predicted). In general, the numerical simulations over-predicted flammable volumes by between 10% and 85%, depending on the opening geometry.

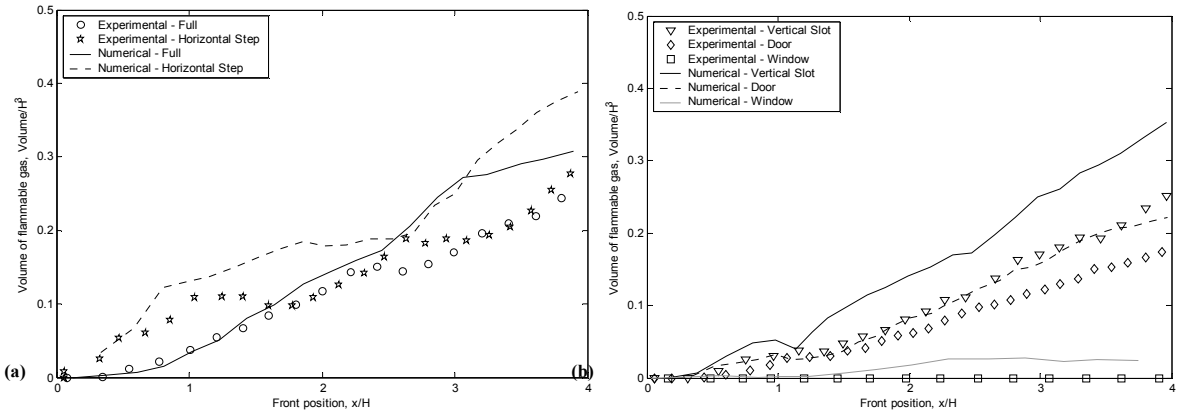

Figure 7-33: Volume of flammable region versus time for different opening geometries: (a) full and horizontal step opening geometries, (b) vertical slot, door and window opening geometries.

Table 7-7: Maximum and minimum ratios of numerical over experimental flammable volumes.

	Full	Horizontal Step	Vertical slot	Door	Window
Minimum Ratio	1.12	1.21	1.21	1.11	-
Maximum Ratio	1.60	1.84	1.74	1.39	-

7.6 Internal Velocity Structure

The internal velocity structure of the backdraft gravity currents was also investigated. The internal velocity structure within backdraft gravity currents affects both mixing and fluid movement, so indirectly influences backdrafts. However, the main reason for analysing the internal velocity structure was to validate the results of the numerical simulations.

General issues relating to the internal velocity structure are addressed in Section 7.6.1. In Section 7.6.2, the accuracy of the experimental data is reviewed. Streamlines, produced from the velocity fields, are discussed in Section 7.6.3. Velocity profiles for the tail region of the gravity current are presented in Section 7.6.4. Finally, Section 7.6.5 compares experimental and numerical velocity time-histories for a point in the flow.

7.6.1 General

Some general issues related to the internal velocity fields are highlighted below.

- The spatial extent of the experimental velocity fields was limited by the field of view of the experimental setup, which extended from $x = 0.67H$ to $x = 2.1H$.
- Horizontal tail velocities were, in general, an order of magnitude larger than vertical velocities, so only horizontal velocity profiles and time-histories were investigated.
- Experimental velocity fields were not generated for the window opening geometry, because the extra salt, required to ensure the flow was fully turbulent, refracted light and made particle identification impractical (see the Experimental Methods chapter).
- The experiments used to generate the velocity fields were not repeated. Therefore, the variability between repeated experimental runs was not determined.

7.6.2 Experimental Accuracy

Errors associated with the particle tracking velocimetry (PTV) technique should be taken into consideration when experimental velocity fields are interpreted, or compared to numerical velocity fields. These errors were described in the Experimental Methods chapter and are summarised below.

- The maximum error in the length scales was approximately 2.5%.
- The maximum error in velocity estimates was approximately 8% of the front velocity. This was caused by a maximum of 4% error from ambient fluid motion and a

maximum of 4% error from particle identification. These errors were both randomly distributed, so typical errors were significantly smaller than 8% of the front velocity.

- The spatial resolution of velocity fields was approximately $0.04H$.

7.6.3 Streamlines

Streamlines were generated to visualise the two-dimensional internal velocity field data. Instantaneous streamlines are lines drawn in an unsteady flow at an instant in time whose tangent at any point is the direction of the velocity vector at that point (Street et al. 1996). As velocities are tangential to streamlines at all points, mass does not cross them.

The streamlines for the numerical simulations were generated from a vertical slice at the mirror boundary, which was located on a plane of symmetry on one side of the numerical domain to halve the computation demand. This mirror boundary is a no-flux, free-slip boundary, where out of plane velocities are zero.

The experimental streamlines were generated from a slice at mid-width of the flow, where some out of place velocities existed due to turbulence. However, these out of plane motions would have been minimal as the flow was essentially symmetric. Assuming out of plane motions (into and out of the page) for these velocity slices were negligible, the relative spacing of the streamlines indicates the relative speed within the flow (a reduced streamline spacing indicates an increased speed).

Experimental and numerical streamlines, extended from $x = 0.67H$ to $x = 2.1H$ as shown in Figure 7-35, and were generated when the front of the gravity current had travelled approximately $x = 2.0H$ and are shown in Figure 7-34. This front position was selected as it enabled the full extent of the gravity current head to be investigated.

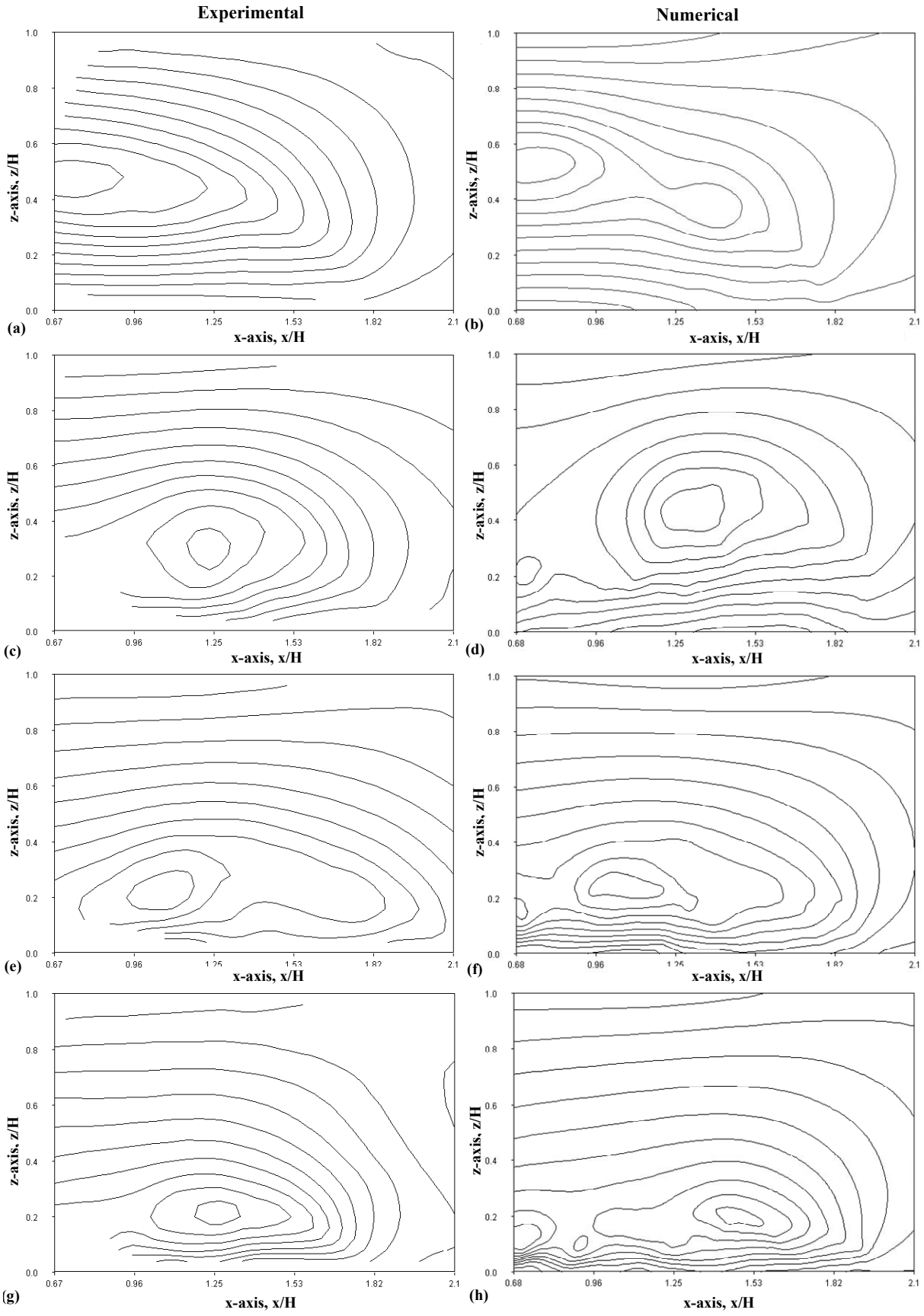

Figure 7-34: Instantaneous experimental and numerical gravity current head streamlines for different opening geometries: (a) & (b) full, (c) & (d) horizontal step, (e) & (f) vertical slot, (g) & (h) door.

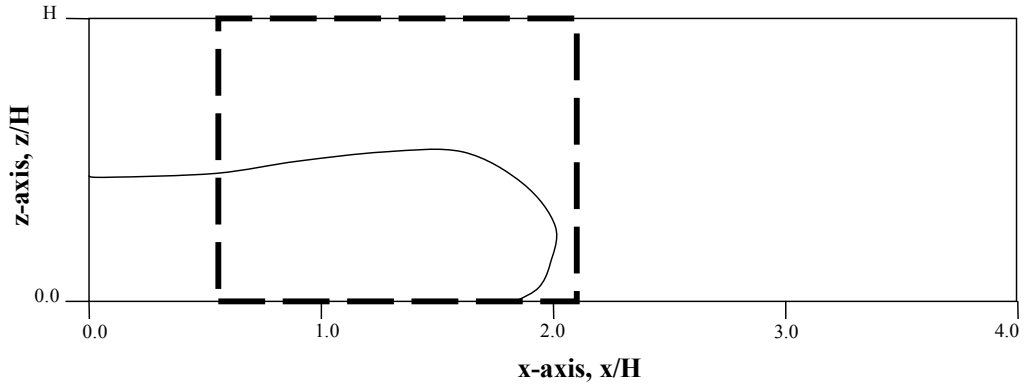

Figure 7-35: Schematic of the region of the flow where experimental streamlines were generated.

The experimental and numerical streamlines for all opening geometries indicated the presence of a single large circulation cell at the head of each flow, which rotated in an anticlockwise direction. This agreed with the result of Kneller et al. (1999), who found mean motion in the gravity current head consisted of a single large vortex. The circulation cell transported fluid from the tail through to the nose, before it was swept back by the counter flowing compartment fluid.

For the full opening geometry, the frame of reference was changed to move with the gravity current front and two circulation cells were visible within the head of the flow in the numerical streamline plot (Figure 7-36 (b)), but only the upper cell was visible in the experimental plot (Figure 7-36 (a)). The numerical result agrees with the findings of Thomas et al. (2003), who found that, in a frame of reference moving with the head, the flow of dense fluid through the head forms two counter-rotating circulation cells. The lower cell was not resolved experimentally in the present study, due to limitations of the experimental accuracy and spatial resolution and because the lower circulation cell was smaller and weaker than the upper cell (Thomas et al. 2003).

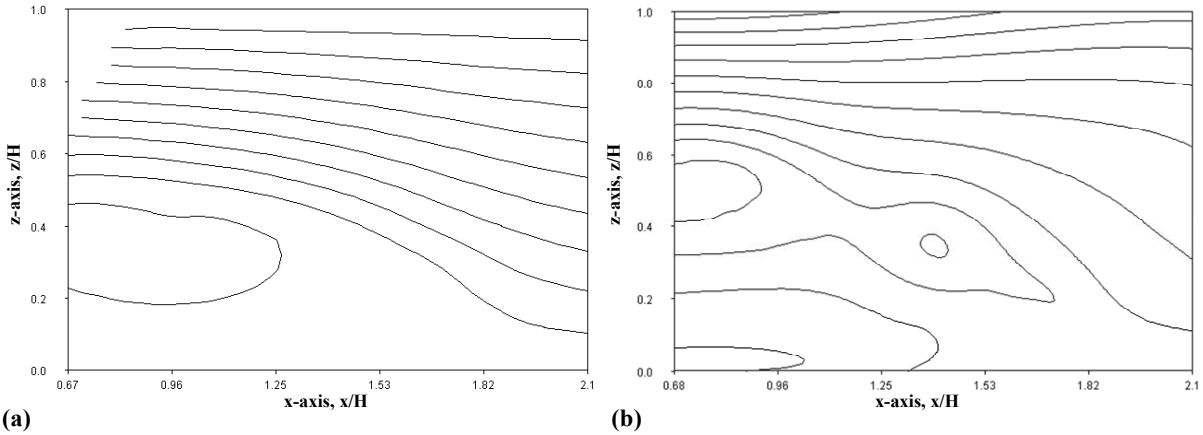

Figure 7-36: Instantaneous streamlines for the full opening geometry with a frame of reference moving with the gravity current head: (a) experimental, (b) numerical.

The location, size and shape of the circulation cells was opening geometry dependent. The circulation cell for the full opening geometry was located at mid-depth of the compartment near $x = 0.7H$ and had an elongated oval shape. The cell for the horizontal step opening was a similar size to that for the full opening, but was circular in shape and was located closer to the lower boundary and nearer the center of the field of view at approximately $x = 1.2H$, $z = 0.25H$. For the vertical slot and door openings, the circulation cells were in smaller in size with an elongated oval shape and were located even closer to the lower boundary at approximately $z = 0.2H$.

The shape and size of the circulation cells was similar between the numerical and experimental streamline plots, but because of the lower spatial resolution of the experimental velocity fields (approximately 0.04H compared to approximately 0.01H from the numerical simulations) they resolved fewer streamlines adjacent to the lower boundary.

The vertical location of the circulation cells was generally consistent between the experimental and numerical data. However, for the horizontal step opening geometry, the numerical circulation cell was offset vertically by approximately *0.2H*. The reason for the offset was a large circulating billow, which dominated the motion within the head of the flow. This billow formed on the leading edge of the initial spill plume as the freshwater flowed into the compartment and was swept into the compartment behind the head of the gravity current, as shown in Figure 7-37 (a) and (b). Later in the flow this billow separated from the head, breaking down and reducing in intensity, as shown in Figure 7-37 (c). Similar types of

billows were found to generate significant differences in the experimental and numerical concentration fields for the horizontal step opening, as discussed in Section 7.5.4. Therefore, this difference was attributed to the highly turbulent nature of the flow being simulated.

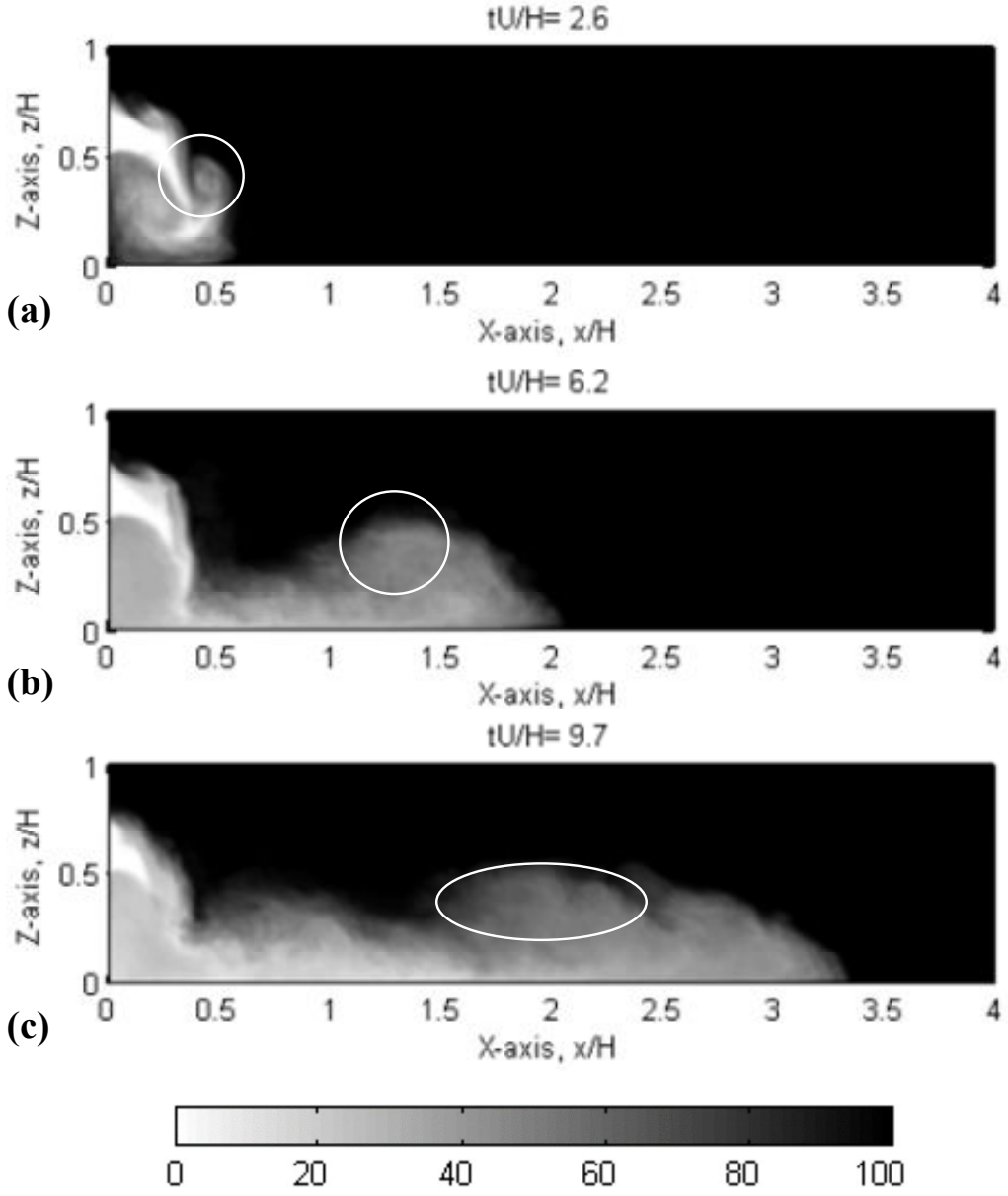

Figure 7-37: Numerical width-integrated relative concentration fields for the horizontal step opening geometry for different times. The location of the circulating billow is highlighted in each frame.

7.6.4 Velocity Profiles

Velocity profiles were created from vertical slices through the velocity fields for the tail region of the gravity currents. The profiles were generated when the front of the gravity current had reached approximately $x \sim 3.5H$, at the times shown in Table 7-8, and were spatially averaged over a width of approximately $0.2H$. Spatial averaging reduced the effects of turbulent fluctuations in the velocity fields and eliminated gaps in the experimental data (where particle matches had not been made between frames), as shown in Figure 7-38, which compares un-averaged and averaged profiles for the horizontal step opening. The averaging region was located between $1.3H < x < 1.5H$, halfway between the inflow and the head of the current, where horizontal velocity gradients were minimal. This region corresponded to the centre of the experimental field of view, where the experimental data was the most reliable. The velocity profiles for the different openings are shown in Figure 7-39.

Table 7-8: Dimensionless times used to generate the average tail velocity profiles

Opening Geometry	Dimensionless time, $t^*=tU/H$
Full	7.5
Horizontal Step	10.6
Vertical Slot	8.8
Door	11.0
Window	17.5

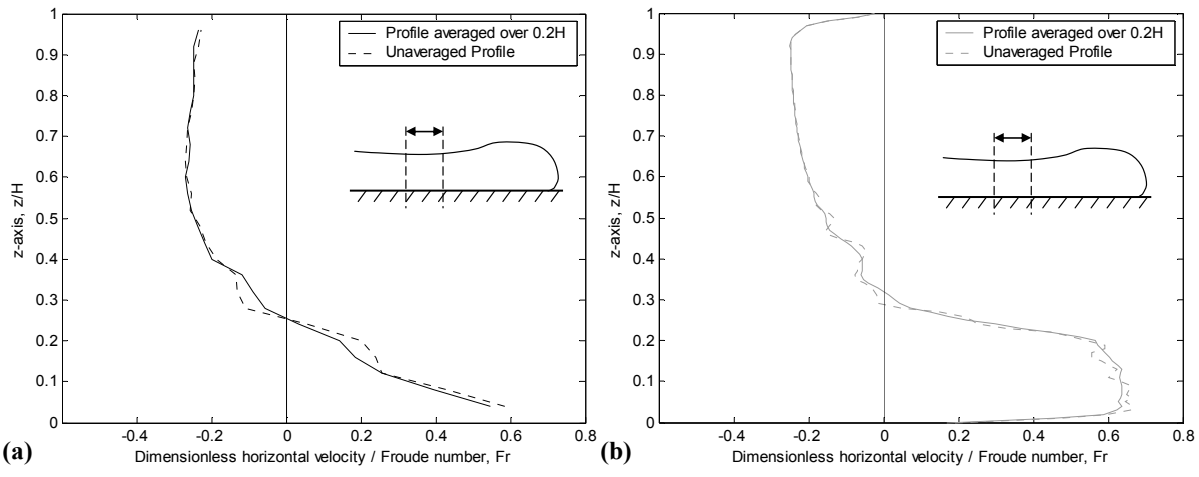

Figure 7-38: Spatially averaged and un-averaged velocity profiles for the horizontal step compartment opening: (a) experimental, (b) numerical.

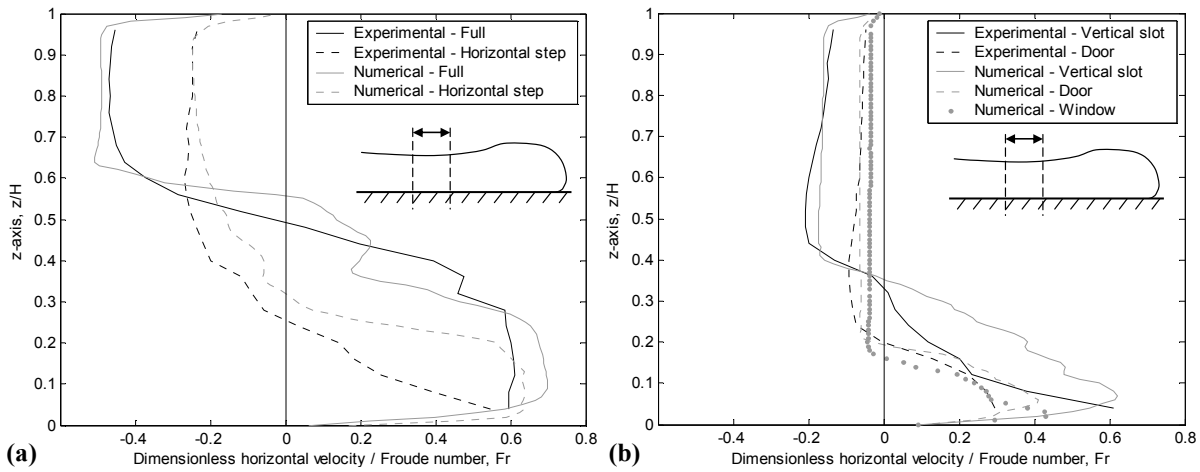

Figure 7-39: Experimental and numerical velocity profiles for different compartment opening geometries: (a) full and horizontal step openings, (b) vertical slot and door openings. Positive indicates flow into the compartment and negative indicates flow out of the compartment.

The experimental velocity profiles were unable to resolve the steep velocity gradients which occurred through the boundary layer, due to the relatively coarse spatial resolution of the experimental velocity fields of approximately 0.04*H*. By comparison the spatial resolution of the numerical velocity fields was approximately 0.01H.

The shape of the velocity profiles was opening geometry dependent. The top and bottom halves of the velocity profile from the full opening geometry were similar in shape, which indicated that the velocities within the gravity current and the counter flowing fluid were similar. At mid depth, in the turbulent mixed layer between the gravity current and counter-flowing fluid, the velocities were significantly lower and more variable. The full opening geometry profiles were similar to the semi-empirical profile suggested by Kneller et al. (1999), shown in Figure 7-40, which was developed for rigid boundary flows with a free surface above and was scaled vertically by the gravity current height (*h*). The gravity current height is approximately half the compartment height ($h \sim 0.5H$) (Simpson 1997).

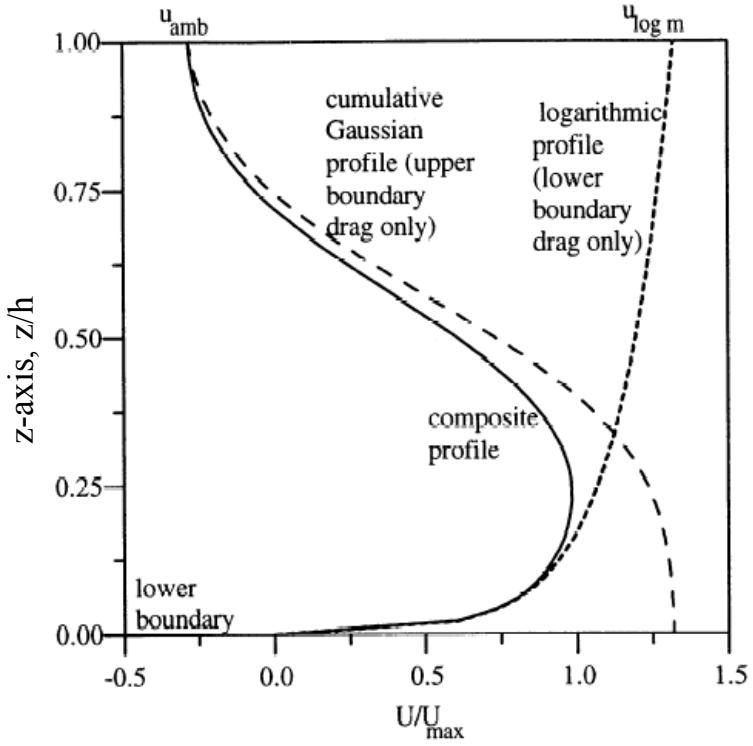

Figure 7-40: Suggested velocity profile for tail of rigid boundary gravity currents with a free surface above. This figure is an extract from Kneller et al. (1999).

The velocity profiles for the horizontal step, vertical slot, door and window opening geometries were a different shape to the full opening velocity profile, due to the increased turbulent mixing. These velocities were large close to the lower boundary and the counter flowing fluid above moved more slowly, but with a relatively uniform velocity.

The height of the maximum velocities within the gravity currents was opening geometry dependent. The approximate heights of the velocity maxima are presented in Table 7-9. For the full opening, the maximum velocity occurred over the range $0.10H < z < 0.20H$, which is comparable to the value of approximately $0.10H$ ($\sim 0.2h$) suggested by Kneller et al. (1999). By contrast the maximum velocity for the other opening geometries was more localised and occurred slightly above the lower boundary, due to the increased mixing that occurred through these openings.

Overall, the velocity profiles showed significantly more variation than the concentration profiles, which were discussed in Section 7.5.5. The increased variation was partially caused

by the two-dimensional nature of the velocity profiles, whereas the concentration profiles were width-integrated.

The shape and magnitude of the experimental and numerical velocity profiles were similar through the counter-flowing region (above the gravity current), but showed more variation within the gravity current, which was believed to be due to the comparatively higher levels of turbulence. Within the gravity currents, the experimental and numerical velocity profiles were comparable for the full and door openings. However, the numerical simulations for the horizontal step and vertical slot openings significantly over-predicted velocities within the gravity current at depths $0.1H < z < 0.3H$ and $0.05H < z < 0.35H$ respectively.

With the limited amount of data available it was not possible to determine whether the substantial differences in the experimental and numerical velocity profiles were associated with the turbulent nature of the flow, or a fundamental difference between the experimental and numerical flows. This is recognised as a limitation of the present study, and is an area where further investigation is required to obtain additional numerical and experimental velocity profile data.

Table 7-9: Approximate height of maximum velocity for the different compartment opening geometries.

Opening Geometry	Approximate height of maximum velocity
Full	0.10H – 0.20H
Horizontal Step	005H - 0.15H
Vertical Slot	0.05H
Door	0.05H
Window	0.05H

7.6.5 Velocity Time-history

The internal horizontal velocity time-history was analysed for a stationary point in the flow, to assess the magnitude of turbulent fluctuations as the gravity current flowed past. The point was located in the centre of the experimental flow field, at $x = 1.39H$, where the experimental data was the most reliable. The vertical location was opening geometry dependent, as shown in Table 7-10, and was situated as close as possible to the height of maximum velocity, which was determined from the velocity profiles in Section 7.6.4. Due to data processing limitations, the experimental periods of analysis were slightly longer than those from the numerical simulations. The point in the flow where these horizontal velocities were measured is indicated schematically by the shaded dot in Figure 7-41 below.

Table 7-10: Vertical location for velocity time-history analysis for different compartment openings.

Opening Geometry	Vertical height of time-history analysis
Full	0.12H
Horizontal Step	0.08H
Vertical Slot	0.04H
Door	0.04H
Window	0.04H

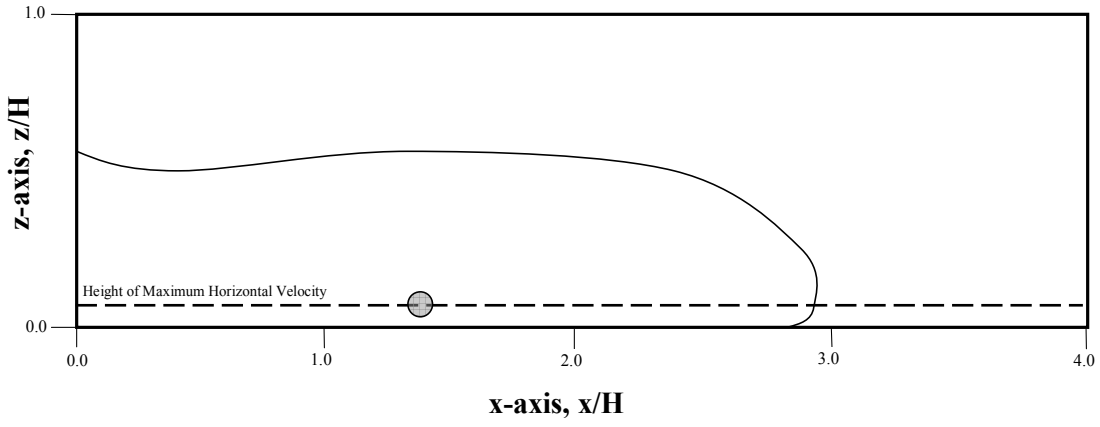

Figure 7-41: Schematic of the region of the flow where the internal horizontal velocity time history was measured. The dashed line represents the height of maximum horizontal velocity and the shaded dot indicates the fixed area of the flow where the average horizontal velocity was measured.

The horizontal velocities were converted to dimensionless form as Froude numbers (based on the compartment height and the initial density difference), as shown in Equation (7-6) below.

$$Fr = \frac{u}{\sqrt{\beta_{initial} g H}} \tag{7-6}$$

The velocity time-histories for each of the different opening geometries are presented in Figure 7-42 (a) to (e). The dashed line in each plot represents the average Froude number for the propagation of the front of the gravity current (from Table 7-2 in Section 7.3.8). For all opening geometries, the rapid increase in Froude number was associated with the arrival of the gravity current front. The arrival time of the front, and the associated ramp up of Froude number was generally captured well by the numerical simulations for all opening geometries. However, the numerical simulations slightly under predicted the front arrival time for the horizontal step and door opening geometries. The fact that the horizontal step opening arrival time was under predicted supported the finding that the numerical simulation over predicted the speed of establishment of the gravity current head (from Section 7.3.5). The reason for the difference in arrival time for the door opening was unclear, as the numerical and experimental front speeds were found to be in agreement in Section 7.3.6.

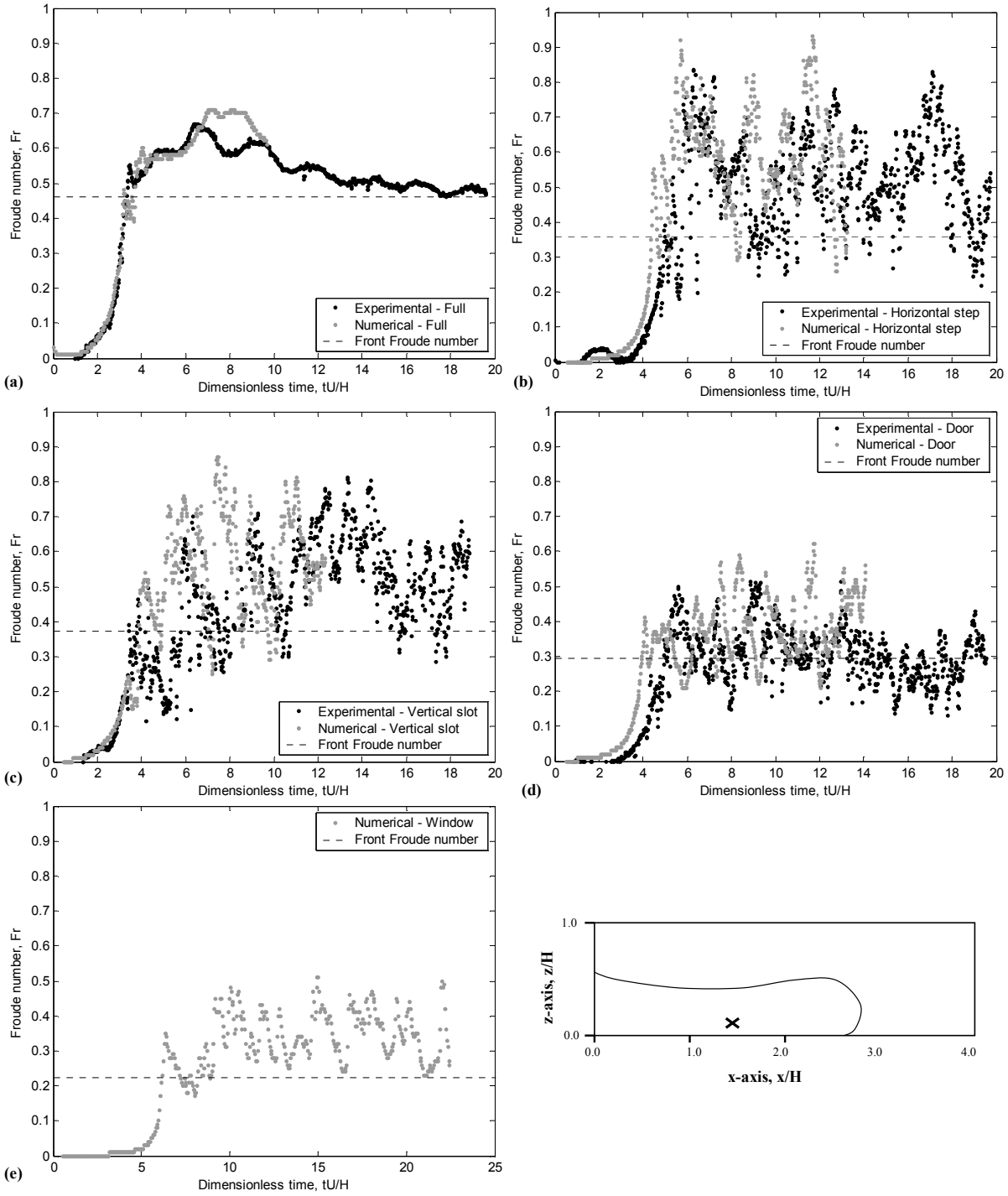

Figure 7-42: Experimental and numerical velocity time-histories for different compartment opening geometries: (a) full, (b) horizontal step, (c) vertical slot, (d) door, (e) window.

The fluctuations in Froude number that occurred after the arrival of the front were associated with the turbulence within the tail of the flow. In general, the magnitude of the Froude numbers and the amount of scatter in the experimental and numerical data was comparable, which indicates that the numerical model successfully replicated the magnitude of the turbulence at the point of the flow being analysed (at $x = 1.39H$ and the depth from Table 7-10).

The amount of scatter for the full opening Froude numbers was significantly less than that for the other opening geometries. This occurred because the shear layer for the full opening was confined to mid-depth, whereas it extended to the lower boundary for the other openings, due to the additional turbulence generated as fluid passed through the respective openings (vertical drop or lateral spreading).

The Froude numbers for the full opening geometry gradually decreased with time, but appeared to level off at a Froude number equal to that of the front. For times in the range $7 < t^* < 9$, the numerical simulation overestimated the magnitude of the Froude number, before converging back to the experimental result. The temporary difference was attributed to the unsteady turbulent nature of the flow, with billows forming and causing turbulence in the tail of the flow at different times in the numerical and experimental flows.

In general, the Froude numbers within the tail appeared to be greater than those at the front of the flow for all opening geometries. This indicated that fluid from the tail was being fed continuously into the head of the flow, which is in agreement with Kneller et al. (1999) who found that average and peak tail velocities were 30% and 50% greater than the peak front velocity respectively. Although not directly comparable to the rigid boundary gravity currents, a study of intrusive lock exchange gravity currents by Lowe et al. (2002) generated comparable results.

7.7 Summary

This chapter has presented and compared the results of experimental and numerical modelling, which investigated gravity currents preceding backdrafts for a number of different compartment opening geometries. Experimental results were generated with saltwater modelling and numerical results were generated with the CFD simulation software FDS. Some of the key findings of the chapter are presented below.

In the later stages of the flows, the bulk front characteristics did not generally change significantly with time and experimental and numerical results were comparable. In this stage, a plot of the local Froude number versus head height for all openings was in agreement with the semi-empirical model from Ungarish and Zemach (2005). This indicated that the front velocities and Froude numbers were governed directly by the local buoyancy conditions. Also, in this stage, the mass fluxes through the compartment openings were shown to be comparable with empirical correlations with literature and the mass fluxes within the head of the gravity currents.

The internal concentration fields and internal velocity fields were found to be highly dependent on opening geometry, due to the varying levels of turbulence and mixing generated by the respective openings. However, the numerical simulations indicted that the concentration fields for all opening geometries, including the three-dimensional openings, were predominantly two-dimensional for front positions greater than approximately 1.5-2.0H.

Generally, experimental and numerical concentration fields were quantitatively similar. However, the numerical concentration fields were slightly lumpier, which was believed to be due to unresolved sub-grid scale eddies, and the relative concentrations for the window opening geometry were over-predicted adjacent to the lower boundary. Numerical potential flammable volumes were over-estimated by 10% to 85%, depending on the opening geometry and the stage in the flow.

Numerical velocity fields were generally in agreement with those from experiment. In general, the numerical simulation accurately predicted the shape and location of streamlines within the head of the flow, the arrival time of the front and the magnitude of turbulent velocity fluctuations within the tail.

CHAPTER 8 CONCLUSIONS

The bulk characteristics and internal flow structure of backdraft gravity currents from a number of different opening geometries were investigated and used to validate the CFD software FDS. Scale saltwater modelling was used to generate Boussinesq, fully turbulent gravity currents for five different opening geometries, typical of fire compartments; a fully open end-wall, a horizontal step, a vertical slot, a door and a window. Experimental concentration and velocity fields were generated using the non-intrusive LA and PTV flow visualisation techniques respectively. Numerical simulations were carried out with FDS to replicate these flows, enabling the experimental and numerical results to be compared directly. The orientation of the results was inverted to match the practical problem being simulated.

Past research (Fleischmann et al. 1993; Fleischmann and McGrattan 1999; Weng and Fan 2002) has also investigated backdraft gravity currents using scale salt-water modelling, however, due to limitations of the experimental flow visualisation techniques employed, a quantitative analysis was only possible for the bulk flow characteristics. The need was identified for additional experiments to provide quantitative measurements of the internal flow structure, an area which has been addressed by the current research.

8.1 Effect of Opening Geometries

The concentration fields showed that the gravity currents generated by the full opening were consistent with lock exchange gravity currents documented in the literature (Fleischmann et al. 1994; Simpson 1997). For front positions greater than approximately 2.0H, a raised nose, approximately 1/8th the depth of the head, was present at the front of the flow, the head angle was approximately 45º and a mixed region existed in the tail region behind the head. Mixing was caused by billows forming at, and breaking off, the head and by lobes and clefts forming due to the gravitational instability of compartment fluid over-run by the nose.

Analysis of the concentration fields for the other opening geometries identified two additional mixing processes, which produced large amounts of mixing adjacent to the opening. These mixing processes were a plume, which formed as fluid flowed though the horizontal step and

window openings, and lateral spreading, which occurred as fluid spread radially after passing through the vertical slot, door and window opening geometries.

Bulk flow characteristics were derived from width-averaged concentration fields. The head heights were based on the equivalent flow depth (assuming no mixing and conservation of buoyancy), the speed of front propagation was used to determine Froude numbers (scaled using the compartment depth, H) and local Froude numbers (scaled using the head height, h). The bulk front characteristics initially fluctuated significantly, but for front positions greater than approximately $x = 3.0H$ did not change appreciably with time. For this phase of the flow, the local Froude numbers were plotted against the head heights for all openings and were shown to closely fit a semi-empirical model from Ungarish and Zemach (2005). This indicated that the local Froude number, and therefore front velocity, of the gravity current head was governed directly by the local buoyancy conditions. The initial conditions, opening geometry and any initial lateral spreading or vertical drops only influenced the local Froude number of the flow indirectly, as they affected internal mixing, which in turn influences the local buoyancy conditions at the gravity current head.

The opening geometry had a large influence on the internal structure of the flows. The concentration fields and velocity fields for the full opening geometry consisted of three distinct layers: an unmixed layer of saltwater flowing out of the compartment along the upper boundary, a central mixed shear layer at mid-depth and an unmixed layer of freshwater flowing into the compartment along the lower boundary. For the other opening geometries, the mixed layer extended down to the lower boundary, due to the increased turbulence generated by these openings.

Potential flammable regions, based on typical initial conditions for backdrafts involving methane fuel (Fleischmann 1994), were identified from the concentration fields. For the full opening geometry, the flammable region was located at mid-depth, except at the head where it curved around the nose at the front of the flow. For the other opening geometries, the flammable region was located close to the lower boundary. Assuming that ignition sources are located near ground level, this may make ignition of full opening geometry backdrafts more difficult.

For the window opening geometry, the flammable region was essentially non-existent for the period of flow investigated. Therefore, a possible fire-fighting tactic could be to ventilate potential backdraft compartments through the smallest hole possible, preventing the formation of flammable mixtures, at least temporarily. Application of water through the opening could then be used to extinguish any potential ignition sources without the risk of a backdraft.

Analysis of the internal velocity fields within the head of the flow identified a single circulation cell for all opening geometries, in agreement with Kneller et al. (1999). This circulation cell transported fluid from the tail through to the nose before being swept back by the counter flowing fluid. For the full opening, the frame of reference was changed to move with the head and the numerical simulation showed two-circulation cells, in agreement with the findings of Thomas et al. (2003). However, the weaker lower cell was not resolved experimentally, due to the coarser spatial resolution of the experimental velocity fields. The velocities within the tail of the flows were found to be greater than the front velocity, which indicated that tail fluid was continuously fed into the head, in agreement with the literature Kneller et al. (1999).

8.2 Validation of Numerical Simulations

In general, the FDS numerical simulations accurately replicated the experimental saltwater flows. The differences that did exist were generally of a similar magnitude as the scatter observed between repeated experiments.

Turbulent flows are a random phenomena (Pope 2000). As the experimental and numerical gravity currents investigated in this study were unsteady and fully turbulent, instantaneous results were not expected to be entirely repeatable and some variability was expected, for example due to eddies forming at slightly different times. However the magnitude of scatter between the experimental and numerical results should be comparable to that between repeated experiments.

The differences between experimental and numerical bulk front characteristics were initially large, but generally converged later in the flow. The differences for the full, horizontal slot, vertical slot, door opening geometries were of a similar magnitude to those observed between repeated experiments. However, the numerical results for the window opening geometry over

predicted the Froude number and head height by approximately 8% when compared with the experimental results, nearly triple the error associated with the other openings.

The numerical compartment opening discharge coefficients for all openings generally converged to a steady state close to the experimental value of 0.6 from Linden (1999). The mass fluxes within the head of the gravity currents were approximated from the bulk flow characteristics and found to be comparable to the mass flux at the compartment inflow.

In general, numerical concentration fields were quantitatively similar to those from experiment, but the numerical fields were slightly lumpier, which was attributed to un-resolved turbulence on scales smaller than the numerical grid ($0.01H$, where H = compartment height). However, the numerical simulation for the window opening geometry over predicted concentrations adjacent to the lower boundary throughout the flow. For the full opening, the numerical simulations under-predicted the rate of break down of turbulent billow structures, which was attributed to slight irregularities, or perturbations, in the experimental initial conditions. This issue was not apparent for the other openings, because the turbulent out of plane motions generated by the respective openings dominated those which developed naturally within the flow. The numerical concentration fields predicted that the gravity current flows from all opening geometries were predominantly two-dimensional for front positions greater than 1.5 to 2.0 compartment heights, in agreement with the experimental observations of Fleischmann (1994). The numerical simulation accurately predicted the location of potential flammable regions for a methane fuel (approximated from the concentration fields), but consistently over-predicted volumes by 10% to 85%, depending on the opening geometry and the stage in the flow.

Comparisons of the internal velocity structure showed that the shape, size and location of experimental and numerical head circulation cells were similar. Numerical and experimental velocity time-histories from a point within the flow were comparable, with numerical results generally predicting both the arrival time of the front and the magnitude of turbulent fluctuations in velocity. Comparisons of experimental and numerical velocity profiles revealed that the shapes and magnitudes were similar through the counter-flowing region, but substantial differences were observed within the gravity currents, partially due to the higher levels of turbulence in this region of the flow.

The differences between the experimental and numerical data for the full, horizontal step, vertical slot and door opening geometries were generally similar to those between the repeated experiments, which suggested that the numerical model was realistically predicting those experimental flows. However, the differences between the experimental and numerical internal flow structure for the window opening geometry were larger, which suggested that there was some fundamental difference between the experimental and numerical flows for the window opening. These differences could either be attributed to errors associated with the experimental technique or the numerical model, but further investigation is required.

8.3 Areas for future investigations

The present research has highlighted a number of areas that could potentially be investigated in future research, as outlined below.

This study revealed that the agreement between the experimental and numerical results for the window opening was significantly worse than for the other four opening geometries investigated. Further work is required to determine if the differences were associated with the experimental technique or the numerical model. The accuracy of the experimental light attenuation flow visualisation technique, which uses line of sight averaging, may have been reduced by the highly three-dimensional nature of the window geometry flow, or the higher salt concentrations required to achieve a turbulent flow. Further experiments using alternative flow visualisation techniques, such as laser induced fluorescence (LIF), are required to investigate. The accuracy of the numerical model may have been compromised by the reduced scale of the window geometry flow, which effectively reduced the grid resolution of the window opening geometry. Additional numerical simulations at finer grid resolutions should be completed to examine this possibility.

This study investigated isothermal gravity currents with Boussinesq density differences. However, backdraft gravity currents may be driven by large temperature variations, where density differences are non-Boussinesq and heat transfer effects are important. Therefore, an extension of the current study could investigate non-Boussinesq flows with heat transfer to identify fundamental differences in the flow behaviour and validate the ability of FDS to simulate these types of flows, which are common in fire scenarios.

Due to the computational restraints associated with this investigation, the grid size could not be reduced below 1% of the compartment height (0.01H). The sensitivity analysis revealed that even at this grid resolution some variability occurred in the results. The numerical grid resolution could be further refined to determine if the experimental and numerical results would converge further and to determine if the apparent lumpiness observed in the numerical concentration fields would decrease.

The present study was not able to determine the cause of the substantial differences observed in the experimental and numerical velocity profiles. Further investigation, involving additional experiments and numerical simulations, is required to determine whether the differences in velocity profiles were associated with the turbulent nature of the flow, or a fundamental difference between the experimental and numerical flows.

The potential flammable regions identified within the flows assumed a methane fuel. The effect of more realistic fuels on the location and extent of the potential flammable regions could be investigated. However, typical initial gas mass fractions would first need to be established experimentally.

Backdrafts commonly occur in residential and industrial locations, where objects, such as desks, shelves and crates, would obstruct the gravity current flows and possibly enhance the level of turbulent mixing. Therefore, realistic objects could be located within the flow field to determine the effects on mixing within backdraft gravity current flows.

CHAPTER 9 REFERENCES

Ballard, C. E. (2004). "The dynamics of free surface gravity currents in lock exchange flows," ME Thesis. Department of Civil Engineering, University of Canterbury, Christchurch, New Zealand.

Barr, D. I. H., and Hassan, A. M. M. (1963). "Densimetric exchange flow in rectangular channels." *Houille Blanche*, 18(7), 739-766.

Baum, H. R. (2000). "Large eddy simulations of fires: from concepts to computations." *Fire Protection Engineering*(Number 6), 36 - 42.

Baum, H. R., Cassel, K. W., McGrattan, K. B., and Rehm, R. G. (1995). "Gravity-current transport in building fires." International Conference on Fire Research and Engineering, Orlando, Florida, 27 - 32.

Baum, H. R., McGrattan, K. B., and Rehm, R. G. (1996). "Large eddy simulations of smoke movement in three dimensions." Interflam '96. International Interflam Conference, C. A. Franks and S. Grayson, eds., London, England, 189-198.

Baum, H. R., McGrattan, K. B., and Rehm, R. G. (1997). "Three-dimensional simulations of fire plume dynamics." Fire Safety Science - Proceedings of the Fifth International Symposium, International Association for Fire Safety Science, 511- 522.

Baum, H. R., and Rehm, R. G. (1984). "Calculations of three dimensional buoyant plumes in enclosures." *Combustion Science and Technology*, 40, 55-77.

Baum, H. R., Rehm, R. G., Barnett, P. D., and Corley, D. M. (1981). "Finite difference calculations of buoyant convection in an enclosure. I. The basic algorithm." National Bureau of Standards, Washington, Washington, DC.

Baum, H. R., Rehm, R. G., and Mulholland, G. W. (1982). "Computation of fire induced flow and smoke coagulation." Nineteenth Symposium (International) on Combustion, The Combustion Institute, Pittsburgh, 921-931.

Baum, H. R. M., K. B.; Rehm, R. G. (1994). "Mathematical modeling and computer simulation of fire phenomena." International Association for Fire Safety Science, 4th International Symposium, M. A. Kashiwagi, ed., Ottawa, Ontario, Canada, 185-193.

Benjamin, T. B. (1968). "Gravity currents and related phenomena." *Journal of Fluid Mechanics*, 31, 209-248.

Beyler, C. (2002). "Flammability limits of premixed and diffusion flames." The SFPE handbook of fire protection engineering, P. J. DiNenno, ed., National Fire Protection

Association ; Society of Fire Protection Engineers, Quincy, Mass. Bethesda, MD., 2-172.

Britter, R. E., and Simpson, J. E. (1978). "Experiments on the dynamics of a gravity current head." *Journal of Fluid Mechanics*, 88(pt 2), 223-240.

Brown, W. G., and Solvason, K. R. (1962). "Natural convection through rectangular openings in partitions. Part I. Vertical partitions. Part II. Horizontal partitions." National Research Council of Canada, Division of Building Research, Ottawa (Ontario), Canada.

Bukowski, R. W. (1996). "Modelling a backdraft incident: The 62 Watts Street (New York) fire." *Fire Engineers Journal*, 56(185), 14-17.

Cenedese, C., and Dalziel, S. (1998). "Concentration and depth field determined by the light transmitted through a dyed solution." 8th International Symposium on Flow Visualisation (1998), C. Grant, ed., Sorrento, Italy.

Clement, J. M. (2000). "Experimental verification of the fire dynamics simulator (FDS) hydrodynamic model," Ph.D Thesis. Department of Civil Engineering, University of Canterbury, Christchurch, New Zealand.

Cox, G., and Kumar, S. (2002). "Modeling enclosure fires using CFD." The SFPE handbook of fire protection engineering, P. J. DiNenno, ed., National Fire Protection Association ; Society of Fire Protection Engineers, Quincy, Mass. Bethesda, MD., 3-194 to 3-218.

DiNenno, P. J. (2002). *The SFPE handbook of fire protection engineering*, National Fire Protection Association ; Society of Fire Protection Engineers, Quincy, Massachusetts.

Dunne, T. (2002). "Delayed backdraft: What we learned." Fire Engineering Magazine, 32 - 40.

Ezer, T. (2005). "Entrainment, diapycnal mixing and transport in three-dimensional bottom gravity current simulations using the Mellor-Yamada turbulence scheme." *Ocean Modelling*, 9(2), 151-168.

Fleischmann, C., Pagni, P., and Williamson, R. (1993). "Exploratory backdraft experiments." *Fire Technology*, 29(4), 298-316.

Fleischmann, C., Pagni, P., and Williamson, R. (1994). "Salt water modeling of fire compartment gravity currents." Fire Safety Science- Proceedings of the Fourth International Symposium, International Association for Fire Safety Science, Ottawa, ON, Canada, 253-64.

Fleischmann, C. M. (1994). "Backdraft phenomena." *NIST-GCR-94-646*, National Institute of Standards and Technology, Gaithersburg, MD.

Fleischmann, C. M., and McGrattan, K. B. (1999). "Numerical and experimental gravity currents related to backdrafts." *Fire Safety Journal*, 33(1), 21-34.

Forney, G. P., and McGrattan, K. B. (2004). *User's guide for smokeview version 4: A tool for visualizing fire dynamics simulation data*, Building and Fire Research Laboratory and National Institute of Standards and Technology, Gaithersburg, MD 20899.

Foster, J. A., and Roberts, G. V. (2003). "An experimental investigation of backdraught." *82*, Fire Research Division, Office of the Deputy Prime Minister, London.

Frederikse, H. P. R., and Lide, D. R. (1997). *CRC handbook of chemistry and physics*, CRC Press, Cleveland, Ohio.

Gojkovic, D., and Bengtsson, L. (2001). "Some theoretical and practical aspects on fire-fighting tactics in a backdraft situation." InterFlam 2001: 9th International Fire Science & Engineering Conference, Edinburgh, Scotland, pp. 1093-1104.

Gottuk, D. T., Peatross, M. J., Farley, J. P., and Williams, F. W. (1999). "The development and mitigation of backdraft: a real-scale shipboard study." *Fire Safety Journal*, 33(4), 261-282.

Grimwood, P., and Desmet, K. (2003). "Tactical firefighting: A comprehensive guide to compartment firefighting and live fire training, version 1.1." http://www.firetactics.com/TAC-VENT2.pdf, date accessed 04/2006.

Grobelbauer, H. P., Fannelop, T. K., and Britter, R. E. (1993). "The propagation of intrusion fronts of high density ratios." *Journal of Fluid Mechanics*, 250, 669-87.

Hacker, J., Linden, P. F., and Dalziel, S. B. (1996). "Mixing in lock-release gravity currents." *Dynamics of Atmospheres and Oceans*, 24(1-4), 183-195.

Hume, B. (2005). "Firefighting in under-ventilated compartments: Literature review." *Fire Research Technical Report 5*, Office of the Deputy Prime Minister, London.

Huppert, H. (1982). "Flow and instability of a viscous current down a slope." *Nature*, 300, 427-429.

Huppert, H. E. (2006). "Gravity currents: A personal perspective." *Journal of Fluid Mechanics*, 554, 299-322.

Huppert, H. E., and Simpson, J. E. (1980). "Slumping of gravity currents." *Journal of Fluid Mechanics*, 99(pt 4), 785-799.

Incropera, F. P., and DeWitt, D. P. (2001). *Fundamentals of heat and mass transfer*, Wiley, New York.

International Organization for Standardization. (1993). "ISO 9705:1993 Fire tests - Full-scale room test for surface products." Geneva, Siwtzerland.

Karlsson, B., and Quintiere, J. G. (2000). *Enclosure fire dynamics*, CRC Press, Boca Raton, Florida.

Kikkert, G. A. (2006). "Buoyant jets with two and three-dimensional trajectories," Ph. D. Thesis, Department of Civil Engineering, University of Canterbury, Christchurch, New Zealand.

Klote, J. H., and Milke, J. A. (2002). *Principles of smoke management*, American Society of Heating Refrigerating and Air-Conditioning Engineers,
Society of Fire Protection Engineers., Atlanta, Ga.

Kneller, B. C., Bennett, S. J., and McCaffrey, W. D. (1997). "Velocity and turbulence structure of density currents and internal solitary waves: potential sediment transport and the formation of wave ripples in deep water." *Sedimentary Geology*, 112(3-4), 235.

Kneller, B. C., Bennett, S. J., and McCaffrey, W. D. (1999). "Velocity structure, turbulence and fluid stresses in experimental gravity currents." *Journal of Geophysical Research*, Volume 104(Issue C3), 5381 - 5392.

Linden, P. F. (1999). "Fluid mechanics of natural ventilation." Annual Reviews Inc, Palo Alto, CA, USA, 201-238.

Lowe, R. J., Linden, P. F., and Rottman, J. W. (2002). "A laboratory study of the velocity structure in an intrusive gravity current." *Journal of Fluid Mechanics*, 456(456), 33-48.

Lowe, R. J., Rottman, J. W., and Linden, P. F. (2005). "The non-Boussinesq lock-exchange problem. Part 1. Theory and experiments." *Journal of Fluid Mechanics*, 537, 101-124.

Marino, B. M., Thomas, L. P., and Linden, P. F. (2005). "The front condition for gravity currents." *Journal of Fluid Mechanics*, 536, 49-78.

Mashuga, C. V., and Crowl, D. A. (1998). "Application of the flammability diagram for evaluation of fire and explosion hazards of flammable vapors." *Process Safety Progress*, 17(3), 176-183.

McCaffrey, B. J. (1979). "Purely buoyant diffusion flames: Some experimental results." *NBSIR 79-1910*, National Bureau of Standards, Washington, DC 20234.

McGrattan, K. B. (2004a). *Fire dynamics simulator (version 4): Technical reference guide*, Building and Fire Research Laboratory and National Institute of Standards and Technology, Gaithersburg, MD 20899.

McGrattan, K. B. (2004b). *Fire dynamics simulator (version 4): User's guide*, Building and Fire Research Laboratory and National Institute of Standards and Technology, Gaithersburg, MD 20899.

McGrattan, K. B. (2005). "Fire dynamics simulator (version 4.06)." Building and Fire Research Laboratory and National Institute of Standards and Technology, Gaithersburg, MD 20899.

McGrattan, K. B., Rehm, R. G., and Baum, H. R. (1994). "Fire-driven flows in enclosures." *Journal of Computational Physics*, 110(2), 285-291.

McGrattan, K. B., Rehm, R. G., Tang, H. C., and Baum, H. R. (1992). "A Boussinesq algorithm for buoyant convection in polygonal domains." *NISTIR 4831*, National Institute of Standards and Technology, Gaithersburg, MD 20899.

Nelson, H. E. (2002). "From phlogiston to computational fluid dynamics." *Fire Protection Engineering*, 13(Winter 2002), 9 - 16.

Nokes, R. (2006a). "Fluidstream version 6.03." University of Canterbury, Department of Civil Engineering, Christchurch, New Zealand, Particle tracking velocimetry software.

Nokes, R. (2006b). *Fluidstream version 6.03: System theory and design*, University of Canterbury, Department of Civil Engineering, Christchurch, New Zealand.

Nokes, R. (2006c). *Fluidstream version 6.03: User's guide*, University of Canterbury, Department of Civil Engineering, Christchurch, New Zealand.

Nokes, R. (2006d). "Imagestream version 5.02." University of Canterbury, Department of Civil Engineering, Christchurch, New Zealand, Image processing software.

Nokes, R. (2006e). *Imagestream version 5.02: System theory and design*, University of Canterbury, Department of Civil Engineering, Christchurch, New Zealand.

Nokes, R. (2006f). *Imagestream version 5.02: User's guide*, University of Canterbury, Department of Civil Engineering, Christchurch, New Zealand.

Patterson, M. D., Simpson, J. E., Dalziel, S. B., and Nikiforakis, N. (2005). "Numerical modelling of two-dimensional and axisymmetric gravity currents." *International Journal for Numerical Methods in Fluids, 8th ICFD Conference on Numerical Methods for Fluid Dynamics: Part 2*, 47(10-11), 1221-1227.

Perry, R. H., Green, D. W., and Maloney, J. O. (1997). *Perry's chemical engineers' handbook*, McGraw-Hill, New York.

Plew, D. R. (2005). "The hydrodynamic effects of long-line mussel farms," Ph.D Thesis. Department of Civil Engineering, University of Canterbury, Christchurch, New Zealand.

Pope, S. B. (2000). *Turbulent flows*, Cambridge University Press, Cambridge ; New York.

Rehm, R. G., and Baum, H. R. (1978). "The equations of motion for thermally driven, buoyant flows." *Journal of Research of the National Bureau of Standards*, Vol 83(No. 3), 297-308.

Rehm, R. G., McGrattan, K. B., Baum, H. R., and Cassel, K. W. (1997). "Transport by gravity currents in building fires." Fifth (5th) International Symposium Fire Safety Science, Y. Hasemi, ed., International Association for Fire Safety Science, Melbourne, Australia, 391-402.

Reynolds, A. (1976). "The variation of turbulent Prandtl and Schmidt numbers in wakes and jets." *International Journal of Heat and Mass Transfer*, 19, 757-764.

Rottman, J. W., and Simpson, J. E. (1983). "Gravity currents produced by instantaneous releases of a heavy fluid in a rectangular channel." *Journal of Fluid Mechanics*, 135, 95-110.

Rubini, P. (2006). "Simulation of fires in enclosures (SOFIE)." Cranfield University, Bedfordshire, MK43 0AL, England.

Shin, J. O., Dalziel, S. B., and Linden, P. F. (2004). "Gravity currents produced by lock exchange." *Journal of Fluid Mechanics*, 521, 1-34.

Shore, D. (1996). "Making the flare safe." *Journal of Loss Prevention in the Process Industries*, 9(6), 363-381.

Simpson, J. E. (1997). *Gravity currents in the environment and the laboratory*, Cambridge University Press, Cambridge, U.K. ; New York, NY, USA.

Smagorinsky, J. (1963). "General circulation experiments with the primitive equations. I. The basic experiment." *Monthly Weather Review*, 91(3), 99-164.

Steckler, K. D., Baum, H. R., and Quintiere, J. G. (1986). "Salt water modeling of fire induced flows in multicompartment enclosures." Twenty-first Symposium (International) on Combustion, The Combustion Institute, 143-149.

Street, R. L., Watters, G. Z., and Vennard, J. K. (1996). *Elementary fluid mechanics*, J. Wiley, New York.

Tannehill, J. C., Anderson, D. A., and Pletcher, R. H. (1997). *Computational fluid mechanics and heat transfer*, Taylor & Francis, Washington, DC.

Thomas, L. P., Dalziel, S. B., and Marino, B. M. (2003). "The structure of the head of an inertial gravity current determined by particle-tracking velocimetry." *Experiments in Fluids*, 34(6), 708-716.

Tieszen, S. R. (2001). "On the fluid mechanics of fires." *Annual Review of Fluid Mechanics*, 33, 67-92.

U.S. Nuclear Regulatory Commission, and Electric Power Research Institute. (2006). "Verification and validation of selected fire models for nuclear power plant applications, volume 6: Fire dynamics simulator (FDS)." *NUREG-1824 and EPRI 1011999*, U.S. Nuclear Regulatory Commission. Office of Nuclear Regulatory Research (RES). Rockville. MD. 2005 and Electric Power Research Institute (EPRI). Palo Alto. CA.

Ungarish, M., and Zemach, T. (2005). "On the slumping of high Reynolds number gravity currents in two-dimensional and axisymmetric configurations." *European Journal of Mechanics, B/Fluids*, 24(1), 71-90.

Weng, W., Fan, W., Yang, L., and Qin, J. (2002a). "Study on gravity currents prior to backdrafts in building fires with different opening geometries." Progress in Safety Science and Technology, Oct 10-13 2002, Science Press, Taian, China, 1194-1198.

Weng, W. G., and Fan, W. C. (2002). "Experimental and numerical study on salt water modeling of gravity current prior to backdraft in compartment." *Journal of Applied Fire Science*, 11(3), 279-289.

Weng, W. G., and Fan, W. C. (2003). "Critical condition of backdraft in compartment fires: A reduced-scale experimental study." *Journal of Loss Prevention in the Process Industries*, 16(1), 19-26.

Weng, W. G., Fan, W. C., and Hasemi, Y. (2005). "Prediction of the formation of backdraft in a compartment based on large eddy simulation." *Engineering Computations (Swansea, Wales)*, 22(4), 376-392.

Weng, W. G., Fan, W. C., Qin, J., and Yang, L. Z. (2002b). "Study on salt water modeling of gravity currents prior to backdrafts using flow visualization and digital particle image velocimetry." *Experiments in Fluids*, 33(3), 398-404.

Yimer, I., Campbell, I., and Jiang, L.-Y. (2002). "Estimation of the turbulent Schmidt number from experimental profiles of axial velocity and concentration for high-Reynolds-number jet flows." *Canadian Aeronautics and Space Journal*, 48(3), 195-200.

Zhu, J. B., Lee, C. B., Chen, G. Q., and Lee, J. H. W. (2006). "PIV observation of instantaneous velocity structure of lock release gravity currents in the slumping phase." *Communications in Nonlinear Science and Numerical Simulation*, 11(2), 262-270.

APPENDIX A

A.1 FDS Historical Development

The Fire Dynamics Simulator (FDS) model has been under rapid development for the last 25 years. This development has been assisted by the advances in computing power, which have occurred over the same time period.

The conservation equations for mass, momentum and energy are the fundamental partial differentials equations that describe the flow of incompressible fluids and were first published over 150 years ago. It is not possible to solve the three-dimensional equations analytically (Klote and Milke 2002) and computationally demanding numerical solutions are required.

In 1978, Rehm and Baum (1978) derived as set of simplified equations that described buoyant movement in fire driven gas flows. They are referred to as low Mach number equations because they do not contain any description of the high frequency acoustic waves that can occur in an elastic fluid. The advantage of filtering out the sound waves that travel faster than those of typical fire applications is that the time step in the numerical solution is determined by flow speeds and not the speed of sound (Klote and Milke 2002), which reduces numerical computation requirements.

The low Mach number equations describe the low speed motion of a gas driven by a chemical heat release and buoyancy forces and incorporate compressibility effects sufficient for thermally driven flows of smoke and hot gases generated in a fire (Klote and Milke 2002). The equations used a spatially uniform mean pressure in both the energy equation and the equation of state, with the spatially non-uniform pressure only appearing in the momentum equation (Rehm and Baum 1978). This means that pressure remains nearly constant in space, but allows for significant variations in density and temperature, typical of fire scenarios.

Rehm and Baum (1978) also demonstrated that the low Mach number equations reduced to the Boussinesq equations, when the rate heat addition was low. The Boussinesq equations can be applied when the density variations are small and assume that the density is constant except where the density difference produces a buoyancy force (Rehm and Baum 1978) reducing the computational requirements.

Soon after development of these governing equations, the first large eddy simulation (LES) simulations were carried out. Baum, Rehm, Barnett and Corley (1981) conducted simulations to model the flow of a two-dimensional, inviscid, non-conducting gas using the Bouissinesq form of the governing equations developed by Rehm and Baum (1978). Fictitious particles were introduced to simulate smoke flow. The work was extended to three-dimensions a few years later (Baum and Rehm 1984). The Boussinesq approximation was still employed, to retain the computational efficiency of the model.

By the early 1990's the advances of computer technology meant that the computations could be extended to include the effects of viscous dissipation and thermal conductivity within the Boussinesq equations (McGrattan et al. 1994; McGrattan et al. 1992). The inclusion of viscous effects meant the grid had to be sufficiently small to resolve boundary layers, so calculations were limited to two dimensions. The orientation of gravity was made a variable, to simplify studies of inclined room geometries. A Schwarz-Christoffel transformation was used to map a polygonal domain onto a rectangular one, so that the rectilinear governing equations could be applied to non-rectangular geometries. The disadvantage of using the transformation was that grid distortion created severe variations in grid cell size around obstructions in the domain, which significantly limited the time-step for the computation (McGrattan et al. 1992).

In the mid 1990's the simulations incorporating viscous and heat transfer effects were extended to three dimensions for both Boussinesq and non-Boussinesq flows (Baum et al. 1996; Rehm et al. 1997). In addition, the equations of motion were expanded to consider the motion of an ideal thermally expandable gas. The polygon mapping routine was removed from the model, to increase computational efficiency, and instead obstructions could be incorporated into a simulation as masked cells.

In 2000, Version 1.0 of the computer software Fire Dynamics Simulator was publicly released. The hydrodynamic solver was based on these low Mach number equations originally presented by Rehm and Baum (1978) and the developments discussed above. The software has undergone regular updates, with the latest version of Fire Dynamics Simulator, Version 4 released in 2005.

A.2 Sample Fire Dynamics Simulator Input File

A sample Fire Dynamics Simulator (FDS) input file is presented below. The input file can be modified in any text editor. The different boundary slip conditions were generated by changing the "SURF_DEFAULT" parameter in the "MISC" line to the appropriate condition from the *Boundary Condition* section. The different opening conditions were specified by adding "&" symbols to the appropriate "OBST" and "HOLE" lines in the *Opening Condition* section.

```
**********************************************************************************************************
                                                Thesis - James McBryde
                                            Fire Dynamics Simulator (Version 4)
**********************************************************************************************************
&HEAD CHID='Full_halfslip_600',TITLE='Final' /
&TIME TWFIN=22. /
&PDIM XBAR0=0.00,XBAR=1.512,YBAR=0.126,ZBAR=0.385 /
&GRID IBAR=600.,JBAR=50.,KBAR=150. /
&OBST XB=0.229,1.512,0.00,0.50,0.00,0.133 /
&MISC NFRAMES=100,GVEC=0,0,-9.805,ISOTHERMAL=.TRUE., INCOMPRESSIBLE=.TRUE.,
      SURF_DEFAULT='1/4slip',BACKGROUND_SPECIES='fresh',DENSITY=998.2,VISCOSITY=0.001002,SC=1. /
&SPEC ID='salt',DENSITY=1003.191,VISCOSITY=0.001002 /
&INIT XB=0.252,1.512,0.00,0.126,0.133,0.385,QUANTITY='salt',VALUE=1003.191 /
**********************************************************************************************************
                                                Boundary Conditions
**********************************************************************************************************
&VENT XB=0.000,0.000,0.000,0.126,0.000,0.385,SURF_ID='OPEN' /
&VENT XB=0.000,1.512,0.126,0.126,0.000,0.385,SURF_ID='MIRROR',COLOR='INVISIBLE' /
&SURF ID='fullslip', VBC=1.0,  RGB=0.80,0.80,0.70 /
&SURF ID='3/4slip',  VBC=0.5,  RGB=0.80,0.80,0.70 /
&SURF ID='halfslip', VBC=0.0,  RGB=0.80,0.80,0.70 /
&SURF ID='1/4slip',  VBC=-0.5, RGB=0.80,0.80,0.70 /
&SURF ID='noslip',   VBC=-1.0, RGB=0.80,0.80,0.70 /
**********************************************************************************************************
                                                Opening Condition
**********************************************************************************************************
      Horizontal Step
OBST XB=0.252,0.252,0.000,0.126,0.133,0.385 /
HOLE XB=0.242,0.262,0.000,0.126,0.133,0.259 /
      Vertical Slot
OBST XB=0.252,0.252,0.000,0.126,0.133,0.385 /
HOLE XB=0.242,0.262,0.084,0.126,0.133,0.385 /
      Door
OBST XB=0.252,0.252,0.000,0.126,0.133,0.385 /
HOLE XB=0.242,0.262,0.084,0.126,0.217,0.385 /
      Window
OBST XB=0.252,0.252,0.000,0.126,0.133,0.385 /
HOLE XB=0.242,0.262,0.084,0.126,0.217,0.301 /
**********************************************************************************************************
                                                Output Files
**********************************************************************************************************
&SLCF DTSAM=0.4,PBY=0.126,QUANTITY='DENSITY' /
&SLCF DTSAM=0.4,PBZ=0.375,QUANTITY='DENSITY' /
&SLCF DTSAM=0.4,PBY=0.126,QUANTITY='U-VELOCITY' /
&SLCF DTSAM=0.4,PBY=0.126,QUANTITY='W-VELOCITY' /
&ISOF DTSAM=1.0,QUANTITY='DENSITY',VALUE(1)=998.3,VALUE(2)=1000.7,VALUE(3)=1003.1 /
&PL3D DTSAM=1.0,WRITE_XYZ=.TRUE.,QUANTITIES(1)='DENSITY',QUANTITIES(5)='VELOCITY' /
&THCP XB=0.252,0.252,0.00,0.126,0.133,0.385,QUANTITY='MASS FLOW',LABEL='Mass-Flow' /
&THCP XB=0.252,0.252,0.00,0.126,0.133,0.385,QUANTITY='VOLUME FLOW',LABEL='Vol-Flow' /
&THCP DTSAM=0.04167,XYZ=0.602,0.126,0.355,QUANTITY='U-VELOCITY',LABEL='U-Vel-history' /
**********************************************************************************************************
&TAIL /
**********************************************************************************************************
```

APPENDIX B

B.1 Light Attenuation Theory

The absorption theory of Lambert-Beer, shown in Equation (1) (Cenedese and Dalziel 1998), may be used to describe light attenuation with distance, as a ray of light passes through a dyed fluid.

$$\frac{dI}{dp} = -\eta I \tag{1}$$

where: I = light intensity

p = distance along light ray

η = rate of light absorption

For a fluid with a uniform dye concentration, c, and a thickness, h, Equation (1) may be integrated along the path of the light ray (from $p = 0$ to $p = h_f$) to give the attenuation ratio shown in Equation (2). In this equation, light intensity is a function of dye concentration and distance along the light ray.

$$\frac{I\left(h_f, c\right)}{I\left(0, c\right)} = e^{-\eta h_f} \tag{2}$$

where: c = dye concentration

$I\left(h_f, c\right)$ = light intensity leaving dyed fluid

$I\left(0, c\right)$ = light intensity entering dyed fluid

h_f = thickness of dyed fluid

c = concentration of dyed fluid

For low dye concentrations, a linear relationship exists between the rate of light attenuation and dye concentration (Cenedese and Dalziel 1998), as shown in Equation (3).

$$\eta = f(c) = (1/a)c + b \tag{3}$$

where: a = empirical constant relating concentration to rate of light attenuation

b = rate of attenuation with no dye present in the fluid

The attenuation ratio may now be written as shown in Equation (4).

$$\frac{I(h_f, c)}{I(0, c)} = e^{-\eta h_f} = e^{-((1/a)c+b)h_f} = e^{-(1/a)ch_f} e^{-bh_f} \tag{4}$$

When no dye is present in the fluid, $c = 0$ the attenuation ration may be written as shown in Equation (5).

$$\frac{I(h_f, 0)}{I(0, 0)} = e^{-f(c)h_f} = e^{-bh_f} \tag{5}$$

where: $I(h_f, 0)$ = light intensity leaving un-dyed fluid

$I(0, 0)$ = light intensity entering un-dyed fluid

Dividing Equation (4) by Equation (5), eliminates the dependence on the term e^{-bh_f} giving Equation (6). Using Equation (6), light intensities leaving the fluid may be used may be used to determine the dye concentration, dependence on the intensity of light entering the fluid is eliminated. Experimentally this means that light intensities may be measured at a single location instead of at multiple locations.

$$\frac{I(h_f, c)}{I(0, c)} \Big/ \frac{I(h_f, 0)}{I(0, 0)} = \frac{I(h_f, c)}{I(h_f, 0)} = e^{-(1/a)ch_f} \tag{6}$$

The attenuation ratio, in Equation (6), is dependent on the product of the fluid thickness and dye concentration, which is also known as the integrated dye concentration. Using simpler notation, Equation (6) may be written as shown in Equation (7). This equation predicts that the light passing through a dyed fluid will decay exponentially as the integrated dye concentration is increased.

$$ch_f = a \ln\left(\frac{I_0}{I}\right) \tag{7}$$

where: $I =$ light intensity leaving dyed fluid

$I_0 =$ light intensity leaving un-dyed fluid

APPENDIX C

C.1 List of Experimental Parameters

The following lists outline the experimental parameters and the associated symbols which are presented graphically in this section.

Dimensionless Parameter	Definition
$x^* = \frac{x}{H}$	Dimensionless distance lengthways down compartment
$z^* = \frac{z}{H}$	Dimensionless distance vertical
$t^* = \frac{tU}{H} = \frac{t\sqrt{\beta_{initial} gH}}{H}$	Dimensionless time
$U = \sqrt{\beta_{initial} gH}$	Dime
$\beta_{initial} = \frac{\Delta\rho_{initial}}{\rho_{comp}}$	Dimensionless initial density difference
$R = \frac{\Delta\rho}{\Delta\rho_{initial}}$	Relative concentration; 0% = ambient fluid (fresh water) 100% = compartment fluid (salt water)

Symbol	Definition	Units
t	Time	s
x	Horizontal co-ordinate lengthways down compartment	m
z	Vertical co-ordinate	m
H	Compartment height	m
Fr	Froude number with based on compartment height	-
R	Relative concentration	-
U	Velocity scale	$m.s^{-1}$
ρ_{comp}	Initial density of compartment	$kg.m^{-3}$
$\Delta\rho$	Density difference	$kg.m^{-3}$
$\Delta\rho_{initial}$	Initial density difference	$kg.m^{-3}$
$\beta_{initial}$	Dimensionless initial density difference	-

C.2 Relative Concentration Field Time Sequences

Width-integrated relative concentration field time sequences are presented below for the different opening geometries for both the experimental and numerical flows. The sequences consist of six frames for each of the flows. The relative concentrations are expressed as a percentage of saltwater (0% indicates freshwater, 100% indicates saltwater).

Experimental – Full opening

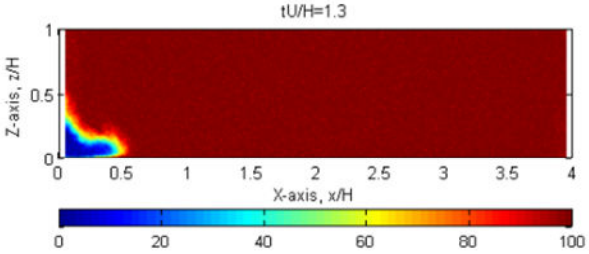

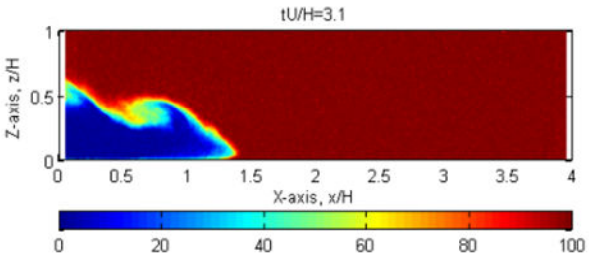

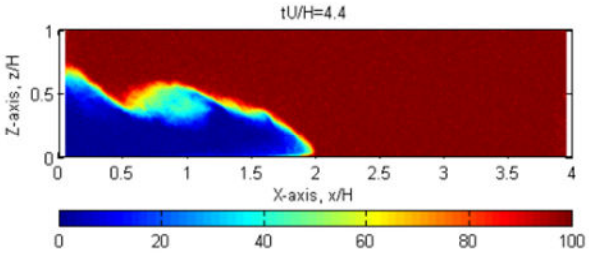

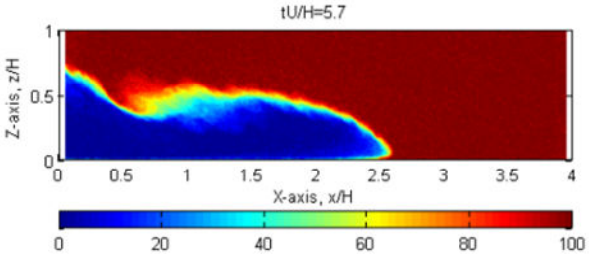

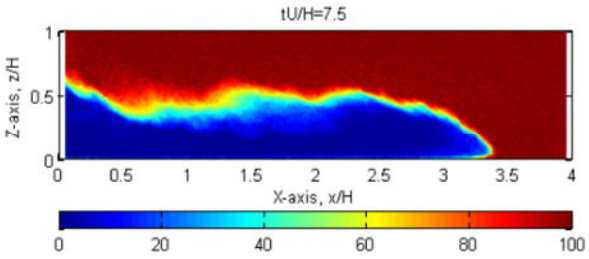

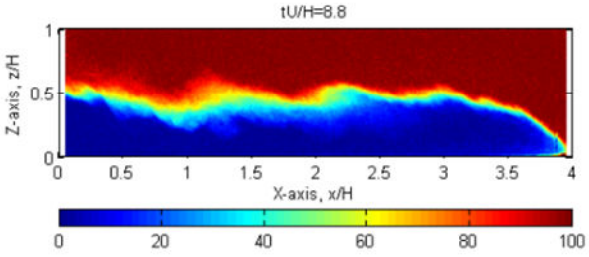

Numerical – Full opening

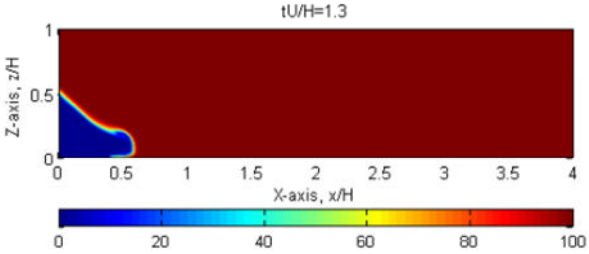

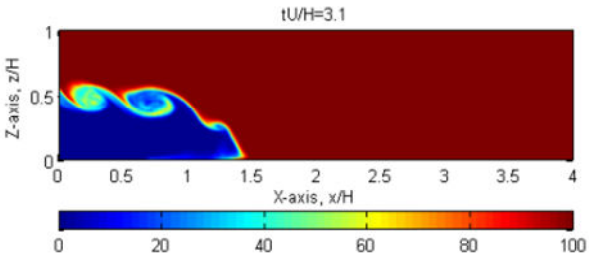

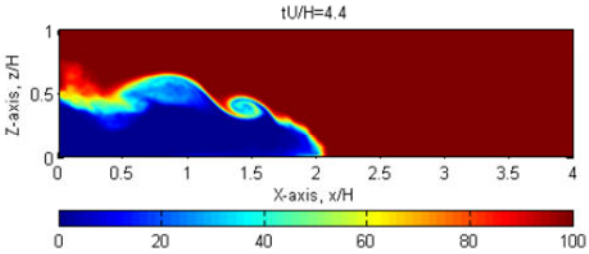

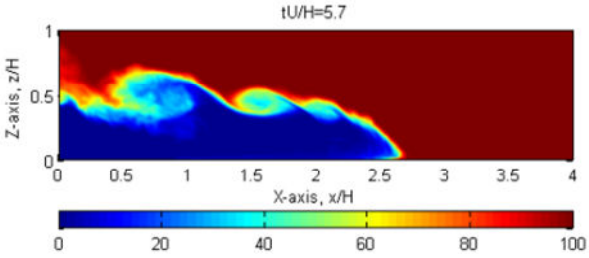

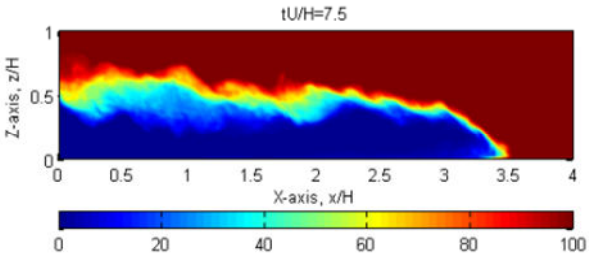

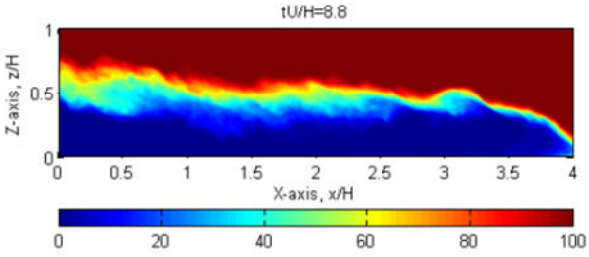

Experimental – Horizontal step opening

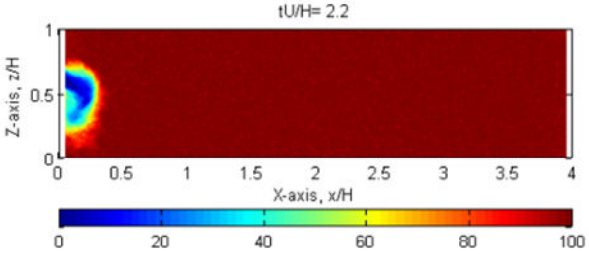

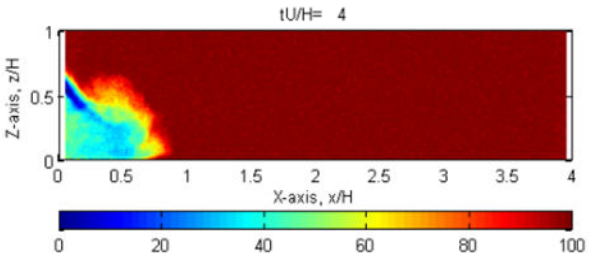

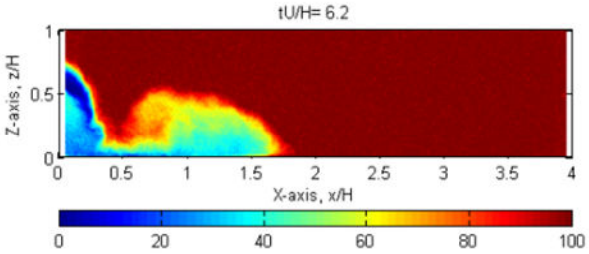

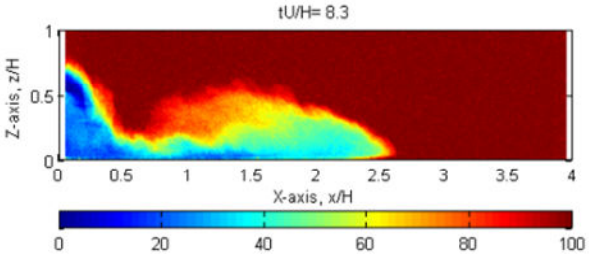

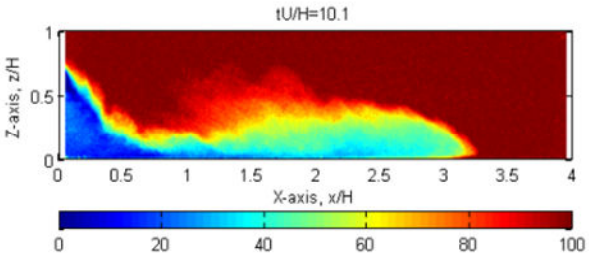

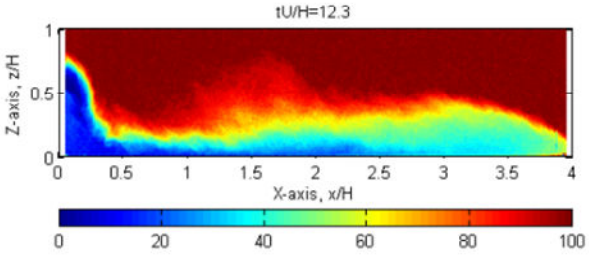

Numerical – Horizontal step opening

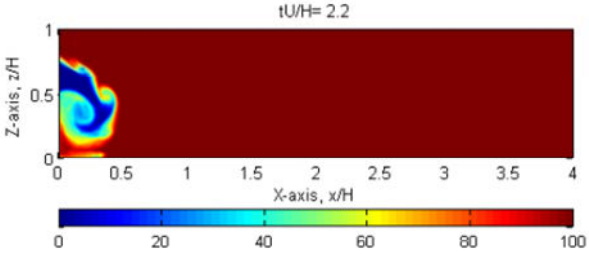

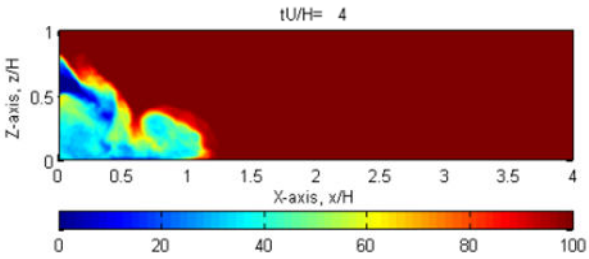

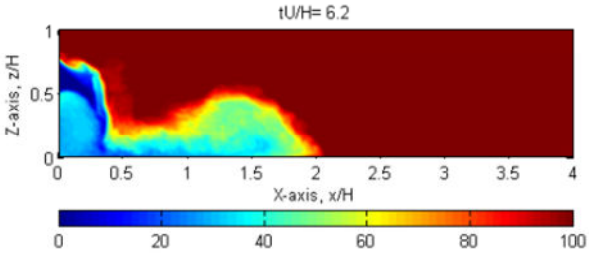

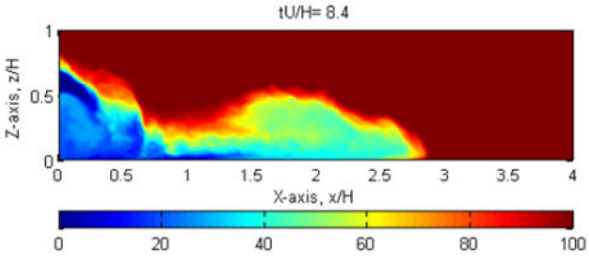

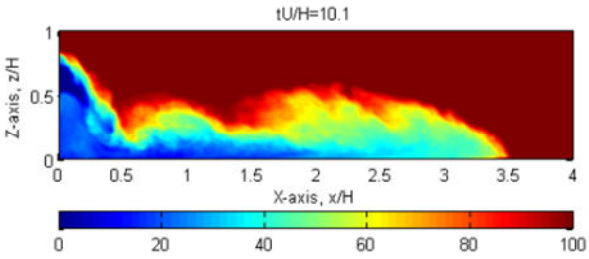

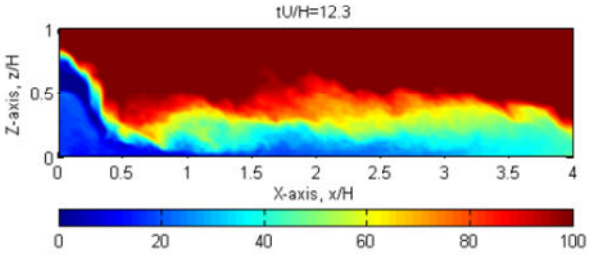

Experimental – Vertical slot opening

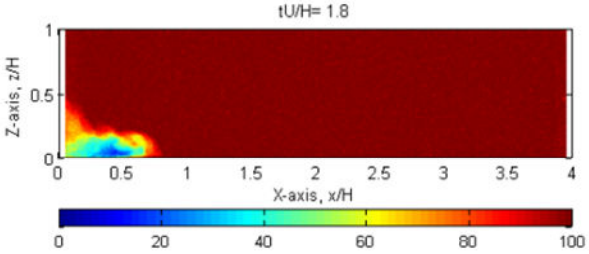

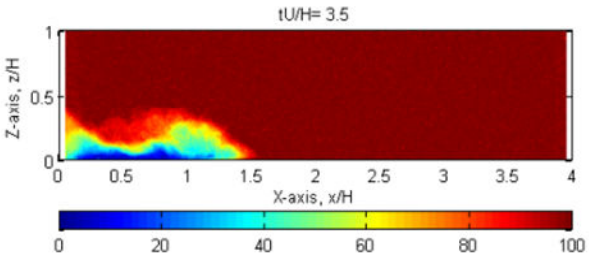

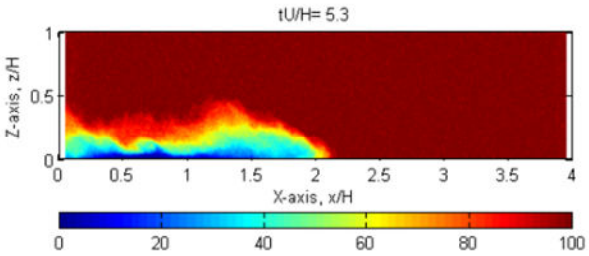

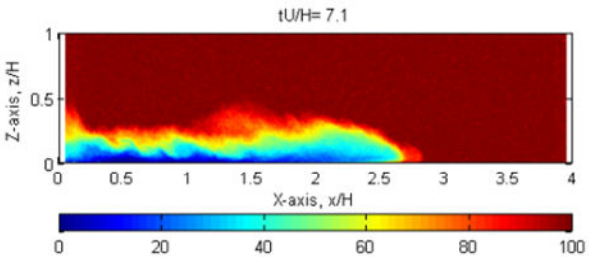

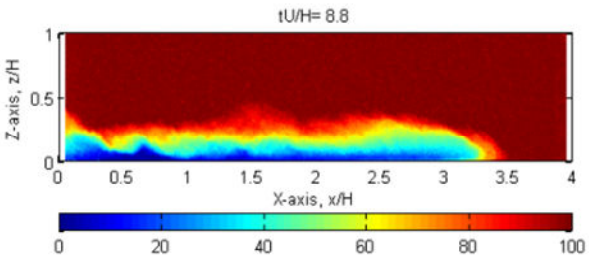

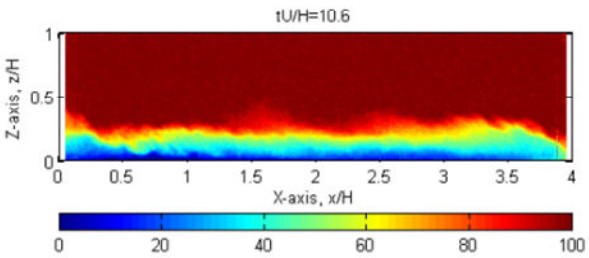

Numerical – Vertical slot opening

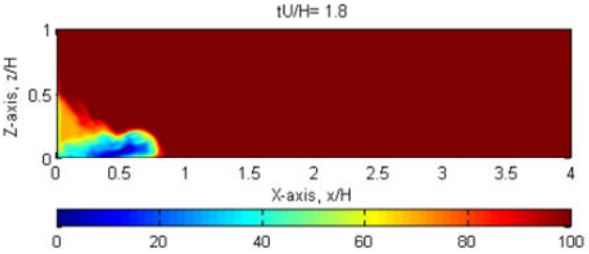

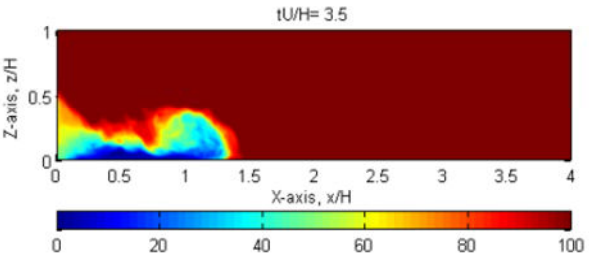

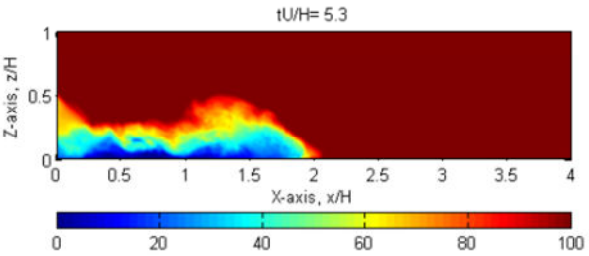

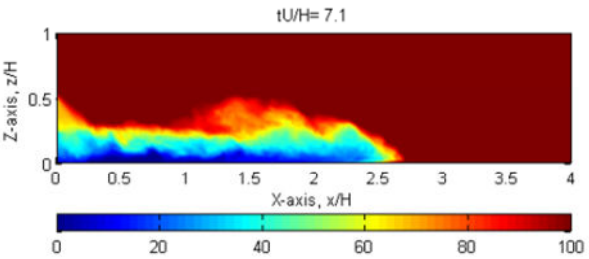

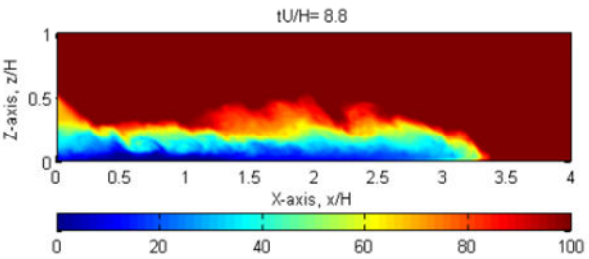

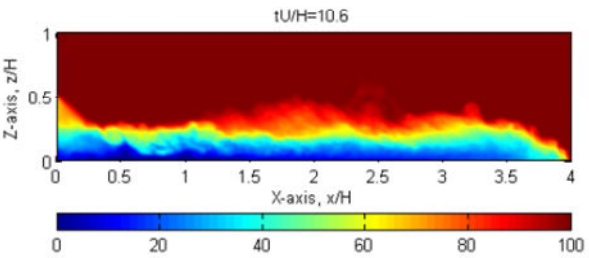

Experimental – Door opening

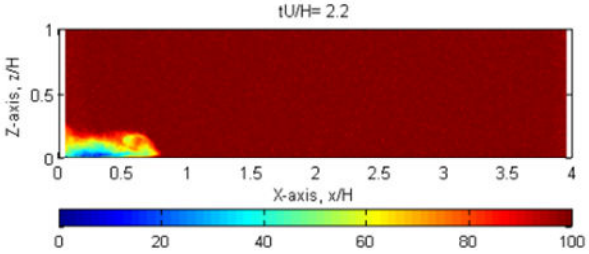

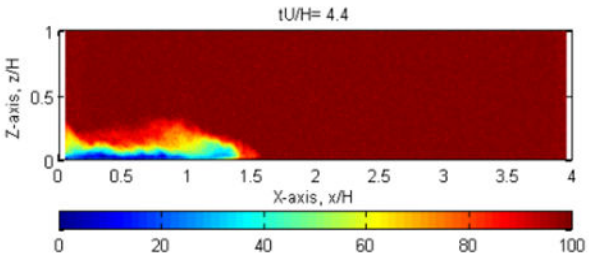

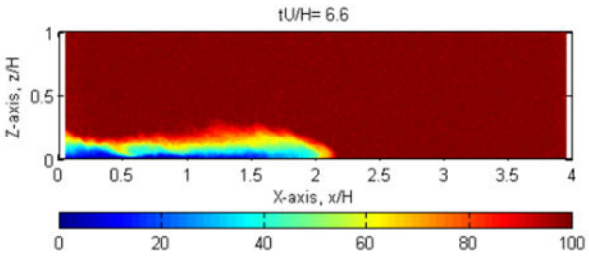

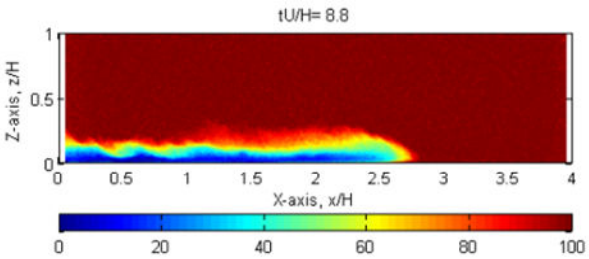

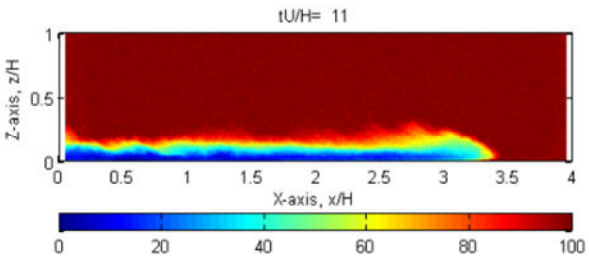

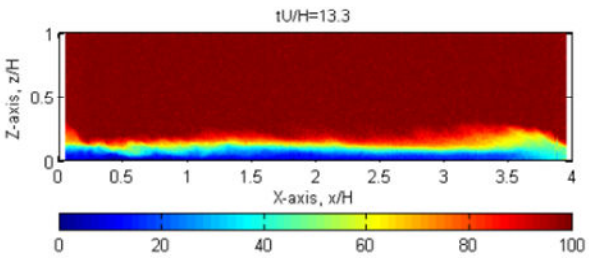

Numerical – Door opening

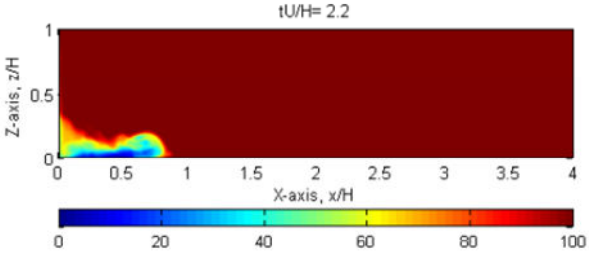

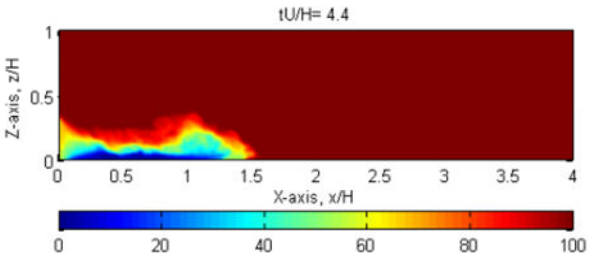

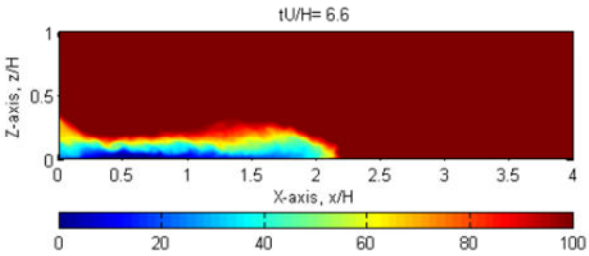

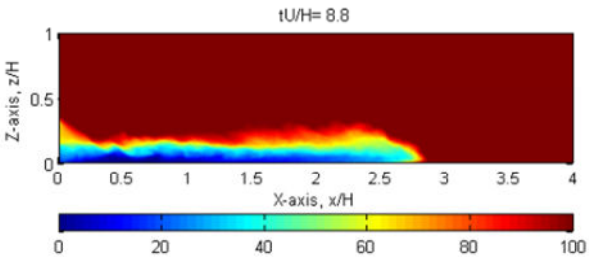

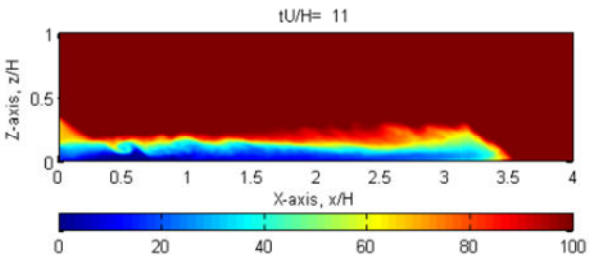

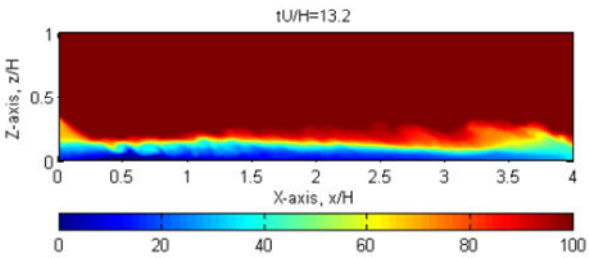

Experimental – Window opening

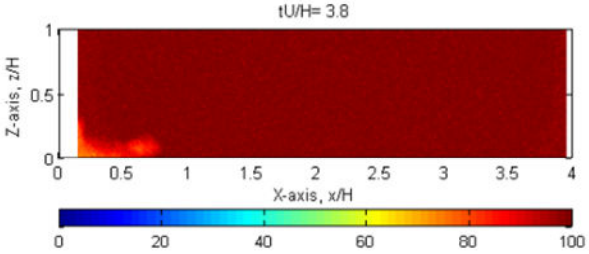

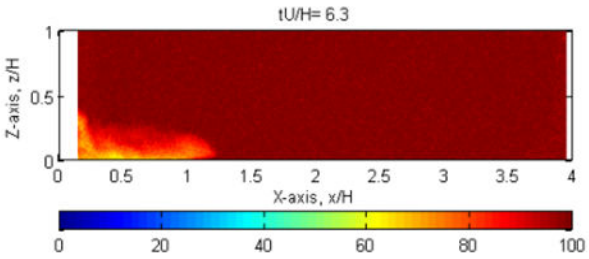

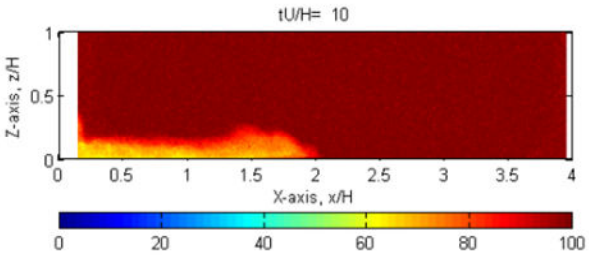

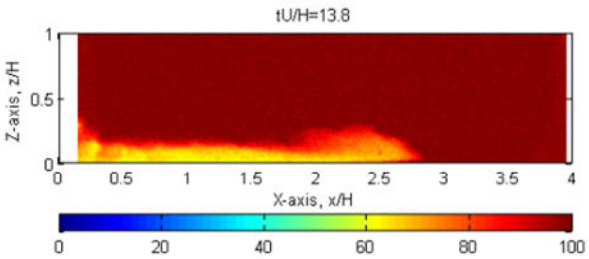

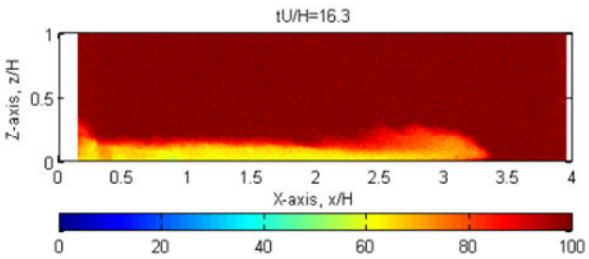

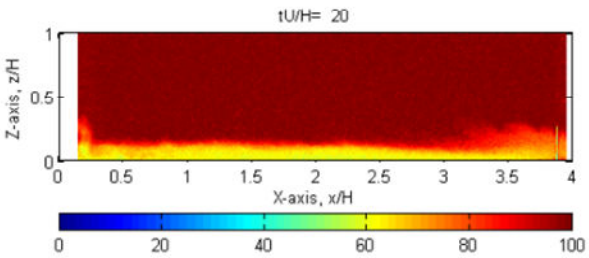

Numerical – Window opening

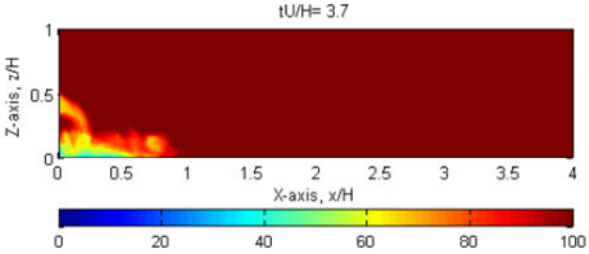

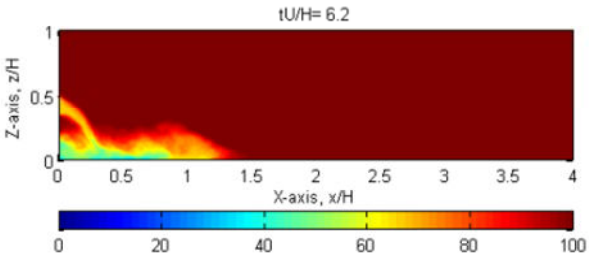

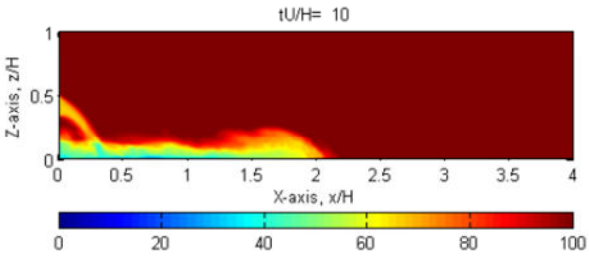

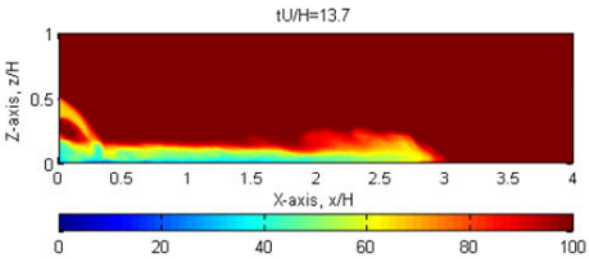

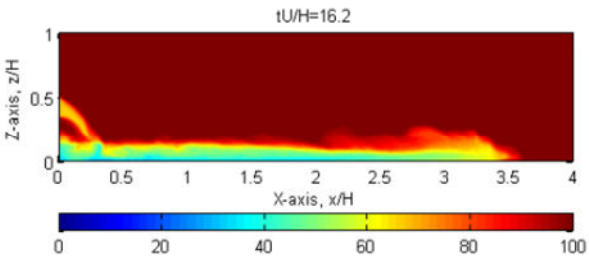

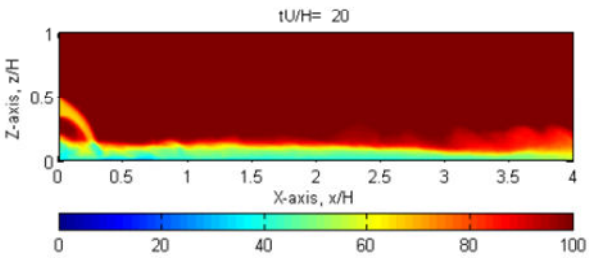

C.3 Magnitude of Difference in Relative Concentration

The magnitude of the difference between the experimental and numerical width-integrated relative concentration field time sequences are presented below for the different opening geometries. The sequences consist of six frames for each of the flows. The scale is in relative concentrations 0% to 50%, with shaded regions representing differences.

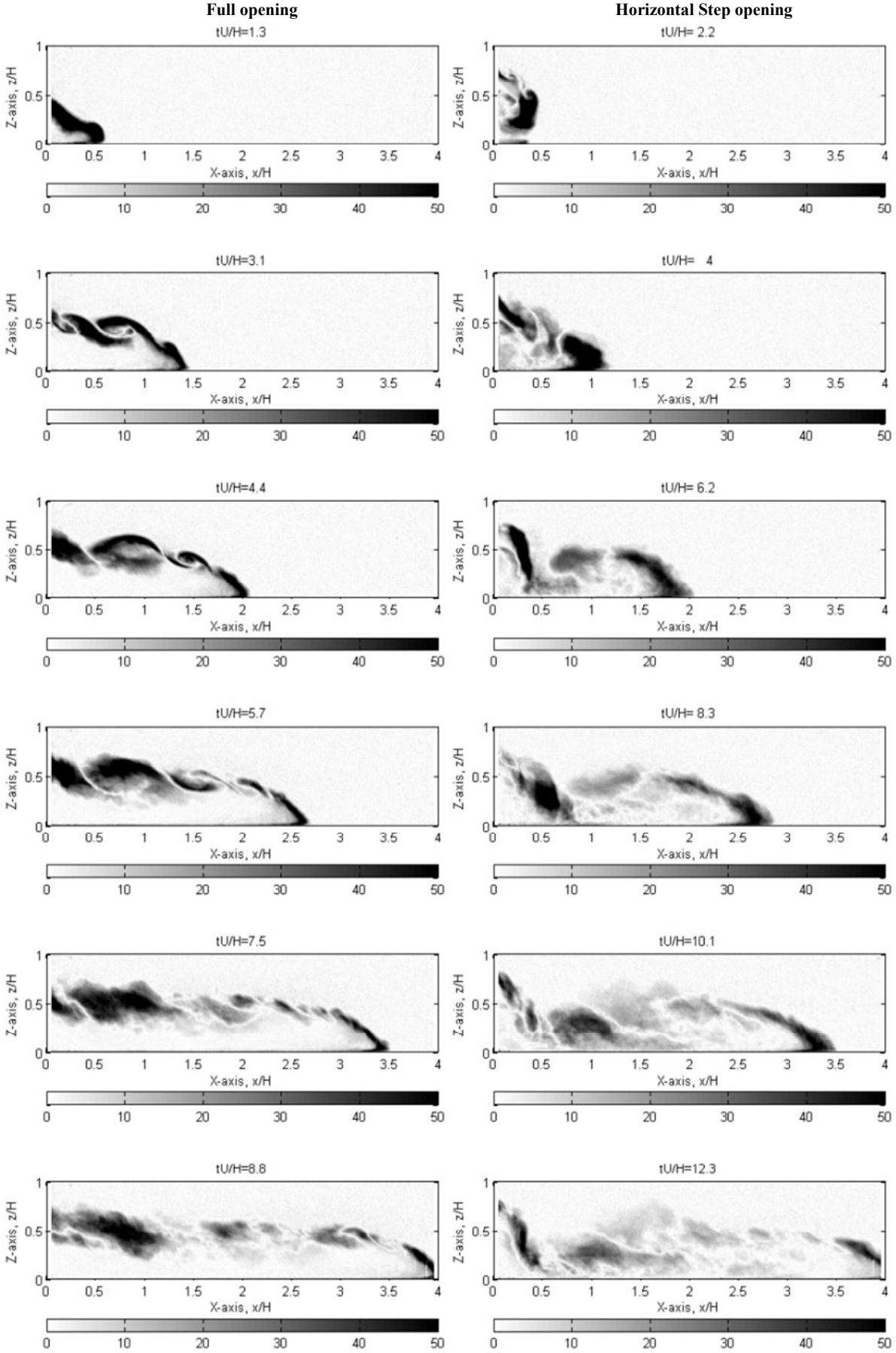
Full opening
Horizontal Step opening
tU/H=1.3
tU/H= 2.2
tU/H=3.1
tU/H= 4
tU/H=4.4
tU/H= 6.2
tU/H=5.7
tU/H= 8.3
tU/H=7.5
tU/H=10.1
tU/H=8.8
tU/H=12.3
Z-axis, z/H
X-axis, x/H

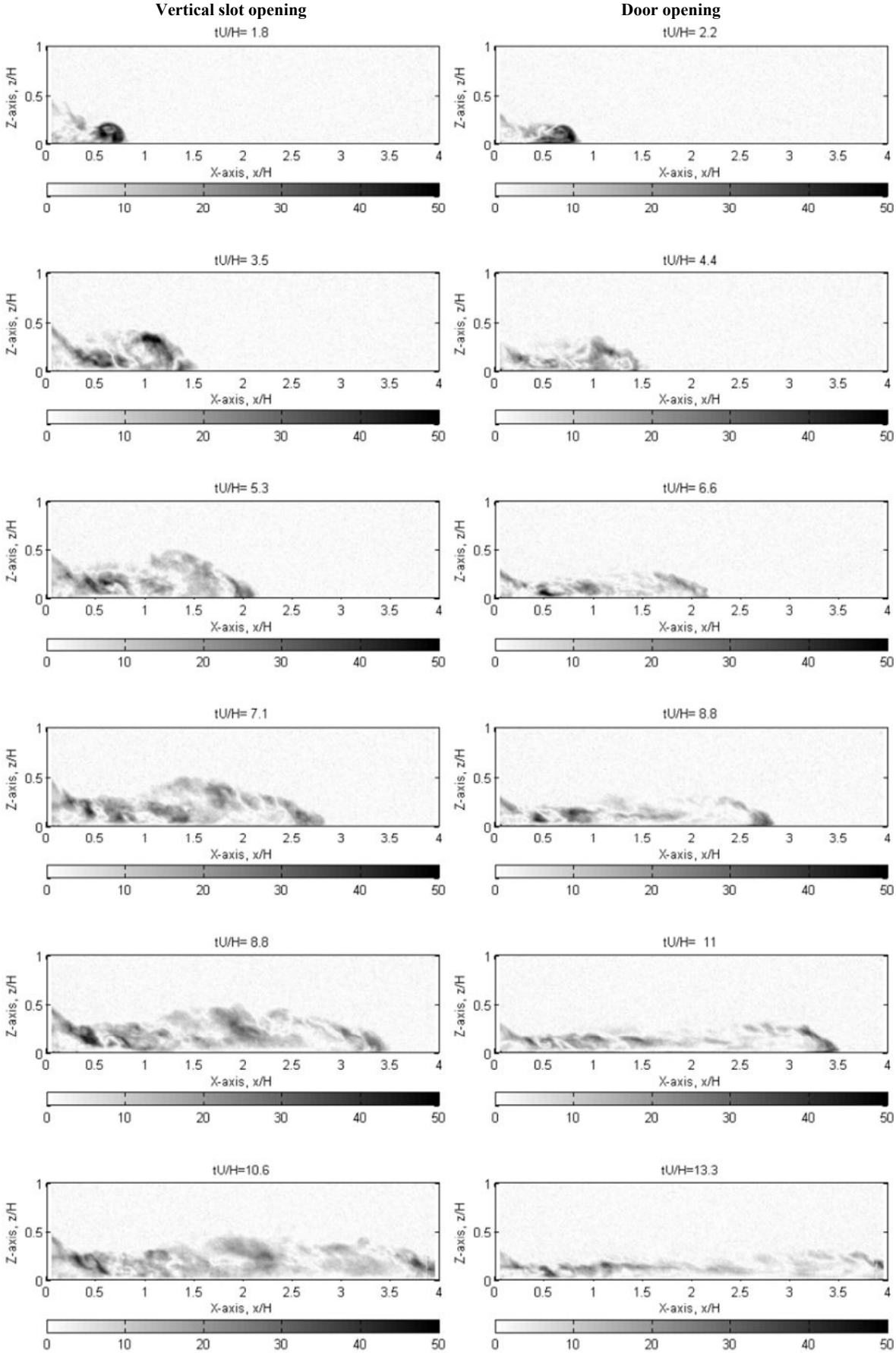
Vertical slot opening
Door opening
tU/H= 1.8
tU/H= 2.2
tU/H= 3.5
tU/H= 4.4
tU/H= 5.3
tU/H= 6.6
tU/H= 7.1
tU/H= 8.8
tU/H= 8.8
tU/H= 11
tU/H=10.6
tU/H=13.3
Z-axis, z/H
X-axis, x/H

Window opening

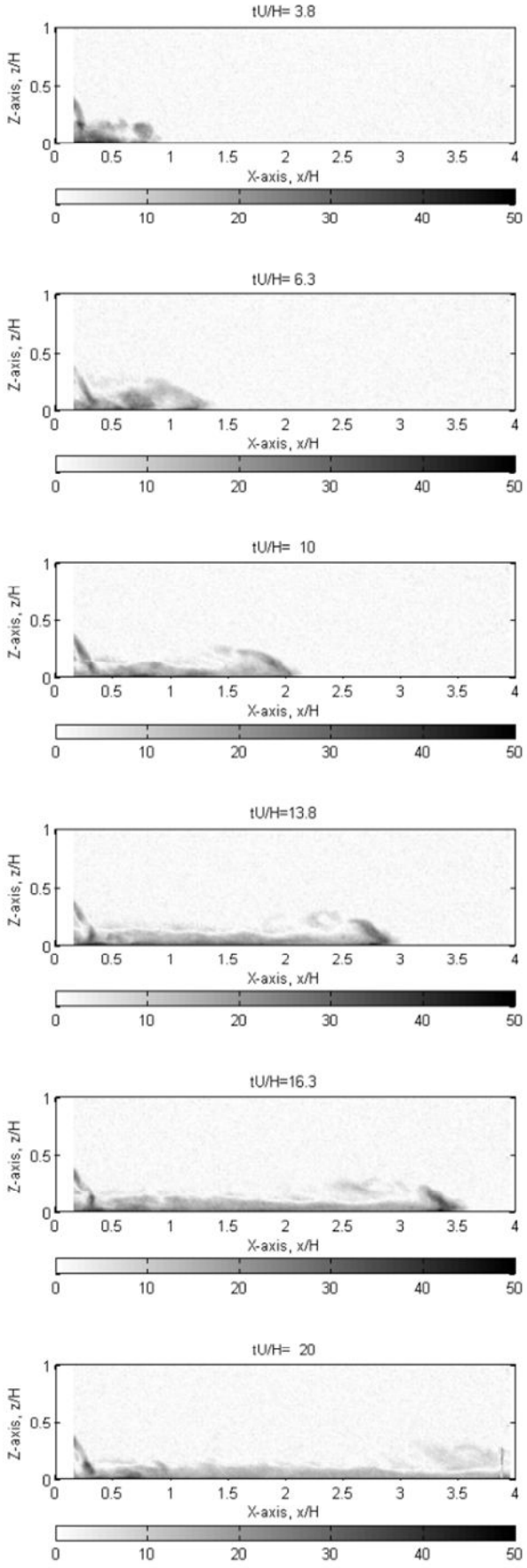

C.4 Predicted Flammable Region Time Sequences

The shaded regions, in the time sequences presented below, indicate the extent of predicted flammable regions at different times. These flammable regions are shaded and represent relative concentrations between 17% and 37%, and apply to a methane fuel with typical initial conditions from the experiments of Fleischmann (1994). Experimental and numerical results are presented for the different compartment opening geometries.

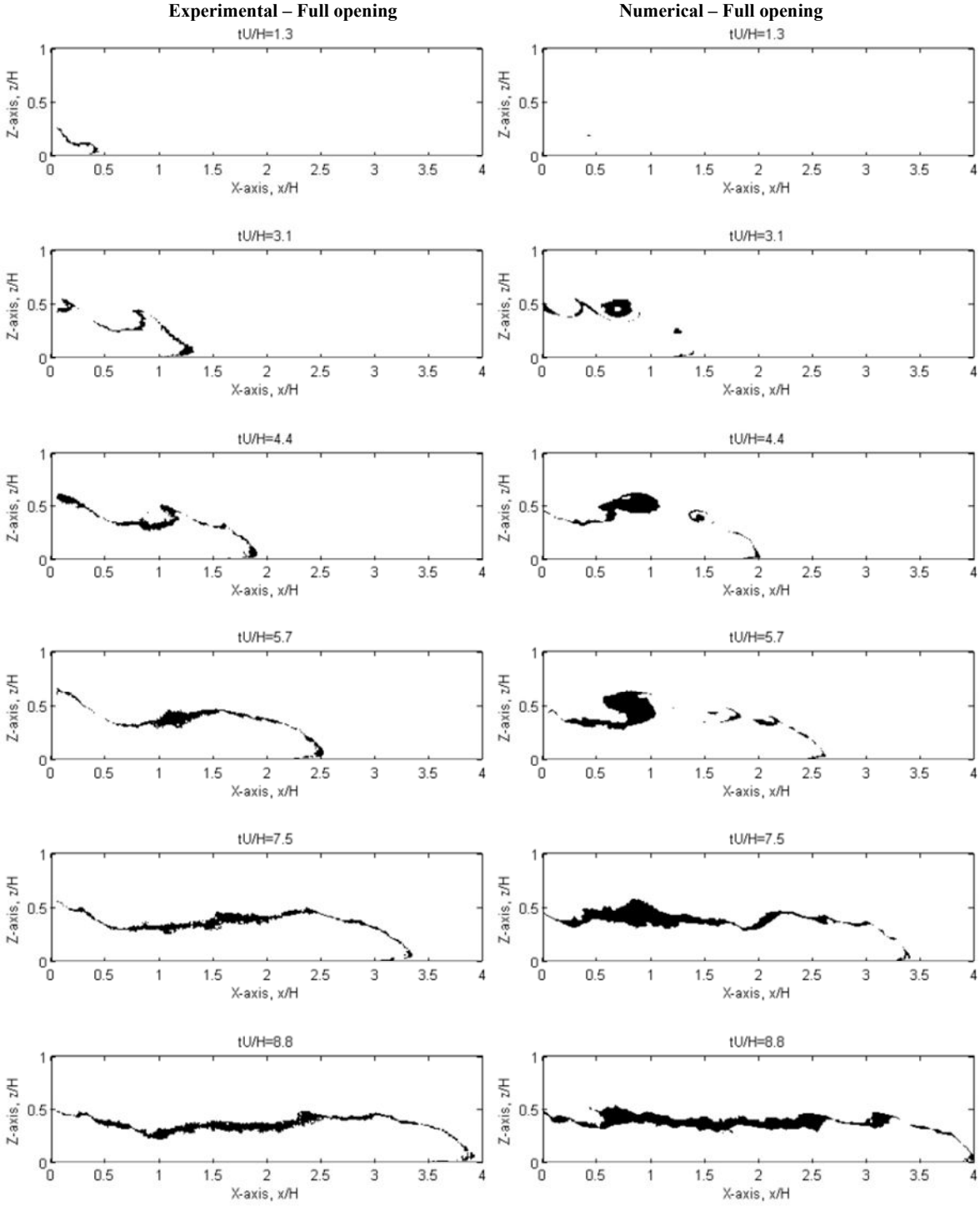
Experimental – Full opening
Numerical – Full opening
tU/H=1.3
tU/H=3.1
tU/H=4.4
tU/H=5.7
tU/H=7.5
tU/H=8.8
Z-axis, z/H
X-axis, x/H

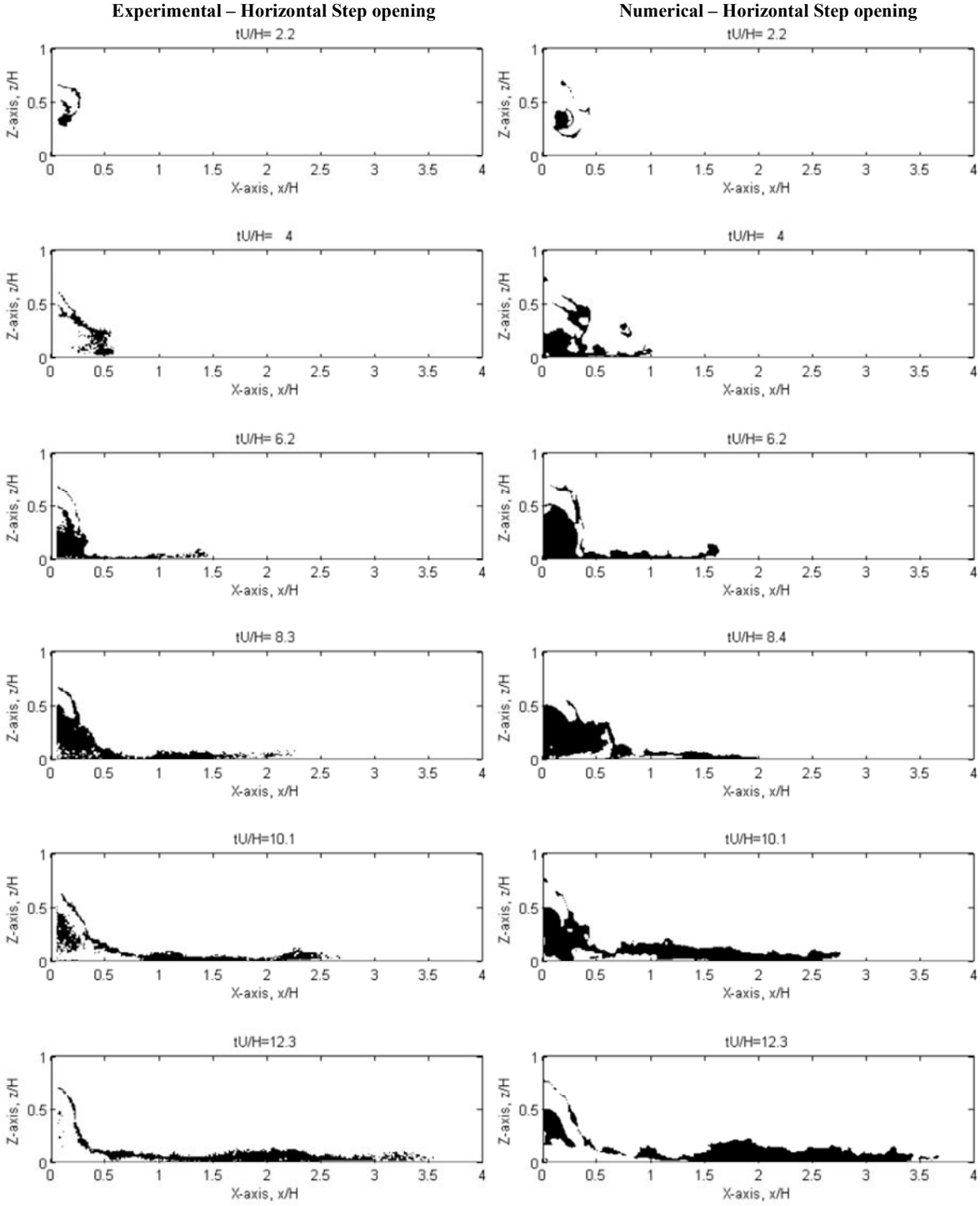
Experimental – Horizontal Step opening
Numerical – Horizontal Step opening
tU/H= 2.2
tU/H= 4
tU/H= 6.2
tU/H= 8.3
tU/H= 8.4
tU/H=10.1
tU/H=12.3
Z-axis, z/H
X-axis, x/H

Experimental – Vertical Slot opening

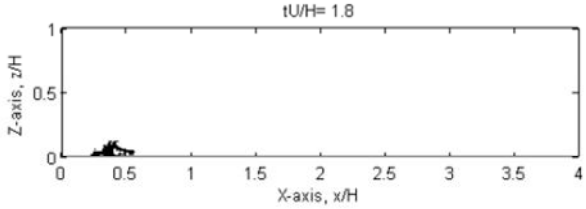

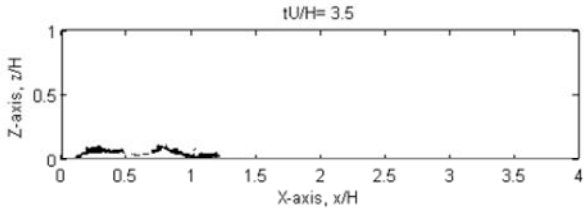

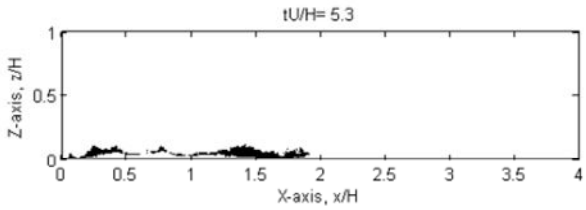

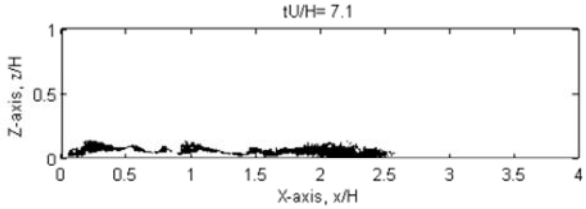

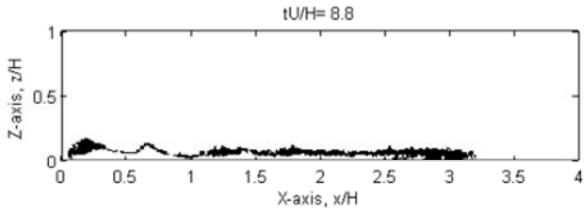

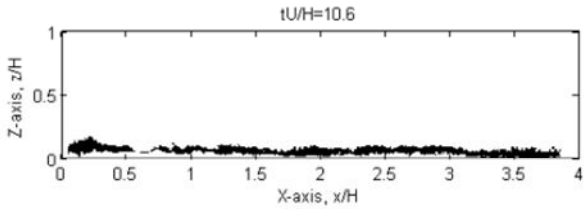

Numerical – Vertical Slot opening

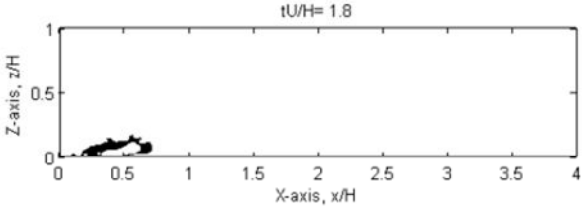

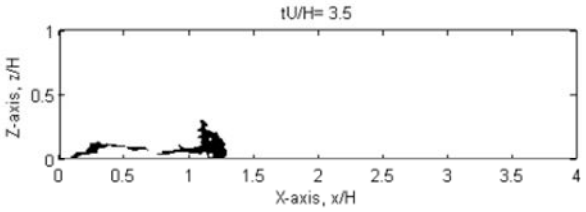

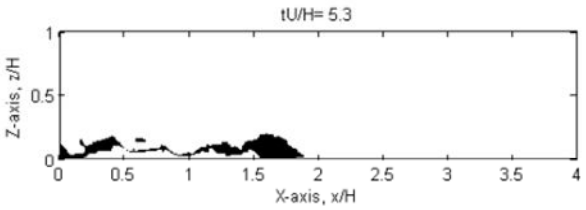

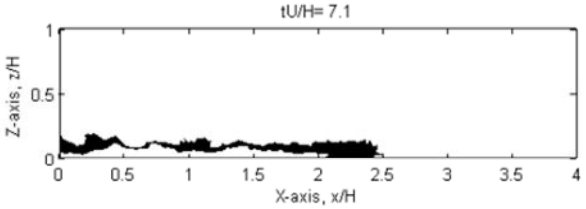

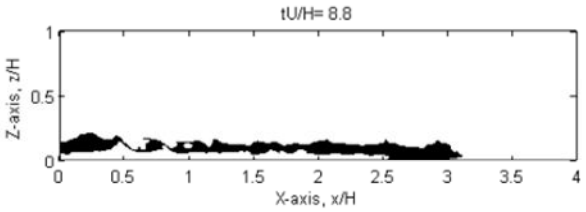

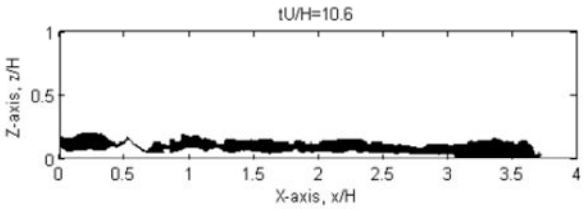

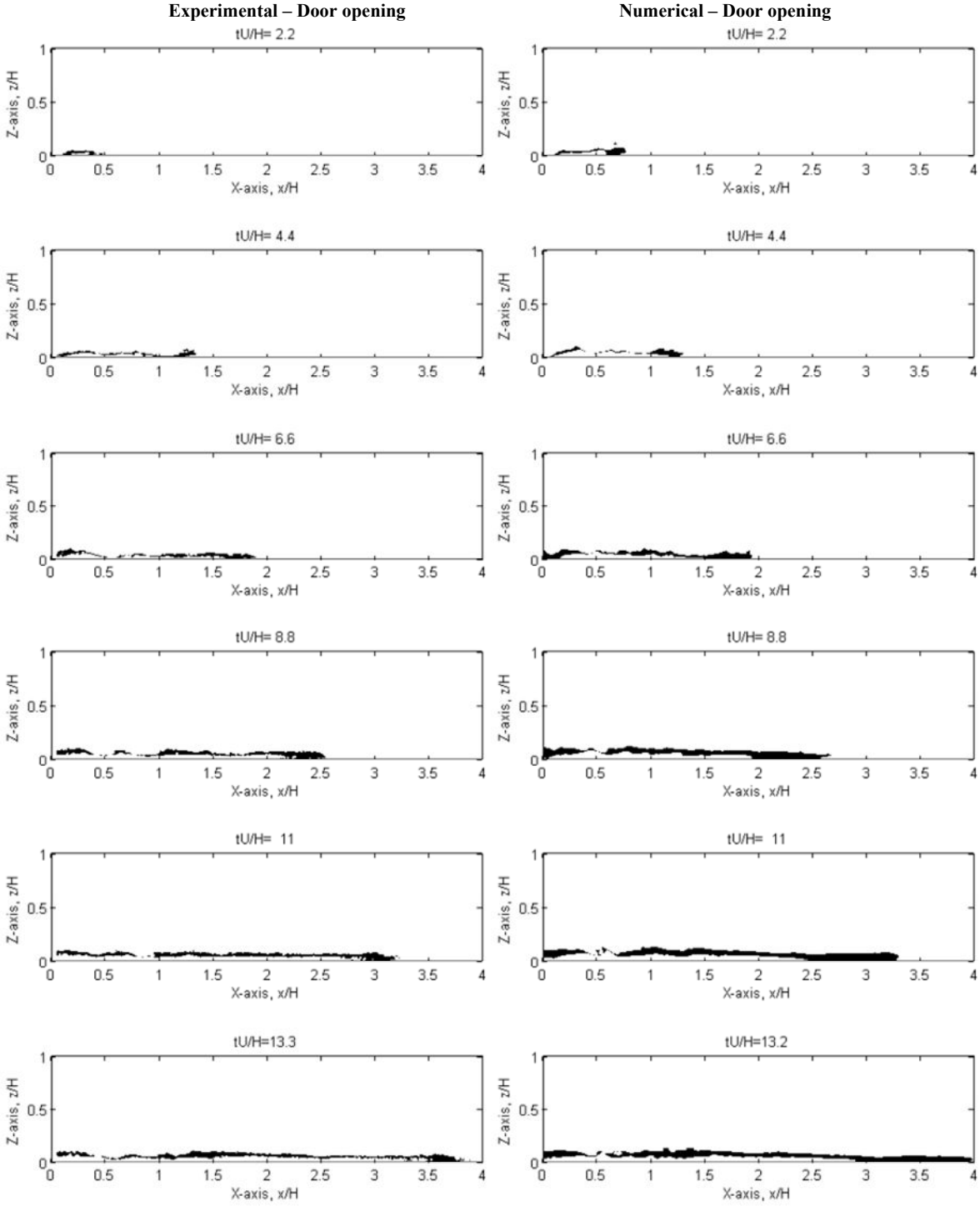
Experimental – Door opening
Numerical – Door opening
tU/H= 2.2
tU/H= 4.4
tU/H= 6.6
tU/H= 8.8
tU/H= 11
tU/H=13.3
tU/H=13.2
Z-axis, z/H
X-axis, x/H

Experimental – Window opening

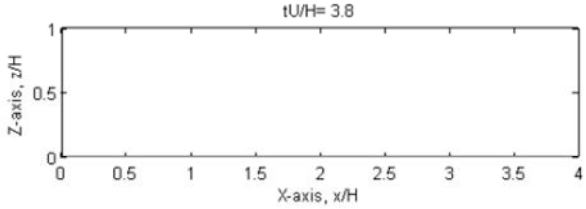

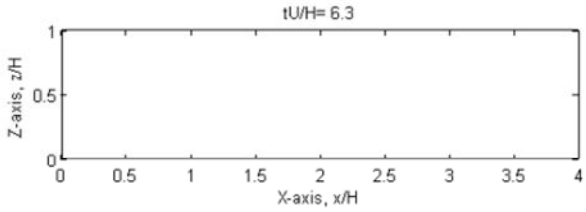

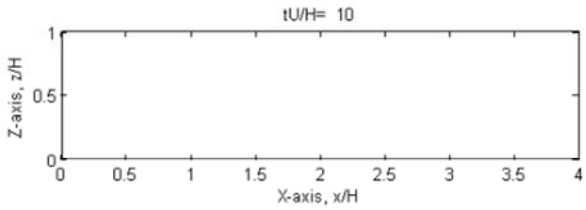

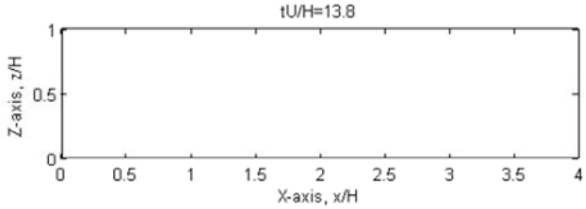

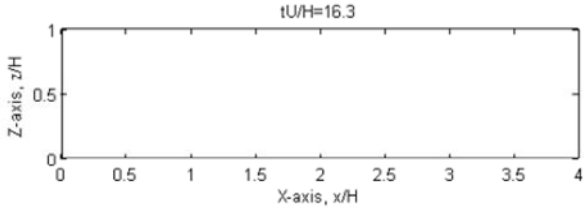

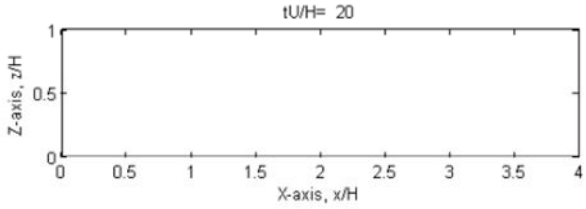

Numerical – Window opening